UNIVERSITY OF LJUBLJANA
FACULTY OF MATHEMATICS AND PHYSICS
PHYSICS DEPARTMENT

Irena Dolenc

Development of Beam Conditions Monitor for the ATLAS experiment

DOCTORAL THESIS

ADVISOR: Prof. Dr. Vladimir Cindro
COADVISOR: Prof. Dr. Marko Mikuž

Ljubljana, 2008

UNIVERZA V LJUBLJANI
FAKULTETA ZA MATEMATIKO IN FIZIKO
ODDELEK ZA FIZIKO

Irena Dolenc

Razvoj sistema za spremljanje kakovosti curka protonov pri eksperimentu ATLAS

DISERTACIJA

MENTOR: Prof. Dr. Vladimir Cindro
SOMENTOR: Prof. Dr. Marko Mikuž

Ljubljana, 2008

Abstract

If there is a failure in an element of the accelerator the resulting beam losses could cause damage to the inner tracking devices of the experiments. This thesis presents the work performed during the development phase of a protection system for the ATLAS experiment at the LHC. The Beam Conditions Monitor (BCM) system is a stand-alone system designed to detect early signs of beam instabilities and trigger a beam abort in case of beam failures. It consists of two detector stations positioned at $z=\pm1.84$ m from the interaction point. Each station comprises four BCM detector modules installed symmetrically around the beam pipe with sensors located at r=55 mm. This structure will allow distinguishing between anomalous events (beam gas and beam halo interactions, beam instabilities) and normal events due to proton-proton interaction by measuring the time-of-flight as well as the signal pulse amplitude from detector modules on the timescale of nanoseconds. Additionally, the BCM system aims to provide a coarse instantaneous luminosity measurement complementary to the main ATLAS luminosity monitor.

Radiation hard sensor devices capable of producing fast signals with 1MIP sensitivity were required for the BCM system. Two different sensor materials were considered: Polycrystalline Chemical Vapour (pCVD) diamond and n-type thin epitaxial (epi) silicon. The annealing study of irradiated epi samples at an annealing temperature of 20°C proved the epi material to be radiation hard in terms of effective dopant concentration. The results were found to agree with the results obtained by a different group at elevated annealing temperatures. However, the performance of epi devices was measured to be inferior to pCVD diamond sensors in terms of BCM detector module signal to noise ratio. Thus, the pCVD diamond was chosen for the BCM sensor material in the end.

Numerous measurements have been performed during the development in order to optimise the BCM system performance. These incorporate characterisation of the diamond sensors, tests of the detector modules with test beam pions and ^{90}Sr electrons as well as tests with the digitisation electronics included. The most relevant results are discussed here. An estimate of the expected BCM system performance at the end of readout chain in ATLAS is also given.

Keywords:
LHC, ATLAS, beam conditions monitor, semiconductor radiation detectors, pCVD diamond sensors, epitaxial silicon sensors, annealing, neutron and proton damage

PACS:
`29.27.Fh`; Beams in particle accelerators: Beam characteristics
`29.40.Wk`; Radiation detectors: Solid-state detectors
`85.30.De`; Semiconductor-device characterization, design and modeling
`29.27.Fh`; Radiation effects on specific materials: Semiconductors

Izvleček

V primeru odpovedi delovanja katerega od elementov pospeševalnika lahko posledične izgube curka povzročijo škodo v notranjih sledilniških detektorjih katerega od eksperimentov. Pričujoča disertacija predstavlja delo opravljeno skozi razvojno fazo zaščitnega sistema načrtovanega za eksperiment ATLAS ob pospeševalniku LHC. Namen tega sistem za spremljanje kakovosti curka (BCM–Beam Conditions Monitor) je detekcija zgodnjih znakov nestabilnosti protonskega curka ter proženje zaustavitve curka v primeru nesreče. Sestavljen je iz dveh detekotrskih postaj pri z=± 1.84 m okrog interakcijske točke. Vsaka postaja obsega štiri detektorske module, ki so postavljeni simetrično okrog curkovne cevi, s senzorji pri r=55 mm. Ta struktura bo omogočala razlikovanje anomalnih dogodkov (inerakcije curka z residualnim plinom v curkovni cevi, interakcije v halu curka, nestabilnosti curka) od normalnih dogodkov, ki so posledica protonskih interakcij. To bo doseženo preko merjenja časa preleta ter amplitude analognih pulzov iz detektorskih modulov na časovni skali ns. Dodatno bo sistem BCM omogočal meritve trenutne luminoznosti kot komplementarno informacijo k glavnemu sistemu za spremljanje luminoznosti pri eksperimentu ATLAS.

Senzorji sistema BCM morajo biti sevalno odporni s hitrimi signali ter občutljivostjo na minimalno ionizirajoče delce. Obravnavali smo dva različna senzorska materiala: polikristalni (pCVD) diamant in tanek epitaksialni silicij tipa n. Izmerili smo časovni razvoj okrevanja efektivne koncntracije primesi in zapornega toka po obsevanju epi diod. Med okrevanjem so bile diode na temperaturi 20°C. Meritve so potrdile visoko sevalno odpornost epi material glede efektivne koncentracije primesi. Rezultati teh meritev se ujemajo z rezultati skupine, ki je podobne meritve opravila za okrevanje pri povišanih temperaturah. Izmerjeno razmerje signal-šum detektorskega modula je bil z epi diodo precej slabši kot s pCVD diamantom. Zato so bili na koncu za senzorski material sistema BCM izbrani pCVD diamanti.

Da bi optimizirali delovanje sistema BCM, smo skozi njegov razvoj opravili različne meritve. Te vključujejo karakterizacijo samih diamantov, preizkušanje detektorskih modulov, tako v testnem curku delcev kot z elektroni iz izvora ^{90}Sr ter meritve, ki vključujejo tudi elektroniko za digitizacijo analognih signalov. Ocenili smo tudi delovanje sistema BCM na koncu bralne verige, ki ga pričakujemo v ATLAS-u.

Ključne besede:
LHC, ATLAS, spremljanje kakovosti curka, polprevodniški detektorji sevanja, pCVD diamantni senzor, epitaxialni silicijev senzor, okrevanje po obsevanju, škoda po obsevanju z nvtroni in protoni
PACS:
`29.27.Fh`; Curki delcev v pospeševalnikih: karakteristike curka
`29.40.Wk`; Detektorji sevanja: polprevodniški detektorji
`85.30.De`; Karakterizacija, načrtovanje in modeliranje polprevodniških detektorjev
`29.27.Fh`; Učinek sevanja na določen material: polprevodniki

CONTENTS

1 Introduction **3**

2 Beam conditions monitor in ATLAS **5**
2.1 The ATLAS experiment at the LHC 6
2.1.1 The Large Hadron Collider 6
2.1.2 The ATLAS detector 7
2.1.3 Beam accidents and protection 10
2.2 ATLAS BCM description 13
2.2.1 Principle of operation and requirements 13
2.2.2 Detector modules and sensors 16
2.2.3 Overall readout scheme 19

3 Solid state detectors **21**
3.1 Basics of Semiconductor and Insulator physics 22
3.1.1 Energy band structure 22
3.1.2 Density of charge carriers 25
3.1.3 Charge carrier transport 27
3.1.4 Charge carrier generation and recombination 29
3.2 Signal generation 34
3.2.1 Trapping of drifting charge 36
3.3 Silicon detectors 38
3.3.1 Principle of operation: p–n junction 38
3.3.2 Silicon detector fabrication 43
3.3.3 Radiation damage in Silicon detectors 46
3.4 pCVD diamond detectors 56
3.4.1 CVD diamond growth 56
3.4.2 Operation of diamond detectors 59

4 Measurements with pCVD diamonds **64**
4.1 I–V measurements 65
4.2 BCM detector modules 69
4.2.1 MGH test beam 69
4.2.2 Test beam at CERN SPS in 2004 75
4.2.3 Test beam measurements in 2006 81

4.2.4 Measurements with ^{90}Sr source . . . 87
4.3 Digitisation with NINO . . . 98
4.3.1 Test beam measurements . . . 98
4.3.2 Measurements with ^{90}Sr source . . . 105
4.3.3 Noise rates of the installed modules . . . 111

5 Measurements with epitaxial silicon material 112
5.1 Radiation hardness . . . 114
5.1.1 Experimental setup . . . 115
5.1.2 Annealing of effective dopant concentration . . . 117
5.1.3 Annealing of leakage current . . . 123
5.2 Measurements with the BCM detector modules . . . 125

6 Conclusions 129

7 Povzetek doktorskega dela 132
7.1 Uvod . . . 133
7.2 Opis sistema BCM pri ATLAS-u . . . 134
7.2.1 Detektorski moduli . . . 137
7.2.2 Celotna bralna shema . . . 138
7.3 Osnove delovanja silicijevih in diamantnih detektorjev . . . 140
7.4 Meritve s pCVD diamanti . . . 142
7.4.1 Detektorski moduli . . . 143
7.4.2 Digitizacija s čipom NINO . . . 147
7.5 Meritve z epitaksialnim silicijem . . . 153
7.5.1 Sevalna odpornost epitaksialnih diod . . . 153
7.5.2 Meritve z BCM detektorskim modulom . . . 159
7.6 Zaključek . . . 161

Acknowledgements 163

Bibliography 164

A Properties of silicon and diamond 170

B I–V measurements of bare diamonds and assemblies 171

C BCM detector modules 174

D NINO electronics board 176

CHAPTER 1

INTRODUCTION

In the past decades a set of theoretical endeavours, concerning the elementary particles and their interactions, lead to the model known as the Standard Model of Particle Physics. In this model all matter is made of two kinds of elementary particles, quarks and leptons, while the interactions between these particles occur via the exchange of force mediator particles. The model requires three generations of matter particles, three types of force mediating bosons and one so–called Higgs boson to account for the particle masses. The Standard Model theoretical predictions of many new phenomena and a large number of new particles have been verified with an exceptional accuracy in a number of accelerator based experiments. However, the Higgs boson has not yet been observed and if found, it will be last missing piece which makes the Standard Model complete in its specific region of validity.

Despite the outstanding success of the Standard Model, a number of cosmological and theoretical issues remain unresolved by this model. Furthermore, there are several indications that the model breaks down at energy scales just above the reach of present experiments. The exact nature of physics beyond the Standard Model is not known. It might evolve supersymmetry (SUSY), extra spatial dimensions or something even more exotic.

A new circular collider, the Large Hadron Collider (LHC), will be put into service in the fall of 2008 at the European Laboratory for Particle Physics (CERN). It is designed to provide a possibility for completing our understanding of the Standard Model and to search for the physics beyond its limits. There will be four large experiments at the interaction points along the LHC tunnel. Two of them, ATLAS and CMS, are designed to explore the full field of physics offered by LHC. ALICE on the other hand is built to study physics of strongly interacting matter, by means of Pb-Pb collisions, while LHCb is a B-physics experiment, dedicated to study the CP violation in B-system, using low intensity proton-proton collisions.

Once in operation, LHC will circulate 2808 bunches per colliding beam, each bunch consisting of 1.1×10^{11} protons at energy of 7 TeV. With enormous energy stored in each of the beams, which will be about 200-times more compared to maximum value in previous accelerators like HERA or Tevatron, LHC will enter a new domain. Safe operation of the machine with such parameters is challenging. Past experiences with beam accidents teach us that experiments should employ a dedicated protection system to protect them from beam failures. For example, at the Tevatron, the beam damaged part of central CDF detector due to misfiring of the beam dump kicker magnet. Therefore, LHC experiments have decided to develop their own protec-

tion systems, so called Beam Conditions Monitors (BCMs), in addition to those provided by the accelerator.

This thesis is concentrating on the BCM system designed to protect the ATLAS experiment. Due to their high radiation tolerance, two different materials have been considered for the sensor part of ATLAS BCM, polycrystalline chemical vapour deposition (pCVD) diamond and n-type epitaxial silicon. Studies, presented here, showed that with pCVD diamond better performance of BCM system in terms of signal to noise ratio. Thus, pCVD diamond was chosen as the sensor material in ATLAS BCM system.

The second chapter of the thesis briefly describes the LHC and ATLAS experiment together with possible beam failures. This is followed by a section which is focused on operation of ATLAS BCM system. Here the basic principle of operation and requirements are explained. A complete description of the system, its detector modules, the overall readout scheme and its role in ATLAS experiment is given.

The third chapter deals with solid state detectors with the main focus on silicon and diamond sensors. After a review of semiconductor and insulator physics the basic principle of operation, manufacturing and radiation hardness for both, silicon and diamond detectors, is discussed.

The last two chapters deal with the studies performed in the scope of this work. The fourth chapter presents the results obtained with pCVD diamond sensors, while the fifth chapter is focused on measurements with epitaxial silicon. Measurements with pCVD diamond include studies of analogue and digital BCM signals during different stages of the ATLAS BCM system development. An estimate of overall BCM system performance in ATLAS is also given. Annealing studies of effective dopant concentration and leakage current at 20°C were performed with irradiated thin epitaxial silicon pad sensors. The results are compared with the results obtained by Hamburg group at annealing temperature of 60°C and 80°C. The performance of BCM detector module, equipped with unirradiated 50 μm epi sensor, was also measured and is presented at the end of fifth chapter.

Chapter 2

Beam conditions monitor in ATLAS

The total energy stored in one beam at LHC will be 350 MJ, which is more than two orders of magnitude above the maximum beam energy stored in previous high energy colliders (Tevatron, HERA). If there is failure in an element of the accelerator, the resulting beam losses could cause damage not only to the machine but also to the experiments. In order to cope with these extreme conditions a protection system has been developed for the LHC. This relies on both passive and active protection. The former is based on absorption and aperture limitation of beam losses by collimators and absorbers. The latter employs fast detection of beam losses by beam loss and beam position monitors, quench detectors, etc. followed by a fast and controlled extraction of the beam. In addition to these protection systems, provided by the machine, all LHC experiments have developed their own protection systems. These Beam Conditions Monitor (BCM) systems are stand-alone system, designed to detect potentially harmful beam conditions and trigger a beam abort on the appropriate time scale if needed. In addition to protection, they also provide the means of monitor particle rates in the experiment.

Since the thesis is focused on the BCM system in ATLAS, this chapter starts with a brief overview of LHC [B$^+$04] and the ATLAS experiment [ATL08]. Possible beam failures and protection against them are given. This is followed by a section, where the basic idea of the ATLAS BCM system is explained together with its requirements. An overall description of the BCM signal processing is presented at the end.

2.1 The ATLAS experiment at the LHC

2.1.1 The Large Hadron Collider

The Large Hadron Collider (LHC) is a proton–proton collider situated in the 27 km long circular tunnel, which was previously used by the LEP collider at CERN, located across the Swiss-French border near Geneva. Its startup is scheduled for fall 2008. The machine will accelerate two proton beams to an energy of 7 TeV per proton and bring them into head-on collision at four interaction points along the LHC ring. The resulting centre of mass energy of the collisions, 14 TeV, will be highest ever achieved. Prior to injection into the LHC, the protons are first accelerated to an energy of 450 GeV through the linear accelerator (Linac), Proton Synchrotron (PS) and Super Proton Synchrotron (SPS). After injection into the LHC, the acceleration continues until the protons reach their final energy of 7 TeV.

The two proton beams, orbiting in opposite directions, are steered around the LHC by more than 1200 superconducting dipole bending magnets, each generating a magnetic field with a

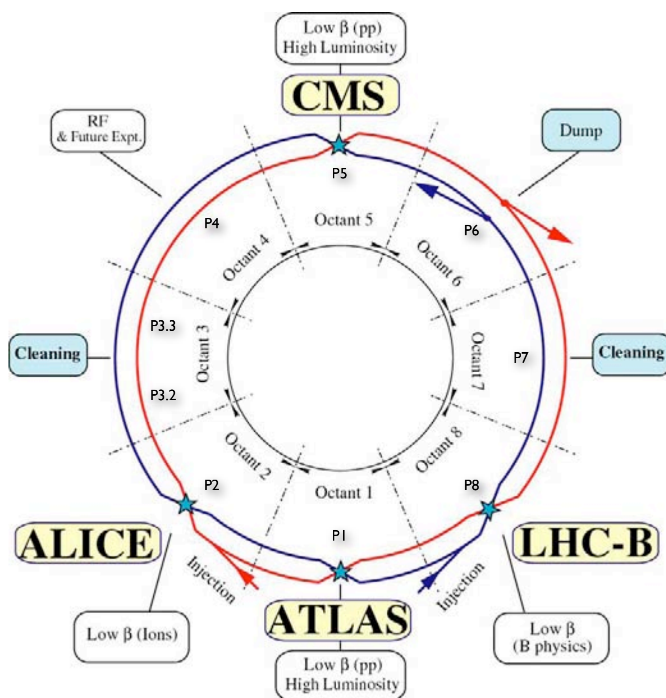

Figure 2.1: *Schematic view of the LHC ring layout.*

strength of 8.4 T. As the two proton beams counter rotate, they must circulate in opposite magnetic fields, therefore requiring separate vacuum beam pipes. The two pipes are housed within the same cryostat and mechanical structure with the 'twin' dipole magnets arranged in way that the return field from one ring provides the field to the other. Hundreds of additional superconducting magnets are installed for focusing and correcting the beam. The superconducting magnets are cooled by super-fluid liquid helium at a temperature of 1.9 K.

The beams will be structured in 2808 closely packed bunches. Each such bunch will contain 1.1×10^{11} protons. It will have a vertical spread[1] of $\sim$380 μm when injected, but will be squeezed to 16 μm at collision point. Its length[2] will be around 7.6 cm. The time interval between two successive bunches will be 25 ns resulting in 4×10^{7} bunch-bunch collisions per second. The rate of any given particle interaction, generated in the collisions is proportional to the interaction cross sections. The proportionality factor, called luminosity, is a parameter of the machine, and depends on the number of particles in the colliding bunches, the frequency of bunch-bunch collisions and the size of beam profile. The LHC design instantaneous luminosity at the interaction points of ATLAS and CMS is $10^{34}\mathrm{cm}^{-2}\mathrm{s}^{-1}$. As the machine is expected to run for 10^{7} seconds per year, this corresponds to an integrated luminosity of 100 fb^{-1} per year. Due to the high instantaneous luminosity, roughly 25 proton-proton collisions per bunch crossing are expected on average.

The LHC ring consists of eight octants joined by eight insertion regions (IR). The layout is shown in figure 2.1. Four of these insertion regions traverse interaction points (P) where the two proton beams collide. The ATLAS experiment is positioned at P1 in IR1. The RF system for acceleration is located in IR4. The clockwise beam is injected near the ALICE experiment (P2) and the anticlockwise beam near the LHCb experiment (P8). The extraction of the two beams is implemented in IR6. Apart from few specific collimators, the main collimating system is located in IR3 and IR7.

2.1.2 The ATLAS detector

Like in most of the colliding beam experiments, the structure of ATLAS (A Toroidal Lhc ApparatuS) follows an approximate cylindrical symmetry. It consists from a central barrel, where the sensor elements form cylindrical layers around the beam pipe, and two end-caps, where the elements are organised in wheels.

The detector coordinate system is right handed and the origin lies in the centre of the detector at the nominal interaction point. The z axis points along the beam line in the anti-clockwise direction, the x axis points towards the centre of LHC ring and the y axis upwards, but is inclined by 0.704 degrees from the vertical to adjust for the tilt of the tunnel. Due to its cylindrical shape, ATLAS usually adopts a polar coordinate system. The polar angle θ is the angle with the z axis, while the azimuthal angle ϕ is the angle from the x axis in xy plane. Instead of polar angle, pseudo-rapidity is often used, defined by $\eta = -\ln(\tan(\theta/2))$.

As shown in figure 2.2 the ATLAS detector measures 44 m in length, 25 m in diameter and

[1]This number corresponds to the RMS of the position in vertical direction

[2]The length refers to RMS of the position in the horizontal direction of the beam.

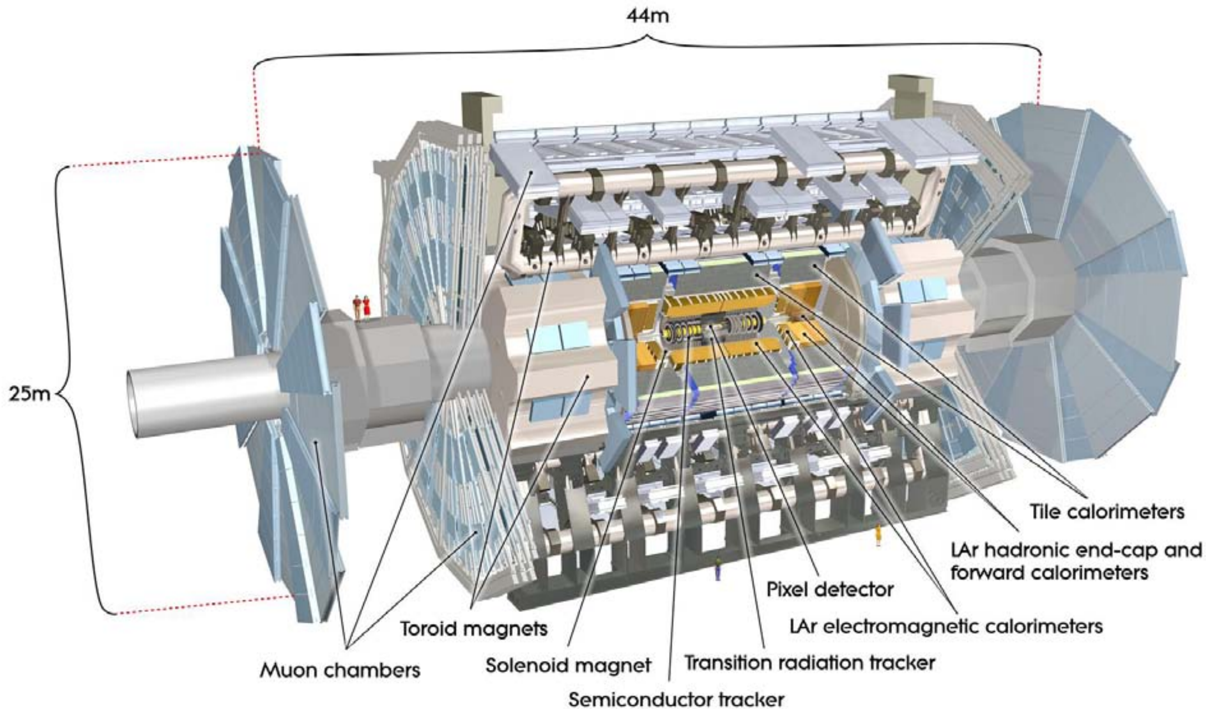

Figure 2.2: *Computer generated image of the ATLAS detector. Source [CDS].*

weighs approximately 7000 tons. It consists of three main sub-systems:

- The **Inner Detector (ID)** is positioned closest to the interaction point in ATLAS. Its primary task is to provide efficient tracking of charged particles in a homogeneous axial magnetic field of 2 T, generated by a central solenoid magnet, which surrounds the Inner Detector. Besides measuring the directions and momenta of charged particles, this tracking system also provides precise vertex reconstruction. Additionally, it has electron identification capabilities, primarily based on transition radiation supplementing the electron identification information provided by the electromagnetic calorimeter. The ID has three components: an innermost silicon **Pixel Detector**, followed by a silicon strip detector (the **SemiConductor Tracker**–SCT), and surrounded by a **Transition Radiation Tracker** (TRT), detector consisting of layers of drift straw tubes. The SCT and Pixel Detector cover the region with $|\eta|<2.5$, while the TRT has an acceptance of $|\eta|<2.0$.

- The goal of the **Calorimeter system**, surrounding the central solenoid magnet, is to stop, measure their energy and distinguish between photons, electrons and hadronic jets. It consists of an electromagnetic (EM) calorimeter in the inner part, covering the region $|\eta|<3.2$, a hadronic barrel calorimeter (Tile Calorimeter) with acceptance of $|\eta|<1.7$, hadronic end cap (HEC) covering $1.5<|\eta|<3.2$ and forward calorimeters (FCAL) covering $3.2<|\eta|<4.9$. All these subsystems are sampling type calorimeters. Liquid argon is used as active material in the inner most parts of calorimeter (EM calorimeter, HEC and FCAL). The EM

calorimeter has accordion shaped lead absorber plates as passive medium interleaved with liquid argon. For the HEC and lower z parts of the FCAL, copper is used as absorber while tungsten is used in the outer parts of FCAL.

- Outside the calorimeter system the **Muon Spectrometer** is located, which is by far the largest sub-detector in ATLAS. Muons with high transverse momentum are involved in many interesting physics signatures, therefore they should be used for triggering and accurately measured. The Muon system provides tracking of muons over large area and a muon trigger for the rest of ATLAS. A strong magnetic field of up to 4 T, generated by super-conducting air-core toroids, ensures that momentum measurements can be performed completely independent of the Inner Detector, where the background levels might be substantial at full luminosity. Four different technologies are implemented throughout the Muon system depending on η and purpose. For precise tracking measurements, Monitored Drift Tubes (MDTs) are used at lower η, while Cathode Strip Chambers (CSCs) are used in the region of $2<\eta<2.7$. Thin Gap Chambers (TGC) in the end-cap region and Resistive Plate Chambers (RPCs) in the barrel region provide the fast muon trigger.

The LHC production cross sections for interesting physical processes are expected to be rather low. The vast majority of events are so called soft QCD interactions, whereas the events which are the main physics subject of ATLAS are very rare. With an event rate (bunch crossing rate) of 40 MHz and expected event size of $\sim$1.5 MBytes in ATLAS one would have to cope with the raw data rate of 40 TBytes/s. Such a huge amount of data cannot be processed with today's technology. Therefore a sophisticated trigger system was developed that selects only interesting events. The online filtering in ATLAS is performed in three trigger levels, which reduce the event rate to $\sim$100 Hz. Each level refines the previous decision by using larger fraction of the available data and more advanced algorithms.

The first level trigger (LVL1) is hardware based and uses reduced granularity information from a set of sub-detectors (calorimeters and muon system) to identify the interesting events.

The LVL1 decision is made by the Central Trigger Processor (CTP) and distributed to all ATLAS sub-detectors by the TTC (Trigger, Timing and Control) system. The TTC system distributes the LHC-synchronised 40 MHz bunch crossing clock, the global bunch crossing and event counter reset together with the LVL1 accept trigger signal (L1A) to all sub-detectors. The LVL1 trigger reduces the event rate to about 75kHz. The LVL1 latency[3] is around 2.5 μs. Therefore the event data from $\sim$100 bunch crossings are held in pipeline memories of the sub-detectors' electronics. If an event is accepted, the information of all sub-detector systems is read out through the readout drivers (RODs) into a number of readout buffers (ROBs), which are part of larger unit, the so called readout system (ROS).

The high level trigger (HLT) comprises the second level (LVL2) and third level (LVL3) triggers, which are software based and running on dedicated computer farms of standard PCs. The LVL2 uses data from all sub-detectors. However, it retrieves the data only from the regions of interest, which are selected by LVL1 trigger. These are regions of detector where interesting objects have been observed and only data from these regions are read from ROBs. The event

[3]LVL1 latency is the time between the bunch crossing and the arrival of the LVL1 decision at the sub-detector.

rate after LVL2 is around 1kHz. The latency varies from 1-10 ms.

Events selected by the LVL2 trigger are then passed to LVL3, which has access to full event and reduces the event rate to about 100 Hz. It uses fully reconstructed event information to select which events should be written to mass storage for off-line analysis.

2.1.3 Beam accidents and protection

The ATLAS experiment, being located furthest away from beam extraction and injections, is rated to be as the 'safest' of all interaction points in terms of possible beam failure scenarios. Furthermore, ATLAS (and CMS as well) has so called Target Absorber Secondaries (TAS) collimators. These are 1.8 m long copper blocks. They are located at z=±18 m away from the interaction point and are intended to protect the inner triplet of cryogenic quadrupoles (Q1) around the interaction point P1 from excessive heat load due to particles from proton-proton collisions. Additionally, TAS also protects the Inner Detector from a variety of beam failures.

The beam interlock system (BIS) at LHC comprises two redundant optical loops per beam, which transport `BeamPermit` signal around the LHC ring. Both pair of loops consists of a clockwise and anticlockwise propagating signal. In each insertion region two beam interlock controllers (BIC) are used to make a logical AND of many `UserPermit` logical signals, which are provided by user systems (experiment BCMs, machine beam loss or beam position monitors etc.). When one of the `UserPermit` signals is set to `False`, the optical signal loops are interrupted which removes the `BeamPermit` signal. This fires the beam dump system and prevents any injection from SPS. The LHC beam dump system employs firing the kicker magnets to extract the beam. The two beams have independent dump systems and each of them contains an empty gap of at least 3 μs in the bunch structure, which is monitored. The extraction of beam is triggered by the BIS and is completed within 270 μs after the `UserPermit` signal was removed at the BIC. Each user system is connected to BIS through user interface CIBU (Controls-Interlocks-Beam-User), which takes the `UserPermit` signal and transmits it to the nearest BIC.

The most likely beam losses are due to failures or wrong settings in the magnet and powering system with about 8000 magnets powered in 1700 electrical circuits. Beam losses occur at different time scales. They can happen either in a single-turn (or a fraction of turn) with a sudden beam loss or during several turns resulting in progressive losses.

Multi-turn losses

Beam failures involving the relatively slow degradation of circulating beam can be due to RF failure, magnet or collimator failure, etc. If larger portions of the LHC ring are affected in these failures, they are likely to be detected by the machine protection system before they reach experiments. However local faults affecting a single IR are possible. In ATLAS (and CMS) the TAS collimators could help limiting the direct hit to the innermost detectors. Multi-turn losses have characteristic time constants ranging from few turns[4] to several seconds, depending

[4]One turn in the LHC ring corresponds to 89 μs.

on the specific failure [Brü01]. The most rapid of such losses would occur due to a failure of the D1 warm magnet, with a time constant of ∼5 turns (430 μs). These magnets are installed close to the P1 interaction point at ATLAS (see figure 2.3). Therefore its time constant in a way sets the response time of the ATLAS BCM system. Considering 270μs is needed for controlled extraction of the beam, this leaves about 150μs for the BCM system to react. However, these elements are likely to have additional inductance added to their supplies to slow down the rate of beam orbit change in order to give the beam dump system time to act.

Single-turn losses

These sudden losses are most likely to occur at injection from the SPS with proton energies of 450 GeV. Here, an incomplete or unsynchronised kicker magnet fire or wrong magnet settings in the transfer line could dramatically effect experiments close to injection point (ALICE, LHCb). However, ATLAS is situated in LHC ring furthest away from the injection regions.

However, wrong magnet settings in any of the experimental IRs during the injection phase could cause local damage and affect only that particular IR (e.g. warm magnet D1 close to ATLAS). Wrong magnet settings at 450 GeV can potentially produce much larger deviations of the beam than at top energy. Again, the presence of TAS collimator renders ATLAS less exposed to such beam failures. A simulation of beam orbits with wrong settings of magnets close to P1 has been performed [Boc04]. Here only one magnet at a time was considered to have wrong power settings. Due to their particularly large bending strength, three magnets in IR1 (D1, D2, MCBX [5]) were identified as potentially dangerous for ATLAS detector. The results among other show scenarios with beam scraping the TAS collimator or beam line (see figure 2.4).

To avoid these beam failures at injection, the injection in an empty LHC ring will always start with a single bunch of low intensity, a so called *pilot bunch*, in order to probe the machine settings. Once the circulating beam is established, the injection of high intensity bunches can start. The pilot bunch intensity has to be low enough to ensure no damage to LHC equipment or experiments' detectors. It is planned for pilot bunch to have 5×10^9 protons (450 GeV) corresponding to 360 J of stored energy.

Single-turn losses can also occur during the beam dump process as well, caused by kicker magnet malfunction (e.g. kicker pre-fire). However, since ATLAS is not close to the beam extraction region, the absorbers and collimators in the beam cleaning and extraction region are expected to handle the problem.

Single-turn losses are handled by passive protection. Slow losses may increase the radiation dose of the detector, but do not necessarily require a beam abort, since recovery of good beam conditions may be possible. For faster circulating beam losses on the other hand, rapid beam abort through BIS is needed. The purpose of the BCM system is to protect the experiment against faster multi-turn failures.

[5]The MCBX orbit corrector magnet is one of the magnets used for the angle and parallel beam separation scheme. D1 is a separation and D2 a recombination dipole magnet.

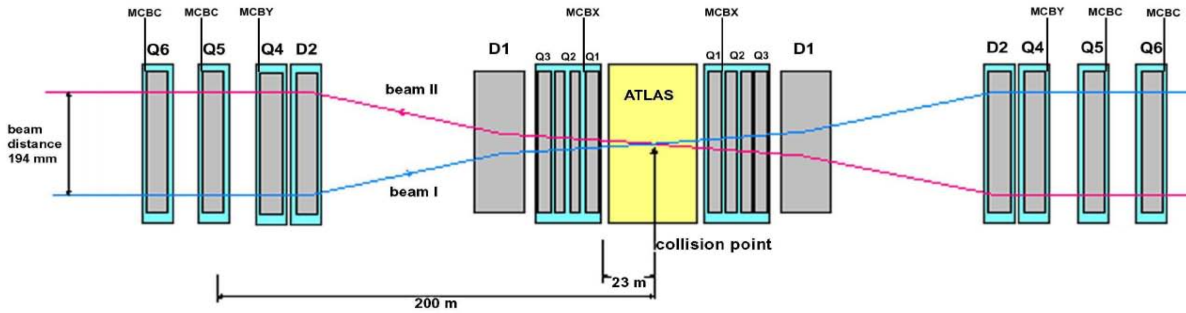

Figure 2.3: *The ATLAS insertion region (IR1) beam optics.*

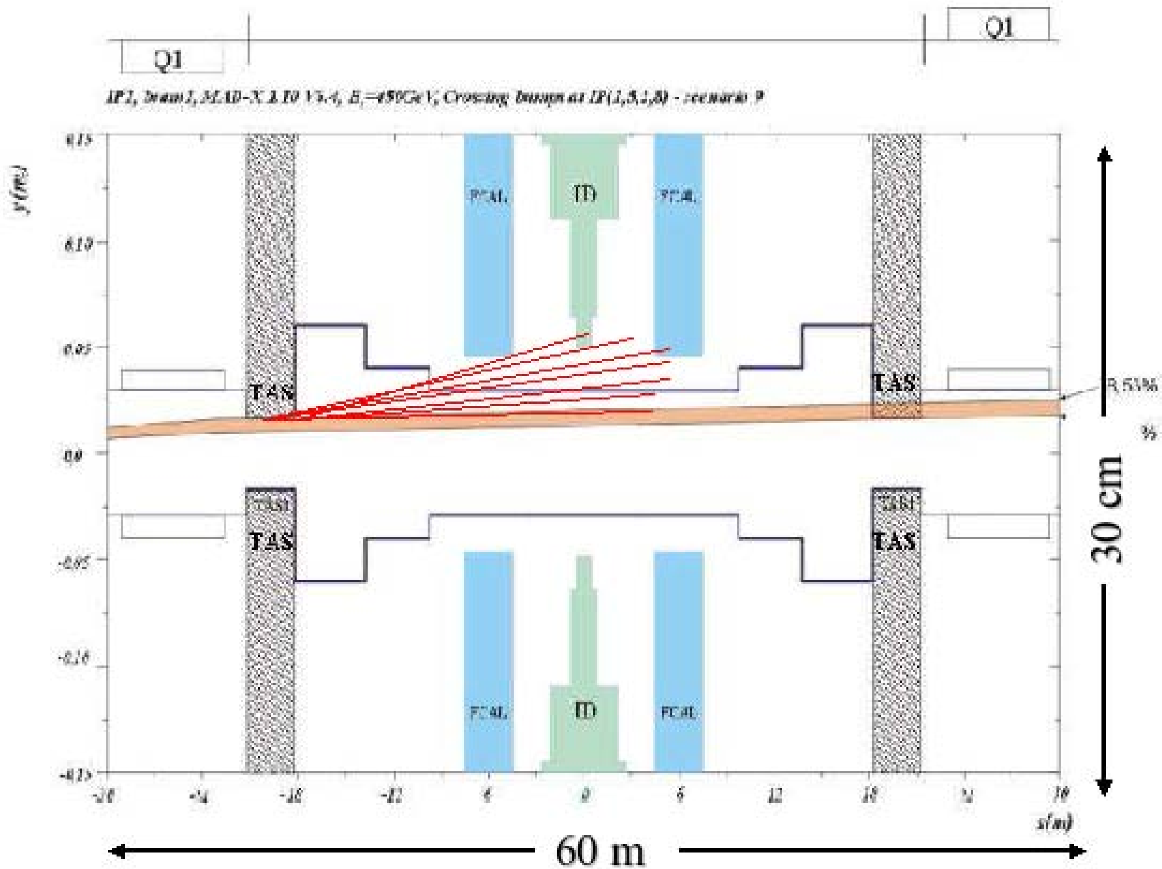

Figure 2.4: *An example of a simulated beam accident scenario at injection [Boc04]. The shaded region represents the range of beam directions which are dangerous for the Inner Detector (ID). In this scenario the beam hits the TAS collimator on the way in and out. Red lines denote shower particles. The horizontal scale shows the whole ATLAS cavern, while the vertical represents the zoom around the beam pipe.*

2.2 ATLAS BCM description

2.2.1 Principle of operation and requirements

The primary goal of the BCM system is to detect the early signs of beam instabilities and protect the experiment against damaging beam losses by initiating a beam abort through BIS if necessary. It will provide real-time monitoring of instantaneous particle rate close to the interaction point in order to distinguish between normal collisions and background events. In addition, it will also provide a coarse luminosity measurement as a complementary information to LUCID [Sou06], the main ATLAS luminosity monitor.

Circulating beam losses, occurring far from ATLAS region, will most likely be detected by machine protection first. However, local magnet failures occurring close to P1 are also possible. These are to be detected by the the BCM system. On the other hand, BCM will probably not be able to react fast enough to the sudden losses of a pilot bunch, caused by wrong settings of magnets close to P1 during injection, but should be able to diagnose them. In both cases, the beam can start scraping the beam pipe and/or TAS collimators, producing a shower of particles upstream the beam. Besides these accidental losses, natural losses are also possible. These include beam halo protons interacting with a TAS collimator close to the entrance of ATLAS cavern and beam-gas interactions, where beam protons interact with residual gas (H_2, CO_2, CH_4,...) in the beam pipe inside the ATLAS cavern. Both result in showers of particles upstream the beam.

If two BCM detector stations are placed symmetrically around the interaction point at $\pm z_{bcm}$, as shown on figure 2.5, shower particles originating upstream ($|z|>|z_{bcm}|$) hit the nearest BCM station at a time δt=$2z_{bcm}/c$ before the station on the other side. On the contrary, collisions occurring every bunch crossing give coincident signals every 25 ns. Thus, in order to optimally distinguish between normal collision and background (accidental or natural beam losses) events, BCM stations should be positioned at z_{bcm}=$\pm$1.9 m corresponding to δt=12.5 ns. This results in shower particles induced by background giving signals in the nearest station 6.25 ns before the proton-proton collision at interaction point (*out-of-time hits*), while the secondary particles from collision reach both stations 6.25 ns after the collision (*in-time hits*). In this way one can use out-of-time hits to identify the background events and in-time hits to monitor the luminosity on a bunch-by-bunch basis.

Eight BCM detector modules were mounted on the Beam Pipe Support structure which supports the Pixel detector as well. This carbon fibre structure also supports the BCM detector power and signal cables. There are four BCM modules on each side of interaction point at z_{bcm}=184 cm, placed symmetrically around the beam line at ϕ=0°, 90°, 180° and 270° (see figures 2.6 and 2.7). They are mounted at 45° towards the beam pipe, with BCM sensors located

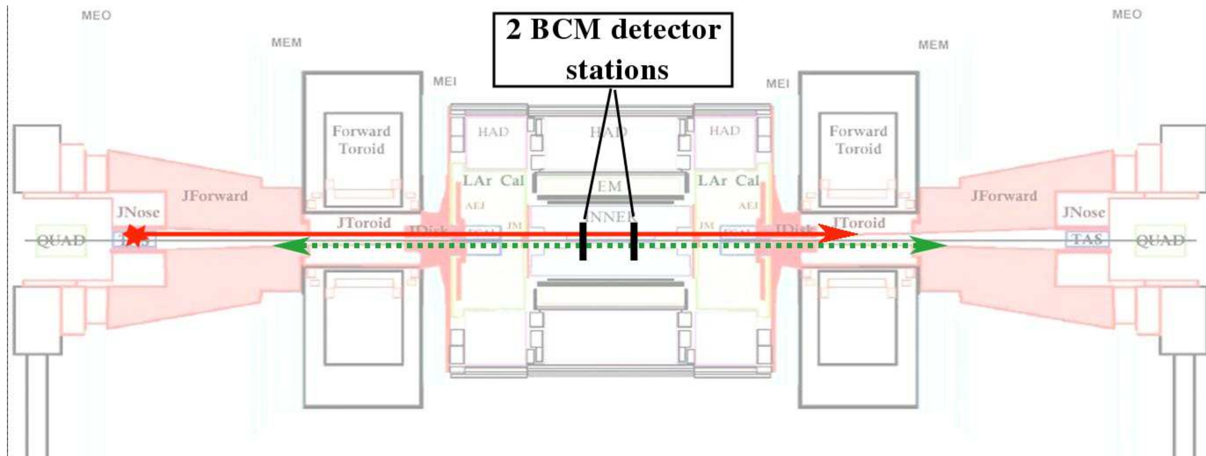

Figure 2.5: *ATLAS detector with two BCM detector stations at $\pm z_{bcm}$. Shower particles (red) reach left stations z_{bcm}/c before interaction occurs and secondary particles from interactions (green) reach this station z_{bcm}/c after interaction and give coincident signals on both BCM stations.*

at r∼55 mm, corresponding to pseudorapidity of η≈4.2.

It is worth mentioning that BCM in ATLAS will be the first BCM system based on bunch-by-bunch measurements. Other BCM systems at LHC experiments as well as BaBar [E+05] and CDF [E+] are based on integration of the accumulated particle flux, by measuring ionisation current in diamond.

A beam accident, where a pilot bunch (450 GeV protons) hits both the ingoing and outgoing TAS collimator as well as the beam pipe, have been considered [Tar]. Simulations predict that one lost proton hitting the TAS collimator on the way in the ATLAS cavern results in 0.06 out–of–time hits in the BCM system. For one lost proton hitting the beam pipe at z=3 m simulation predicts around 0.14 hits in the BCM system. The case of one 7 TeV proton hitting the TAS was also studied, the results give 1.15 of hits in the BCM system. On the other hand an estimate, obtained by simulation of proton-proton collisions in ATLAS at LHC designed luminosity, gives around 0.40 hits per proton-proton interaction.

In order to be able to optimally distinguish between the normal collisions and background, the BCM should be sensitive to single minimum ionising particles (MIPs). This sensitivity is also required for the luminosity assessment. The hostile radiation environment and high rate of interactions pose harsh requirements for BCM sensors and electronics. In 10 years of LHC operation, the radiation field at sensor location is expected to amount to about 10^{15} particles (mostly pions) per cm^2 and an ionisation dose of ∼0.5 MGy. Since bunch crossings occur with 40 MHz rate (every 25 ns), fast processing of BCM signals is needed. Thus, signal pulses with rise time of ∼1 ns, width of ∼3 ns and baseline restoration below 10 ns are necessary.

Installed BCM modules are covered with layers of Pixel detector services. Any intervention is unlikely to be approved since it would require disassembling a substantial part of those services. Thus, a simple and robust design of BCM detector modules was required with no risky components built in.

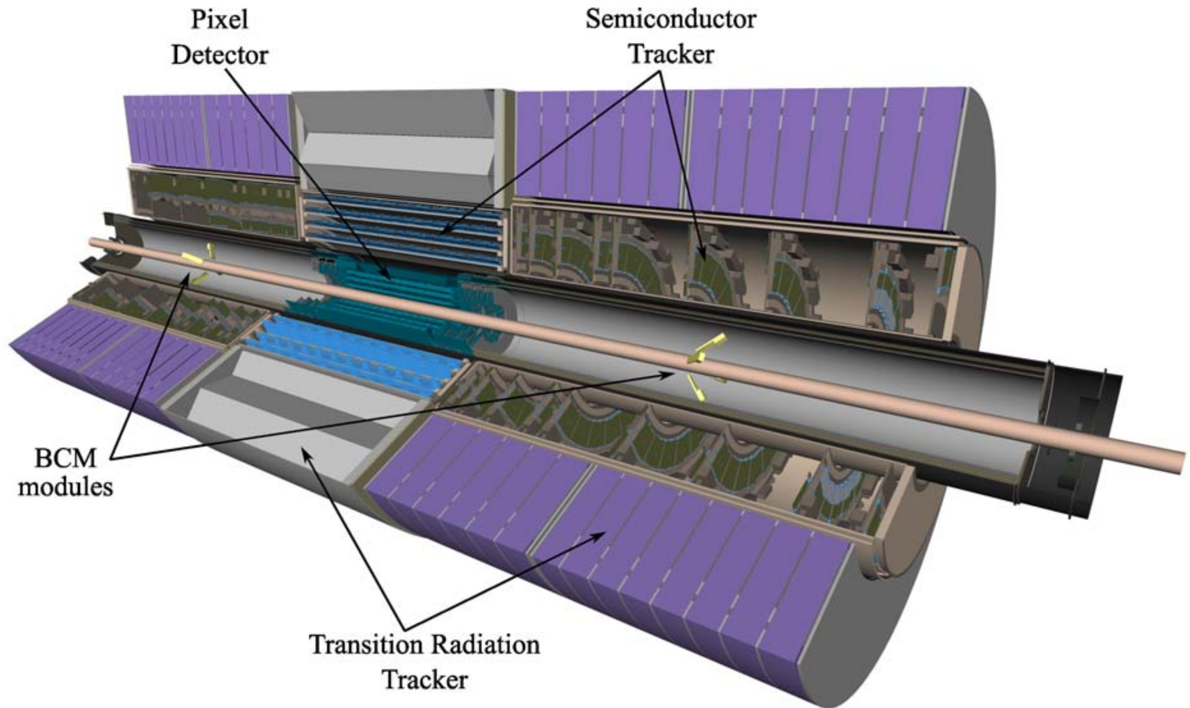

Figure 2.6: *Position of BCM detector modules inside the Inner detector.*

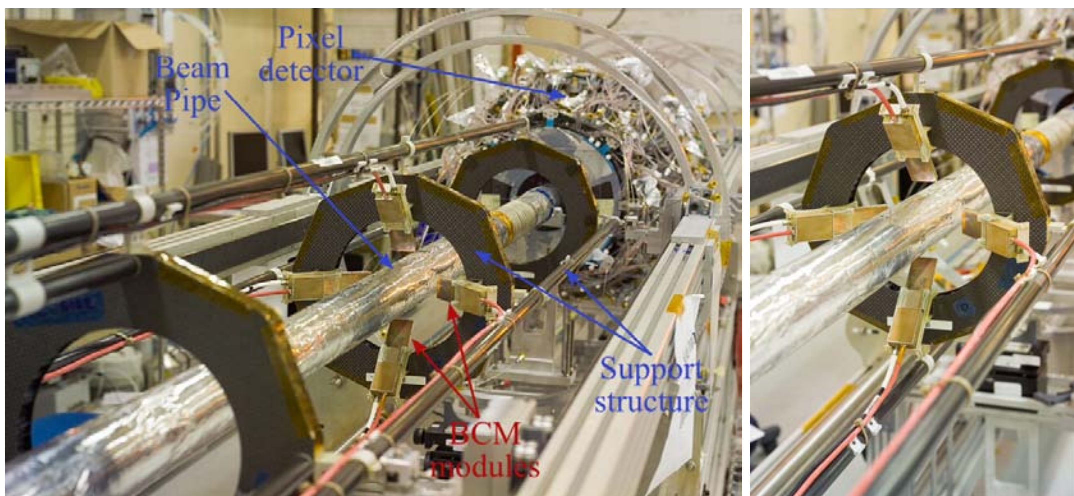

Figure 2.7: *BCM detector modules mounted on the Beam Pipe Support Structure. The pictures were taken during installation of the Pixel Detector and its services.*

2.2.2 Detector modules and sensors

Epitaxial silicon and pCVD diamond were considered for the active sensor material in ATLAS BCM detector system. As will be shown in chapters 4 and 5 pCVD diamond detector was finally chosen due to its better performance in terms of signal–to–noise ration (SNR). The pCVD diamond sensor material was developed by CERN RD42 collaboration [RD4] in cooperation with Element Six Ltd [E6]. Sensors are around 500 μm thick with a 1×1 cm^2 surface. Both sides of the sensors have 8×8 mm^2 proprietary radiation hard Ti-Pt-Au contacts made at Ohio State University.

The timing properties of the current signal induced by particles passing the sensor are determined by high drift velocity of charge carriers and short trapping times even before the irradiation. In order to achieve high and narrow current pulses, the sensors will be operated close to saturation velocity (>10^7 cm/s), at a bias voltage of $\pm$1000 V corresponding to an electric field of 2 V/μm. Radiation hardness of the pCVD diamond sensors was tested for fluences up to 2.2×10^{15} protons per cm^2 yielding a signal degradation of only 15% [A$^+$03]. In addition to proven radiation hardness and fast signal formation pCVD, diamonds exhibit very low leakage current, allowing an operation at room temperature without cooling. At 1000 V, a typical sensor has a leakage current below 100 pA and a charge collection distance (see section 3.4.2 for definition) of $\sim$220 μm.

In order to increase the signal amplitude, two diamond sensors, acting as a single signal current source are used. Signals from the two diamonds are summed before they are amplified. This summation is achieved by mounting the two diamonds in stack. The electrodes of the two diamonds inside the stack, facing each other, are shorted at ground potential and connected to the amplifier. The two outside electrodes of the stack are connected to the bias voltage. The drift field of 2 V/μm is achieved in both of the diamonds, when a bias voltage of $\pm$1000 V is applied to the stack. When a charged particle, arising either from a proton-proton collisions or as a secondary product of e.g. lost protons, traverse the diamond stack, an induced current pulse is generated in each of the diamonds and the two current signals are added on the common signal readout line. This stacked configuration is further denoted as a “double–decker diamond assembly”.

In the final sensor assemblies, shown on figure 2.8 the two diamonds are attached to two alumina (Al_2O_3) ceramic inserts that have Au-Pt metal traces on them and merge the signal planes. This stack of diamonds is glued onto an alumina ceramic baseboard, which has metal traces for routing the signal and bias voltage lines. The ceramic baseboard with diamonds is then glued to the bias voltage line in the module box. The upper diamond in the assembly is positioned slightly closer to the edge of the module box, in a way that an angle $\alpha\sim45^o$ is formed between the normal to the sensor surface and the line connecting the centres of two diamonds (figure 2.9, top). In this way, the acceptance area is enlarged due to better matching of the two diamonds’ electrode areas, given that the BCM modules are mounted at 45° towards the beam pipe in ATLAS. The merged signal from the upper electrode of the lower diamond is lead via wire bonds to a G10 printed circuit board, which takes this signal to the readout amplifiers. The high voltage is supplied via small metallised holes in the ceramic baseboard to the bottom plane of the bottom diamond and through wire bonds to the top plane of the upper diamond. Redun-

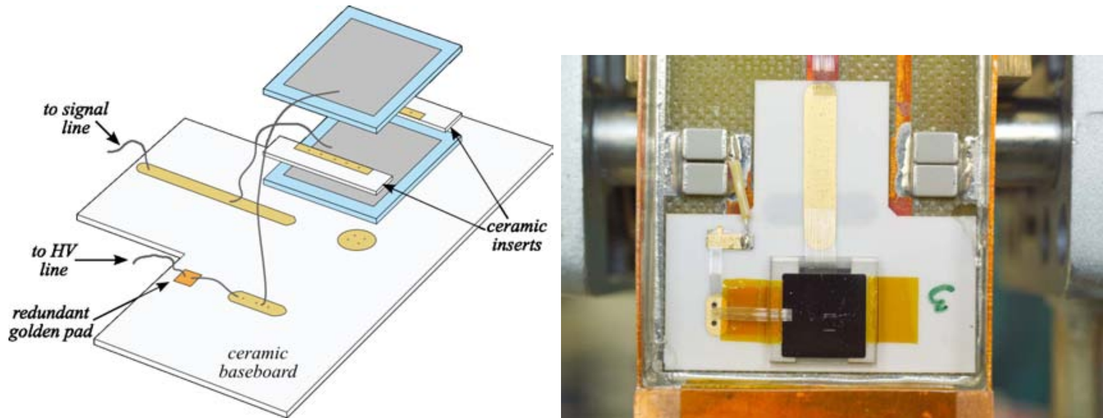

Figure 2.8: *Left: A diamond double decker assembly with ceramic inserts and baseboard used in the final modules. Right: Picture of the ceramic assembly in the module.*

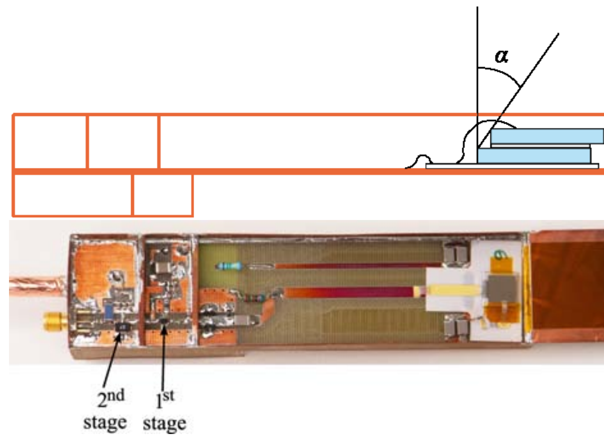

Figure 2.9: *Top: Schematic picture of a detector module with diamond double decker as seen from the side. Bottom: Layout of the two amplification stages in the module.*

dantly, the high voltage is supplied to the upper diamond with additional golden pad via wire bonds. The sensors are attached to ceramic inserts and baseboards with *StayStik571* conductive glue pads that remain elastic up to 130°C and particle fluences beyond 10^{16}cm^{-2}.

The signal is fed through a 5 cm long 50 Ω transmission line on the printed circuit board to the front-end amplifier. In this way the radiation field at the amplifier location is decreased by about 30%. The front-end electronics was designed by Fotec [FOT]. It consists of a two stage RF current amplifier utilising a 500 MHz Agilent MGA-62563 GaAs MMIC low noise amplifier in the first stage and the Mini Circuit Gali-52 In-Ga-P HBT broadband microwave amplifier in the second stage (figure 2.9 bottom). Each stage provides an amplification of 20 dB, with the first stage exhibiting a noise factor of 0.9 dB.

The sensor assembly and front-end electronics are mounted in a module box, designed to shield the RF. Each of the amplification stages is placed in a separate shielded compartment. The amplified signal is fed into a high quality 50 Ω coaxial cable. The amplification stages and the output are all AC coupled. The input is protected against discharges with protection diodes.

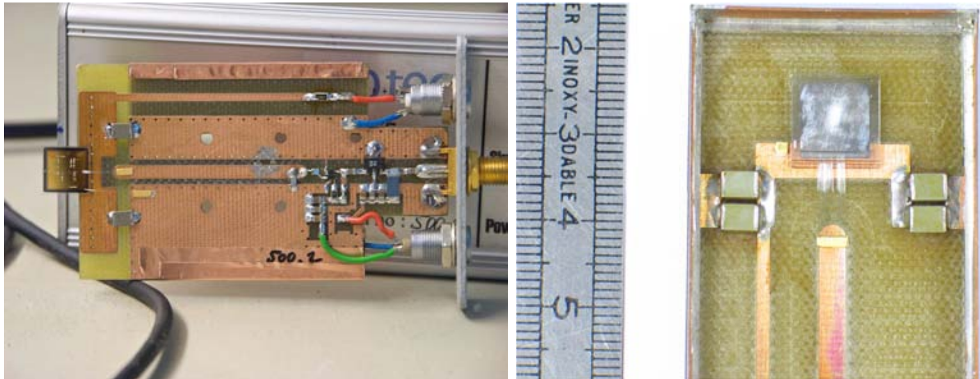

Figure 2.10: *A BCM prototype detector module, with a diamond glued to the high voltage line (left) and a final module with double decker assembly without ceramic inserts and baseboard (right).*

The module boxes are made of G10 material with the inner sides covered with a 35 μm thick Cu layer. All G10 plates constructing the modules labelled as F40X are 0.4 mm thick except the base plate and the plates isolating the compartments. Modules labelled as F42X differ from modules F40X by the thickness of the plane at the connector side (figure C.1 in appendix C), which in case of F42X boxes equals1.4 mm instead of 0.4 mm.

High voltage is supplied by ISEG EHQ-8210 units [ISE], modified to enable a current monitoring resolution of 1 nA. Low voltages needed for amplifiers in the front-end electronics, 3 V and 11 V, are provided by a modified version of power supplies custom made for the ATLAS SCT detector [B^+]. These power supplies are located in ATLAS USA15 service cavern, Here, low and high voltages are merged into a single multi-core power cable routed to each detector module.

In the initial tests, a prototype version of the BCM module was used, labelled as 500.X. In this version, the electronics with sensors were housed in an aluminium box. The box had two $20\times38\,\mathrm{mm}^2$ openings, one above and one below the sensors, covered with copper tape (figure 2.10, left). In the final modules, thin G10 plates were used instead of thick aluminium for housing in order to minimise dead material. The front end electronics in the prototype version used a slightly different electronic circuit, but the two amplifiers were the same as in the final version (see figure C.2 in appendix C). With the prototype modules it was observed that the baseline is restored in about 10 ns after the particle incidence. Thus, in the final version some of the components in the circuitry were changed in order to improve the baseline restoration. Additionally, two protection diodes, which were not present in the prototypes, were added.

Later tests were carried out with final detector modules, equipped with double decker diamond assemblies which did not have the ceramic inserts for merging the signal planes in the diamond stack. Instead, golden pads were used for merging the two diamonds together. Also, some of these diamond assemblies did not include the ceramic baseboard, but were glued directly to the high voltage line on the printed circuit board in the module (figure 2.10, right). The high voltage to the top electrode of the upper diamond was supplied via wire bonds, extending from the golden pad glued on the high voltage line. Similarly, the merged signal, taken from the

middle of the diamond stack, was routed via wire bonds to a golden pad, glued to the signal line.

2.2.3 Overall readout scheme

A schematic of the BCM readout system and its connection with ATLAS system is shown in figure 2.11. Analogue signals from each BCM detector module are routed through 14 m of coaxial cable[6] to the region behind the ATLAS calorimeter. Less radiation tolerant electronics can be used here, since lower radiation levels are expected (ionisation dose of ~10 Gy in 10 years). This electronics utilises a NINO chip [A$^+$04] for digitisation of analogue signals. The NINO ASIC was originally developed for time-of-flight measurements of the ALICE RPC detector by CERN-MIC. It features radiation tolerant design fabricated on 0.25μm IBM technology. Its LVDS output signal exhibits a rise time of ~1 ns and ~25 ps jitter. It has 8 differential input channels and serves as amplifier and discriminator with a time-over-threshold (TOT) measurement capability. NINO converts the input analogue signal into a digital signal a fixed time after the input signal arrival. The width of the resulting digital output signal is correlated to the amplitude of the input signal. The charge seen at the input is encoded in terms of time-over-threshold.

Each BCM module is connected to one custom electronics board with a NINO chip. A schematic picture of the board is shown in figure D.1 in appendix D. The board first filters the input signal through a low-pass filter of the fourth order with a 200 MHz bandwidth limit. This additional filtering was included since studies showed that it improves the signal–to–noise ratio of BCM detector module as will be shown in section 4.2.1. After filtering, the signal is

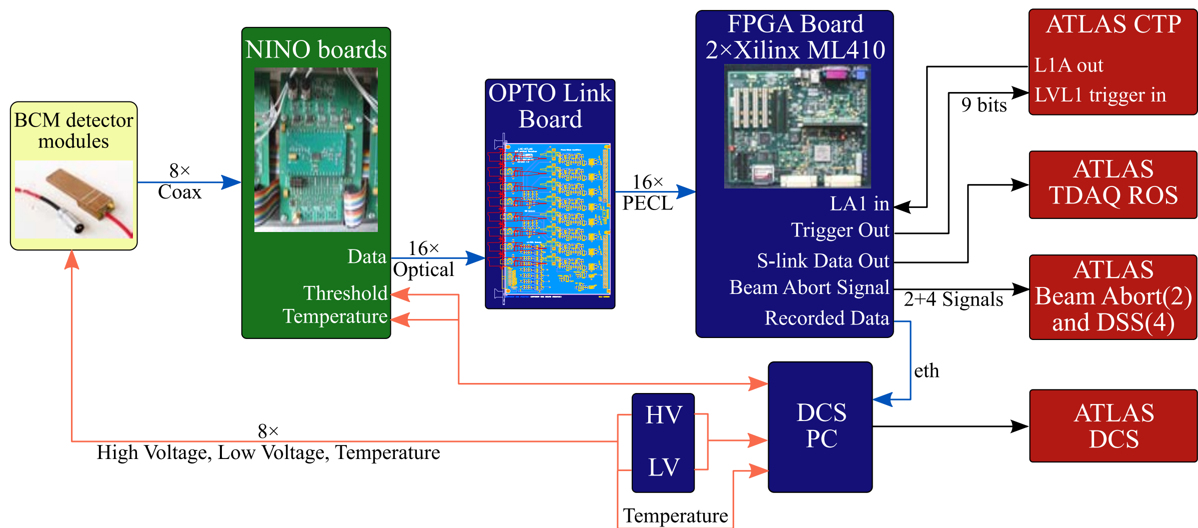

Figure 2.11: Overview of the BCM readout and supply chain.

[6]The first 2 m (Gore 41 cable) are routed inside and the following 12 m (Andrew HELIAX FSJ1) outside of the Pixel detector.

split into two parts in approximate ratio of 1:11 in order to increase the NINO dynamic range, since the TOT response of NINO as a function of NINO threshold saturates quickly (see section 4.3.2). These two signals are then fed into two NINO chip inputs. The resulting two TOT digital signals from the NINO chip are further converted into optical signal with radiation tolerant laser diodes (Mitsubishi FU-427SLD-FV1). All 16 (2 for each detector module) optical signals are transmitted through 70 m of optical fibres to the ATLAS USA15 service cavern. Here, they are routed to an optical receiver board where they are received by photo diodes (Lightron LP3A4-SNC1) and converted to PECL electrical signals. These signals are further connected to two Xilinx ML410 development boards for processing the data. Each board is based on a Xilinx Vitrex-4 FPGA (Field Programmable Gate Array) chip and features 8 RocketIO serial input/output channels that will sample the received signals with a frequency of 2.56 GHz. The RAM, present on Xilinx boards, acts like a ring buffer and stores the BCM signal information for about 3×10^{6} last LHC bunch crossings.

The FPGA will process the signals in real-time by extracting the signal pulse width, which encodes the TOT from NINO, and signal arrival time of each of the 8 modules. Additional analysis performed with the FPGA includes determination of in-time and out-off time hits, rates and trends of rates of each module or coincidences for different combination of modules. The BCM system will provide different information through the FPGA to the several ATLAS and LHC systems:

- **LHC Beam Abort** In case of beam failures, two redundant signals, indicating that beam conditions in the ATLAS Inner detector have reached the unacceptable levels, will be sent to the BIS through the ATLAS CIBU system, which will result in beam abort.

- **ATLAS Detector Safety System (DSS)** This hardware interlock system guards the experimental equipment and acts to prevent damages from any detected faulty situation. The BCM system has 4 electrical connection to DSS in order to send warnings or alarm signals.

- **ATLAS Detector Control System (DCS)** A PC, integrated into the ATLAS DCS system, is used to monitor the temperature of detector modules and NINO electronics boards as well as to control the high and low voltages. The FPGA is connected to this PC via Ethernet. Thus, more sophisticated information (average rates, histograms, etc.), obtained from processed signals, is available to ATLAS and LHC control through DCS. In case of a beam abort, all recent information from BCM, currently stored in ring buffer of FPGA, is transfered through DCS for post mortem analysis.

- **ATLAS Data Acquisition (DAQ)** The FPGA also acts as a ROD. Upon receiving a L1A signal, the processed data from the FPGA will be sent to the ATLAS DAQ system through a standard optical link used in ATLAS (S-link). Digitised information about signal arrival times and their widths will be stored as part of the ATLAS DAQ data stream.

- **ATLAS LVL1 trigger** BCM system will also provide information to the ATLAS LVL1 trigger in a form of 9 bits, allowing for triggering on topologically interesting events if required.

CHAPTER 3

SOLID STATE DETECTORS

3.1 Basics of Semiconductor and Insulator physics

3.1.1 Energy band structure

The periodic lattice of crystalline materials establishes allowed energy bands for electrons within the solid. These energy bands consist of a large number of closely spaced electron energy levels and may be separated by gaps or ranges of forbidden energies. The band, which is at 0 K temperature , the highest filled band is called the *valence band* and the next higher band is called the *conduction band*. The region between these two bands is the *bandgap energy*, E_g.

We can categorise solids according to the size of bandgap, E_g. Conductors either have overlapping valence and conduction bands or a partially filled conduction band. Semiconductor and insulator both have bandgap. They are very similar, but the primary difference between these two categories is in the size of the bandgap. Insulators have larger bandgap compared to semiconductors. Evidently, the distinction is not a sharp one, but roughly speaking, the bandgap in most important semiconductors is less than 2 eV and frequently as low as few 0.1 eV. Completely filled bands do not contribute to the electrical conductivity of the crystal. Electrical properties of the crystal are determined by the electrons in the almost empty conduction band and holes in valence band. A *hole* is considered as the absence of an electron from the otherwise full valence band. At zero temperature one has a completely filled valence and completely empty conduction band in semiconductor or insulator. However, when the temperature is not zero, there is a non-vanishing probability that some electrons will be thermally excited into the conduction band, leaving behind holes in the valence band, thus creating a weak conductivity.

The energy band structure of semiconductors or insulators is rather complex. It is usually obtained with the use of Bloch theory, where electronic levels are stationary solutions of the Schrödinger equation in the presence of the periodic potential of the ions. In a *direct semiconductor*, the conduction band minimum occurs at the same point in k-space as the valence band maximum. While in *indirect semiconductor* the minimum energy in conduction band is shifted by a $\mathbf{k}$-vector relative to the valence band maximum energy. In this case, a transition of an electron into the conduction band is only possible if electron acquires additional momentum. This additional momentum can be transfered by a phonon.

Diamond and silicon crystals are formed of carbon or silicon atoms respectively in a diamond lattice structure, consisting of two face centred cubic lattices, displaced along the diagonal of the cubic unit cell by one quarter of the length of diagonal [PK95]. Figure 3.1 shows the calculated band structure of diamond along several symmetry directions. For both the minimum of

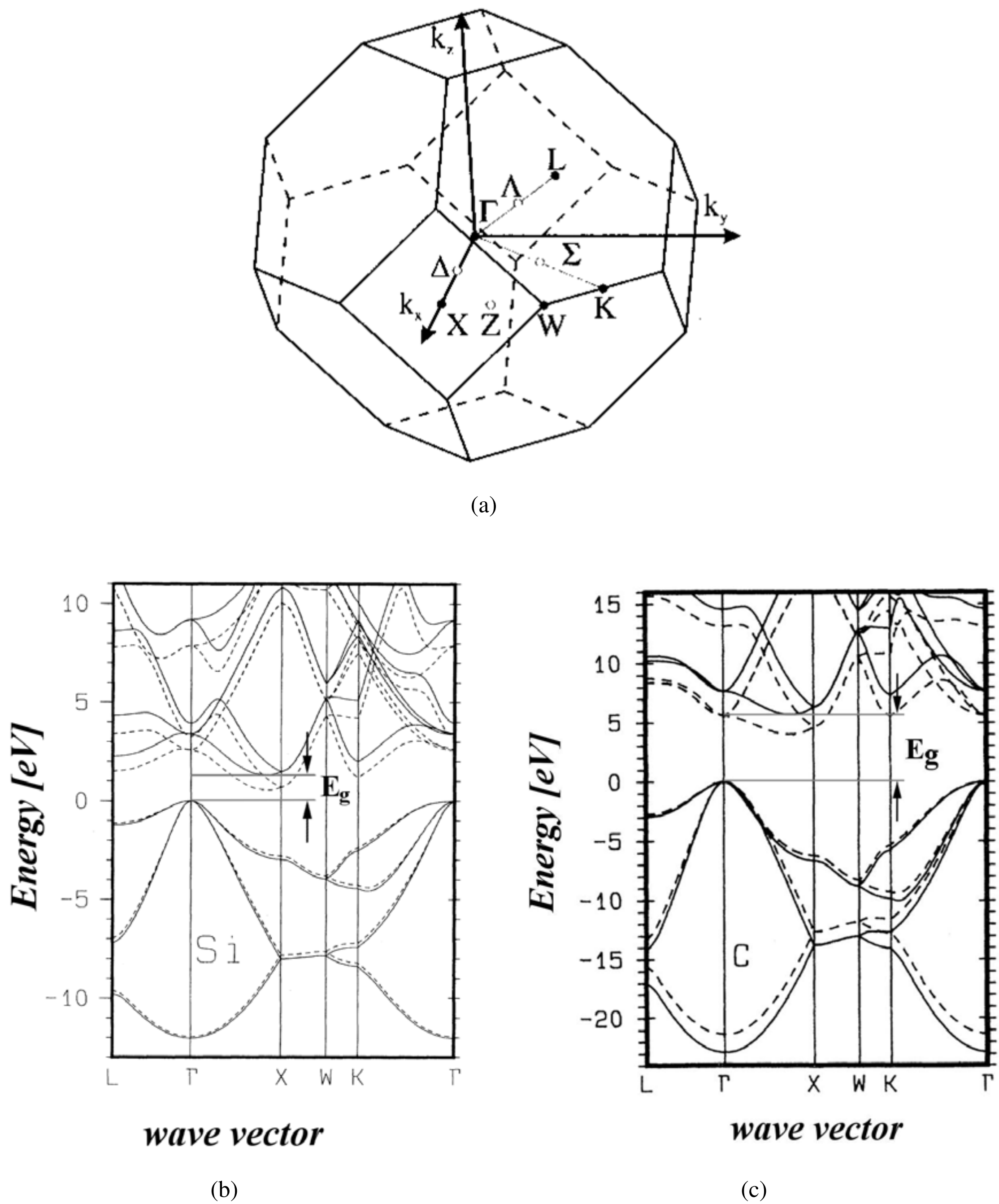

Figure 3.1: *(a) The first Brillouin zone for a diamond lattice with the most important symmetry points (Γ, K, L, W, X) and symmetry lines (Λ, Δ, Σ, Z). Calculated band structure of silicon (b) and diamond (c) crystal respectively [R^{+}93]. Spin-orbit interaction effects were not included due to their negligible size. Solid and dashed lines display results of two different calculations, where the solid line results gives better agreement with experimental data.*

the conduction band is located at different $\mathbf{k}$ points within the Brillouin zone from the Γ point[1]. Therefore, diamond and silicon are indirect gap materials. The measured value of E_g at 300K is 5.47 eV for diamond [C$^+$64] and 1.12 eV for silicon [Thu75].

In the semi-classical model for the behaviour of electrons in a crystal, electrons act very much like free electrons, except that it is necessary to use a modified mass parameter rather than the actual free-electron mass [AM76]. The modified mass parameter, or *effective mass*, includes most of the interactions between the electron and the periodic crystal potential due to the presence of atoms without the valence electrons. Electrons in the conduction band are found almost exclusively in levels near conduction band minima, while holes are confined to the neighbourhood of the valence band maxima. Here, the band structure (energy vs. wave vector for the carriers) can be approximated by the quadratic forms they assume in the neighbourhood of these extrema [AM76]:

$$E(\mathbf{k}) = E_c + \frac{\hbar^2}{2}\sum_{ij} k_i(\mathbf{M}_{\mathbf{h}}^{*\,-1})_{ij}k_j \qquad \text{(electrons)}, \tag{3.1}$$

$$E(\mathbf{k}) = E_v - \frac{\hbar^2}{2}\sum_{ij} k_i(\mathbf{M}_{\mathbf{e}}^{*\,-1})_{ij}k_j \qquad \text{(holes)}, \tag{3.2}$$

$$(\mathbf{M}_{\mathbf{e,h}}^{*\,-1})_{ij} = \pm\frac{1}{\hbar^2}\left(\frac{\partial^2 E}{\partial k_i \partial k_j}\right)_{\mathbf{k}\text{ at max, min}} \tag{3.3}$$

where $\mathbf{M}_{\mathbf{e}}^*$ and $\mathbf{M}_{\mathbf{h}}^*$ are electron and hole effective mass tensors with indices i, j running over tensor components, E_c is the energy in the minimum of conduction band, E_v is the energy of maximum of valence band and the origin of k-space was taken to lie at band minimum or maximum. If there is more than one minimum or maximum, there will be one such term for each of them. One can find a set of orthogonal principal axes for each of those points, in terms of which the tensors $\mathbf{M}_{\mathbf{e,h}}^*$ have diagonal forms, giving an ellipsoidal shape to the constant energy surfaces about the extrema.

Silicon has six equivalent cigar-shaped conduction band minima at points in the ΓX direction and equivalent axes ($\langle 100\rangle$ directions), with the longitudinal effective mass (along the axis) $m_{el}^* = 0.98m_0$ and transverse effective mass m_{et}^*=$0.19m_e$ [Sze81], both expressed in units of free electron mass m_0. There are two degenerated valence band maxima located at $\mathbf{k}$=0, which are spherically symmetric in the quadratic approximation. These two bands are referred to as the light and heavy hole bands, with a light hole effective mass m_{hl}^*=$0.16m_0$ and a heavy hole effective mass $m_{hh}^* = 0.49m_0$. There is also the third band, split-off hole band, with maximum located at Δ_{hso}=0.044 eV [BM85, Z$^+$60] below the valence band maximum and a split-off hole effective mass m_{hso}^*=0.29m_0. This band is separated from the other two only by spin-orbit coupling and it can be a significant source of carriers at room temperatures.

Diamond is structurally similar to silicon. It has six conduction band minima along the $\langle 100\rangle$ axis and a degenerated valence band extremum at $\mathbf{k}$=0, like silicon. The measured longitudinal and transverse electron effective masses in diamond are m_{el}^*=1.4m_0 and m_{et}^*=0.36m_0 [N$^+$80] respectively, while heavy and light hole effective masses were found to be m_{hh}^*=2.12m_0 and m_{hl}^*=0.7m_0. Spin-orbit splitting of the valence band for diamond is very small. The split-off valence band is experimentally found to be only about Δ_{hso}≈6 meV below the valence band maximum [Rau62], with a split-off hole effective mass of m_{hso}^*=1.06m_0 [Rau62].

[1] Γ point is the centre of Brillouin zone ($\mathbf{k}$=0), where maximum of the valence band is situated.

3.1.2 Density of charge carriers

An important property of any semiconductor or insulator at a given temperature T is the number of charge carriers per unit volume. The Fermi function provides the probability that an energy level E is occupied with an electron in thermal equilibrium

$$F(E) = \frac{1}{1 + \exp\left(\frac{E-E_F}{k_B T}\right)} \tag{3.4}$$

which has a value of 1 for energies that are more than a few $k_B T$ below the Fermi energy[2] E_F. It equals $1/2$ for $E = E_F$ and decreases exponentially for energies, which are a few $k_B T$ larger than E_F. The density of electrons in the conduction band, n, and density of holes in the valence band, p, is given by [AM76]:

$$n = \int_{E_c}^{\infty} dE\, g_c(E) F(E); \qquad p = \int_{-\infty}^{E_v} dE\, g_v(E)(1 - F(E)). \tag{3.5}$$

Here g_c and g_v are the densities of energy states in the conduction and valence band respectively. For the case of non-degenerate semiconductor ($(E_c - E_F)$, $(E_F - E_v) \gg k_B T$) the Fermi function can be approximated by a Boltzmann statistical factor giving [AM76]

$$n = N_c(T)\, \mathrm{e}^{\left(-\frac{E_c - E_F}{k_B T}\right)}; \qquad p = P_v(T)\, \mathrm{e}^{\left(-\frac{E_F - E_v}{k_B T}\right)}. \tag{3.6}$$

Here N_c and P_v are called the *effective density of states* in conduction and valence band. They can be calculated as

$$N_c = 2\left(\frac{2\pi m^*_{de} k_B T}{h^2}\right)^{3/2}; \qquad P_v = 2\left(\frac{2\pi m^*_{dh} k_B T}{h^2}\right)^{3/2}. \tag{3.7}$$

under the assumption that the densities of energy states increase as the square root of energy, $g_{c,v} \propto |E - E_{c,v}|$. m^*_{de} and m^*_{dh} are the *density of state effective masses* for electrons in the conduction band and holes in the valence band respectively. The $(m^*_{de})^3$ can be calculated as the product of the principal values of the conduction band effective mass tensor (its determinant). If there is more than one conduction band minimum, one must add g_c terms under the integral in equations 3.5 for each of them. In case of several equivalent conduction band minima and several minima that can contribute significantly to number of charge carriers, each with energy $\Delta_{e,i}$ below those equivalent minima, one obtains

$$(m^*_{de})^{3/2} = M_c \sqrt{m^*_{1,1} m^*_{2,1} m^*_{3,1}} + \sum_{i=2} \sqrt{m^*_{1,i} m^*_{2,i} m^*_{3,i}}\, [\exp\left(-\Delta_{e,i}/k_B T\right)]^{3/2} \tag{3.8}$$

[2] Energy E_F is actually the chemical potential, but in the context of semiconductors it is usually called the Fermi level, see [AM76], footnotes on pages 142 or 573.

where M_c is the number of equivalent minima, and $m_{j,1}$, $m_{j,2}$, $m_{j,3}$ are the effective masses along the principal axis of the ellipsoidal energy surface near the j-th minimum. (m^*_{dh}) is found similarly.

Charge carrier densities depend on the presence of impurities. If impurities contribute significantly to the number of charge carriers, one speaks of an *extrinsic semiconductor*. But impurities affect the determination of n and p only through the value of the Fermi energy. Thus, equations 3.6 remain valid even in the extrinsic case.

An *Intrinsic semiconductor* contains no, or in practice very few, impurities. In this case, the number of conduction band electrons equals the number of holes in the valence band. Therefore, the intrinsic density of electron or hole charge carriers can be calculated by

$$n_i = \sqrt{np} = \sqrt{N_c P_v} \exp\left(-\frac{E_g}{2k_B T}\right). \tag{3.9}$$

If one defines E_i as the value of the Fermi energy in the intrinsic case and compares equations 3.6 with equation 3.9, one finds

$$E_i = E_v + \frac{1}{2}E_g + \frac{3k_B T}{4} \ln\left(\frac{m^*_{dh}}{m^*_{de}}\right). \tag{3.10}$$

In an intrinsic semiconductor the Fermi level lies close to the middle of the bandgap. With the use of intrinsic carrier density n_i and intrinsic Fermi level E_i one can reformulate the generally valid equations 3.6 in a more useful form:

$$n = n_i \, \mathrm{e}^{\left(\frac{E_F - E_i}{k_B T}\right)} \qquad\qquad p = n_i \, \mathrm{e}^{\left(\frac{E_i - E_F}{k_B T}\right)}. \tag{3.11}$$

In the extrinsic case, impurities are incorporated into the crystal structure of the semiconductor, either unintentionally, due to lack of control during growth of the crystal, or they can be added on purpose (doping) in order to alter the number of free electrons or holes. This in general introduces energy levels in the bandgap. Shallow levels are considered to be energy levels that are close to valence or conduction band. Impurities that supply additional electrons to the conduction band are called *donors*, and *acceptors* if they supply additional holes to (capture electron from) the valence band. If a group IV semiconductor is considered (Si, Ge, diamond C), *shallow donors* are usually atoms that have in addition to four electrons, needed for the covalent bond, one electron which is donated to the conduction band, leaving the remaining foreign atom in a positively charged state. These states are located near the conduction band. On the other hand *shallow acceptors* are missing one electron. In order to complete the missing bond they accept an electron from valence band, thus creating a hole in the valence band. In this case the final atom is negatively charged. Shallow acceptors are located near the valence band.

In general, donors are defined as impurities with one energy level in the bandgap, which can assume neutral or positive charge state, while the acceptors can be neutral or negative. Which charge state the impurity is found to be in depends on its energy level position in the bandgap and temperature. At room temperature almost all shallow donors near the conduction band ($\sim k_B T$ below), and shallow acceptors near the valence band are ionised, since the energy

needed for the electron (hole) to jump from donor (acceptor) state to conduction (valence) band is comparable with k_BT. Thus at high enough concentration of impurities of a certain type, the number of electrons in the conduction band approximately equals the number of donors, or the number of holes in the valence band approximately equals the number of acceptors. The relation $n = p = n_i$ is no longer valid as in pure semiconductor, but the relation

$$n_i^2 = np \tag{3.12}$$

still holds. This relation is called the *mass action law* and it states that the added concentration of the charge carriers of certain type increases the rate of recombination, shifting the equilibrium between electrons and holes.

If the concentration of donors, N_D, exceeds the concentration of acceptors N_A (ie. n>p), the material is called n*-type*, with electrons as majority carriers. If on the other hand, N_A>N_D (ie. p>n), the material is defined as being p*-type*, with holes as majority carriers. In silicon, the standard doping element serving as a donor is phosphorus, while for doping with acceptors boron is usually used.

In a doped semiconductor, the Fermi level adjust itself in order to preserve overall charge neutrality, which demands

$$n + N_A^- = p + N_D^+, \tag{3.13}$$

where N_D^+ and N_A^- are concentrations of ionised donors and acceptors respectively. In the case of shallow dopants, most of these impurity atoms are ionised at room temperature, thus $N_D^+ \approx N_D$, $N_A^- \approx N_A$. The concentration of electrons and holes follow from equations 3.12 and 3.13.
For a highly doped n-type sample (ie. $N_D \gg N_A$, $N_D - N_A \gg n_i$) the Fermi level can be obtained by [Sze81]

$$E_F = E_c + k_BT \ln\left(\frac{N_D}{N_c}\right) \tag{3.14}$$

and similarly for a p-type sample

$$E_F = E_v - k_BT \ln\left(\frac{N_A}{P_v}\right). \tag{3.15}$$

As shown by equation 3.10, the Fermi level in an intrinsic semiconductor lies close to the middle of the bandgap. If donor impurities are introduced, the Fermi level shifts closer to the conduction band, increasing the concentration of free electrons. On the other hand, acceptors shift the Fermi level closer to the valence band.

3.1.3 Charge carrier transport

In the semi-classical model, the motion of electrons and holes in conduction and valence band respectively can be described as free with an effective mass. Charge carriers are scattered by imperfections of the crystal lattice due to thermal lattice vibrations and other sources such

as crystal defects and impurities. The average displacement of carriers due to random motion is zero if no external electric field is applied. In the presence of electric field the charge carriers are constantly accelerated, but continuous scattering limits the average charge carrier velocity to a constant value. The relation between the net average drift velocity $\mathbf{v}^{(\mathbf{dr})}$ and electric field $\boldsymbol{\varepsilon}$ is called the *mobility* μ:

$$\mathbf{v_e}^{(\mathbf{dr})} = -\frac{e_0\tau_e^s}{m^*_{c,e}}\boldsymbol{\varepsilon} = -\mu_e\boldsymbol{\varepsilon} \quad \text{(electrons)} \tag{3.16}$$

$$\mathbf{v_h}^{(\mathbf{dr})} = \frac{e_0\tau_h^s}{m^*_{c,h}}\boldsymbol{\varepsilon} = \mu_h\boldsymbol{\varepsilon} \quad \text{(holes)} \tag{3.17}$$

Here τ_e^s and τ_h^s are the mean times between scattering events for electrons and holes respectively, while $m^*_{c,e}$ and $m^*_{c,h}$ are electron and hole conductivity effective mass respectively. They differ due to the different curvatures the of conduction and valence bands. At low values of the electric field, where the velocity change due to acceleration in the field is small compared to the thermal velocity, the mobilities are constant. At higher electric field strengths the linearity between the drift velocity and electric field breaks down as the drift velocity becomes independent of applied electric field and saturates at the *saturation velocity*, v^{sat}. As scattering of charge carriers occurs on crystal imperfections, which are due to thermal vibrations and impurity atoms, mobilities $\mu_{e,h}$ also depend on temperature and doping concentrations [Sze81]. In an anisotropic medium, where the directions of current differs from the direction of field, the mobilities (and conductivity effective masses) can be a tensors.

The current density due to drift of charge carriers $\mathbf{j}^{(\mathbf{dr})}$ can be obtained as the sum of current densities due to drift of electrons in the conduction band, $\mathbf{j_e}^{(\mathbf{dr})}$, and holes in the valence band, $\mathbf{j_h}^{(\mathbf{dr})}$,:

$$\mathbf{j_e}^{(\mathbf{dr})} = -e_0 n\mathbf{v_e^{dr}} = e_0 n\mu_e\boldsymbol{\varepsilon} \tag{3.18}$$

$$\mathbf{j_h}^{(\mathbf{dr})} = e_0 p\mathbf{v_h^{dr}} = e_0 p\mu_h\boldsymbol{\varepsilon} \tag{3.19}$$

$$\mathbf{j}^{(\mathbf{dr})} = \mathbf{j_e}^{(\mathbf{dr})} + \mathbf{j_h}^{(\mathbf{dr})} = e_0(n\mu_e + p\mu_h)\boldsymbol{\varepsilon}. \tag{3.20}$$

Defining the electrical resistivity ρ as

$$\rho = \frac{1}{e_0(n\mu_e + p\mu_h)}, \tag{3.21}$$

one can rewrite the current density in the form of Ohm's law

$$\mathbf{j}^{(\mathbf{dr})} = \frac{1}{\rho}\boldsymbol{\varepsilon}. \tag{3.22}$$

Since the mobilities depend on temperature as a modest power law, the temperature dependence of the resistivity in the intrinsic region will be dominated by the exponential dependence $\exp{(E_g/2k_BT)}$ of the carrier concentration.

In the presence of an inhomogeneous distribution of charge carriers, the diffusion will even out the carrier density variations and carriers will diffuse from regions with higher density to

regions where the density is low. This process is mathematically described by the diffusion equation

$$\mathbf{j}_\mathbf{e}^{(\mathbf{dif})} = e_0 D_e \nabla n \qquad \mathbf{j}_\mathbf{h}^{(\mathbf{dif})} = -e_0 D_h \nabla p. \tag{3.23}$$

Here $\mathbf{j}_\mathbf{e}^{(\mathbf{dif})}$ and $\mathbf{j}_\mathbf{h}^{(\mathbf{dif})}$ represent the current density due to diffusion of electrons and holes respectively, while D_e and D_h are diffusion constants. Mobility and diffusion are related to each other by Einstein equation [AM76]

$$D_{e,h} = \frac{k_B T}{e_0} \mu_{e,h}. \tag{3.24}$$

3.1.4 Charge carrier generation and recombination

In a semiconductor with indirect bandgap (like Si, Ge and diamond), direct band-to-band transitions between conduction and valence band are suppressed as they require a large momentum transfer to the crystal lattice. Recombination and generation of charge carriers instead occur through localised energy states in the bandgap, that provide stepping stones for electrons and holes traversing the forbidden gap. These energy states in the forbidden gap are due to the presence of impurities and crystal defects leading to lattice structural imperfections, which are introduced during the crystal-growing process or by radiation damage. They can be placed in two categories: shallow and deep states. Shallow states are located near their related band edge ($\approx k_B T$ away): acceptor is near the valence and donor near the conduction band. Deep states are those which are positioned deeper than shallow states.

A simple donor state is defined as a defect state with one energy level in the bandgap, which can take two different charge states, neutral or positive. While simple acceptors with one energy level in the bandgap can take neutral or negative charge state. In general, a single defect can have several energy levels and charge states. Which charge state a defect is found to occupy is determined by the interaction of the defect level with the conduction and valence bands. According to the work of W. Shockley, W. T. Read [SR52] and R. N. Hall [Hal52] this can be described as a statistical process. Changing the charge state of the defect is accomplished by one of the four competing reactions taking place: capture or emission of electron or hole, as shown in figure 3.2. If complications from defects with several energy levels of same charge or with degenerated energy levels are ignored, then, as will be shown in the next section, emission and capture processes are related to each other in such way that a non-degenerated defect is characterised by the following quantities [Lut96]:

- k energy levels $E_{t,k}$ which describe the energy involved in changing the charge states $k-1$ and k

- $k+1$ charge states with charge $Q_{t,l}$ ($l = 0, ...k$) ordered from most positive to most negative,

- *k electron capture cross sections $\sigma^t_{n,k}$*

- *k hole capture cross sections $\sigma^t_{p,k}$*

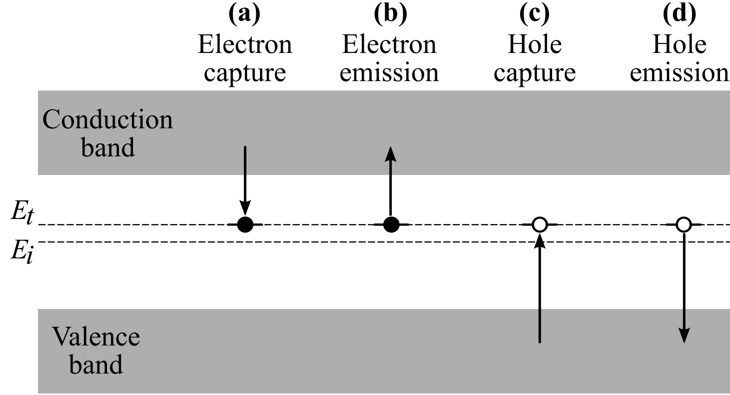

Figure 3.2: *Charge carrier capture and emission processes for a defect with an energy level E_t. Arrows label the carrier transition.*

For simplicity we will restrict ourselves to simple donors and acceptors, which have only one energy level and two charge states. They are completely described by the corresponding energy level and the two cross sections. Consider a non-degenerated defect state with energy level E_t, concentration N_t and capture cross sections σ_n^t and, σ_p^t. The rates of the four processes are then given as:

- $R_n = v_e^{th}\sigma_n^t n N_t(1 - P(E_t)) = c_n^t n p_t$ for the capture of an electron from the conduction band
- $G_n = \epsilon_n^t N_t P(E_t) = \epsilon_n^t n_t$ for the emission of an electron to the conduction band
- $R_p = v_h^{th}\sigma_p^t p N_t P_t(E_t) = c_p^t p n_t$ for the capture of a hole from the valence band
- $G_p = \epsilon_p^t N_t(1 - P(E_t)) = \epsilon_p^t p_t$ for the emission of a hole to the valence band

Here n and p represent densities of free electrons and holes, while ϵ_n^t and ϵ_p^t are their *emission probabilities* regarding the defect with energy E_t. The *capture coefficients* for electrons and holes,c_n^t and c_p^t respectively, are defined as the product of the thermal velocity of the carrier type considered, $v_{e,h}^{th}$, and its capture cross section, $\sigma_{n,p}^t$

$$c_{n,p}^t = v_{e,h}^{th}\sigma_{n,p}^t \tag{3.25}$$

$P_t(E_t)$ labels the average occupation probability of the defect considered, so that

$$n_t = N_t P_t(E_t) \tag{3.26}$$

is the density of considered defects which are *occupied* (with electrons). Similarly

$$p_t = N_t(1 - P_t(E_t)) \tag{3.27}$$

represents the density of defects which are *not occupied*, so that $N_t = n_t + p_t$.

If all four competing processes are taken into account, the rate of change of the average defect occupancy is given by

$$\frac{dn_t}{dt} = (G_p - R_p) - (G_n - R_n) = (c_n^t n + \epsilon_p^t)(N_t - n_t) - (c_p^t p + \epsilon_n^t)n_t, \tag{3.28}$$

where $(G_p - R_p)$ and $(G_n - R_n)$ represent the hole and electron excess generation rate respectively.

An *electron-hole recombination* event is process (a) on figure 3.2 followed by (c), while a *generation* event is (b) followed by (d). In these cases the defect interacts with both conduction and valence band and is called a *generation-recombination centre*. A third type of event is *trapping* which is either (a) followed by (b), or (c) followed by (d). In both cases a carrier is captured and subsequently emitted back. Here the defect interacts with only one of the bands and is called a *trap*.

Simple defects in thermal equilibrium

Thermal equilibrium considerations allow the derivation of a relationship connecting capture and emission processes of electrons and holes. Consider again a non-degenerated defect state with energy level E_t and concentration N_t. In thermal equilibrium the average electron occupation probability for this state is described by the Fermi function:

$$P_{eq}(E_t) = F(E_t) = \frac{1}{1 + \exp\left(\frac{E_t - E_F}{k_B T}\right)} = \frac{1}{1 + \chi_{E_t}/\chi_{E_F}}, \tag{3.29}$$

where the short hand notation

$$\chi_E = \exp\left(\frac{E - E_i}{k_B T}\right) \tag{3.30}$$

has been used. Furthermore, in thermal equilibrium the rates of capture and emission must be equal separately for electrons and holes. This follows from the requirement that electron and hole concentration, as well as the average defect occupation probability, do not change since there is no net flow of electrons between the valence and conduction band. Thus

$$G_n = R_n, \quad \Longrightarrow \quad N_t F(E_t)\epsilon_n^t = nc_n^t N_t(1 - F(E_t)), \tag{3.31}$$

$$G_p = R_p, \quad \Longrightarrow \quad N_t(1 - F(E_t))\epsilon_p^t = pc_p^t N_t F(E_t). \tag{3.32}$$

With the use of equations 3.11 this allows one to obtain the connection between the emission probabilities and capture coefficients

$$\epsilon_n^t = \frac{1}{\tau_{\epsilon,n}^t} = n_i c_n^t \chi_{E_t} \tag{3.33}$$

$$\epsilon_p^t = \frac{1}{\tau_{\epsilon,p}^t} = n_i c_p^t \frac{1}{\chi_{E_t}}. \tag{3.34}$$

Here $\tau_{\epsilon,n}^t$ is the mean time needed for the occupied defect to change its charge state by electron emission and $\tau_{\epsilon,n}^t$ is defined in analogous way. Similarly, $\tau_{c,n}^t$ and $\tau_{c,p}^t$ defined as

$$\frac{1}{\tau_{c,n}^t} = nc_n^t \tag{3.35}$$

$$\frac{1}{\tau_{c,p}^t} = pc_p^t \tag{3.36}$$

describe the mean time needed for unoccupied or occupied defect to change its charge state by electron or hole emission respectively. The relations 3.33 and 3.34 depend only on defect properties and not on n and p, thus, they hold in non–equilibrium situations as well. As emission probabilities are related to capture cross sections, simple defects will be fully described by the energy level E_t and electron and hole cross sections σ_e^t and σ_h^t.

Equation 3.33 shows that electron emission probabilities for defects in the upper half of the bandgap are much higher than those for the defects in the lower half of the bandgap. Similarly, it follows from equation 3.34 that the hole emission rate is generally higher for defects in the lower part of the bandgap than for those in the upper part of the bandgap.

Simple defects in a general stationary situation

In a non-equilibrium situation, the Fermi function can no longer be used to describe the average occupation of defects. In a general stationary state, the average occupation of a defect does not change in time, $dn_t/dt = 0$. Therefore, the excess generation rates for holes and electrons have to be equal, $(G_p - R_p) = (G_n - R_n)$, and we can find average occupation probability to be

$$P(E_t) = \frac{c_n^t n + \epsilon_p^t}{c_n^t n + \epsilon_p^t + c_p^t p + \epsilon_n^t} = \left(\frac{c_p^t p + c_n^t n_i \chi_{E_t}}{c_n^t n + c_p^t n_i / \chi_{E_t}} + 1 \right)^{-1} \tag{3.37}$$

where in the last step the relations between capture coefficients and emission probabilities have been used. Thus the excess generation rate is given by

$$U = G_n - R_n = G_p - R_p = \beta_t (n_i^2 - pn), \tag{3.38}$$

$$\beta_t = N_t \frac{c_n^t c_p^t}{c_n^t n + c_p^t n_i / \chi_{E_t} + c_p^t p + c_n^t n_i \chi_{E_t}}. \tag{3.39}$$

These equations have been derived under the assumption that only one type of simple defect is present. The generalisation for many different simple defects is obtained by summing β_t over the different types of the defects.

Simple defects in the space charge region

Here we consider defects in the space charge region (SCR) that is formed in a reversely biased p^+–n junction which is the basic structure of a silicon detector. We assume that the free carrier concentration in the SCR is negligible, $n_i \gg n \approx p \approx 0$[3], so there are no free carriers available for capture. Thus, only emission processes are important in this case. Emission in the absence of capture can only take place by alternating hole end electron emission, i.e. generation of electron-hole pairs.

The average occupation probability of a defect with energy E_t in the SCR can be determined

[3]This is a good assumption in case of reversely biased diode with bias voltage $V \gg k_B T/e_0$ and low leakage current.

from equation 3.28 with the assumption that capture can be neglected compared to emission processes and with the requirement that in a stationary state average occupation of the defect does not change in time ($dn_t/dt = 0$). Thus $G_p = G_n$ which gives

$$P_{scr}(E_t) = \left(1 + \frac{c_n^t}{c_p^t}\chi_{E_t}^2\right)^{-1} \tag{3.40}$$

for the average occupation probability in SCR and

$$\begin{aligned} G_{scr} &= G_n = G_p = N_t P_{scr}(E_t)\epsilon_n \\ &= N_t P_{scr}(E_t) n_i v_e^{th} \sigma_e \chi_{E_t} = N_t n_i \frac{c_n^t c_p^t}{c_n^t \chi_{E_t} + c_p^t/\chi_{E_t}}. \end{aligned} \tag{3.41}$$

for the generation rate.

It is reasonable to assume that capture cross sections of electrons and holes are approximately of the same order of magnitude. In this picture, defects with E_t more than a few $k_B T$ above the intrinsic Fermi level E_i are expected to be predominately unoccupied (more positive) state and those below E_i in an occupied (more negative) state. Thus, the intrinsic Fermi level, E_i, qualitatively plays a similar role in the SCR as the Fermi level does in thermal equilibrium giving the following role to simple defects in the SCR:

- Donors above E_i are predominately positively charged, while acceptors below E_i are negatively charged,
- Donors below E_i and acceptors above E_i are most of the time neutral.
- There is a transition region between the two situations described above. This region extends a few $k_B T$ around the intrinsic level.

As mentioned before, levels in the bandgap can act as traps for drifting charge. Each level can trap both electrons or holes and by that change its charge state. A defect can trap a hole, if it is occupied, and an electron, if it is empty. Thus from the above statements it follows that in the SCR both acceptors and donors above E_i mainly trap electrons and we refer to them as *electron traps*. While those below E_i mainly trap holes and are called *hole traps*. The defects near the middle of the bandgap around E_i act like generation centres and due to alternating emission of holes and electrons in most cases contribute a major part to the leakage current in a reversely biased diode [Sze81].

3.2 Signal generation

Ionising particles, passing through a semiconductor detector volume, generate electron-hole pairs along their path. Electrons and holes are then separated by electric field, if applied. The drift of these mobile charges in electric field induces a current signal on attached electrodes. This section deals with calculation of the induced current qualitatively described by Ramo's theorem [Ram39].

Consider a system of conducting electrodes and the potential, ϕ, of electrostatic field between them (see figure 3.3, left). Let Q_i and ϕ_i denote the induced charge and voltage applied on i-th electrode. Let S be the sensing electrode for current signal induced by the drifting charge, q. Surround each of the electrodes with an equipotential sphere close to its surface, $\partial\mathcal{V}_i$, and also enclose the drifting charge q with a small equipotential sphere, $\partial\mathcal{V}_q$. Call the potential at this sphere ϕ_q. Application the Gauss' law yields the following:

- $$\int\limits_{\partial\mathcal{V}_q} \frac{\nabla\phi}{\epsilon_0} dS = -q, \qquad \int\limits_{\partial\mathcal{V}_i} \frac{\nabla\phi}{\epsilon_0} dS = -Q_i. \tag{3.42}$$

- For the space between electrodes, with the volume inside all the equipotential spheres around the electrodes and drifting charge excluded, it holds that $\nabla^2\phi$=0.

Next, consider a different situation where the charge q is removed and the electrode S raised to a potential ${\phi'}_S \neq 0$, which results in the potential, ${\phi'}_q$, at the location where the charge q was present before (see figure 3.3, right). Gauss' theorem now gives:

- If we call the new potential as ϕ', then

$$\int\limits_{\partial\mathcal{V}_q} \frac{\nabla\phi'}{\epsilon_0} dS = 0, \qquad \int\limits_{\partial\mathcal{V}_i} \frac{\nabla\phi'}{\epsilon_0} dS = -{Q'}_i. \tag{3.43}$$

- For the region between electrodes, including the site where the charge q was situated, it holds $\nabla^2\phi'$=0.

According to Green's theorem it holds that

$$\int\limits_{\mathcal{V}} \left(\phi'\nabla^2\phi - \phi\nabla^2\phi'\right) dV = \int\limits_{\partial\mathcal{V}} \left[\phi\nabla\phi' - \phi'\nabla\phi\right] dS. \tag{3.44}$$

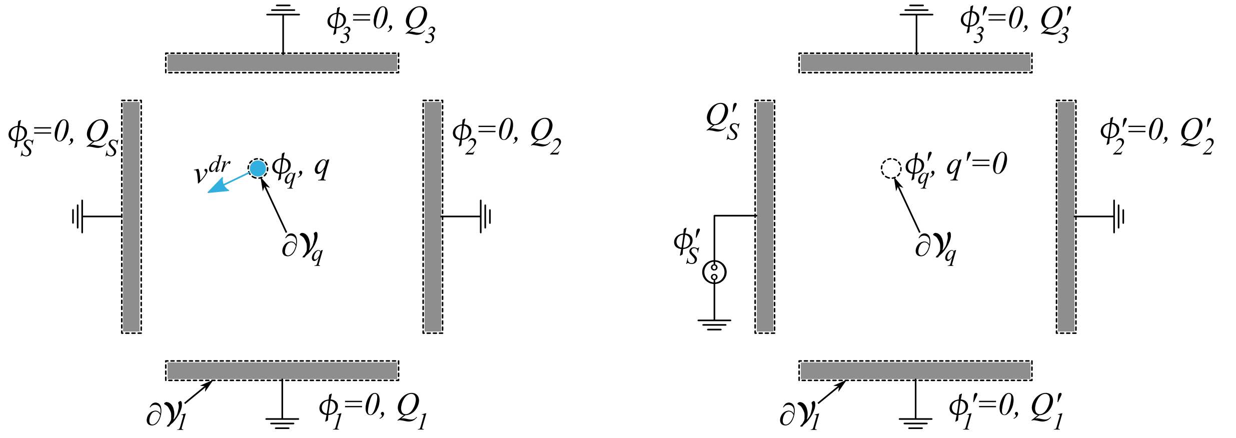

Figure 3.3: *Two electrostatic situations considered in derivation of current induced due to the motion of a charge q. Dotted lines denote the equipotential surfaces around each electrode and q.*

Here $\partial\mathcal{V}$ is the boundary surface of volume $\mathcal{V}$. If we choose the volume $\mathcal{V}$ to be bounded by equipotential spheres around the electrodes $\mathcal{V}_i$ and the tiny sphere around drifting charge $\mathcal{V}_q$, the left-hand side of the equation 3.44 vanishes. Then, with the use of the results given by Gauss' theorem, the right-hand side can be written as

$$\sum_i Q'_i\phi_i + q'\phi_q = \sum_i Q_i\phi'_i + q\phi'_q, \tag{3.45}$$

where the summation runs over all electrodes while Q_i and Q'_i represent the charges induced on i-th electrode in both electrostatically possible situations. Let the potentials and induced charges on all electrodes (apart from the electrode S) be the same in both cases (ie. $Q_i = Q'_i$, $\phi_i = \phi'_i$ where $i \neq S$). Since in the second situation the charge is not present (ie. q'=0) we find

$$Q'_S\phi_S = Q_S\phi'_S + q\phi'_q, \tag{3.46}$$

We choose the zero of potential in such a way that $\phi_S = 0$, thus

$$0 = Q_S\phi'_S + q\phi'_q, \quad \text{or} \quad Q_S = -q\frac{\phi'_q}{\phi'_S} = -q\phi_w \tag{3.47}$$

The induced charge on electrode S depends only on the potential ϕ'_q, caused by electrode S when raised to the potential ϕ'_S, and it does not depend on potential of other electrodes in the system. Thus we can choose the other electrodes to be grounded (ie. $\phi'_i = \phi_i = 0$ for $i \neq S$).

We call the unit-less quotient $\phi_w = \frac{\phi'_q}{\phi'_S}$ the *weighting potential*. It can be obtained by solving the Laplace equation $\nabla^2\phi_w = 0$ with boundary conditions: $\phi_w = 1$ at the surface of sensing electrode and $\phi_w = 0$ on surfaces of all other electrodes.

From equation 3.47 it follows that the current induced on electrode S is

$$I_S = \frac{dQ_S}{dt} = -q\frac{d\left(\frac{\phi'_q}{\phi'_S}\right)}{dt} = -q\frac{d\phi_w}{dt} = -q\frac{\phi_w}{d\mathbf{r}}\frac{d\mathbf{r}}{dt} \tag{3.48}$$

Here $\mathbf{r}$ is the position of the charge drifting in the electric field. If we define $\boldsymbol{\varepsilon_w} = \nabla\phi_w$ as the *weighting field* (or *Ramo's field*) and take $\frac{d\mathbf{r}}{dt}$ as the drift velocity of charge q in electric field, we obtain

$$I_S = -q\mathbf{v}^{\mathbf{dr}}\boldsymbol{\varepsilon_w} \quad (3.49)$$

From equations 3.16, 3.17 and 3.49 one can obtain the time dependence of the induced signal current. The weighting field $\boldsymbol{\varepsilon_w}$ depends only on the geometry of the electrode system and determines how the motion of charge couples to a specific electrode. In general it has a form quite different from the real electric field.

In the case of a simple diode pad detector, which has two parallel electrodes with lateral dimensions much larger than the detector thickness, the weighting field is given by $\varepsilon_w = -\frac{1}{D}$. Hence, the current induced by a drifting electron or hole can be expressed as

$$I_{e,h} = -\frac{q}{D}v^{dr}_{e,h}. \quad (3.50)$$

The connected front-end electronics measures either the current amplitude in case of a *current sensitive* amplifier or the current integral (the charge) in case of a *charge sensitive* amplifier. A detector-amplifier is said to work in the charge sensitive regime if the time constant of signal generation is much lower than the shaping time of the readout electronics. On the other hand a system is current sensitive if the time constant of signal generation is much higher than the shaping time of the readout electronics.

The number of electron-hole pairs generated by an ionising particle along its track is proportional to the particle's energy loss. The energy, E_{e-h}, needed to create an electron-hole pair in a semiconductor is proportional to the bandgap, so that materials with higher bandgap energy yield less signal charge. E_{e-h} for a specific semiconductor is always higher than its bandgap energy. This is due to the additional excitation of phonon states, which transfer the energy to the lattice. The measured value for silicon is E_{e-h}~3.6 eV [Bic88] while for diamond it is E_{e-h}~13 eV [K+75, C+79b]. The average ionisation energy loss of minimum a ionising particle in thin silicon and diamond detector is around 2.9 MeV/cm and 4.7 MeV/cm respectively [Zha94]. This gives around 8000 electron-hole pairs per 100 μm of silicon while around 3600 pairs are created in 100 μm of diamond.

3.2.1 Trapping of drifting charge

Some of the charge carriers, released by the ionising particle traversing the detector, can be trapped during the drift. While the charge carrier is trapped its drift velocity is zero and according to equation 3.50 it does not contribute to the induced signal current. If we assume that $N(0)$ charges, either electrons or holes, have been released at time t=0, then the number of charges trapped in the time interval dt is

$$dN = -N\frac{1}{\tau^{eff}_{e,h}}\,dt, \quad (3.51)$$

where $1\tau_{e,h}^{eff}$ represents the electron or hole trapping probability per unit time. The solution of 3.51 gives an exponential decrease of drifting charge carriers with time

$$N(t) = N(0)\, e^{-\frac{t}{\tau_{e,h}^{eff}}}. \tag{3.52}$$

The trapped charge is eventually released after some time. However, if the emission times are longer then the measurement time than the trapped charge does not contribute to the induced signal current.

3.3 Silicon detectors

In every detector some leakage current will be observed when an external voltage is applied to it. Random fluctuations in this leakage current tend to obscure the small signal current induced by an ionisation event and can represent a significant source of noise. In order to improve the signal-to-noise ration, a p–n junction under reverse bias is used instead of pure silicon as a sensor material. Therefore, a silicon detector is essentially a diode (p–n junction) or array of diodes, operated under reverse bias, where the depleted region acts like an ionisation chamber.

In this section some basic properties of silicon diode are first considered. This is followed by a brief review of how silicon crystals are grown and processed into silicon devices. Finally, the effects induced in a silicon detector when it is exposed to intense radiation is discussed.

3.3.1 Principle of operation: p–n junction

A p–n junction is obtained when dopant concentration changes from the surplus of acceptors $N_{A,p}$ on one side (p side) to a surplus of donors $N_{D,n}$ on the other side (n side). The gradients of electron and hole densities near the junction trigger a diffusive migration of majority carriers across the junction, where they recombine with minority carries. Due to the presence of immobile ionised acceptors and donors, this charge migration leaves the p region with a net negative and the n region with a net positive space charge. The ionised donors and acceptors around the junction form a *depletion* or *space charge region* (SCR), in which an electric field, opposing the migration, is formed. The diffusion of carriers is completely stopped when the Fermi energies on the both sides of junction are levelled.

The value of the potential ϕ at any point across the junction, can be found from the Poison equation

$$\nabla^2\phi = -\frac{\rho_e}{\epsilon\epsilon_0} \tag{3.53}$$

where ϵ is the dielectric constant of the sensor medium and ρ_e the space charge density. Some properties of the p–n junction can be derived if we take the following idealised distribution for the space charge density:

$$\rho_e(x) = \begin{cases} e_0 N_{D,n}, & x_n > x > 0 \\ -e_0 N_{A,p}, & -x_p < x < 0 \\ 0, & \text{else} \end{cases} \tag{3.54}$$

where x_n and x_p represent the depth of the SCR on the n and on p side respectively (see figure 3.4). Here we have assumed that there are no charge carriers in the SCR and that all the dopants

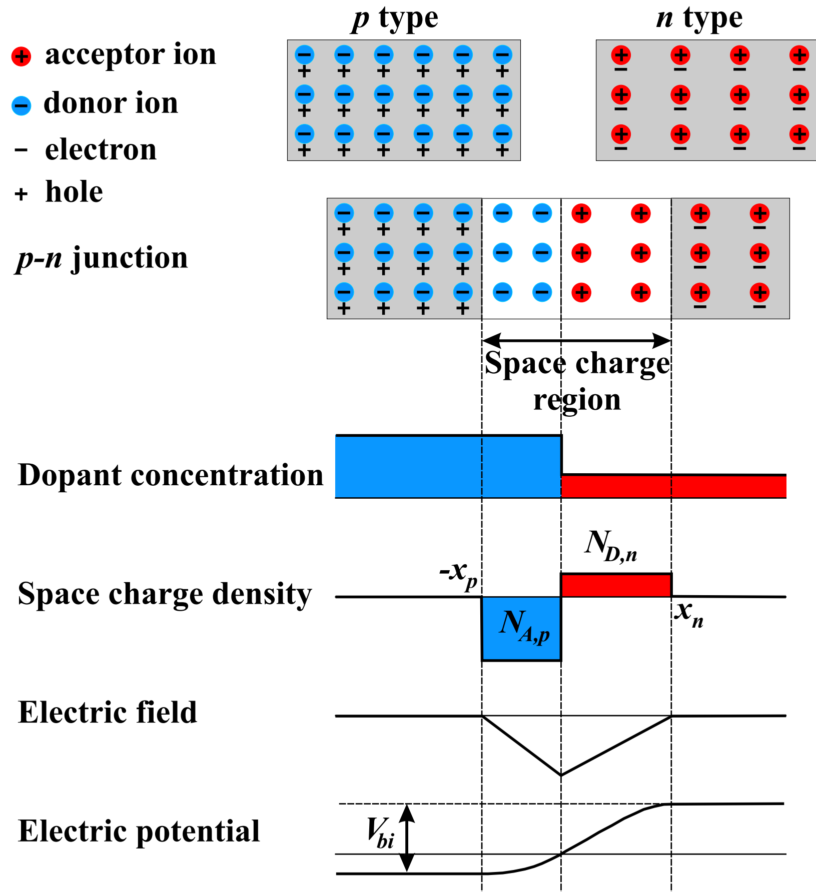

Figure 3.4: *Dopant concentration, space charge density, electric field strength and potential across the p–n junction.*

are ionised with a concentration which exhibits an abrupt change at the junction (the abrupt junction approximation). By integrating the Poisson equation with this $\rho_e(x)$, one obtains the solution for the electric field $\varepsilon(x) = -\frac{d\phi}{dx}$ and potential $\phi(x)$ as shown in figure 3.4.

The potential difference across the SCR when no external voltage is applied is called the *built-in potential*, V_{bi}. This can be obtained from the requirement that the solution of ϕ for the either side of the junction matches at x=0

$$V_{bi} = \frac{e_0}{2\epsilon\epsilon_0}\left(N_{A,p}x_p + N_{D,n}x_n\right). \tag{3.55}$$

The potential difference V_{bi} corresponds to the difference between the values of Fermi energies of the neutral material on the p and n sides. Thus, with the use of equations 3.14 and 3.15, we can write

$$V_{bi} = \frac{1}{e_0}(E_F^n - E_F^p) = \frac{1}{e_0}\left(E_g + k_B T \ln\left(\frac{N_{D,n}N_{A,p}}{N_c P_v}\right)\right). \tag{3.56}$$

The condition of overall electrical neutrality of the system states

$$N_{A,p}x_p = N_{D,n}x_n, \tag{3.57}$$

This shows that the depth of the SCR on each side of the junction is inversely proportional to the doping concentration on that side. Using equations 3.56 and 3.57, we can express the SCR width on both sides as a function of the built-in potential

$$x_p = \sqrt{\frac{2\epsilon\epsilon_0 V_{bi}}{e_0 N_{A,p}(1 + N_{A,p}/N_{D,n})}} \tag{3.58}$$

$$x_n = \sqrt{\frac{2\epsilon\epsilon_0 V_{bi}}{e_0 N_{D,n}(1 + N_{D,n}/N_{A,p})}} \tag{3.59}$$

In most silicon detectors the doping concentration of one side is much higher than that of the other side. Choosing the p side to have a much higher doping concentration than the n side (a so called p^+ side[4]) results in $x_p \ll x_n$. In this case, the full width of the SCR can be approximated by the width on the weakly doped side

$$w_{scr} = x_n + x_p \approx x_n \approx \sqrt{2\frac{\epsilon\epsilon_0 V_{bi}}{e_0 N_{D,n}}} \tag{3.60}$$

Therefore, in a p^+–n junction the n-type silicon serves as the active volume of the detector, while the p-type is necessary only to deplete it of free carriers and it can be very shallow.

Typically, the acceptor concentration on the heavily doped p^+ side is higher than $10^{18}\,\text{cm}^{-3}$ and the concentration of donors on the n side below $10^{12}\,\text{cm}^{-3}$. At room temperature this gives a built-in potential of the order of 1 V and the depth of SCR to few 10 μm.

The electric field, existing in the SCR, causes any electrons created there to be swept toward the neutral n side, while holes are similarly swept toward the p side. Thus, the SCR is devoid of charge carriers and exhibits a very high resistivity compared to the n or p type materials on either side of the junction. This makes the SCR an attractive medium for the detection of particles.

Influence of external voltage

Electron-hole pairs, created in the SCR by a traversing ionising particle, are separated by the electric field present in the SCR and their motion induces an electrical signal on the electrodes attached to the diode. Electron-hole pairs created outside the SCR recombine with free charge carriers, since there is no electrical field that would swept them out of that region. Therefore, this charge can not be detected unless it enters the SCR.

The depth of the SCR can be altered by applying an external voltage, V, to the junction. If V is of the same polarity as V_{bi} then the depth of the SCR, w_{scr}, will increase. This voltage is called a *reverse bias*. If the applied bias has the opposite polarity as V_{bi} then the depth of SCR is decreased and we speak of a *forward bias*. Since, for the detection of particles an increase of the SCR is desired, a reverse bias is applied to a silicon detector during its operation. In

[4]The "+" labels high concentration of dopants, in this case acceptors.

this case V_{bi} in equation 3.60 can be replaced by $V_{bi} + V$, where V represents the reverse bias. Usually $V \gg V_{bi}$, so that V_{bi} can be omitted and

$$w_{scr}(V) = \sqrt{\frac{2\epsilon\epsilon_0 V}{e_0 N_{D,n}}}. \tag{3.61}$$

Thus, the voltage that is needed to fully deplete the detector, V_{FD}, called the *full depletion voltage*, quadratically depends on the detector thickness, D,

$$V_{FD} = \frac{e_0 N_{D,n} D^2}{2\epsilon\epsilon_0}. \tag{3.62}$$

Capacitance of a p^+–n junction

We consider a p^+–n diode under a reverse bias voltage, V. The junction capacitance is associated with the voltage dependent charge in the SCR and can be obtained as [Sze81, Lut99]

$$C(V) = \left.\frac{dQ(V')}{dV'}\right|_{V'=V}. \tag{3.63}$$

where dQ is the charge increment appearing on either side of the junction as a result of a widening of the SCR on that side due to an incremental increase of the applied voltage, dV'. Using equation 3.61, one obtains

$$C(V) = S\sqrt{\frac{e_0\epsilon\epsilon_0 N_{D,n}}{2V}} = \frac{\epsilon\epsilon_0 S}{w_{scr}}. \tag{3.64}$$

where S is the area of the diode. The junction capacitance decrease with increasing reverse bias voltage as $C \sim \sqrt{1/V}$. It reaches a constant value when the SCR covers the whole detector volume, since increasing the voltage above V_{FD} does not further increase the charge.

Increasing the bias voltage will increase the sensitive volume and decrease the capacitance of the detector. This is beneficial for detection of charged particles traversing the detector, since it increases the signal charge and reduces the electronic noise. Therefore the operation voltage of the detector is usually set above its full depletion voltage. However, the maximum voltage one can apply is limited as at high enough electric field an electrical breakdown occurs and the reverse bias current increases drastically[5].

The width of the SCR can also be increased by reducing the dopant concentration. Ultimately, this is limited by the minimum residual impurity levels in the crystal. In practice, the lightly doped n side of a silicon detector can include both donor and acceptor impurities. If the donor and acceptor concentration in the n bulk of a p^+–n junction are of the same order of

[5]There are two mechanisms that can cause breakdown[Lut99]. An avalanche breakdown occurs when the electric field is high enough for charge carriers to acquire sufficient energy to form secondary electron-hole pairs which ultimately leads to a destructive avalanche. A Zener breakdown is described as quantum mechanical tunnelling of electrons through the bandgap from valence to conduction band due to electric field alone. This breakdown mechanisms is dominant for highly doped p–n junctions.

magnitude then $N_{D,n}$ in equations 3.61, 3.62 and 3.64 must be replaced by the difference of the ionised donor and acceptor concentration N_{eff}, called *effective dopant concentration* N_{eff},

$$N_{D,n} \Longrightarrow |N_{eff,n}| = |N_{D,n} - N_{A,n}| \,. \tag{3.65}$$

This is true for the n type material, obtained by donor compensation, which is often used in silicon detectors. The replacement 3.65 must also be considered if radiation induced defects are present in the bulk.

Leakage current of a p^+–n junction

In thermal equilibrium, $V = 0$, both electron and hole current vanish. This, however, does not mean that there is no carrier flow across the junction. Instead, as many electrons (or holes) flow in one direction as in the other[6]. When $V \neq 0$, this balance is disrupted.

The current of a reverse biased diode is called *leakage* or *reverse current*. This current is of primary interest in radiation detectors since it is a source of noise. There are two main contributions to the leakage current running through the SCR:

- *Diffusion current* which is due to diffusion of charge carriers from the neutral region on one side of the SCR to the neutral region on the other side,
- *Generation current* due to recombination–generation processes in the SCR.

The generation current represents the dominant contribution to the leakage current in highly irradiated and most non-irradiated silicon devices [Sze81]. It is due to alternating emission of electrons and holes from the defects in the SCR, where capture processes can be neglected (see section 3.1.4). The electron-hole pairs generated in the SCR are immediately separated by the electric field and swept to the neutral regions giving rise to the generation current. Since the emission probability exponentially depends on the position of the defect energy level in the bandgap (equations 3.33 and 3.34), defects with energy levels close to the middle of bandgap are most effective in contributing to generation current. If the emission centres are distributed uniformly throughout the SCR, one may simply calculate the generation current originating from the SCR by multiplying the depletion volume with the generation rate G_{scr} from equation 3.41 [Spi05, Lut99, Sze81]

$$\begin{aligned} I_{scr} &= e_0 G_{scr} w_{scr} S = e_0 w_{scr} S \sum_{\mathrm{t}} G^t_{scr} \\ &= e_0 w_{scr} S n_i v_{th_e} \sum_{\mathrm{t}} N_t P_{scr}(E_t) \sigma^t_n \chi_{E_t}. \end{aligned} \tag{3.66}$$

where the summation runs over all types of defect states present. This current is proportional to the width of the SCR. Thus, as long as the diode is not fully depleted I_{scr}, rises proportionally with $\sqrt{V}$.

[6] The drift current due to electrical field present in the SCR exactly cancels the diffusion current.

The bulk generation current strongly depends on the temperature, T, at which it is measured. This temperature dependence comes from the intrinsic carrier density n_i, the defect occupancies P_t, the electron thermal velocity v_{th_e}, the electron capture cross sections σ_{e_t} and factor χ_{E_t}. If only defects near the middle of the bandgap ($E_t \approx E_i$) are considered and capture cross sections are taken to be independent of temperature while $v_{th} \propto \sqrt{T}$ is assumed, then one obtains the following leakage current temperature dependence

$$I_{scr} \propto T^2 \exp\left(\frac{E_g}{2k_B T}\right). \tag{3.67}$$

A significant contribution to the leakage current can also come from the currents generated in the region of the detector surface. The main source of these surface currents are the fixed ionic charges at the semiconductor surface that induce image charges in the semiconductor and cause the formation of surface channels (or surface SCR regions). These channels modify the junction SCR and give rise to surface leakage currents which are hard to control since they are strongly influenced by mechanical damage, humidity and other contamination of the detector surface. However, in real detectors several protecting guard rings are usually added, which collect these surface currents.

3.3.2 Silicon detector fabrication

The basic unit for device fabrication is a silicon wafer, a disk of single crystal silicon with diameter ranging from 1 to 6 inches and thickness between 200 and 2000 μm. It can be obtained by slicing a single-crystal ingot which is manufactured from a polysilicon rod by the Czochralski or the float zone technique. Another way of producing a silicon wafer is epitaxial growth where silicon atoms are deposited on a single crystal substrate. The introduction of impurities in the silicon crystal can be performed at different stages of wafer production: during the production of polysilicon, during the ingot growth, during the epitaxial growth or by diffusion into the wafer itself.

This section gives a brief description of different growth techniques for monocrystalline silicon. Subsequently a simplified production sequence in planar technology, which is today's standard method for processing of silicon detectors, is given.

Detector grade silicon growth

Czochralski silicon (Cz) Most of the silicon used for electronics is grown by this method. Here, the starting high purity polysilicon material is melted together with additional dopants as required for the final resistivity (figure 3.5(a)). It is held in a rotating (clockwise) quartz (SiO_2) crucible which is surrounded by the graphite susceptor of the furnace. A seed-holder, containing the single crystal seed of a suitable orientation (e.g. $\langle 111 \rangle$), is placed on the surface of the liquid silicon from above and slowly drawn upwards while being rotated (counter-clockwise). The progressive solidification of molten silicon, drawn after it, yields the formation of continuous crystal extending from the seed with the same characteristics as the seed. The whole system

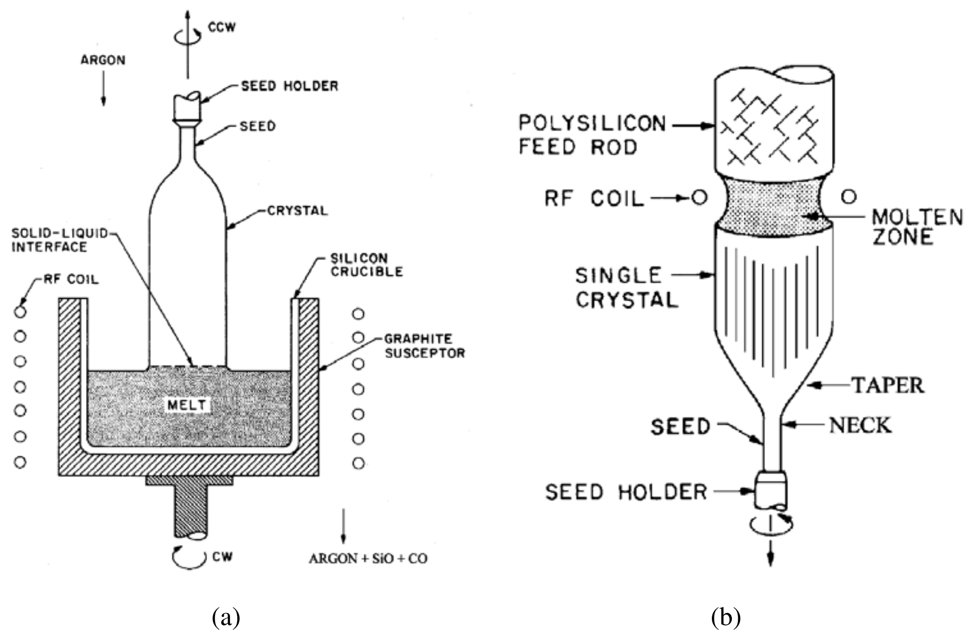

Figure 3.5: *Schematic setup for the Czochralski (a) and float zone process (b). Source [Sze02].*

is held at ambient atmosphere of an inert gas, usually argon.

High concentrations of impurities are introduced into the melt from the crucible wall. The most important one is oxygen which can lead to formation of unwanted electrically active defects[7]. The highest resistivity of commercially available Cz wafers is 100 Ωcm. Therefore, the standard Cz material is not suitable for the detector production which requires high resistivity silicon. The next important impurity is carbon which is electrically neutral impurity. The typical concentrations of the most common impurities in standard Cz silicon, O and C, are (5–10)$\times 10^{17}$cm^{-3} and (5–50)$\times 10^{15}$cm^{-3} respectively.

The magnetic Czochralski method (MCz) offers a better control of oxygen incorporation in the silicon lattice. This method is the same as the Cz method except that a strong horizontal or vertical magnetic field is applied during the crystal growth which serves to control the convection fluid flow and with this the migration of contaminations into the crystal[8]. With the MCz method, lower oxygen concentrations and more homogeneous distribution of impurities can be obtained compared to standard the Cz method.

The float zone method (FZ) In this method a polysilicon rod is held in a vertical holder with a single crystal seed at the bottom. Both are rotating and a radio frequency heater is used to melt a small zone of the rod (see figure 3.5(b)). As the polysilicon rod is moved upwards,

[7]These are so called oxygen related thermal donors.

[8]For example, in the horizontal MCz method, the transversal magnetic field suppresses convection which causes a decrease in oxygen atoms moving from the crucible to the growth interface. This effectively creates a liquid silicon crucible around the centre of the silicon melt, which can trap contaminations.

the molten zone is moved along with it and solidifies into single crystal. This process can be repeated several times in order to obtain a high purity material. Typical O and C concentrations are below $5\times10^{15}\text{cm}^{-3}$.

Unlike in the Cz method, the silicon molten zone is not in contact with any substance except with ambient gas which may only contain doping gas[9]. Thus, more pure and higher resistivity silicon can be obtained with the use of float zone technique. Resistivity levels in the range 10–50 kΩcm can be obtained, although normally levels are around 5 kΩcm for n–type material.

Epitaxial growing In epitaxial growth, single crystal films are grown on a single crystal silicon substrate. The crystal structure of the epi-layer is defined by the lattice structure and surface orientation of the substrate. There are many different epitaxial growing techniques. For epitaxial silicon production, vapour-phase epitaxy (VPE) is usually used with low resistivity Cz silicon as a substrate. Silicon is most commonly deposited on the substrate from $SiCl_4$ at approximately 1200°C through the reaction:

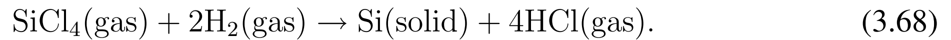

$$\mathrm{SiCl_4(gas) + 2H_2(gas) \rightarrow Si(solid) + 4HCl(gas).} \tag{3.68}$$

An additional etching reaction competes with this deposition reaction:

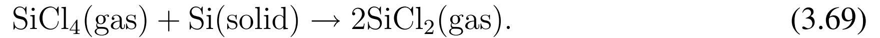

$$\mathrm{SiCl_4(gas) + Si(solid) \rightarrow 2SiCl_2(gas).} \tag{3.69}$$

Small concentrations of $SiCl_4$ results in low growth rates while too high concentrations result in etching. Therefore, the optimum concentration has to be carefully chosen. The dopants are introduced together with $SiCl_4$ during the epitaxial growth[10].

During the crystal growth, impurities from the Cz substrate diffuse into the epi-layer, resulting in higher concentrations of O and C in epi-wafers than in FZ wafers.

Processing of silicon detectors

Before processing can start, wafers are mechanically lapped and polished on both faces in order to obtain silicon wafers with suitable thickness and smooth surface. These wafers are then ready for detector processing. Today's semiconductor detector processing is to a large extent based on planar technology, which was originally developed in the field of micro-electronics and later adapted to detector grade silicon processing by J. Kremmer [Kem80]. Here, a brief description of this technique is given. For more information see [Sze02, Lut99, Spi05, Kem80, Kem84].

First the wafer surface is passivated through the creation of an oxide (SiO_2) layer at elevated temperature (around 1000°C). This oxide layer protects the wafer during the processing and later the detector itself from contaminations. Furthermore, it establishes a well-controlled termination for the "dangling bonds" where the crystal lattice is truncated and eliminates surface leakage current. Then, using photo-lithographic and etching techniques, windows are opened in the oxide to enable doping of these areas by ion implantation, while the oxide masks the rest

[9] The doping of FZ material is obtained by adding the doping gas to the inert atmosphere. The doping gas for n– (p–) type material is PH_3 (B_2H_6).

[10] As in the case of the FZ technique, gaseous B_2H_6 is used as p–type dopant and PH_3 as n–type.

of the surface. With appropriate masks any geometry of pads or strips is feasible. The n^+ strips or pads are implanted with B, while P or As is used for p^+ strips. After implantation, the wafers are annealed in order to reduce the radiation damage in implanted layers. Finally, in order to provide good electrical contact, the implanted layers are metallised (usually with Al), again with the use of photo-lithographic techniques. The wafer is then ready to be cut into individual detectors.

Alternatively, the junctions can be created by diffusion. The oxide layer can still be used as an effective mask. The dopant impurities react with oxide to form glass. Above areas, where junction are to be formed, the thickness of glass increases until the entire oxide layer is converted to glass. On the other hand, the thicker oxide above non-junction areas is not completely converted and therefore masks these areas in the next step when the dopants at junction areas diffuse through the glass into silicon.

3.3.3 Radiation damage in Silicon detectors

Radiation induced damage in silicon detectors can roughly be divided into surface and bulk damage.

An incoming charged particle can lose its energy through ionising and non–ionising energy loss (NIEL) mechanisms. Surface damage is mainly caused by charge carriers liberated in the oxide (SiO_2) layers due to passage of ionising radiation. This leads to accumulation of charge carriers trapped at the oxide–silicon interface, causing unwanted parasitic fields and subsequent breakdown. Surface damage depends on detector design and can be controlled to a certain extent by proper design and manufacturing process. More details about surface damage can be found in [Lut99], [Spi05].

Due to fast recombination of charge carriers in the bulk, ionising energy loss does not lead to bulk damage. Bulk damage is caused by non-ionising energy loss interactions, which result in displacement of silicon atoms out of their lattice site. The resulting defects introduce deep level states in the bandgap, which alters the electrical characteristics of the bulk crystal. The radiation studies in this work are focused on the bulk damage, since this is the principle obstacle to long term operation for silicon detectors used in high energy physics experiments with high radiation fields.

Generation of defects

Radiation induced bulk damage occurs when incident particles transfer sufficient kinetic energy to the crystal lattice to displace a silicon atom out of its lattice site. This results in formation of a silicon interstitial atom (I) and a vacancy (V). This pair of point defects is called a *Frenkel pair*, while the lattice atom, dislodged by an incoming particle, is known as a *Primary Knocked-on Atom* (PKA). The minimum recoil kinetic energy required for displacement, E_R, was measured to be between 11 eV and 25 eV, depending on the direction [CRG]. If the kinetic energy, imparted in recoiled PKA, is sufficiently high, further silicon atoms can be knocked out.

Along its path, the recoiled PKA loses its energy through two competing energy loss mechanisms, ionising and non-ionising. Low energy recoils will usually create only point defects. However, non-ionising interactions prevail at the end of any heavy recoil's track, which results in a dense agglomerate of point defects. These highly disordered regions are referred to as *defect clusters*. In order to create a defect cluster, a recoil energy above about 5 keV is needed [L+80]. Both, point defects along the particle's path and clusters at the end of heavy recoils are responsible for bulk damage effects.

Another NIEL mechanism of damage is through nuclear reactions of impinging particles with silicon nuclei. The resulting high energy fragments can be involved in the damage process.

Both components of a Frenkel pair are very mobile above 150 K in silicon. Thus, at room temperature, interstitials and vacancies are not stable and a part of them will anneal by annihilation. Simulations show that about 60% of overall Frenkel pairs produced annihilate, rising to 75% to 90% inside defect clusters [S+89]. The remaining vacancies and interstitials diffuse through the crystal lattice and react with other defects or impurity atoms always present in silicon crystal (O, C, P, B,...). to form new type of point defects that can be immobile at room temperature. The formation of these defect complexes is complicated and only partly understood. Since the formation depends on temperature, defect complexes that are stable at room temperature may become mobile or even break up into their constituents at elevated temperatures.

Point defects and defects inside defect clusters introduce energy levels in the bandgap and can deteriorate the detector performance, depending on their concentration, energy level and corresponding electron and hole capture cross-sections.

Comparison of radiation damage measurements

Radiation induced damage in silicon crystal depends on the type and energy of the impinging particles. The displacement efficiency of an impinging particle is described by a *displacement damage function*, which takes into account various types of interactions between particle and silicon atoms. The displacement damage function, $D(E)$, is measured in units of MeVmb and gives a measure of the average kinetic energy, deposited in the crystal lattice in the form of displacement damage by an incoming particle with energy E. It is given by [L+87]

$$D(E) = \sum_k \sigma_k(E) \int_0^{E_R^{max}} f_k(E, E_R) P(E_R) dE_R. \qquad (3.70)$$

Here, E_R is the kinetic energy of the recoiled PKA which was displaced by an impinging particle with energy E. The index k indicates all possible interactions between the incoming particle with energy E and silicon atoms in the lattice resulting in displacement of a PKA. The function $P(E_R)$, known as the Lindhard partition function, represents the portion of the recoil energy, E_R, that is deposited in the form of further displacement damage[11] and $f_k(E, E_R)$ gives

[11] $P(E)$ can be analytically calculated by a relation derived by Robinson [Rob76], based on the electronic screening theory of Lindhard [L+63].

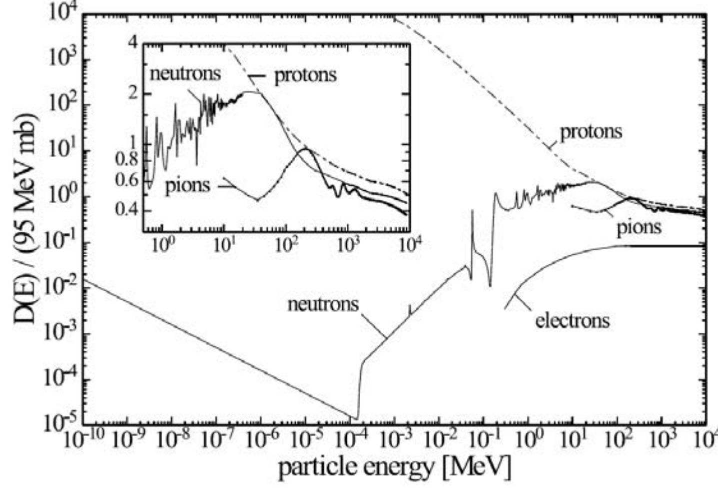

Figure 3.6: *Displacement damage function $D(E)$, normalised to 95 MeV mb (value for 1 MeV neutrons), for protons [HA93, HA99, S⁺99], pions [HA99], electrons [S⁺99] and neutrons [G⁺93, K⁺92, HA99].*

the probability for the generation of a PKA with recoil energy E_R by an incoming particle with energy E through interaction k with the corresponding cross section σ_k. The integration is done over all possible recoil energies, E_R. Figure 3.6 shows the displacement damage function dependence on particle energy for protons, neutrons, pions and electrons.

The total energy per unit volume, deposited in silicon crystal in form of NIEL displacement damage due to irradiation, is given by

$$\epsilon_{NIEL} = N_{Si} t_{irr} \int_0^\infty \frac{d\phi}{dE} D(E) dE, \tag{3.71}$$

where N_{Si} is the concentration of silicon atoms, $\frac{d\phi}{dE}$ is the incoming particle flux spectral distribution and t_{irr} the irradiation exposure time.

Usually integrated flux (fluence), Φ, is used as a measure for degree of irradiation. The damage produced by specific irradiation is usually compared to the damage produced by mono-energetic neutrons of 1 MeV of the same fluence. Irradiation with particles A, that have spectral distribution $\frac{\phi_A}{dE}$, produce the same NIEL as 1 MeV neutrons if

$$\epsilon_{NIEL} = N_{Si} t_{irr} \int \frac{d\phi_A}{dE} D(E) dE = N_{Si} \Phi_{eq} D_n(1\,\mathrm{MeV}), \tag{3.72}$$

where $D_n(1\,MeV)$ denotes the displacement damage function value for 1 MeV, with a standard value 95 MeVmb [AST85]. Therefore, Φ_{eq} represents the equivalent fluence of 1 MeV neutrons, which would have produced the same NIEL as the fluence

$$\Phi_A = t_{irr} \int \left(\frac{\phi_A}{dE}\right) dE \tag{3.73}$$

of particles actually applied. If one defines the hardness factor as

$$\kappa_A = \left(\frac{1}{D_n(1\,\mathrm{MeV})}\right)\left(\frac{\int \frac{d\phi_A}{dE} D_A(E)dE}{\int \frac{d\phi_A}{dE} dE}\right) \tag{3.74}$$

it then follows

$$\Phi_{eq} = \kappa_A \Phi_A. \tag{3.75}$$

According to so called *NIEL scaling hypothesis*, the observed radiation induced damage effects in silicon bulk are proportional to the energy deposited in the NIEL interactions and do not depend on particle type or type of silicon material for a given NIEL. For a given type of particles with energy spectrum $d\Phi_A/dE$ and fluence Φ_A one can calculate the corresponding κ and Φ_{eq}. If the NIEL hypothesis holds, then the calculated Φ_{eq} represents the fluence of 1 MeV neutrons which would cause the same damage as actually observed. Thus, the Φ_{eq} could then be used to compare the damage efficiency of different particles with different energy spectra. However, numerous violations of NIEL hypothesis have been observed [L$^+$01, Kra03]. Despite that, the NIEL scaling is still used for the normalisation of fluence of different particles and energies.

The maximal kinetic energy transfered to the recoiled silicon atom, E_R^{max}, follows from relativistic kinematics of a central interaction

$$E_R^{max} = 2E_k \frac{E_k + 2m_p c^2}{M_{Si} c^2} \tag{3.76}$$

where M_{Si} is the mass of silicon atom, E_k is the kinetic energy of impinging particle and m_p its mass [L$^+$80]. Taking into account the displacement threshold energy of $E_R \approx 25\,\mathrm{eV}$ and the threshold energy of $E_R \approx 5\,\mathrm{keV}$ for cluster production one can obtain that neutrons need a kinetic energy above ∼185 eV for production of Frenkel pairs and more than 35 keV to produce a cluster. Electrons, on the other hand, need a kinetic energy of about 225 keV to produce a Frenkel pair and more than about 8 MeV to produce a cluster. Thus light electrons will produce more point defects than neutrons with the same kinetic energy. Since protons and neutrons have almost identical mass, the calculated threshold energies are essentially the same. However, the NIEL of charged particles is mainly due to Coulomb interactions with the silicon nuclei. On the other hand, neutral particles, such as neutrons, do not undergo Coulomb interactions. They interact manly via elastic scattering with the nucleus. Due to Coulomb interactions protons more likely impart their energy to the silicon lattice in small fractions. Therefore, protons will create less defect clusters than neutrons. With increasing energy of the impinging proton, it becomes more likely that it is also able to split the nucleus directly. Hence, the resulting damage will look more similar to the damage caused by neutron irradiation.

Time evolution of defects

Radiation induced defects can be divided into three groups regarding their time development after creation:

- Defects or defect complexes can be stable in time.

- Defect complexes can decay into their components (dissociation), if the lattice vibration energy is sufficient to overcome the binding energy.
- Defects become mobile at certain temperatures and migrate through the crystal lattice until they react with other defects to form new defect complexes or are gathered at sinks (surface, dislocations, etc.).

Formation of new defects and dissociation can lead to transformation of an electrically active defect into a non-active one or the other way around.

The dissociation or migration of defects into sinks, $X \rightarrow Y$, can be described by a first order process. Here, the rate, with which the defect is disappearing into sinks or decaying, is proportional to the concentration of defect at that time, N_X,

$$\frac{dN_X}{dt} = -\frac{dN_Y}{dt} = -k_1 N_X. \tag{3.77}$$

Integration of this equation leads to exponential decrease of N_X

$$N_X(t) = N_X^0 \mathrm{e}^{-t/\tau_1}, \quad \tau_1 = \frac{1}{k_1} \tag{3.78}$$

$$N_Y(t) = N_X^0 \left(1 - \mathrm{e}^{-t/\tau_1}\right), \tag{3.79}$$

where N_X^0 and N_Y^0 represent the initial X and final Y defect concentrations respectively, and k_1 the reaction constant for the first order process involved.

Formation of defect complexes through reaction of two defects X_A+$X_B \rightarrow Y$ can be described by the differential equation

$$\frac{dN_{X_A}}{dt} = \frac{dN_{X_B}}{dt} = -\frac{dN_Y}{dt} = -k_2 N_{X_A} N_{X_B}. \tag{3.80}$$

If the two starting defects have similar initial concentrations, $N_{X_A}^0$=$N_{X_B}^0$=N_X^0, or we have a reaction between defects of the same type, the solution is given by

$$N_X(t) = \frac{N_X^0}{1 + t/\tau_2}, \quad \tau_2 = \frac{1}{N_X^0 k_2} \tag{3.81}$$

$$N_Y(t) = N_X^0 \left(1 - \frac{1}{1 + t/\tau_2}\right), \tag{3.82}$$

which describes the second order process. Here, k_2 represents the reaction constant for the second order process taking place. However, if one of the reaction partners has much higher concentration than the other, $N_{X_A}^0 \gg N_{X_B}^0$, the dynamics of the process can again be described by the first order equation with $k_1 = k_2 N_{X_A}^0$.

The energy needed for dissociation of a defect or formation of a new defect is supplied by the lattice vibrations. Therefore, the reaction constant strongly depends on temperature. Since the lattice vibrations are governed by Maxwell-Boltzmann statistics, the probability of sufficient

energy transfer from the lattice vibration to the defect exponentially depends on temperature. This gives

$$k_{1,2} \propto \exp\left(-\frac{E_a}{k_B T}\right) \Longrightarrow \frac{\tau_{1,2}(T_0)}{\tau_{1,2}(T_1)} = \frac{k_{1,2}(T_1)}{k_{1,2}(T_0)} = \exp\left[\frac{E_a}{k_B}\left(\frac{1}{T_0} - \frac{1}{T_1}\right)\right], \tag{3.83}$$

where E_a is the *activation energy* for defect dissociation or reaction involved.

The concentration of defects generated directly by irradiation, is proportional to the equivalent fluence. At a given time after irradiation the concentration of a certain type of defect, N_t, formed either directly by irradiation or indirectly through the decay of primary defect or reaction its reaction with other defects, is given by

$$N_t = g_t \Phi_{\text{eq}} f_t. \tag{3.84}$$

Here, g_t is the creation amplitude and $f_t \in [0, 1]$ describes the evolution of the defect with time. If the defects are stable in time $f_t = 1$. If the defect evolution is described by a first order process, then f_t depends exponentially on time (see equation 3.78, 3.79). For the second order process, f_t depends on both time and fluence (see equations 3.81, 3.82). Thus, the characteristic time, τ_1, for the first order process is independent of fluence. This is not the case for the second order process, since here, the characteristic time depends on fluence through its dependence on defect concentration (see equation 3.81).

Influence of defects on detector operation

The presence of radiation induced defects changes the macroscopic detector properties in several ways. The main bulk damage effects are manifested as

- Change in the *effective dopant concentration*, N_{eff}, which affects the full depletion voltage, V_{FD}.
- Increase of the *leakage current*, which results in increased noise and contributes to high power consumption and therefore heat.
- Deterioration of the *charge collection efficiency* due to trapping of signal charges.

In the following each of these effects is described.

Effective dopant concentration Prior to irradiation, the concentration of deep levels is negligible and the effective dopant concentration can be determined from the difference between shallow donor and acceptor dopant concentration, $N^0_{eff} = N^0_D - N^0_A$.

Irradiation introduces different new defect levels in the bandgap. Depending on their occupancy, these defect levels can contribute to the effective space charge and therefore change the effective dopant concentration, N_{eff}. Ionised acceptor like levels (occupied with electron) contribute negative space charge while ionised donors (not occupied with electron) contribute

positive space charge. As described in section 3.1.4, in the SCR the levels located a few k_BT below the intrinsic Fermi level, E_i, are mostly occupied (with electrons), while levels a few k_BT above E_i are mostly unoccupied. Thus, only acceptors in the lower part and donors in the upper part of the bandgap will contribute to the space charge and effective dopant concentration. The effective dopant concentration is given as

$$N_{eff}(T) = \sum_{\text{donors}} N_k(1 - P_k(T)) - \sum_{\text{acceptors}} N_k P_k(T) + N_D^0 - N_A^0. \tag{3.85}$$

where T denotes the temperature at which N_{eff} is measured. The index k runs over all different donor and acceptor like irradiation induced defects in the first and second sum respectively, and P_k represents the occupancy of the k-th defect with concentration N_k.

The starting material is usually of n-type due to the doping with phosphorus donors. Irradiation leads to deactivation of these donors due to transformation of phosphorus atoms to vacancy-phosphorus complexes, so called E–centres[12]. This process, called *donor removal*, reduces the positive space charge and is responsible for the decrease of V_{FD} with irradiation at lower fluences (figure 3.7). In parallel, deep acceptor levels are introduced with irradiation, resulting in an increase of the negative space charge. The continuous generation of negative space charge leads to space charge sign inversion, where the silicon bulk undergoes type inversion and effectively starts to behaves like p–type. This is followed by a rapid increase of V_{FD} with fluence. Thus, at high enough fluences the full depletion voltage may grow too high for normal operation of the device.

Measurements showed that oxygen enriched FZ silicon material exhibits slower increase of V_{FD} with fluence [L$^+$01]. However, while pion and proton irradiated oxygen enriched samples exhibit the same improvement compared to standard FZ material, neutron damage does not, indicating a violation of the NIEL hypothesis (figure 3.7). This is attributed to creation of deep acceptors which is suppressed in oxygen enriched material, since the presence of high oxygen concentration favours the production of electrically non-active complexes. The effect of oxygen depends on the ratio of produced point defects and clusters. The effect is stronger for charged hadron irradiations, when more point defects are produced, and much weaker for neutron irradiations, when mostly clusters are formed.

The time development of irradiation effects in N_{eff} is subjected to three components: short term annealing (N_A), long term reverse annealing (N_Y) and stable damage (N_C). Hence, the irradiation induced change in effective dopant concentration, with respect to its initial value before irradiation, N^0_{eff}, can be described as

$$\Delta N_{eff}(\Phi_{\text{eq}}, T, t) = N^0_{eff}(T) - N_{eff}(\Phi_{\text{eq}}, T, t) \tag{3.86}$$
$$= N_A(\Phi_{\text{eq}}, T, t) + N_Y(\Phi_{\text{eq}}, T, t) + N_C(\Phi_{\text{eq}}, T). \tag{3.87}$$

where $t = t(T_a)$ indicates the annealing time at a certain annealing temperature T_a.

The short term annealing component, N_A, is attributed to the annealing of acceptors. This results in a decrease of full depletion voltage with annealing time for the case of type-inverted

[12] An E-centre, formed by $V + P_s \rightarrow VP_s$, is a deep acceptor with energy in the upper part of the bandgap, $E_C - 0.45$ eV.

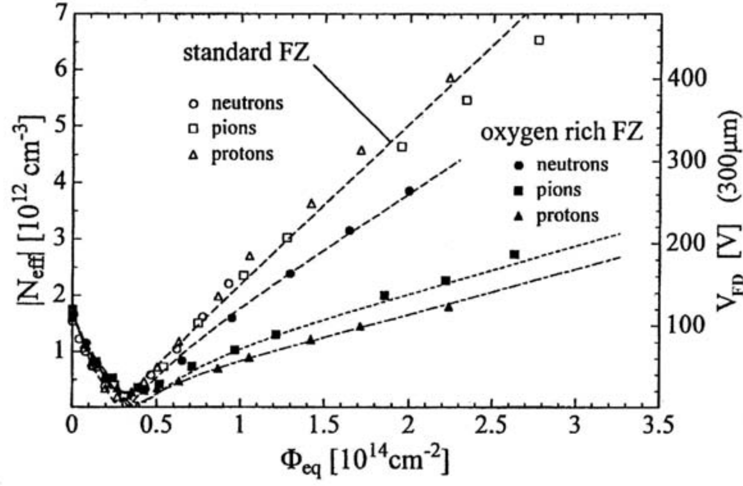

Figure 3.7: *Dependence of N_{eff} on accumulated equivalent fluence for standard FZ and oxygen enriched FZ silicon material irradiated with reactor neutrons (Ljubljana), 23 GeV protons (CERN) and 192 MeV pions (PSI). Source [Mol99].*

detectors (the negative N_{eff} is becoming less negative) or an increase of V_{FD} with time for non-inverted detectors (the positive N_{eff} is becoming more positive). Both cases lead to a reduction of ΔN_{eff}, which is described by an exponential decay with time with amplitude proportional to the fluence. The contribution of the short term component governs the annealing behaviour of N_{eff} at short annealing times.

The stable damage component N_C does not depend on annealing time. It consists of two contributions. First is an incomplete donor removal, which depends exponentially on fluence. The second component describes the fluence proportional introduction of stable acceptors.

The effect of long term annealing component, N_Y, is opposite to the short term one. In the long term the space charge is becoming more negative[13], leading to an increase of V_{FD} at prolonged annealing times[14]. The long term component is interpreted as the build-up of acceptor like states during annealing and was observed to follow a first order process.

Leakage current The generation current gives the main contribution to the leakage current of irradiated and even most non-irradiated silicon detectors. The deep level defects, introduced by irradiation, enhance the alternating emission of electrons and holes in the SCR, which increases the leakage current. It has been shown that this increase is proportional to the irradiation fluence and independent of the silicon material (n– or p–type, FZ, epi or Cz, different resistivity) as well as the type of irradiating hadrons (neutrons, protons, pions) [Mol99]. It can be described by

$$\Delta I_{scr} = \alpha V_{scr} \Phi_{\mathrm{eq}}, \tag{3.88}$$

[13] N_{eff} is decreasing.

[14] If no type inversion is observed immediately after irradiation, then the type inversion occurs during the long term annealing.

where $V_{scr} = w_{scr}S$ represents the SCR volume while α is called the *leakage current damage constant*. The α value depends on the the annealing time, annealing temperature T_a and the temperature, T_m, at which the current is measured. However, for the same experimental conditions, a universal annealing behaviour of α is observed, which is usually described by the following parametrisation

$$\alpha(T_a, t) = \alpha_0 + \alpha_I \exp(-t/\tau_I) - \beta \ln(t/1\text{min}). \tag{3.89}$$

Here, the first term denotes the defects which are stable in time (f_t=1), the second term accounts for decaying of defects with time constant of τ_I (f_t=$\exp(-t/\tau_I)$) and the last term describes the long term annealing, which effectively follows a logarithmic dependence.

Trapping times Radiation induced deep level defects diminish the life time of signal charge carriers, since part of the drifting charge, Q, released by a traversing ionising particle, can be trapped by these defects. Drifting charge decreases exponentially with a time constant τ^{eff} (see equation 3.52)

$$Q(t) = Q(0)\mathrm{e}^{-\frac{t}{\tau^{eff}}}. \tag{3.90}$$

If the emission times of traps are longer than the measurement time, then the trapped charge does not contribute to the induced current signal. Therefore, after irradiation the signal induced can be significantly smaller compared to the value before irradiation.

Generally all energy levels in the bandgap represent traps for electrons and holes. In the SCR, donors and acceptors with energy levels a few k_BT above E_i are predominantly unoccupied (with electrons). Therefore, they are considered as electron traps since they mainly trap electrons. Similarly, acceptors and donors with energy levels a few k_BT below E_i trap mostly holes.

The probability per unit time for charge carrier to be trapped by a defect with energy level E_t depends on the charge carrier thermal velocity $v^{th}_{e,h}$, the defect capture cross sections $\sigma^t e$ and $\sigma^t h$ and density of certain defect type available to trap. Thus

$$\frac{1}{\tau^t_e} = v^{th}_e \sigma^t_e (1 - P_t(T)) N_t \quad \text{and} \tag{3.91}$$

$$\frac{1}{\tau^t_h} = v^{th}_h \sigma^t_h P_t(T) N_t \tag{3.92}$$

$$\tag{3.93}$$

give the electron and hole trapping probabilities respectively. τ^t_e and τ^t_h represent the average time spent by a free charge carrier in the SCR before it is trapped by the defect of type t. The effective trapping probabilities for electrons and holes, τ^{eff}_e and τ^{eff}_h, can be obtained by summing over different types of traps

$$\frac{1}{\tau_{eff_{e,h}}} = \sum_t \frac{1}{\tau_{t_{e,h}}}. \tag{3.94}$$

Measurements show that probabilities $1/\tau^{eff}_e$ and $1/\tau^{eff}_h$ scale linearly with equivalent fluence, indicating that their annealing behaviour is governed by a first order process [Kra03].

Hence, the effective trapping probabilities at a given temperature and time after irradiation can be parametrised with

$$\frac{1}{\tau_{eff_{e,h}}} = \beta_{e,h}(t,T)\Phi_{\text{eq}} \tag{3.95}$$

where β_e and β_h are called the *effective electron* and *hole trapping damage constant* respectively. During the annealing, β_e exhibits an initial decrease followed by saturation. On the other hand in the annealing behaviour of β_h the saturation is reached after an initial increase.

The effective trapping probabilities were observed to be independent of oxygenation level and resistivity [Kra03]. However, it was also observed that charge trapping does not scale according to the NIEL hypothesis, since charged hadrons were found to induce more trapping compared to neutrons at the same NIEL equivalent fluence.

3.4 pCVD diamond detectors

Diamond possesses some properties which make it an attractive material for particle detector applications. Due to its large bandgap of 5.5 eV, diamond detectors exhibit very low leakage currents. High thermal conductivity and low leakage current make diamond a material whose devices may be operated without cooling. Its low dielectric constant (ϵ=5.7) results in a low detector capacitance and thereby low noise performance of the associated detector electronics. Also, a high saturation drift velocity and high breakdown electric field strength of diamond enable one to design a system with fast signal response.

The attractive properties of diamond as a particle detector were first demonstrated by using monocrystalline natural diamond stones of high electronic quality [K^+74, C^+79a, K^+77]. The main disadvantage of the natural diamond detectors are small size, high cost due to extremely rare detector-grade natural diamond. Moreover, electronic properties of natural diamond stones can vary strongly. Only with the advent of microwave plasma chemical vapour diamond growth reactors (MWPCVD), diamond became a viable option for particle detectors due to reduced variability and large detector size.

In this section the growth of chemical vapour (CVD) diamonds is first explained. This is followed by a description of the basic principle of diamond detectors where the concepts of charge collection distance and drift length are explained in the context of signal creation.

3.4.1 CVD diamond growth

Early attempts to synthesise diamond artificially using graphite, another commonly occurring form of carbon, as starting material, proved to be extremely difficult. This was mainly because graphite is the thermodynamically stable allotrope of carbon at temperatures up to the melting point at normal pressure. The diamond phase is the stable form (see figure 3.8) only at extremely high pressure (in excess of 2 GPa). A high activation barrier separates the two phases inhibiting the transformation of graphite to diamond. This large activation barrier, which makes diamonds so rare, is also responsible for its existence. Once formed, diamond will spontaneously convert to the thermodynamically more favourable graphite phase, but only on a time scale of millions of years. Therefore diamond is said to be metastable at normal pressure and temperatures up to its melting point. Greater pressures are required to bring graphite and diamond into equilibrium with one another as the temperature is increased.

Most of the early efforts to produce artificial diamond involved mimicking the process which occurs in nature, the crystallisation at very high temperature and extreme pressure. This process forms the basis of the high temperature high pressure (HTHP) growth technique which

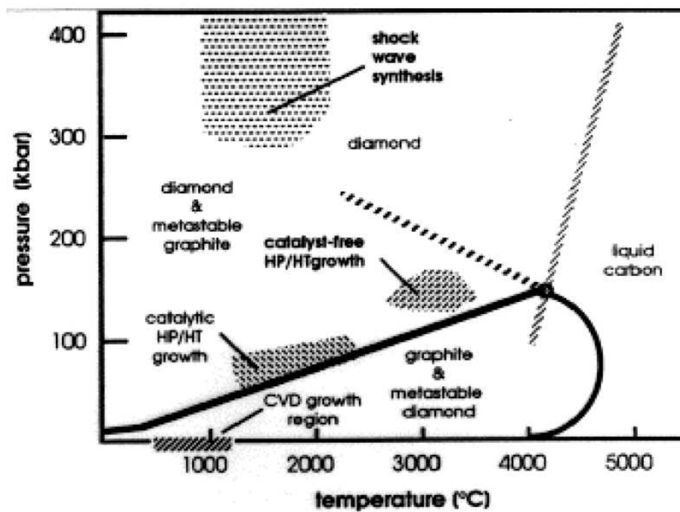

Figure 3.8: *Carbon phase diagram with indications of regions for diamond synthesis. Source [Bac90].*

is operated near in the stable diamond regime of the carbon phase diagram. In the HTHP process, graphite is compressed in a hydraulic press to few GPa, heated to over 2000K in the presence of of suitable metal catalyst and left until diamond crystallises. The diamonds synthesised via the HTHP method are used for a wide range of industrial processes that rely on diamond's hardness and wear resistance properties (such as cutting, polishing and grinding), but they fail to serve in electronic applications due to their size and crystal quality.

Larger dimensions and higher crystal quality, essential for electronics applications, can be achieved by means of the chemical vapour deposition (CVD) method. This technique is operated under moderate pressure (from a few 10 kPa to a few MPa) and slightly elevated temperature (below 1000°C) in the region of diamond metastability. Lower temperature and pressure than in HTHP diamond synthesis make CVD diamond growth techniques more advantageous in terms of equipment and energy cost.

The CVD technique involves a gas phase chemical reaction occurring above a suitable solid surface (substrate) which causes deposition onto the surface. Diamond is grown in a mixture of gases containing carbon and hydrogen and a possible admixture of oxygen to enhance the growth rate. Carbon is deposited on a heated substrate in a form of diamond and graphite through decomposition of hydrocarbon gases. Graphite usually deposits much faster than diamond. However, graphite is etched by H and O atoms and OH radicals. Thus diamond growth is a competition between the formation and etching of graphite and requires a careful tuning of growth parameters.

All CVD techniques for producing diamond films require activation of the gas phase carbon-containing precursor molecules. This activation can involve thermal methods (hot filament), electric discharge (DC, RF, or microwave) or a combustion flame (oxyacetylene torch). Figure 3.9 shows a generalised CVD growth environment. The process gases (CH_4, H_2) on their way towards the substrate pass the activation region (e.g. hot filament or electric discharge),

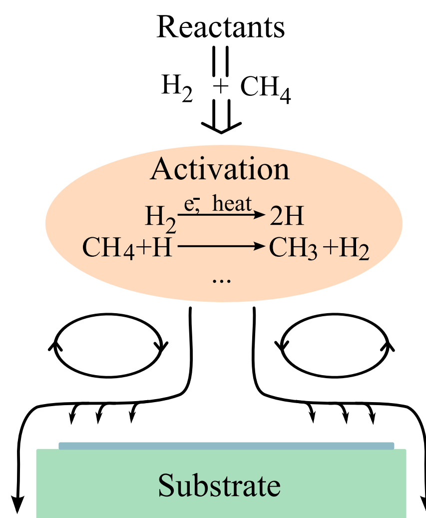

Figure 3.9: *Generalised schematic of the chemical process occurring in a CVD diamond reactor.*

which provides energy to the gaseous species. The activation causes molecules to fragment into reactive radicals and atoms (CH_3 radicals and atomic H), creates ions and electrons and heats up the gas to temperatures approaching a few thousand Kelvins. After the activation region, these reactive fragments undergo a complex set of reactions before they strike the substrate. Here, they can either adsorb and react with substrate surface, desorb again back into gas phase or diffuse around close to the surface until they find an appropriate reaction site. When a surface reaction occurs, one possible outcome is diamond formation, if the conditions are suitable.

Different reactor types have been used for CVD diamond growth [PK95] . The diamond samples used in this work were produced with microwave plasma CVD reactor (MWPCVD). Generally in a MWPCVD reactor (figure 3.10(a)), process gasses are introduced into a reactor chamber which contains the substrate to be coated. Microwave power is coupled into the chamber via dielectric window (usually quartz) in order to create a discharge. The chamber is an integral part of an electromagnetic cavity and consequently its geometry has a strong influence on the location and the extent of the microwave discharge. The cooled substrate is immersed into the plasma within the cavity. The microwaves couple energy into the gas phase electrons, which in turn transfer their energy to the gas through collisions. As a result of these collisions, the process gas is heated and chemical reactions in the gas phase lead to formation of diamond precursors which impinge on the substrate surface.

Substrate used for CVD diamond growth can be either diamond or other material. Silicon is widely used as a substrate material due to its availability, low cost and acceptable lattice structural mismatch. Diamond films grown on non-diamond substrate are typically polycrystalline (pCVD diamonds) in nature. Once the randomly oriented micro crystallites have nucleated at the nucleation sites on the substrate surface, the growth proceeds in three dimensions until the crystallites coalesce. From this point the lateral growth of crystallites is limited by the neighbouring crystallites. This results in polycrystalline film with many grain boundaries and defects exhibiting a columnar structure that extends upwards from the substrate. The growth speed of

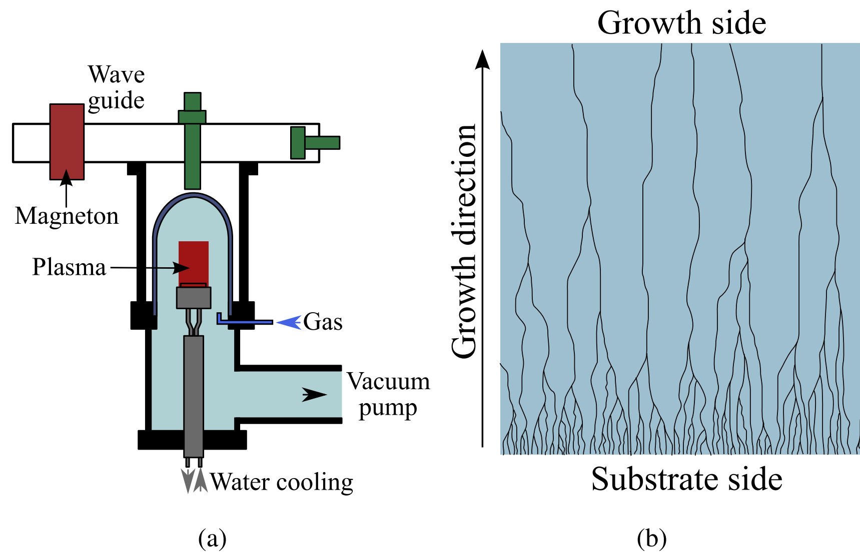

(a) (b)

Figure 3.10: *Schematic picture of a microwave plasma CVD reactor (a). Schematic side view of a pCVD diamond sample (b).*

crystallites depends on their orientation and gas phase parameters. The slow growing crystallites can be overgrown by faster growing neighbours. Therefore, as the film becomes thicker the width of crystallites increases while the number of the grain boundaries and defects decreases (see figure 3.10(b)). The side attached to the substrate is termed the *substrate or nucleation side* while the side facing the grown species is called the *growth side*. The quality of the substrate side is typically very poor due to the small size of crystallites and high density of grain boundaries. The quality increases with film thickness, and the best quality is observed on the growth side [Z^+93, Zha94, P^+94, Mei99]. For this reason the diamonds used for particle detectors are separated from its substrate and a part of the substrate side is removed (lapped) by mechanical polishing (e.g. thinning from 800μm to 500 μm).

3.4.2 Operation of diamond detectors

Due to the high resistivity of diamond no depletion region is needed in diamond detectors to reduce the intrinsic carrier density. It is enough to apply two electrodes across the material and supply sufficiently high potential difference V to create an electric field inside the diamond. Its high resistivity prevents occurrence of significant currents.

Figure 3.11 shows the basic principle of diamond particle detector with thickness D. The bias voltage V applied between the electrodes generates an electric field equal to that of an ideal plate capacitor with strength $|\boldsymbol{\varepsilon}| = \frac{V}{D}$. An ionising particle traversing the diamond leaves a trail of electron-hole pairs, and the drift of electrons and holes in the applied electric field induces a current pulse on the electrodes. According to Ramo's theorem, the current induced by a charge

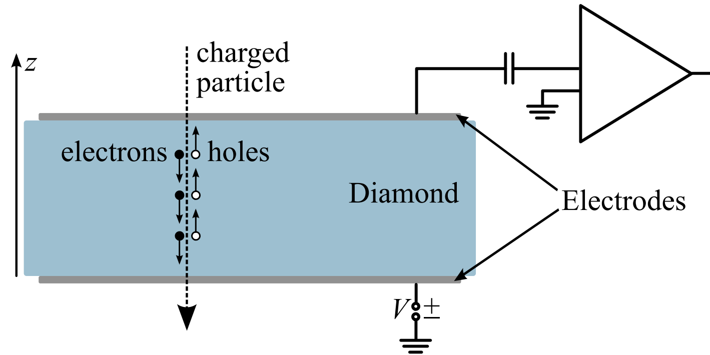

Figure 3.11: Schematic layout of diamond particle detector.

q drifting in a uniform electric field can be calculated as (see equation 3.50)

$$I = \frac{qv^{dr}}{D} \tag{3.96}$$

where v^{dr} denotes the drift velocity. The induced charge can be obtained by integrating this equation over time.

In real crystals, defects in the form of impurities, dislocations, stacking faults and grain boundaries distort the band structure, introducing additional energy levels in the band gaps. These additional energy levels can act as trapping centres. Thus, the time that an electron or hole can drift is limited by its trapping time $\tau_{e,h}^{eff}$ and the distance to the electrode towards which it is drifting.

In the case of a polycrystalline material, like pCVD diamond, the trapping time is not constant across the material. On a microscopic scale this material is a composition of single crystalline grains of different sizes and orientations. These crystallites, which constitute the film, grow in a columnar form, widening their diameter with film thickness. The lattice is highly distorted at the boundaries of crystallites. Therefore, the electrical properties close to these boundaries differ from the properties of the regions inside the grains. The impurity concentration is strongly enhanced at grain boundaries [M$^+$96, O$^+$98]. Grain boundaries are considered to be areas with higher density of electrically active traps, where charge carriers are very likely to be trapped or recombine [M$^+$99a, Oh99]. Thus, the performance of pCVD diamond devices strongly depends on the microscopic quality of the sensor material and is generally degraded due to the presence of defects incorporated into the material bulk during the growth process, mainly at the grain boundaries[15]. The electronic properties tend to improve as a function of film thickness which appears to be due to the increase in grain size from the substrate to the growth side that occurs during the growth.

The product of electron or hole drift velocity $v_{e,h}^{dr}$ and its trapping time $\tau_{e,h}^{eff}$ defines the *electron* or *hole drift length* respectively

$$\delta_{e,h}^{dr} = v_{e,h}^{dr} \tau_{e,h}^{eff}. \tag{3.97}$$

[15]These defects can be interstitial carbon atoms, vacancies or impurity atoms (typically O and N) forming point defects. At grain boundaries many point defects are agglomerated in clusters or layers of defects (planar defects).

Using relations 3.16 and 3.17 between carrier drift velocity and its mobility, one can obtain

$$\delta_{e,h}^{dr} = \tau_{e,h}^{eff} \mu_{e,h} |\varepsilon|. \tag{3.98}$$

The sum of electron and hole drift lengths is defined as the *carrier drift length*

$$\delta^{dr} = \delta_e^{dr} + \delta_h^{dr} = (\tau_e^{eff} \mu_e + \tau_h^{eff} \mu_h)|\varepsilon|. \tag{3.99}$$

In case of infinite sensor material dimensions and $v_{e,h}^{dr} \ll v_{e,h}^{th}$, the carrier drift length represents the average distance that and electron-hole pair drift apart before they are trapped. At lower electric fields it is proportional to the applied electric field strength, but saturates at the higher electric fields due to saturation of drift velocity.

The quality of pCVD diamond as a particle detector is usually given in terms of a measured quantity called the *charge collection distance*, defined as [Zha94]

$$\delta^{ccd} = D \frac{Q_{ind}}{Q_{gen}}, \tag{3.100}$$

where Q_{gen} represents the charge generated by an ionising particle along its track and Q_{ind} denotes the induced charge actually measured. The charge collection distance is usually quoted at 1 V/μm, but in this work they are quoted at 2 V/μm unless stated otherwise, since the BCM diamond sensors will be operated at this field.

The relation between δ^{ccd} and δ^{dr} can be obtained by integrating the induced current from equation 3.96 over time. For an ensemble of N^0 electrons created at a point z, the number of free charges after drifting a distance Δz is given by $N(\Delta z) = N^0 e^{-(\Delta z/\delta_e^{dr})}$ (see equation 3.52). Thus, if an electron–hole pair is created at a distance z from the negative electrode (figure 3.11), then the charge Q_{ind}^1 induced on the negative electrode due to the drift of this pair can be calculated from equation 3.96 as

$$\begin{aligned} Q_{ind}^1(z) &= \int_0^{D-z} \frac{e_0}{D} \mathrm{e}^{-z'/\delta_e^{dr}} \, dz' + \int_0^z \frac{e_0}{D} \mathrm{e}^{-z'/\delta_h^{dr}} \, dz' \\ &= \frac{e_0}{D} \left[\delta_e^{dr} (1 - \mathrm{e}^{-\frac{D-z}{\delta_e^{dr}}}) + \delta_h^{dr} (1 - \mathrm{e}^{-\frac{z}{\delta_h^{dr}}}) \right] \end{aligned} \tag{3.101}$$

where drift lengths $\delta_{e,h}^{dr}$ were assumed to be independent of z. The first integral refers to electron and the second one to hole drift. The total charge, Q_{ind}, induced by an ionising particle traversing the diamond can be obtained by summing the contributions from all generated electron–hole pairs along its path. If the density of electron–hole pairs generated along the particle track is given by $\rho_q(z)$ then

$$Q_{ind} = \int_0^D \frac{\rho_q(z)}{D} \left[\delta_e^{dr} (1 - \mathrm{e}^{-\frac{D-z}{\delta_e^{dr}}}) + \delta_h^{dr} (1 - \mathrm{e}^{-\frac{z}{\delta_h^{dr}}}) \right] dz \tag{3.102}$$

Assuming that the density of generated electron-hole pairs is constant along the particle track, $\rho_q(z) = Q_{gen}/D = e_0 N/D$, this gives

$$Q_{ind} = \frac{Q_{gen}}{D} \sum_{k=e,h} \delta_k^{dr} \left[1 - \frac{\delta_k^{dr}}{D} \left(1 - \mathrm{e}^{-D/\delta_k^{dr}} \right) \right] \tag{3.103}$$

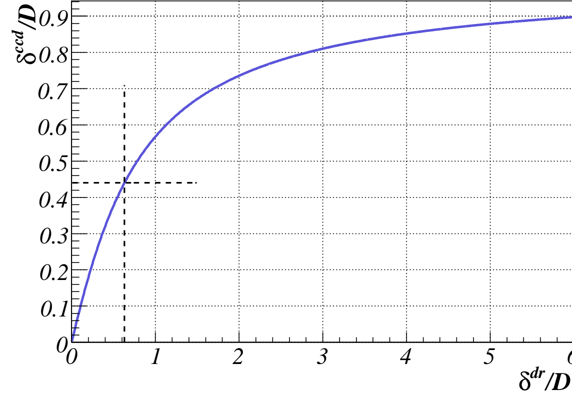

Figure 3.12: *Charge collection distance δ^{ccd} dependence on drift length δ^{dr}, both in units of detector thickness. The dependence was calculated from equation 3.104 where δ_e^{dr}=δ_h^{dr} has been assumed. The dotted lines denote their values for diamond sensors used in this work. Assumptions leading to this dependence are discussed in text.*

where N denotes the number of electron-hole pairs generated. By comparing equations 3.100 and 3.103 one obtains the following relation between drift and charge collection distance

$$\delta^{ccd} = \sum_{k=e,h} \delta_k^{dr} \left[1 - \frac{\delta_k^{dr}}{D} \left(1 - \mathrm{e}^{-D/\delta_k^{dr}} \right) \right] \tag{3.104}$$

If drift lengths $\delta_{e,h}^{dr}$ are much larger than the detector thickness, then $\delta^{ccd}{\sim}D$. On the other hand, if $\delta_{e,h}^{dr}{\ll}\ D$ then $\delta^{ccd}{\sim}\delta_e^{dr}{+}\delta_h^{dr}{=}\delta^{dr}$. Figure 3.12 shows the charge collection distance dependence on drift length where $\delta_e^{dr}{=}\delta_h^{dr}$ has been assumed. For a typical diamond sample used in this work, with $D\ \sim\ 500\,\mu$m and $\delta^{ccd}{\sim}220\,\mu$m at 2 V/$\mu$m, this gives a drift length of $\delta^{dr}{\sim}315\,\mu$m at 2 V/$\mu$m.

The exposure of a pCVD diamond detector to ionising radiation can substantially increase the measured charge collection efficiency [F$^+$92, B$^+$98]. Also an increase in leakage current of the detector is usually observed [B$^+$03]. This phenomenon is called *priming* or *pumping*. It is attributed to filling of deep level traps in diamond bulk with charge carriers generated by the ionising radiation. In order to enhance the charge collection distance, it is therefore common procedure to irradiate pCVD diamond detectors with β particles before their use, thus creating an amount of free charge carriers. The created free charge is trapped by the defects and it passivates the deep level traps, which have long emission times [16]. To pump a pCVD diamond, a fluence of the order of 10^{10} minimum ionising particles per cm^2 or a comparable amount of ionisation from other sources is generally sufficient [H$^+$00]. However, the priming effect strongly depends on the quality of the sample, producing higher increase in charge collection efficiency for low-quality samples (ie samples with lower charge collection distance, higher concentration of defects). The pumped state is conserved for months [H$^+$00] if the diamond is kept in dark

[16]In contrast to deep level traps, shallow ones remain active at room temperature. Their emission times are much shorter. Thus, they capture the charge carrier only for short time period.

and at room temperature. To the present knowledge the pumping process is fully reversible [F$^+$99] and depumping can be achieved with exposure to heat or UV light.

While pumping leads to signal enhancement, the same mechanism can give rise to *polarisation effect* which can deteriorate the signal. When applying a bias voltage to a diamond detector, the trapped charge creates a polarisation field that opposes the applied electric field, thus reducing the effective electric field inside the bulk and causing a decrease in signal. Polarisation gives rise to effects such as polarity inversion of charge pulses, when the bias voltage is switched off. Another effect is hysteresis behaviour. When cycling between two opposite values of applied electric filed $|\boldsymbol{\varepsilon}|$ one can obtain a hysteresis loop of measured $\delta^{ccd}(|\boldsymbol{\varepsilon}|)$ or leakgae current.

Due to its large displacement energy (E_R~37–48 eV [K$^+$01] per C atom), diamond material is expected to be inherently radiation tolerant. Recently, a theoretical analysis of NIEL in diamond and silicon was performed. These simulations indicate that diamond has lower NIEL than silicon [B$^+$07, K$^+$07] which could lead to smaller damage effects in diamond. Radiation damage causes two effects in diamond detectors: the decrease in signal with increasing fluence due to trapping of drifting charge and the change in leakage current. While in silicon sensors the strong increase of leakage current requires cooling in order to avoid reverse annealing effects, in diamond sensors the leakage current is negligible at room temperature and usually decreases after irradiation [Mei99]. A more important radiation damage effect in diamond sensors is the degradation of signal due to trapping of drifting charge. The results of irradiations with 24 GeV protons from PS at CERN show that a decrease of up to 15% can be expected in most probable signal charge measured with slow electronics (integration time of few μs) for a diamond sensor with initial $\delta^{ccd}(\mathrm{at}\,2\mathrm{V}/\mu\mathrm{m}) \sim 220\,\mu$m when irradiated with a fluence of 2.2×10^{15}protons/cm^2 [K$^+$07, K$^+$08].

CHAPTER 4

MEASUREMENTS WITH PCVD DIAMONDS

This chapter deals with measurements performed with pCVD diamond samples during the development phase of the BCM system. In the first part the current–voltage (I–V) characteristics, measured with bare diamond samples and double decker ceramic assemblies, are presented. This is followed by results obtained with BCM detector modules. The modules were tested with β electrons from ^{90}Sr in a laboratory setup and with test beam particles (KEK, CERN PS and SPS, MGH) at various stages of their development. Only the most relevant results are presented here. In the last part of this section, the results with prototype and final NINO boards are described. An estimation of NINO chip performance in ATLAS is also given. As described in section 2.2.3 the input analogue signal is split in ratio of about 1:11 into two NINO chip inputs. All measurements presented here were performed with the higher signal input channel.

The BCM diamond sensors will be fully pumped during the operation of ATLAS due to constant flux of ionizing particles. Thus, prior to the tests described here, all diamond samples were exposed to 37 MBq ^{90}Sr source for one day in order to stabilize the pumping effect.

Unless stated otherwise, all diamond samples had the same porperties as the ones used in detector modules installed in ATLAS. These properties are given in section 2.2.2.

4.1 I–V measurements

The current–voltage (I–V) characteristics were measured for all pCVD diamond samples at our disposal in order to check the quality of the samples and its contact metallisation. An illustration of the setup is shown in figure 4.1. Measurements were performed at room temperature. A sample was mounted in an electrically shielded light-tight aluminium box. A high precision Keithley 6517 electrometer was used as a combined source and measuring unit. Voltage was applied to the bottom contact, while the top contact was connected to the ground (figure 4.1). Samples had no guard ring structure. Thus, the measured current was the sum of the current flowing through the bulk and over the sample's surface.

The profile of a diamond sample is typically not perfectly rectangular shape, but has one side wider than the other (see figure 4.1). Thus, when stating the orientation of the sample, sides will be further denoted as the '*wide side*' and the '*narrow side*'.

The I–V characteristic was measured in voltage loops, where voltage was changed in steps of 10 V from 0 V to 1000 V and then back to 0 V, for both voltage polarities. After flipping the diamond sample, these two measurements were repeated. The current was measured 5 s after the voltage was changed for each voltage step. The currents were acquired automatically using a PC with a GPIB interface to the voltage source. The acquisition software was written in Labview [Lab]. All samples were properly cleaned with an ultrasonic cleaner before these measurements.

The intrinsic sensitivity of the Keithley 6571 unit is ~1 fA, but the sensitivity achieved was worse, due to the finite resistance of the cables used in setup. In order to estimate this sensitivity, an I–V measurement was performed without a sample with the result presented in figure 4.2. From here, one estimates that the achieved sensitivity was of the order of 0.1 pA.

The I–V curve characterises both contacts and diamond sample. Samples which at low electric fields exhibit linear current–voltage dependence and symmetric behaviour with respect to

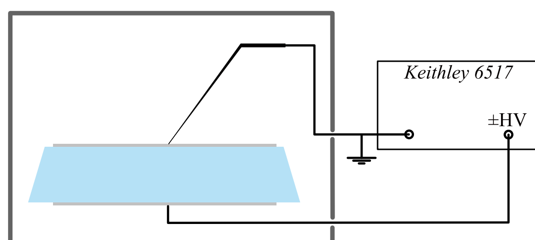

Figure 4.1: *Setup used for probing the I–V characteristics of diamond samples. Voltage was applied to the sample's bottom contact (the contact facing the support table), while the top was grounded. For the case shown on this figure, voltage was applied to the wide side of the diamond sample, facing the support table.*

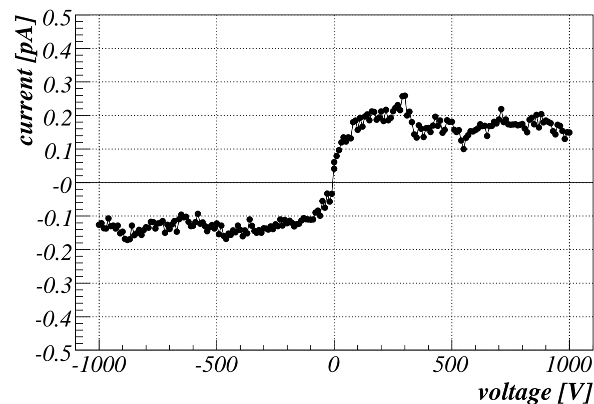

Figure 4.2: *I–V measurement performed without a diamond sample.*

the electric field orientation are said to have Ohmic contacts. Rectifying contacts on the other hand, can give an I–V curve that is not symmetric with respect to the direction of electric field even at lower electric fields. Figure 4.3 shows typical I–V curves obtained with one of the pCVD diamond samples for both orientations of the sample. At lower voltages (up to ± 500 V, depending on the sample) approximately linear behaviour is observed. However, the measured curves do not exactly follow the ideal Ohmic characteristic. The two leakage current measurements at 0 V, corresponding to the beginning and end of each voltage loop, do not match. This hysteresis can be attributed to polarisation effect, caused by an internal electric field, which counteracts the external bias field and lowers the current. Thus, the 5 s delay between the voltage change and leakage current measurement was too short for the leakage current to stabilise. Nevertheless, the resistivity was estimated from the almost linear part of I–V curves with the use of Ohm's law (equation 3.22). The resistivity of diamonds was found to be of the order of 10^{16} Ωcm.

At high electric fields the I–V curves show a non-linear behaviour resembling a soft breakdown. The voltage at which the breakdown occurs depends on the bulk and surface properties of the diamond sample. For some of the samples, the breakdown occurred at different electric field strengths, when the curves, measured for different electric field polarities in the sample, were compared. This could be due to the polycrystalline structure observed in pCVD diamonds, where the size of grain boundaries increases along the growth direction of the crystal. Grain boundaries are areas, where charge carriers are likely to be trapped. The local electric fields arising from the trapped charges, can either match or oppose to the externally applied electric field [Kag].

In some cases, the two I–V characteristics for the same electric field direction in the sample, but different sample's orientation in the setup, showed different breakdown voltages. This can be attributed to the asymmetry of the setup, where on the bottom contact (facing the support table) the voltage was applied to the whole surface, while the potential to the top contact was applied through the probing needle contacting only small spot on the top metallisation.

The I–V measurements of the diamond samples served as a measure when deciding on the orientation of each sample in double-decker assembly. Once the voltage polarity for the

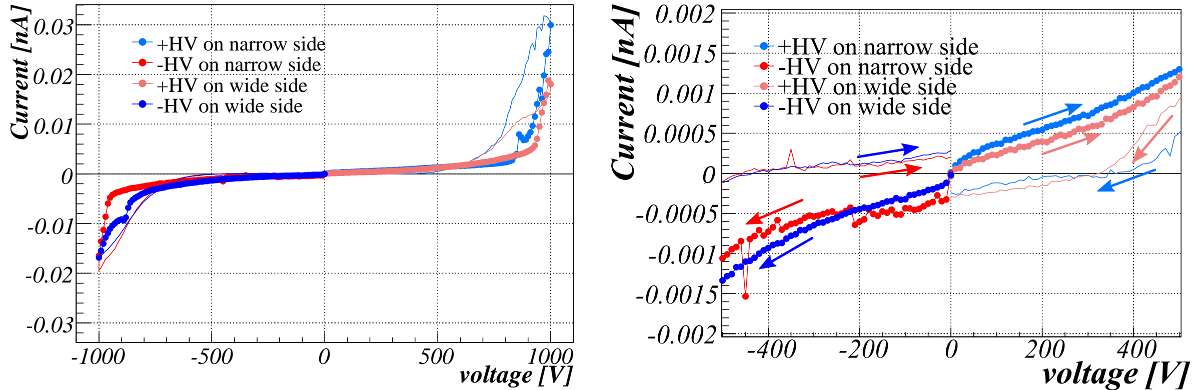

Figure 4.3: *Left: Measured I–V characteristic for sample A382-11. Blue curves denote the measurements with more positive potential applied to the narrow side and red curves represent the case of more positive potential applied to the wide side. Note that for each colour light and dark curves should match, since they refer to the same direction of the electric field. Thick curves represent the ramping up from 0 V to ±1000 V, while the thin curves refer to ramping back down to 0 V. Due to polarisation effect the curves with and without markers do not match. The plot on the right shows a magnified part of plot on the left. The voltage ramping direction is marked by arrows.*

assembly was chosen, the two samples were assembled with the orientation that gave lower currents in the I–V measurement. Samples that at ±1000 V exhibit currents above ±1 nA for both electric field polarities were considered as unacceptable for assembling. Those samples were re-metallised and re-tested.

Table B.1 in Appendix B summarises the currents at ±1000 V applied to the narrow or wide side of the diamond samples. The first sixteen diamonds in the table were mounted in the modules that were installed in ATLAS, while the rest were used for spare detector modules.

After mounting a diamond double-decker configuration onto a ceramic baseboard, the I–V characteristic of such a diamond ceramic assembly was probed. These measurements were performed in order to check if the better voltage polarity (the one giving lower currents) agreed with the polarity that was chosen when deciding on the orientation of the samples in assembly. The setup used here was the same as used for the I–V characterisation of bare diamond samples. High voltage was applied to the bottom golden pad of the ceramic baseboard, while the signal line was grounded. Measurements were performed in the same way as for individual diamond samples. Voltage was changed in steps of 10 V first from 0 V to +1000 V and then back to 0 V. Current was again measured 5 s after the voltage was changed at each step. The voltage loop for negative polarities was performed in the same way. An example of an I–V characteristic obtained with a ceramic assembly is shown in figure 4.4. The currents at ±1000 V (2 V/μm), extracted from I–V curves of ceramic assemblies, are given in table B.2 in Appendix B. Table also summarises the orientation of diamonds in ceramic assemblies used in the final BCM detector modules. The first eight assemblies in the table were mounted in modules installed in ATLAS, while the other three were used for spare modules.

Time stability of leakage current of diamond ceramic assemblies at 1000 V was also

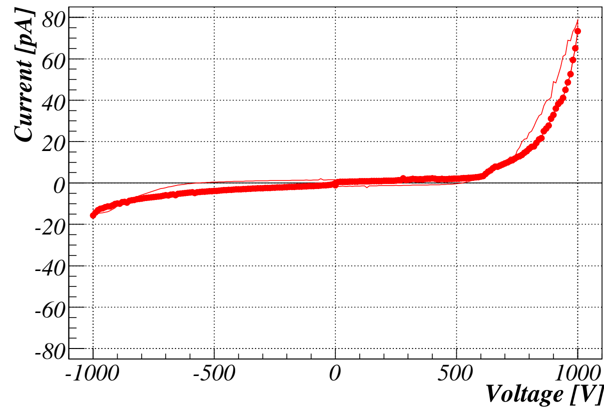

Figure 4.4: *Measured I–V characteristic of diamond ceramic assembly C1.*

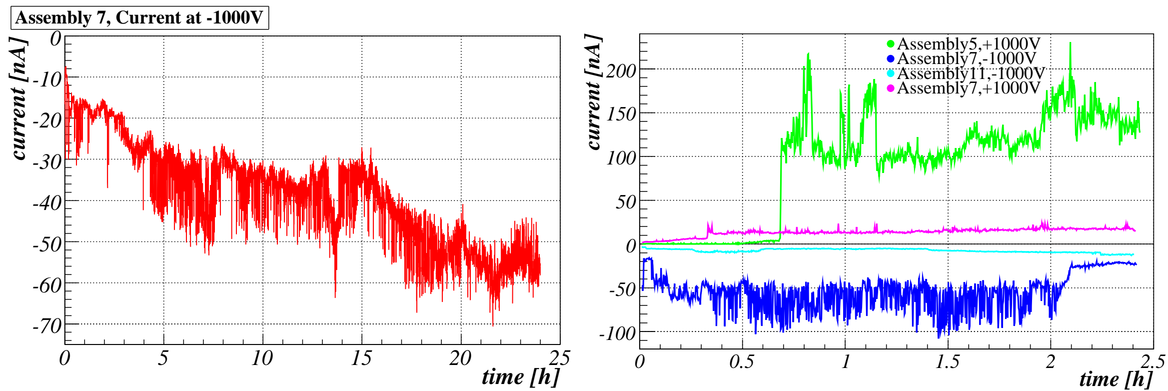

Figure 4.5: *Leakage currents measured with diamond ceramic assemblies at electric field of* ± 2 *V/μm.*

checked. Some examples of measured time evolution of leakage currents from diamond ceramic assemblies are presented in figure 4.5. It has been observed that at electric fields as high as 2 V/μm the current does not stabilise even on a time scale of days. In addition it showed quite erratic behaviour on a timescale of minutes, rising and falling by a factor as high as ten. This phenomenon, which is not yet understood, has been observed before in the BaBar experiment at lower electric fields of 1 V/μ [E$^+$05]. However, it has also been observed, that the excess current vanishes, if the BCM module with diamond is placed in a strong magnetic field. This will be discussed in more detail in section 4.2.4 where the diamond leakage currents in BCM module are presented. Table B.2 reports the currents of diamond ceramic assemblies measured at certain period of time after voltage of ± 1000 V was applied to the diamonds in each assembly.

4.2 BCM detector modules

4.2.1 MGH test beam

In October 2004 the first prototype version (see section 2.2.2) of BCM modules was tested with a low energy proton beam at the Massachusetts General Hospital (MGH) in Boston. The protons with beam energy of 125 MeV and 200 MeV, available at MGH, provided signals equivalent to 3.8 and 2.7 minimum ionising particle (MIP) signals respectively in diamond. The flux of particles in the beam was chosen to be 1.8×10^5protons/cm^{2}s, and a collimator with diameter of 13 mm was used to collimate the beam.

Two modules with identical front end electronics were used to investigate the signal properties. Measurements were taken at two different inclinations of diamond sensors with respect to the beam direction, ϑ=0° and ϑ=45°. One of the modules (module 500.2) was equipped with a single 10×10 mm^2 pCVD diamond sensor of 470 μm thickness with a charge collection distance of $\delta^{ccd}\sim$220 μm. The bottom side of this sensor had a 8×8mm^2 square electrode. Its top side was metallised with 3×3 square Cr/Au pads, covering an effective area of 7.5×7.5mm^2. The pads were interconnected with wire bonds to the module signal line, while the guard ring structure was grounded (figure 4.6). The other assembly (module 500.4) was constructed from two back-to-back 10×10 mm^2 sensors, connected to the same front end electronics. Each of the sensors in this double decker configuration was 360 μm thick with a charge collection distance

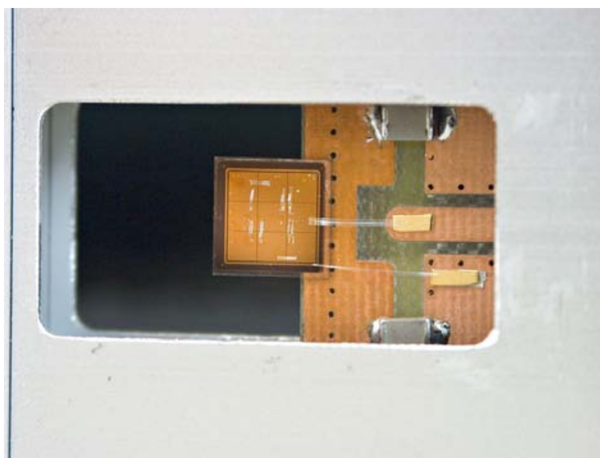

Figure 4.6: *Picture of a diamond sensor CDS110, glued to the high voltage line of a BCM prototype detector module 500.2.*

Module number	**Diamond label**	**Sensor thickness [μm]**	**Charge collection dist. δ^{ccd} [μm]**	**Metallisation**
500.2	CDS110	470	~220	3×3 square 2.5×2.5 mm^2 pads with 0.03 m distance between pads
500.4	CDS154	360	~160	8×8 mm^2
	CDS155	360	~160	8×8 mm^2

Table 4.1: *BCM modules and diamond sensors used in MGH test beam.*

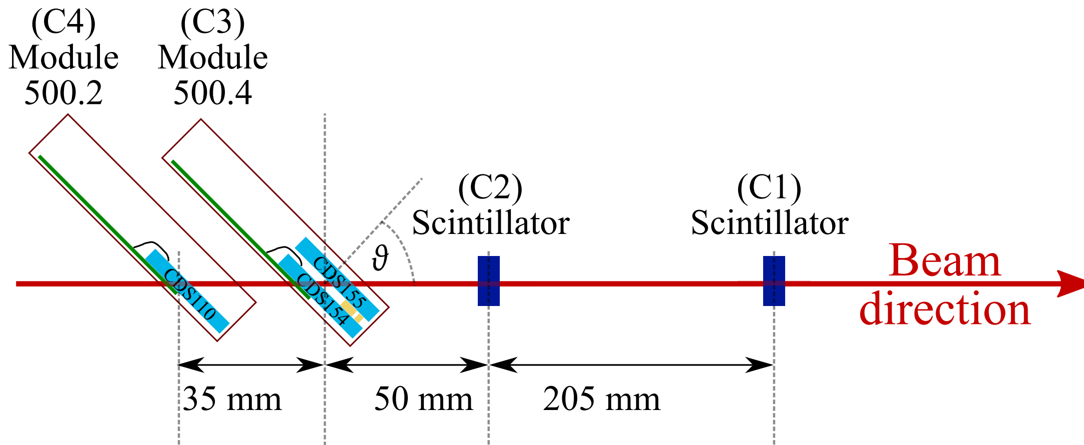

Figure 4.7: *Experimental setup for the test beam measurements at MGH in Boston.*

of δ^{ccd}~160μm, and 8×8 mm^2 Cr/Au square electrode on both sides. No guard ring structure was present on these sensors. The upper diamond was not shifted closer to the edge of the module, as in the final assemblies (see figure 4.7). The properties of the sensors are listed in table 4.1. Module 500.2 was operated at +950 V and module 500.4 at +720 V bias voltage providing an electric field of 2 V/μm in the sensors.

The BCM signals were read out via 16 m long coaxial cable and recorded with a LeCroy Wavemaster 8600A digital oscilloscope. Signal waveforms were recorded with a sampling frequency of 10 Gsamples/s and an analog bandwidth of 6 GHz. However, the actual bandwidth was limited to 500 MHz due to the front end amplifier. The readout of the oscilloscope was triggered by one or both of the two scintillators, mounted after the BCM modules along the beam line, or by one of the scintillators (with overlapping effective area of 4×4 mm^2) and one of the BCM modules. A schematic view of the setup is shown in figure 4.7. The trigger settings for each data run are listed in table 4.2.

In the off-line analysis a baseline correction was performed by finding the mean value of data points in a fixed time interval well before the signal pulse for each event and shifting the event waveform by this value. For the tests described here, a 10 ns time interval for sampling the baseline was taken.

The analysis started with a calculation of the average waveform, obtained by adding all the recorded waveforms. For each event, signal amplitude was extracted as the highest value in the event waveform. This search was performed in a short time window around the pulse peak position, found in the average waveform. Three different methods of searching for this maximum

value were tested on data from the run 10:

- The signal amplitude was taken as the highest reading found in a 2.1 ns time interval, corresponding to 21 time bins.
- A third degree polynomial was fitted to the event waveform data in a 1.3 ns time interval and signal amplitude was taken as the maximum value of the fitted function found in this time interval.
- Same as the second method, except that $\left(\frac{t-t_0}{\tau}\right)^n \mathrm{e}^{-(t-t_0)/\tau}$ was used for the fit function[1].

From a convoluted Landau-Gauss fit to the amplitude distribution, the most probable (MP) signal amplitude was estimated. The MP amplitude values, obtained by using the three different methods, were compatible at the 5% level. Thus, we decided to use the first method for signal amplitude extraction in the off-line analysis for the rest of the runs.

In order to extract the noise, a single datum point, sampled at a fixed time before the signal pulse, was histogrammed. Noise was estimated as the width σ_n of Gaussian function, fitted to the resulting noise distribution. In the analysis of test beam data described in this section the noise was sampled about 20 ns before the signal amplitude.

The same procedure for noise and amplitude extraction was used for all of the test beam and laboratory measurements reported here. Throughout this thesis the signal to noise ratio (SNR) is referred to as the ratio between the MP signal amplitude and noise value σ_n obtained from the amplitude and noise distributions respectively.

Figure 4.8 shows typical events, average waveforms and persistency plots obtained in the MGH test beam measurements. Measurements were performed for two different inclinations of the modules with respect to the beam, ϑ=0° and ϑ=45° where ϑ denotes the angle between the beam direction and normal to the sensor surface (see figure 4.7). An example of amplitude and noise distribution for ϑ=45° is shown in figure 4.9. There are two peaks in the amplitude distribution obtained from module 500.4 which was equipped with two diamonds. The lower of two peaks was observed to be at about half of the value of higher peak for all of the runs taken at ϑ=45°. This can be attributed to misalignment of the sensors in the double decker configuration of module 500.4, either due to electrode size mismatching and/or due to imperfect alignment of the electrodes in the beam. Thus, the lower of two peaks corresponds to a particle traversing only one diamond in the stack. Two signal amplitude peaks were not observed in the data runs taken when modules were placed perpendicular (ϑ=0°) to the beam (see figure 4.9(c)), indicating better alignment of the central electrode areas with the trigger in this case.

Noise σ_n and MP amplitudes obtained from the noise and signal amplitude distributions are listed in table 4.2 for all the data runs taken. In order to compare the results from runs at different beam energies, the MP amplitude obtained directly from the Landau-Gauss fit was scaled to the MP value that would correspond to 1 MIP. The resulting values are shown in figure 4.10, together with the noise value σ_n, for each of the runs. The average values of this MP

[1]The shape of the output voltage signal after injection of an instant current pulse $Q_{in}\delta(t)$ is given by $\left(\frac{nt}{\tau}\right)^n \mathrm{e}^{-\frac{nt}{\tau}}$ for a CR-RC^n shaping circuit [Spi05]. Here the time constant τ (peaking time) for the differentiator (CR) and the n integrators (RC) in the circuit is assumed to be the same.

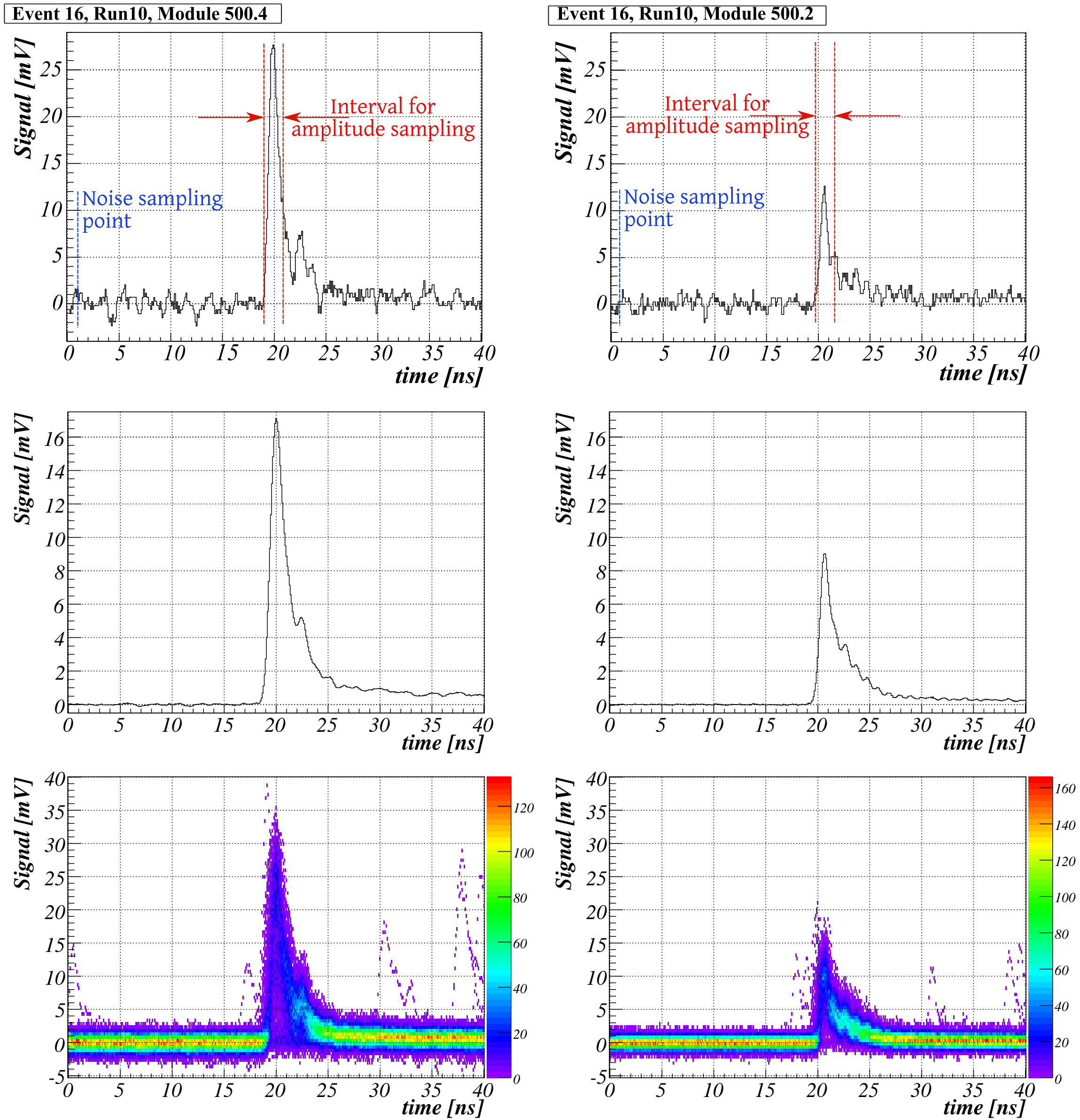

Figure 4.8: *Single event (top), average waveform (middle) and two-dimensional histogram (bottom) containing all recorded waveforms (persistency plot) for module 500.4 (left), and module 500.2 (right), obtained from data run 10 (ϑ=45°).*

signal amplitude for 1 MIP and noise σ_n, in case of ϑ=45° or 0° for both modules, are listed on the figure and indicated by the straight lines.

Module 500.4, with two back-to-back thinner sensors on the same amplifier input, gave about two times higher MP amplitude compared to the modules 500.2, equipped with one thicker sensor. Amplifier-detector system is assumed to be operating close to current sensitive mode. Therefore, the signal amplitude should not depend on the thickness of the sensors used. In a double decker assembly, signals from the two sensors are passively summed before

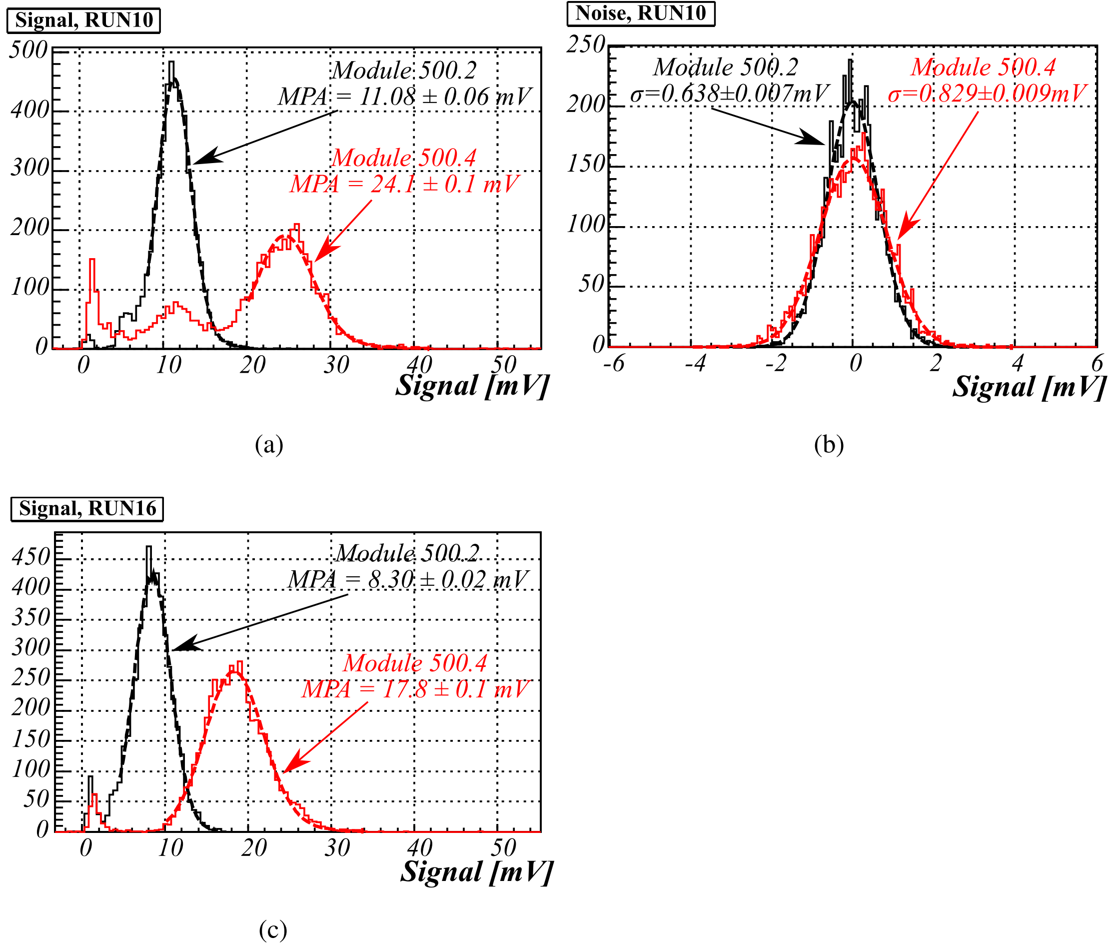

Figure 4.9: *Amplitude distribution of 3.8 MIP signals, obtained at MGH test beam, when modules were inclined by (a) ϑ=45° (run 10) and (c) ϑ=0° (run 16). Figure (b) shows typical noise distributions. Red colour labels results for module 500.4 and black for module 500.2. Doted lines indicate the convoluted Landau-Gauss fits to amplitude or Gauss fits to noise distributions. The most probable amplitude (MPA) and noise RMS (σ_n) obtained from those fits are written above the graphs. The errors stated here are the values returned by the fit procedure.*

amplification and one can expect the signal amplitude of a double decker to be two times higher than for the single sensor. On the other hand, noise value σ_n for module 500.4 was increased by only 30% compared to module 500.2, resulting in more than 50% higher SNR for the double decker assembly.

In general, the noise depends on detector capacitance and leakage current where the exact relation varies depending on the front-end electronics of the system [Spi05]. If capacitance was the dominating factor for noise, then the use of a double decker assembly should double the noise compared to a single sensor with the same thickness as each of the sensor in double decker. One would than expect for the difference in noise between the modules under tests to be much higher than the observed 30%. Thus, these results show that the use of double decker configuration is advantageous compared to single sensor configuration.

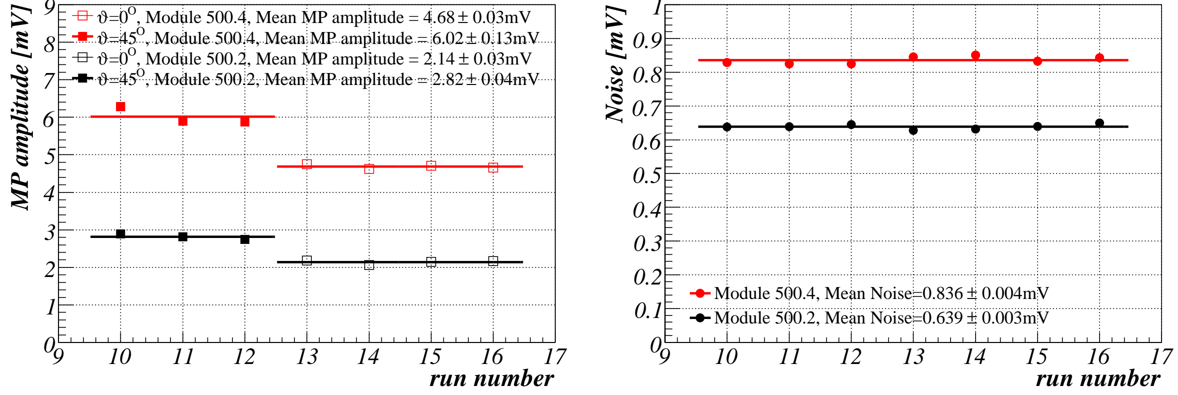

Figure 4.10: *MP amplitude (left) and noise σ_n (right) extracted from the data runs taken at MGH test beam. Red (black) markers label the results obtained for module 500.4 (500.2). In the left plot, closed markers show the results obtained for sensors inclined by ϑ=45°, while open markers refer to runs where sensors were placed perpendicularly to the beam. Lines denote the mean values, which are also presented in legends together with their standard errors.*

Inclining the modules by ϑ=45° does not give any change in noise σ_n as expected, but it increases the MP amplitude by a factor of ∼1.3, which differs from the expected geometrical factor of $\sqrt{2}$. This difference can be attributed to the misalignment of sensors, resulting in electrode edge effects, which can lower the amplitude to some degree.

Run	T_p [MeV]	Trigger	ϑ [^{o}]	Module 500.4 MP Ampl. [mV]	Module 500.4 Noise [mV]	Module 500.2 MP Ampl. [mV]	Module 500.2 Noise [mV]
10	125	C1(145 mV)& C4(2.0 mV)	45	24.06 ±0.12	0.829 ±0.009	11.08 ±0.06	0.638 ±0.007
11	200	C1(145 mV)& C4(1.5 mV)	45	16.27 ±0.08	0.825 ±0.009	7.77 ±0.05	0.639 ±0.007
12	200	C1(145 mV)& C4(1.0 mV)	45	16.21 ±0.08	0.825 ±0.009	7.59 ±0.05	0.645 ±0.007
13	200	C1(140 mV)& C4(1.0 mV)	0	13.12 ±0.07	0.845 ±0.009	6.02 ±0.04	0.628 ±0.007
14	200	C1(140 mV)& C2(200 mV)	0	12.76 ±0.07	0.851 ±0.009	5.64 ±0.06	0.632 ±0.007
15	125	C1(140 mV)& C2(200 mV)	0	18.02 ±0.01	0.832 ±0.009	8.23 ±0.09	0.639 ±0.007
16	125	C1(140 mV)& C4(1.0 mV)	0	17.86 ±0.01	0.843 ±0.009	8.30 ±0.02	0.650 ±0.007

Table 4.2: *Beam energy (T_p), inclination of sensors (ϑ) and trigger settings for different data runs taken at MGH test beam. Observed MP amplitudes and noise values σ_n are presented in the last four columns. The trigger settings of each data run are listed in the third column. C1, C2, and C4 refer to scintillators and module 500.2, where the same labelling as shown in figure 4.7 is used. Trigger levels are listed in parenthesis.*

4.2.2 Test beam at CERN SPS in 2004

In order to investigate the response of BCM modules to true MIPs, prototype BCM modules were exposed to a 110 GeV/c H8 pion beam at the CERN SPS in November 2004. This test provided us to evaluate the signal and timing properties of BCM modules in conditions similar to the normal operation conditions expected in the ATLAS experiment. Two modules, both equipped with a double decker diamond assembly, were tested. The properties of the sensors used in this test are listed in table 4.3. Module 500.4 was already used in the MGH test beam.

BCM signals were read out through a 16 m long coaxial cable, and recorded with a LeCroy 564A digital oscilloscope with a sampling frequency of 4 Gsamples/s and an analogue bandwidth limit (BWL) of 1 GHz or 200 MHz applied. The highest BWL that can be applied on the oscilloscope, used in these tests, is 1 GHz, which exceeds the 500 MHz BWL of the amplifiers in front end electronics. Thus, when 1 GHz BWL was used at the oscilloscope, the bandwidth was limited by the original 500 MHz.

Trigger signal was provided by two scintillators placed upstream and downstream of the modules as shown in figure 4.11. The modules were tested with different positive and negative bias voltages applied providing drift fields up to ±2 V/μm. Measurements were performed for

Module number	**Diamond label**	**Sensor thickness [μm]**	**Charge collection dist. δ^{ccd} [μm]**
500.3	CDS159	515	~218
	CDS160	515	~218
500.4	CDS154	360	~160
	CDS155	360	~160

Table 4.3: *BCM modules and diamond sensors tested in the CERN SPS test beam in November 2004. Both sides of all sensors were metallised with 8×8 mm² square electrodes and no guard ring structure was present.*

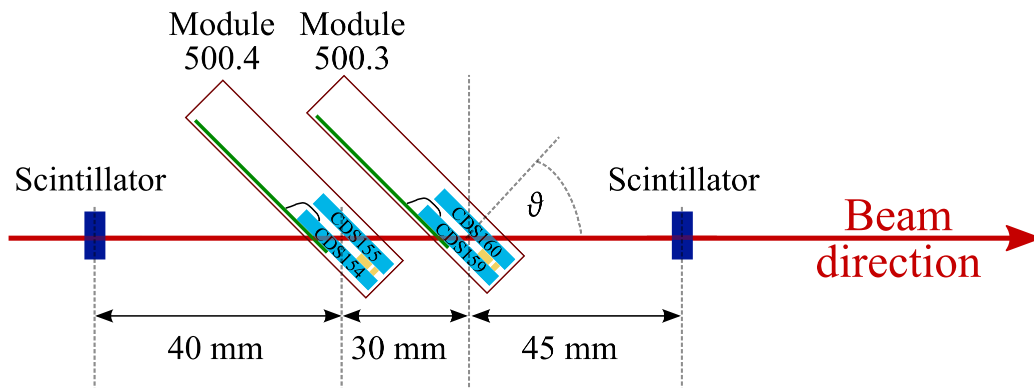

Figure 4.11: *Experimental setup at test beam at CERN in November 2004.*

ϑ=0° and 45° angles of beam incidence, as in the case of tests at the MGH in Boston.

In the off-line analysis, a time interval of 10 ns, well before the signal pulse, was used for sampling the baseline for the baseline correction. In order to obtain the signal amplitude distributions, the amplitude was extracted from a 2.25 s time interval (9 time bins) around the point with highest value found in the average waveform. The MP amplitudes for different setups are listed in table 4.4 and shown in figure 4.12. For some of the setups, the data were collected in several different data runs. In these cases the MP amplitude stated in table 4.4 and shown in figure 4.12 represents the mean value with its error. Noise distributions were obtained by sampling the datum point at time about 20 ns before the signal pulse. The noise σ_n extracted from Gaussian fit to noise distribution for each run as a function of applied electric field is shown in figure 4.12. Error on noise σ_n indicated here is the value returned by the fit procedure.

The following observation can be made from the results presented in figure 4.12 and table 4.4:

- Inclining the modules by ϑ=45° increases the signal by a factor of $\sqrt{2}$ as expected.
- Results for noise σ_n agree with test beam measurements at MGH, where the noise was found to be independent of applied bias voltage. However, a wider spread in noise σ_n for module 500.4 can be observed in figure 4.12, which can be attributed to improper grounding and shielding due to bad closing of this module. The mean value for noise σ_n with its RMS, calculated from the runs with 1 GHz BWL applied is listed in table 4.4 and indicated in figure 4.12 by the blue dotted lines for both modules. For the case of 200 MHz BWL, green markers denote the noise value σ_n returned by the fitting procedure, which is also listed in table 4.4.
- When modules are operated at $\sim$2 V/μm electric field and ϑ=45°, applying 200 MHz BWL decreases the signal from module 500.3 by 32% and by 35% for module 500.4 compared to the values obtained at 1 GHz BWL. On the other hand, noise σ_n was decreased by 53% for module 500.3 and 58% for module 500.4, resulting in the SNR increase from 8.0 to 11.5 and from 7.3 to 11.3 for module 500.3 and 500.4 respectively. Thus including a 200 MHz low-pass filter appears to be beneficial.

The rise time of a signal pulse is generally expressed as the time interval between points of 10% and 90% amplitude. This time difference was determined for each recorded event by fitting two straight lines around the pulse peak, one on the rising and one on falling part of the pulse. The intersection point of these two lines was used to estimate the amplitude value and its position. The time points of 90% and 10% of estimated amplitude were then determined from the line fitted on the rising part of the pulse and their time difference was taken as the pulse rise time. Figure 4.13(a) shows examples of rise time distribution, obtained at 2 V/μm for both 1 GHz BWL and 200 MHz BWL. The mean value of the rise time distributions as a function of the electric field applied to the sensor is presented in figure 4.14(a) for both cases.

The full width at half maximum (FWHM) of each pulse was extracted by searching for the points with signal equalling 50% amplitude on both sides of the signal pulse. The search started at the point of pulse peak. When a signal level lower than 50% amplitude was reached, a straight line interpolation between this and the previous point was used to estimate the time

ϑ [^{o}]	BWL [GHz]	Module 500.3 Voltage [V] (field [$\frac{V}{\mu m}$])	Module 500.3 MP ampl. [mV]	Module 500.3 Noise [mV]	Module 500.4 Voltage [V] (field [$\frac{V}{\mu m}$])	Module 500.4 MP ampl. [mV]	Module 500.4 Noise [mV]
0	1	+750 (+1.5)	2.23	0.502 ±0.002	+350 (+0.97)	2.06	0.60 ±0.01
		+1000 (+1.9)	2.85 ±0.01		+650 (+1.8)	3.3 ±0.1	
45	1	+500 (+0.97)	2.32		+350 (+0.97)	2.77	
		+750 (+1.5)	3.33		+550 (+1.5)	3.75	
		+1000 (+1.9)	4.03 ±0.05		+650 (+1.8)	4.4 ±0.1	
45	1	-500 (-0.97)	3.70 ±0.02		-350 (-0.97)	3.27 ±0.02	
		-750 (-1.5)	4.16		-550 (-1.5)	4.03	
		-1000 (-1.9)	4.47 ±0.07		-650 (-1.8)	4.29 ±0.03	
45	0.2	+1000 (+1.9)	2.73	0.237 ±0.002	+650 (+1.8)	2.87	0.253 ±0.002

Table 4.4: Summary of noise σ_n and MP amplitudes obtained with 1MIPs delivered by CERN SPS for different setups. Here, BWL represents the bandwidth limit applied on the oscilloscope. The MP value and its error were calculated as the mean and its RMS if the data for a specific setup were collected in different runs. The noise values σ_n were obtained similarly assuming noise to be independent on ϑ and bias voltage.

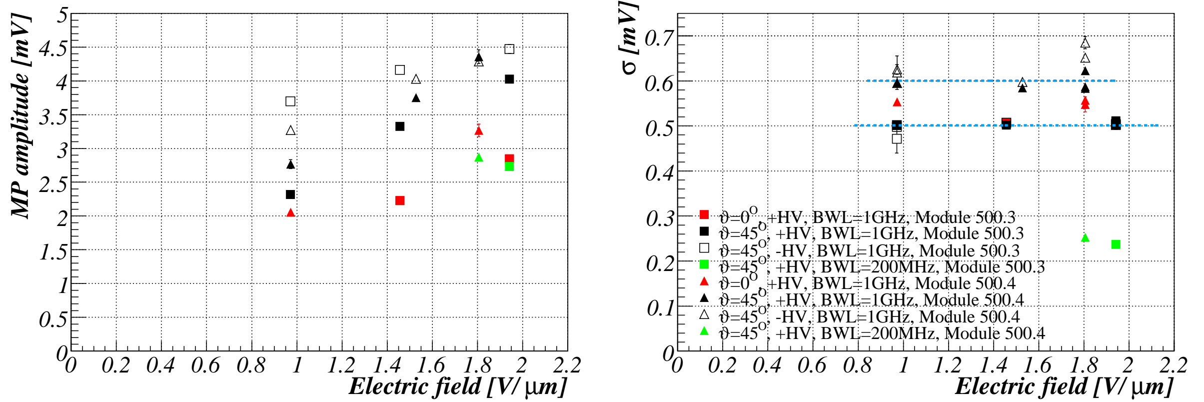

Figure 4.12: Left: MP amplitude (from table 4.4) dependence on applied electric field for two different inclinations ϑ of sensors and two different BWL at the readout. Right: Noise σ_n extracted from different data runs as a function of electric field applied to sensors. ±HV in the legend refers to positive or negative polarity of applied voltage. Blue lines represent the mean noise value σ_n averaged over all the noise points obtained for each module in case of 1 GHz BWL.

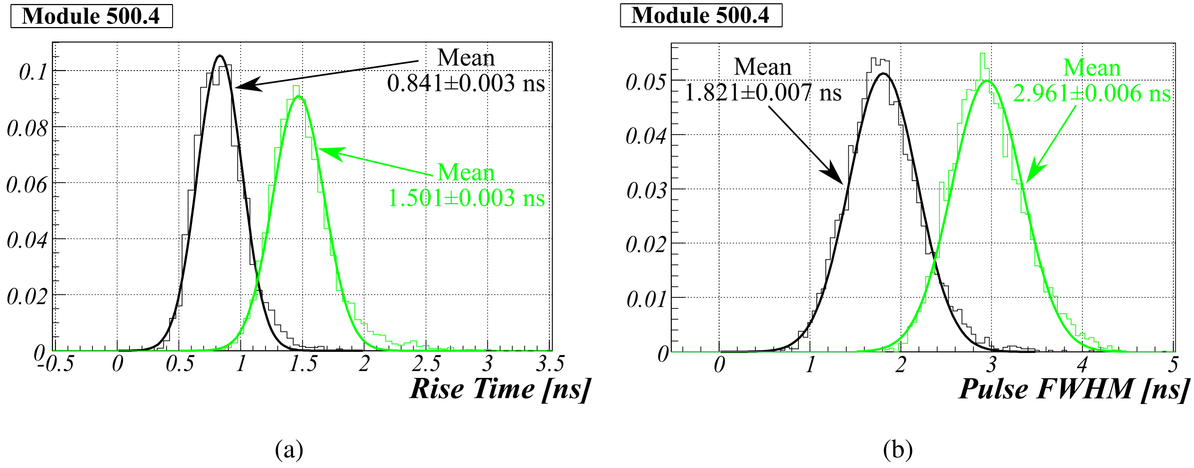

(a) (b)

Figure 4.13: *(a) Pulse rise time and (b) FWHM width distributions obtained for module 500.4 at 2 V/μm electric field and 1 GHz (black) or 200 MHz BWL. Mean of the distributions and its standard error are written on the plot.*

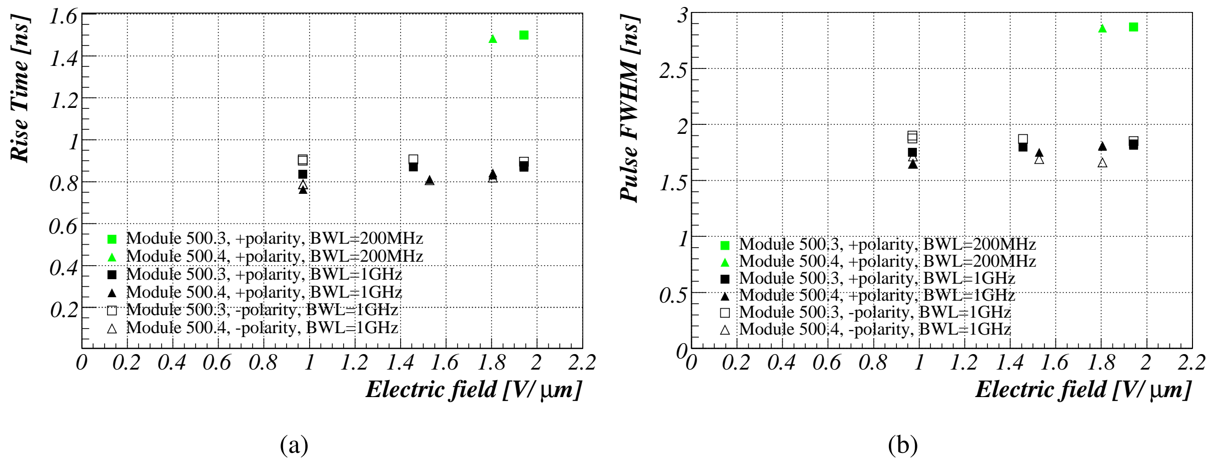

(a) (b)

Figure 4.14: *(a) Pulse rise time and (b) FWHM width as a function of electric field for 1 GHz (black) and 200 MHz (green) BWL. Square markers show the results for module 500.3 and triangles for module 500.4. Open and closed markers distinguish between negative and positive polarity of applied bias voltage.*

of 50% amplitude. The time difference between the 50% amplitude points found on both sides of the signal pulse was taken to be the FWHM width of the pulse. An estimation of amplitude value and position was needed in this procedure. The same estimation as for determination of amplitude distribution was used here. Figure 4.13(b) shows the FWHM pulse width distribution, measured at 2 V/μm for the two bandwidth limits. The mean of FWHM pulse width distribution dependence on electric field is presented in figure 4.14(b).

The results show no rise time and pulse width dependence on electric field. The ionisation current signal from the sensor rises to its highest value immediately after the drifting charge is created. Following the initial rise, the pulse decays exponentially with a characteristic time

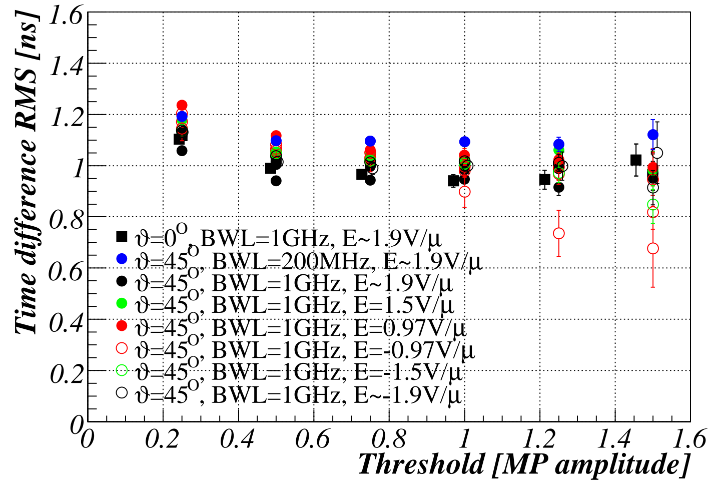

Figure 4.15: *Time difference RMS as a function of threshold (in units of MP amplitude) for the two BWL used at readout. Black, red and blue colours mark different applied electric fields. Open markers show the results obtained for negative and closed for positive polarity of applied bias voltage. Square and triangle markers distinguish between values obtained when sensors were inclined by ϑ=0° and 45° respectively. Green colour marks the result for the case of 200 MHz BWL applied at readout, while 1 GHz BWL was used in all other cases.*

corresponding to the trapping time, since trapping is dominating in pCVD diamonds. The pulse amplitude depends on the drift velocity and thus on the electric field, while the signal shape does not change with electric field, if the trapping time is independent of electric field even at high saturated drift velocities. Since the characteristic times of the following electronics does not change with electric field, the output pulse width and rise time are not expected to depend on electric field.

Limiting the bandwidth from 1 GHz to 200 MHz increases the rise time by more than 70% and increases the pulse width by about 60%. The increase for both, rise time and pulse width, was expected, since slower electronics flattens the signal.

In order to extract the timing resolution for each event, the time of signal crossing a fixed threshold for module 500.3 was subtracted from the time of threshold crossing found for module 500.4. The search for this time of threshold crossing was performed from the pulse peak down the rising part of the pulse, until the signal level lower than threshold was found. An interpolation with a straight line between two points around the threshold level was used to estimate the point of threshold crossing. Assuming that both modules exhibit the same timing resolution, the RMS of this time difference distribution, divided by $\sqrt{2}$, can be taken as an estimate for timing resolution of BCM analogue signals. However, in the measurements presented in this section the event waveforms recorded for each module did not result from the same trigger signal. The resulting time difference has an additional contribution due to the trigger scintillator, which is expected to be the same for all data runs. Therefore, only a qualitative comparison of the results with different module settings, in terms of applied electric field and BWL, is possible here.

Figure 4.15 shows the RMS of the time difference distribution as a function of the threshold

value. Same electric field was applied to sensors in both modules and two different bandwidth limits used at the readout. Note that the threshold is given in units of MP amplitude. At higher thresholds, the extracted values poorly estimate the resolution due to the lower statistic of events with amplitudes above the threshold.

The timing resolution comes from two sources:

- *Jitter* is the timing variation caused by noise effects on the pulse being analysed. If signals with fixed amplitude are considered, the time of threshold crossing fluctuates due to modulation of instantaneous signal level by the noise. The determining parameters for this effect are signal slope at the threshold level and noise. The variance of timing distribution or jitter is

$$\sigma_{\text{jitter}} = \frac{\sigma_n}{(dS/dt)_{S_{\text{thr}}}}, \tag{4.1}$$

  where σ_n is the RMS noise and $(dS/dt)_{S_{\text{thr}}}$ the signal slope evaluated at the threshold level S_{thr}.

- The time at which the signal crosses a fixed threshold depends on the amplitude height. As the amplitude varies, the time of signal crossing the threshold shifts. Thus, variations in signal amplitude broaden the timing distribution. This phenomenon is called *time walk*.

Amplitudes of diamond signals follow a Landau distribution. The absolute contribution of jitter and walk to the timing resolution is difficult to estimate. However, the effect of different BWL or electric field, shown in figure 4.15, can be qualitatively explained, by assuming that the shape of the signals (rise time and width) depends only on BWL:

- The timing resolution improves with increasing bias voltage. Since we are comparing the results at fixed threshold in units of MP amplitude the contribution of time walk at different electric fields is the same while the jitter is different. Higher electric field gives signals with higher amplitudes which have larger slopes at given threshold (in MP amplitude units) while the noise does not change with increased electric field. Therefore, the contribution of jitter is smaller at higher electric fields.

- Comparing the results obtained with the two different bandwidth limits at the readout when $\sim$2 V/μm electric field was applied we see that limiting the bandwidth from 1 GHz to 200 MHZ deteriorates the timing resolution. However, the observed RMS time differences differ by less than 0.1 ns for the threshold range considered in the analysis.

An estimate of BCM analogue signal timing resolution was possible from the test beam measurements performed in 2007. These results will be discussed in section 4.3.1.

4.2.3 Test beam measurements in 2006

During the summer 2006, test beam measurements in CERN PS (T9, T11) and SPS (H8) pion beams were carried out. All the final services available at the time were used, including power and signal cable connections together with low voltage power supplies for front end electronics and high voltage supplies providing the electric field in the sensors. Thus, one of the objectives of these test beam measurements was to test the performance of the full BCM system. Furthermore, the uniformity of the sensors' active surface was checked and the possibility of using the NINO chip in the BCM system was studied with the first prototype NINO boards. However, the results with NINO will not be discussed here. More relevant test beam results are presented in section 4.3.1.

A picture of the setup used is shown in figure 4.16. Four BCM detector modules were placed in the beam simultaneously. The signals from two of them were fed into NINO boards. The NINO output waveforms were recorded by a CAEN [CAE] V1729 12-bit VME ADC with 2 GHz sampling frequency and an analogue bandwidth of 300MHz. Signal waveforms from the other two modules were first amplified with an ORTEC FTA810 340 MHz bandwidth amplifier and then recorded with the CAEN ADC as well.

Position information of incident particles was provided by Bonn ATLAS telescope, with a spatial resolution of $\sim$10 μm in direction perpendicular to the beam. The telescope consists of four 300 μm thick double sided silicon micros-trip detector planes. Detailed description of the telescope can be found in references [Tre02, T$^+$02]. Telescope and BCM readout were triggered by coincidence signal of two plastic scintillators. The events, as seen in both of the systems, were recorded synchronously, by their separate data acquisition systems and the data were matched later in the off-line analysis.

Apart from the last few data runs, which were taken in H8 beam line, detector modules were placed in the beam in a way that the acceptance area of the two diamonds in the module was smaller than in case when the modules were positioned with respect to the particle tracks

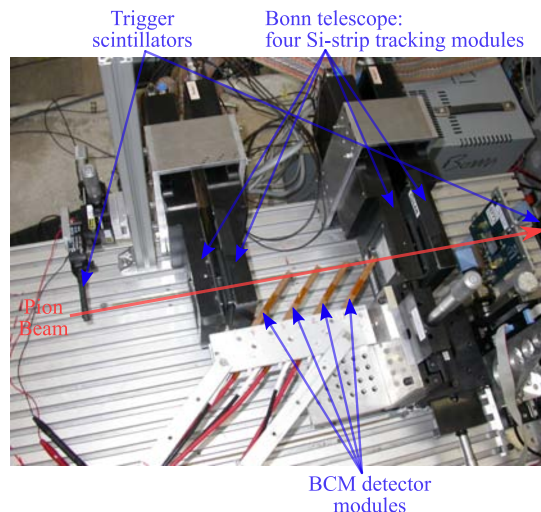

Figure 4.16: *Picture of the setup used for test beam measurements at CERN SPS in 2006.*

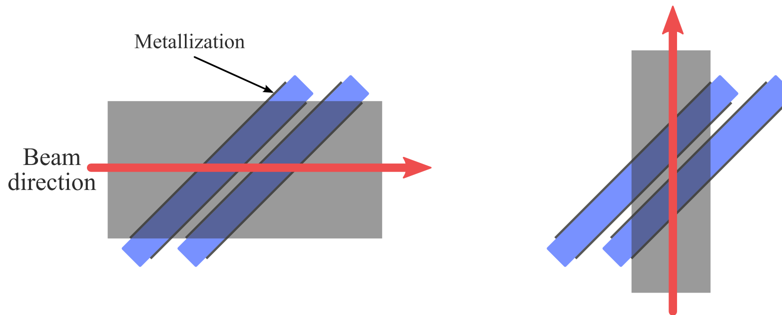

Figure 4.17: *Position of diamonds in double decker assembly with respect to the beam, when position as anticipated for ATLAS (left) and during test beam measurements when not aligned as in ATLAS (right). Shaded region marks part of the beam where the traversing particle leaves a signal in both of the diamonds in the stack.*

as envisaged for ATLAS (see figure 4.17). Furthermore, in the H8 measurements, only part of detector active area was aligned with the trigger scintillators.

The pions in T11 and T9 beam-line had momenta of 3.5 GeV/c and 12 GeV/c respectively, while in H8 beam line 20 GeV/c and 100 GeV/c pions were used, all providing 1 MIP signals. With the lower energy pions some influence of scattering can be expected. According to [Y$^+$06] the projected scattering angles are distributed according to Moliére distribution. However, Gaussian distribution of central 98% of the projected angular distribution is a good approximation. The width of Gaussian approximation is given by

$$\vartheta_0 = \frac{13.6\mathrm{MeV}z}{\beta cp}\sqrt(\frac{x}{X_0})\left(1 + 0.038\ln\left(\frac{x}{X_0}\right)\right), \tag{4.2}$$

where p, βc and z are the momentum, velocity and charge number of incident particles, while x and X_0 are the thickness and radiation length of the scattering material. This gives ϑ_0 around 0.04^o, 0.01^o, 0.007^o and 0.001^o in case of 3.5 GeV/c, 12 GeV/c, 20 GeV/c or 100 GeV/c pions traversing four double decker diamond assemblies at 45° with respect to the beam as in our setup. For module positioned first along the beam direction, the deviation is estimated to be 0.5 mm for 3.5 GeV pions and of the order of 0.1 mm for 12 GeV pions. In case of the 20 GeV pion beam, the deviation drops below 0.1 mm and is of the order of 0.01 mm for 100 GeV pions.

In the off-line analysis events with pion tracks leaving a hit in at least three out of four silicon telescope planes and good track fit quality were selected. These tracks were interpolated on the diamond double decker central plane. The amplitudes of detector module signals were searched in a 2.5 ns time window. The amplifier used for amplifying the analogue signals is asymmetric and amplifies signals of only one polarity (see figure 4.18). Due to this asymmetric amplification it was not possible to determine the zero signal level. Therefore, no baseline correction was performed on analogue signal waveforms. Figure 4.18 shows a typical distribution of analogue signal amplitudes in units of ADC counts. Here, only events with pion tracks traversing the diamond central region was considered. Asymmetric amplification also hinders the estimation of noise σ_n for the analogue signals. Thus, MP amplitudes and noise σ_n of analogue data will not be discussed here. An example of a noise distribution, sampled at around 300 ns before the signal pulse, is shown in figure 4.18 as well.

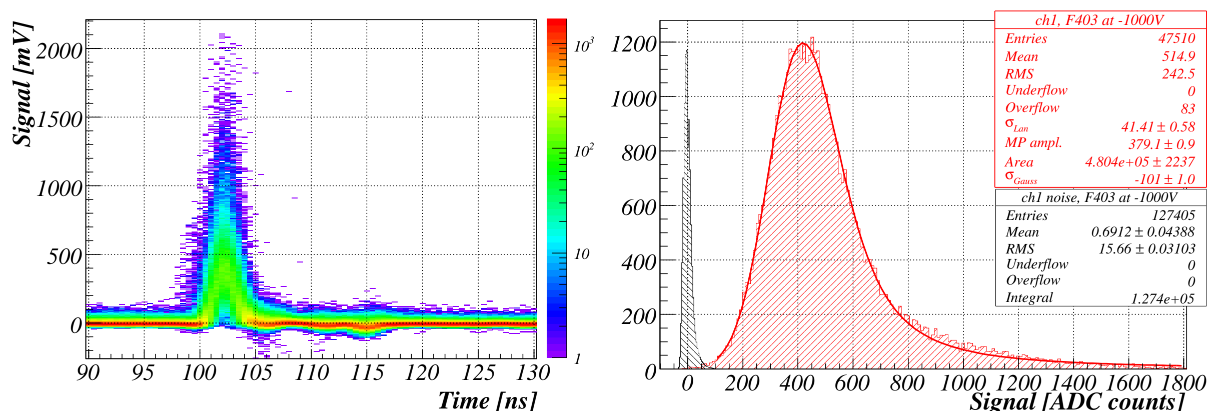

Figure 4.18: *Left: Two-dimensional histogram of all recorded waveforms for module F403 at −1000 V. Right: Noise (black) and amplitude (red) distributions for module F401. Only events with particle passing the central part of diamond active area were considered. Due to asymmetric amplification of ORTEC amplifier, positive excursions of signals are more pronounced compared to negative on waveform histogram and longer tail in the positive side of noise distribution can be observed.*

The response of the detector was scanned in steps of 0.1 mm over an area larger than the detector's surface. At each step, the fraction of tracks with analogue signal above the chosen threshold was calculated where the tracks in area of 0.2×0.2 mm^2 around the position of the step were considered. Examples of these efficiency plots with different thresholds are presented in figures 4.19 and 4.20. The plots in figure 4.19 were obtained from the T9 data where the detectors were not aligned as anticipated for ATLAS while the plots in figure 4.20 were made with H8 data with alignment as in ATLAS. One can observe that the distance, where efficiency drops from its central value to 0 along the x axis, is longer on the T9 plots since this region covers the area where only one of the diamonds in double decker configuration contributes to the signal. On the other hand a steep drop in efficiency can be observed on H8 plots in x and y direction[2]. Non-uniformity in efficiency can be observed on all of these plots. In order to exclude the statistical fluctuations as the cause of this non-uniformity, a longer period of data taking, during which the sensors were not moved, was divided in two parts with no mutual events. The result, presented in figure 4.21, shows that the same pattern can be observed for both time periods. Thus, non-uniformity can be attributed to the grain structure of the diamonds in double decker.

The level and size of non-uniformities depend on the quality of diamond samples in double decker assembly. For example, comparison of figures 4.20 and 4.21 shows that module F408 has samples of higher quality than module F403. However, both of the modules show quite uniform response at threshold of 0.5MP amplitude, while with increasing threshold the non-uniformity becomes more pronounced.

[2]The drop occurs over distance ∼0.2 mm corresponding to the size of the 0.2×0.2 mm^2 region used used for efficiency calculation in each step.

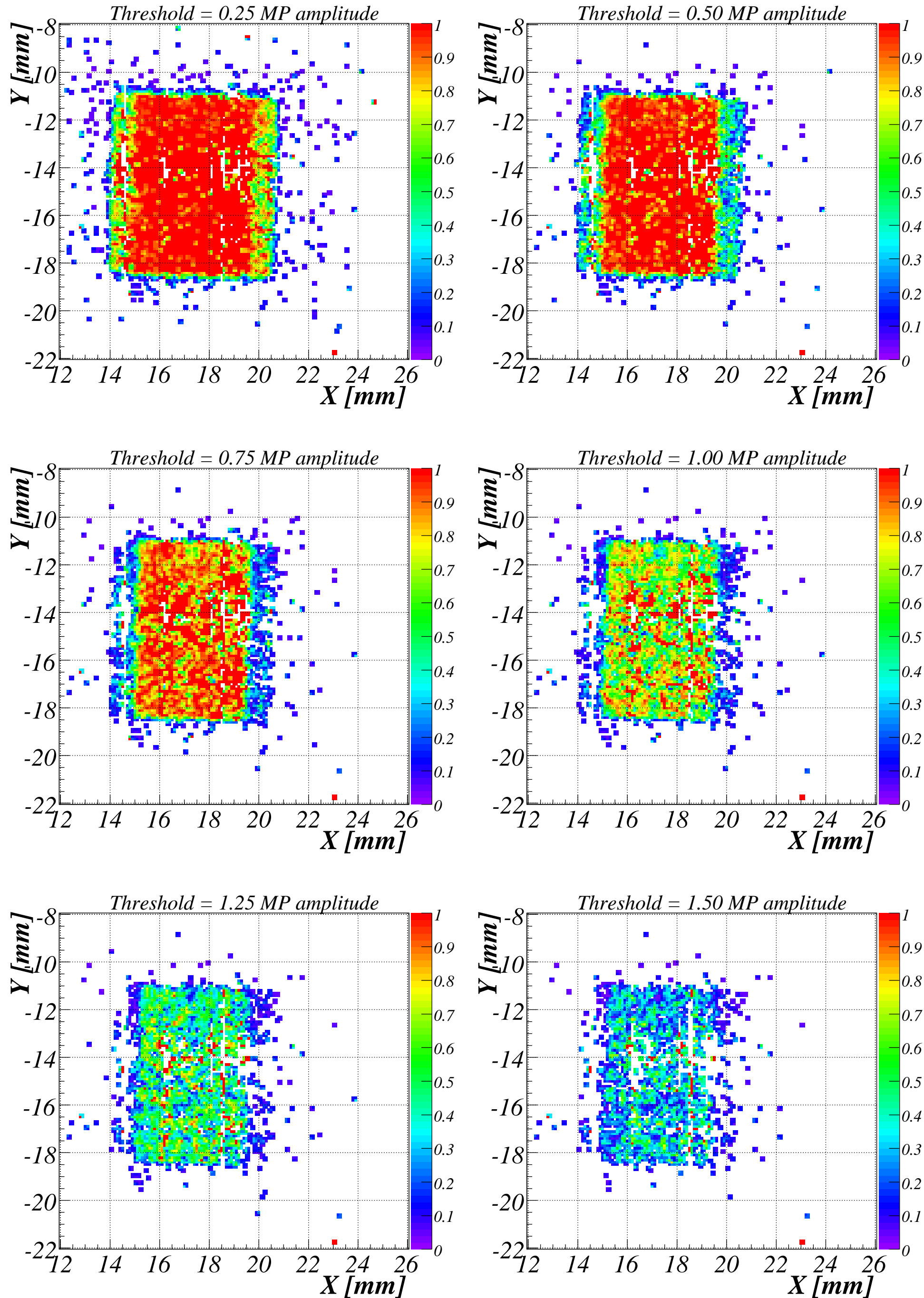

Figure 4.19: *Efficiency of analogue signals scanned over the diamond area in steps of 0.1 mm for module F408 at +1000 V. Efficiency was calculated as the fraction of pion tracks in 0.2×0.2 mm² with signal amplitude higher than the threshold value in each step. The threshold values for each plot are given in units of MP amplitude. The plots were extracted from the T9 data where modules were not aligned with the beam as in ATLAS.*

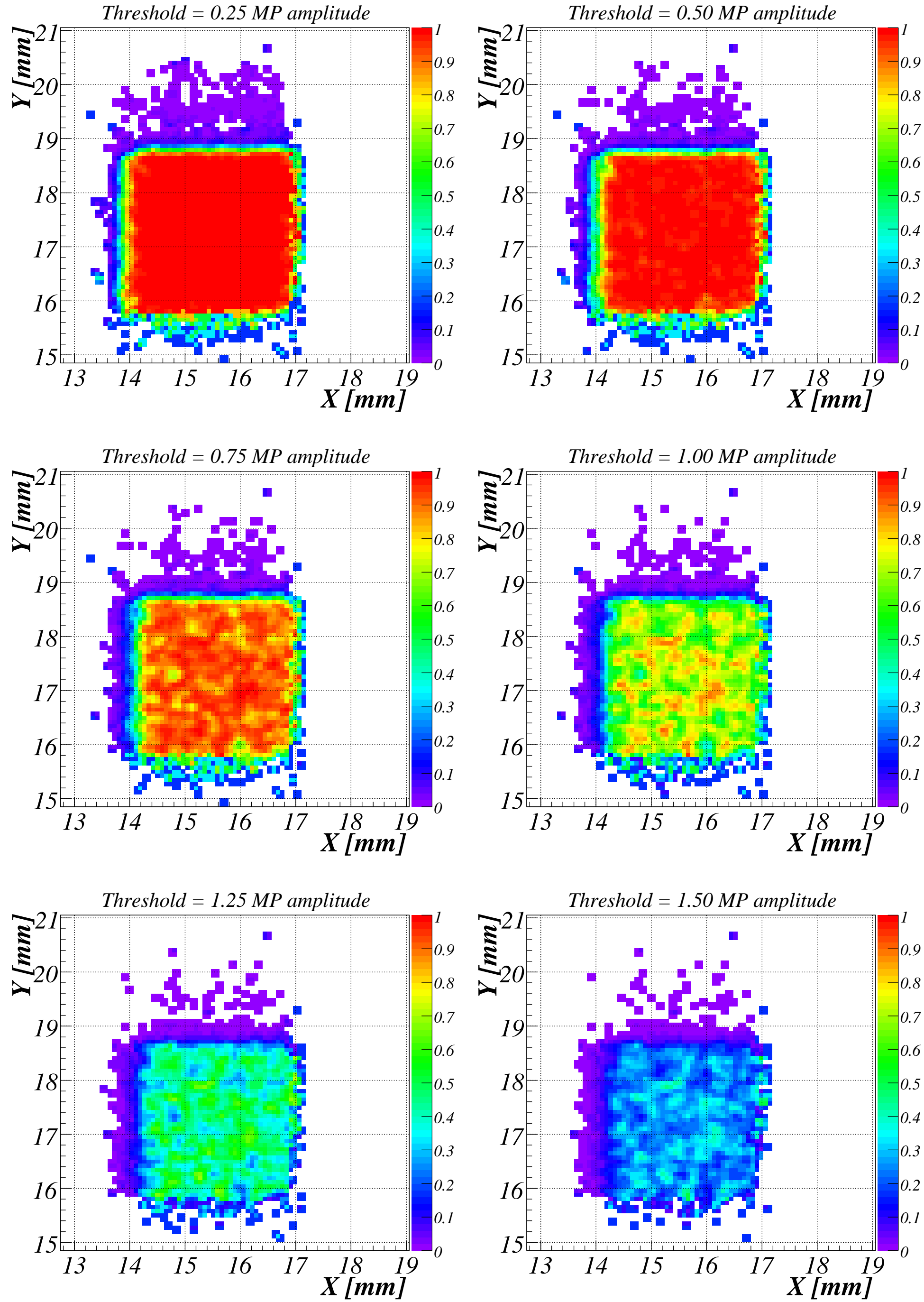

Figure 4.20: *Efficiency of analogue signals scanned over the diamond area in steps of 0.1 mm for module F408 at −1000 V. Efficiency was calculated as the fraction of pion tracks in $0.2{\times}0.2\,mm^2$ with signal amplitude higher than the threshold value in each step. The threshold values for each plot are given in units of MP amplitude. The plots were extracted from the data collected in H8 beam line when module was positioned as anticipated in ATLAS.*

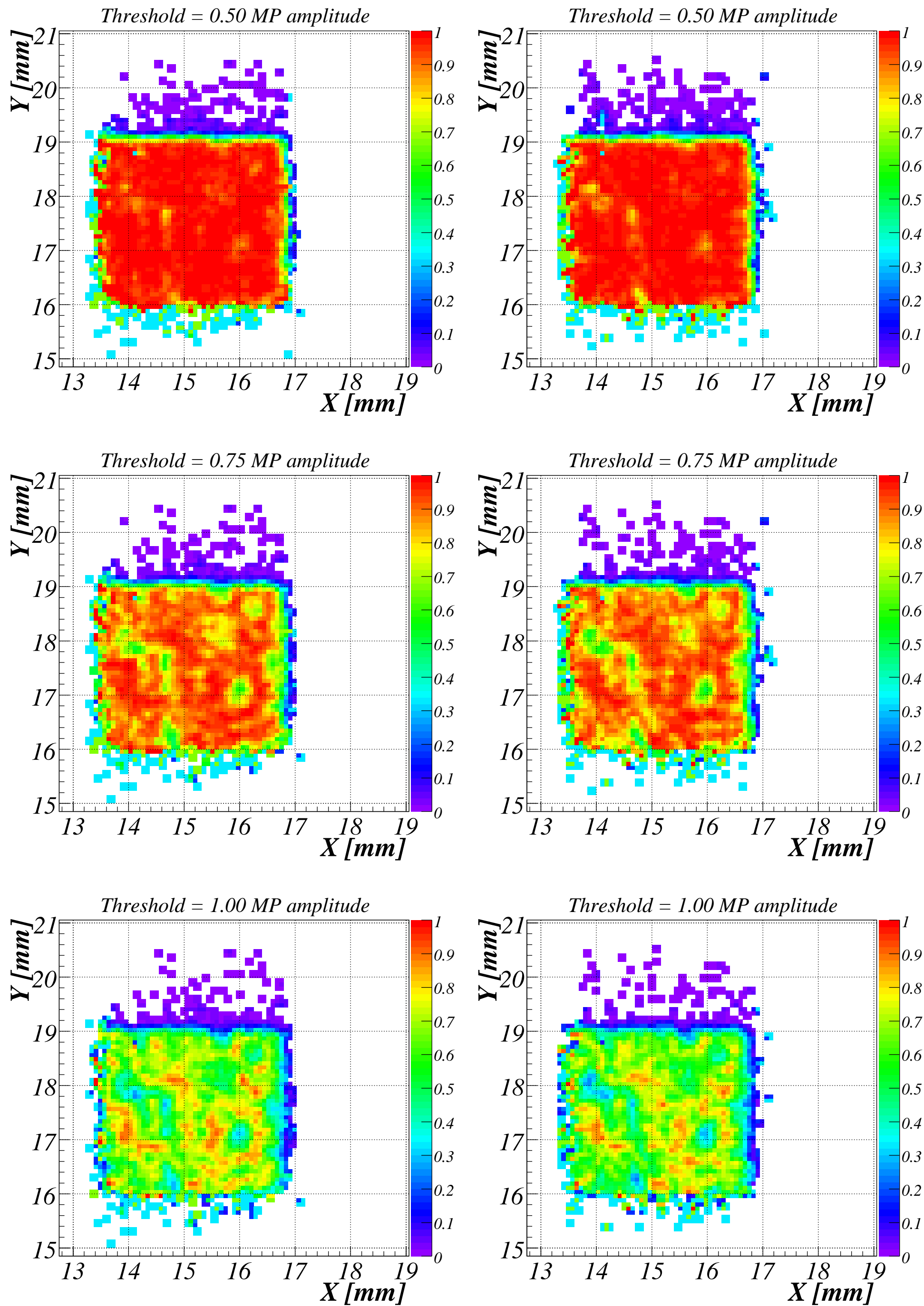

Figure 4.21: *Efficiency scan over diamond surface for module F403 at −1000 V and positioned as expected in ATLAS. The plots were obtained from data collected in two different time periods with left plots corresponding to the first and right to the second period.*

4.2.4 Measurements with ^{90}Sr source

In this section measurements with the final detector modules, performed with ^{90}Sr as a source of MIP signals, are presented. The standard setup used in these tests is shown in figure 4.22. It consisted of a ^{90}Sr as a source of β-electrons, mounted above the detector module. Two 2.5 mm thick aluminium collimators were used, where one was placed between the detector module and source, and the other one between detector module and a scintillator. The collimators had opening of 2 mm diameter aligned to the centre of the diamond sensor. Scintillator was mounted below the bottom collimator and, providing a trigger for MIP signals, produced by electrons penetrating the diamond assembly. The acceptance area of the scintillator was approximately $3\times4\,\mathrm{mm}^2$, which was less than diamond active area ($8\times8\,\mathrm{mm}^2$), but more than collimator opening area.

Voltage was supplied by Keithley 237 high voltage measure-source unit [Kei], which was also used to monitor the current of the BCM detector module under test. Signal waveforms from BCM modules were read out through 0.5 m coaxial cable and recorded by a LC564A LeCroy oscilloscope with a sampling frequency of 4 Gsamples/s. Voltage scans for negative and positive polarity, with 200 MHz or 1 GHz BWL applied at the oscilloscope, were performed with each module under test. In order to stabilise the polarisation effect, the measurement at a certain voltage started 300 s after applying the bias voltage. After each recorded event, a time delay of 1 s was used before the oscilloscope was ready to accept the next trigger signal. Voltage control and acquisition of signal waveforms together with leakage currents were performed automatically, using a PC with a GPIB interface to the oscilloscope and Keithley unit. The software for data acquisition and instrument control was written in LabView [Lab].

The detector modules in these tests were equipped with a double decker diamond assembly in the configuration as envisaged for the final BCM modules installed in ATLAS detector. However, in some of the initial tests ceramic baseboards and inserts were not used when constructing this assembly. Unless stated otherwise, the pCVD diamond sensors, used in measurements described in this section, were $\sim$500 μm thick with $1\times1\,\mathrm{cm}^2$ surface and charge collection distance of $\delta^{ccd}\sim$220 μm. Square proprietary electric Ti-Pt-Au contacts, covering $8\times8\,\mathrm{mm}^2$ of the top and bottom surfaces, were made at Ohio State University.

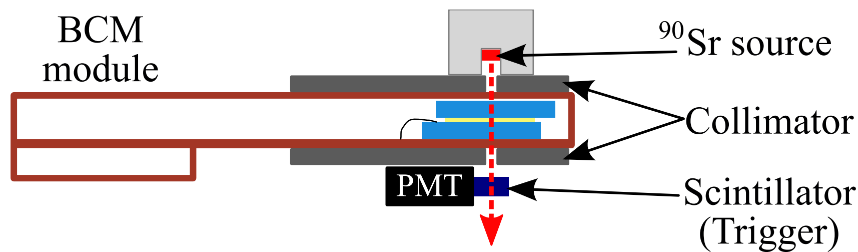

Figure 4.22: *Schematic picture of the setup used for measurements with ^{90}Sr source.*

Testing of detector modules

For the initial tests, three BCM detector modules (F401, F402, F403) were assembled with diamonds. Here, the diamond double decker configuration did not include a ceramic baseboard and inserts. Instead, golden pads were glued between the two diamonds, and the assembly was glued directly onto the high voltage line in the detector module (see figure 2.10, right). One of the modules, namely F403, had diamond samples thinned from the original 500 μm to 300 μm and therefore higher electric fields in diamond could be reached. These diamonds along with those in module F402 were metallised with Cr-Au instead of Ti-Pt-Au contacts. The former were later re-metallised with the Ti-Pt-Au contacts, before they were assembled for the installation in ATLAS.

Four voltage scans, constituting a voltage loop, were performed with each of these module. The first two scans were used to evaluate the response for positive and the last two scans for negative polarities of voltages applied to the diamonds:

- Scan m1: Voltage was changed from 0 V to +1000 V (+2V V/μm electric field) in steps of 200 V. 200 MHz BWL was applied at the readout oscilloscope during the scan.
- Scan m2: The scan started at the final voltage of m1 scan and was continued in steps of -200 V back to 0 V. Here, 1 GHz BWL was applied on the oscilloscope during the scan.
- Scan m3: Starting from 0 V, the voltage was decreased in steps of -200 V down to -1000 V. The bandwidth was limited to 200 MHz at the readout.
- Scan m4: In the last scan 1 GHz BWL was used at the readout and the voltage was changed from the end point of m3 scan back to 0 V in steps of 200 V.

In each step 3000 events were recorded with the exception of last step of m1 and m3 scans, where 15000 events acquired, with a typical trigger rate was around 5-20 Hz. Since the acquisition rate was limited by 1 s time delay between two recorded events, about 6h were needed for m2 and m4 scans and up to 9.5h to complete one m1 or m3 scan, where the last voltage step took $\sim$4.5h. For the module with thinner diamonds (F403), the voltage was changed in steps of $\pm$140 V in order to achieve comparable change in electric field.

Noise and amplitudes were extracted in the same way as described in section 4.2.1. The noise sampling point together with intervals for signal extraction and baseline correction are indicated in figure 4.23, where a typical recorded event for the two different bandwidths applied is shown.

Figure 4.24(a) shows amplitudes and their most probable values as a function of time in one of the m1 voltage scans, during which the bias voltage was increasing. A slight decrease of signal amplitude with time after each voltage change can be observed, which is due to polarisation effect causing an internal electric field that counteracts the external bias. This effect stabilises in a certain time after the voltage has been changed, where for every voltage change a different stabilisation period appears. Similarly, for voltage scans during which the bias voltage is decreasing, a depolarisation effect can be observed, where signal amplitude is increasing with time after the voltage change (see figure 4.24(b)). Polarisation and depolarisation effects

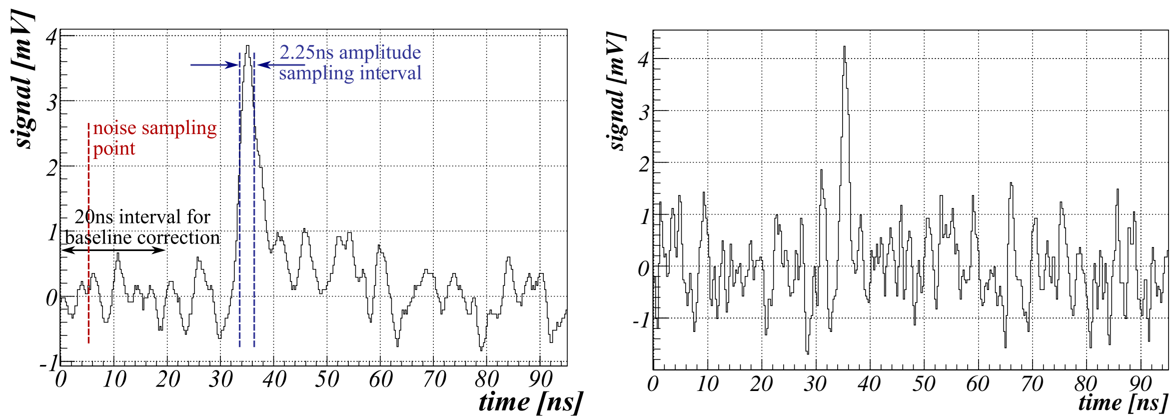

Figure 4.23: *Typical MIP signal recorded by LeCroy LC564A oscilloscope with 200 MHz (left) or 1 GHz (right) bandwidth applied on it during measurements with ^{90}Sr source.*

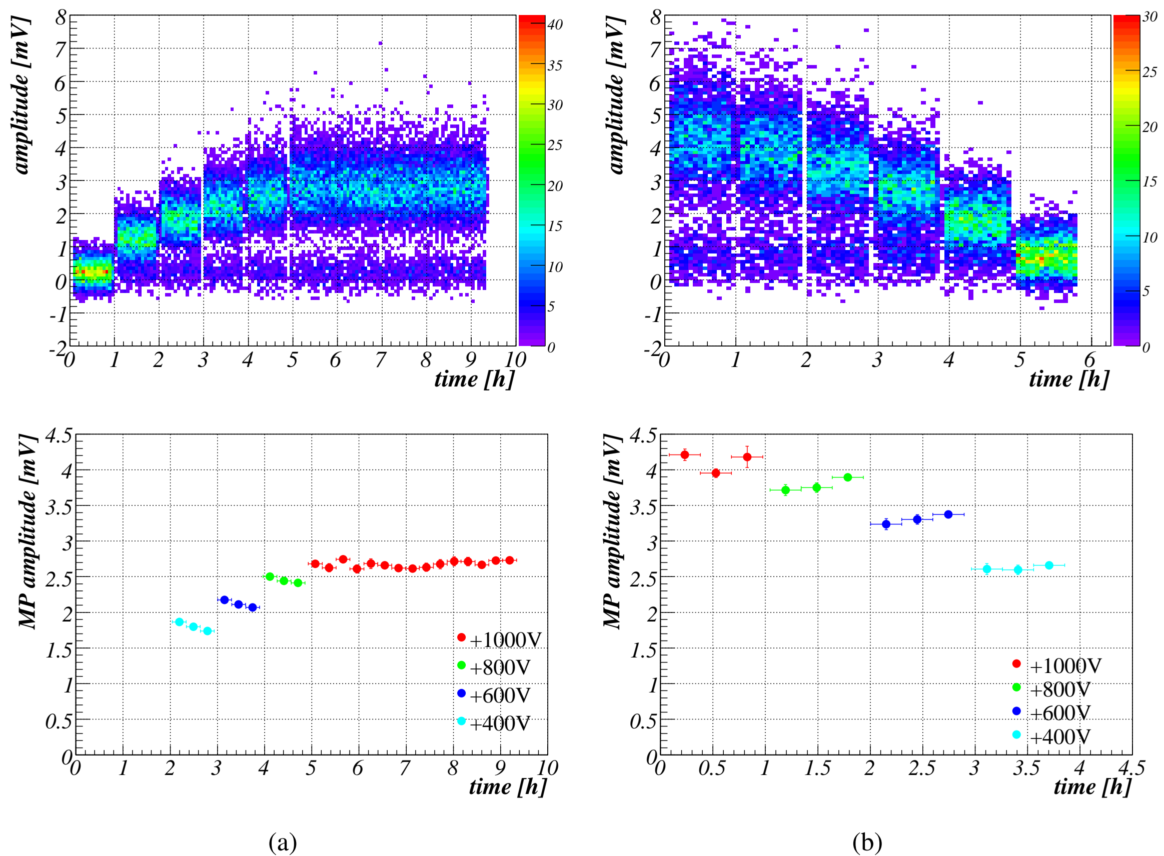

Figure 4.24: *Amplitude and amplitude MP value versus time during the m1 (a) and m2 (b) voltage scan with module F402. Each point in MP amplitude time curves was extracted from a 17 min time interval, which corresponds to ∼1000 recorded events.*

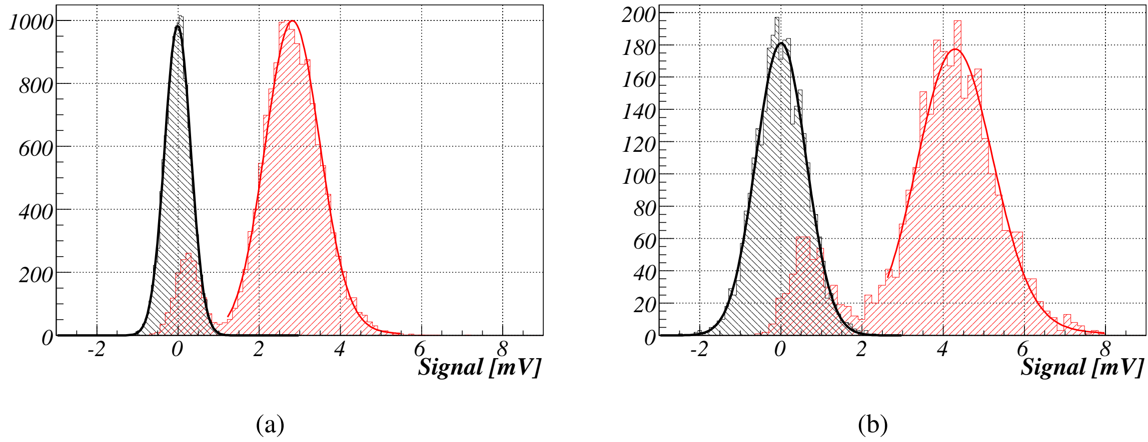

(a) (b)

Figure 4.25: *Noise (black) and amplitude (red) distribution for module F402, obtained from scan m1 (a) with a 200 MHz BWL and scan m2 with a 1 GHz (b) at a bias voltage of 1000 V.*

depend on the applied bias voltage. At ± 2 V/μm electric field no significant change in signal amplitude has been observed in our scans, while the effect of polarisation and depolarisation is visible for lower electric fields. This implies that a 300 s delay of data recording after the voltage change was enough to stabilise the effect in case of 2 V/μm, while being too short for lower electric fields[3]. When estimating the MP amplitude at certain electric field, all events recorded at that field were included. Therefore, the difference between estimated MP amplitude and its stable value is larger for lower electric fields. Typical amplitude and noise distributions obtained at 2 V/μm are shown in figure 4.25.

Noise RMS σ_n and SNR values as a function of applied electric field, extracted from the scans, are shown in figure 4.26. Their values at 2 V/μm electric field are reported in table 4.5. As already observed from the test beam measurements with prototype detector modules, these measurements again support that limiting the bandwidth to 200 MHz improves the SNR. The BCM MP amplitude is decreased by less than 35%, while noise σ_n is decreased by almost 50%, resulting in SNR increase by a factor $\sim$1.3. This was also confirmed in the off-line analysis of waveforms recorded at full bandwidth. Here it was shown that the optimum SNR is reached when a first order low pass filter with the pole at 200–400 MHz is applied (figure 4.27).

No significant difference in noise σ_n can be observed between modules with thick and the module with thin diamonds. Furthermore, noise σ_n can be found to be independent on electric field for fields as high as 3 V/μm. Although thinning the diamonds does not affect the noise, the performance with thin diamonds is measured to be inferior compared to those with the thick ones even at higher electric fields. With thin diamonds saturation of signal amplitude due to saturation of charge carrier drift velocity can be observed at higher electric fields. The fact that, at a given electric field, lower signal amplitudes are observed with thinner diamonds, implies that our amplifier does not operate as an ideal current sensitive amplifier.

[3]Shorter stabilisation time at 2 V/μm suggests that this electric field strength is close to the saturation field, where the drift velocity of charge carriers saturates.

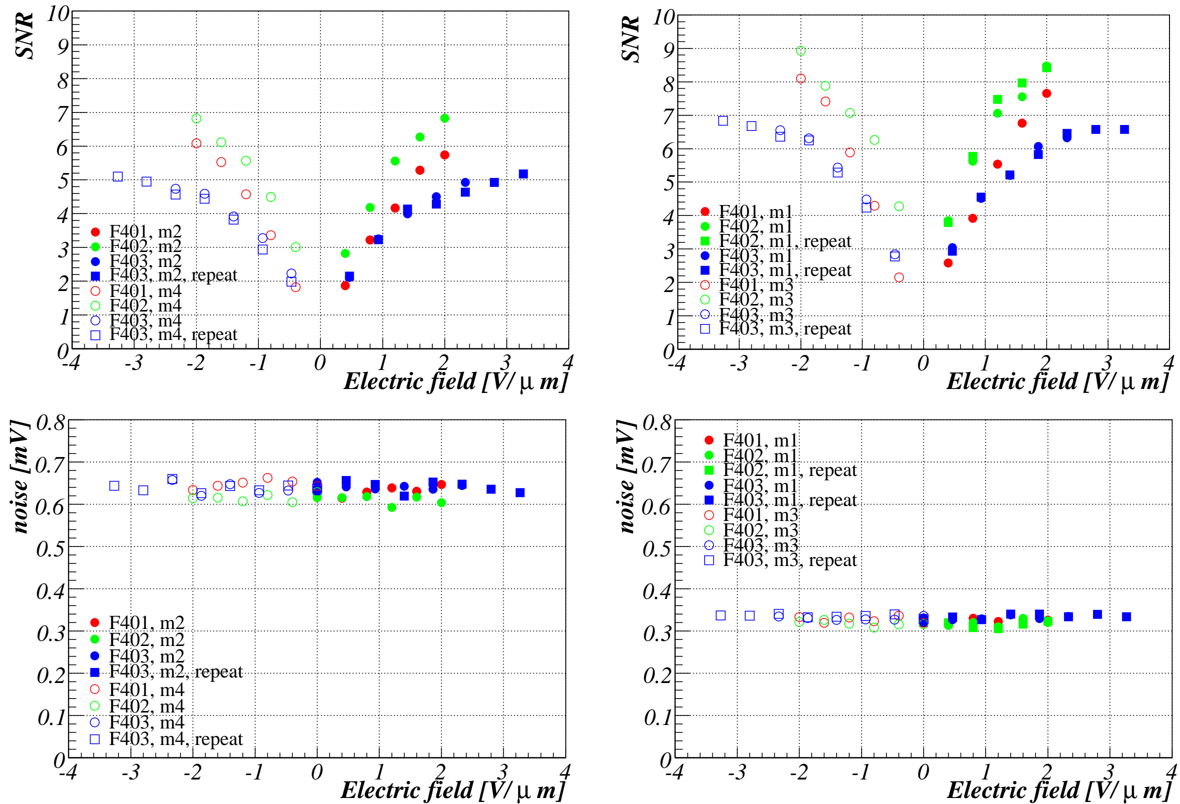

Figure 4.26: *Noise σ_n and SNR obtained for modules, assembled without ceramics. Results were extracted from the ^{90}Sr voltage scans with 1 GHz (left) or 200 MHz (right) applied on the oscilloscope.*

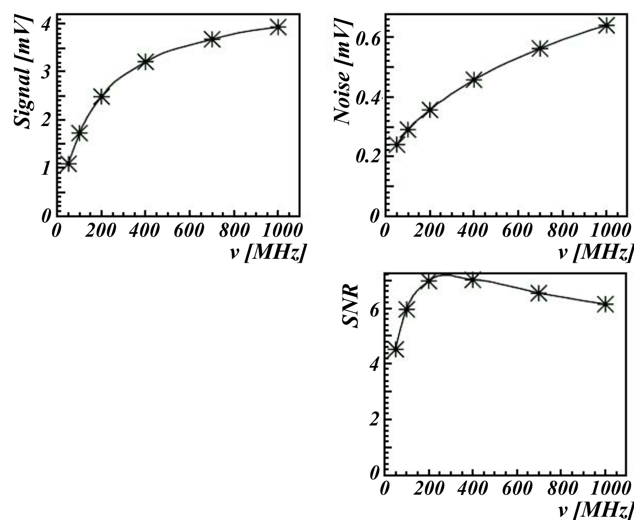

Figure 4.27: *Signal, noise and SNR as a function of cut-off frequency of a first order low pass filter, when applied to the BCM module waveforms recorded at full bandwidth.*

Module		**F401**	**F402**	**F403**
Diamond samples	top	CDS-163	A230-10w	A230-7 (300 μm)
	bottom	46TO-4	A230-8w	A230-5 (300 μm)
Scan m1 at +2 V/μm and 200 MHz BWL	MP [mV]	2.49±0.01	2.71±0.05, 2.72±0.01	2.12±0.01 2.16±0.03
	noise [mV]	0.326±0.002	0.320±0.002, 0.323±0.002	0.335±0.002 0.334±0.005
	SNR	7.6	8.5 8.4	6.3 6.5
	Current [nA]	∼450	∼130, ∼60	∼1500 ∼250
Scan m2 at +2 V/μm and 1 GHz BWL	MP [mV]	3.71±0.03	4.12±0.04	3.18±0.04 3.04±0.05
	noise [mV]	0.65±0.01	0.604±0.009	0.644±0.009 0.647±0.009
	SNR	5.7	6.8	4.9 4.7
	Current [nA]	∼650	∼150	∼1800 ∼1500
Scan m3 at -2 V/μm and 200 MHz BWL	MP [mV]	2.70±0.01	2.88±0.01	2.19±0.01 2.16±0.02
	noise [mV]	0.333±0.002	0.321±0.002	0.334±0.002 0.340±0.005
	SNR	8.1	9.0	6.6 6.4
	Current [nA]	∼250	∼200	∼1100 ∼550
Scan m4 at -2 V/μm and 1 GHz BWL	MP [mV]	3.86±0.05	4.2±0.1	3.12±0.04 3.02±0.04
	noise [mV]	0.634±0.009	0.614±0.009	0.657±0.09 0.66±0.01
	SNR	6.1	5.8	4.7 4.6
	Current [nA]	∼270	∼150	∼1500 ∼1600

Table 4.5: *Table of MP amplitudes, noise σ_n, SNR and leakage currents of BCM detector modules measured at ±2 V/μm (±700 V for F403 with thinned diamonds or ±1000 V for other two modules) during the voltage scans. The currents stated here were measured at the end of the voltage step, thus about 1h and around 4.5h after 2 V/μm field was applied in m1, m3 and m2, m4 voltage scans. Errors on MP amplitude and noise σ_n were the values returned by the fitting procedure.*

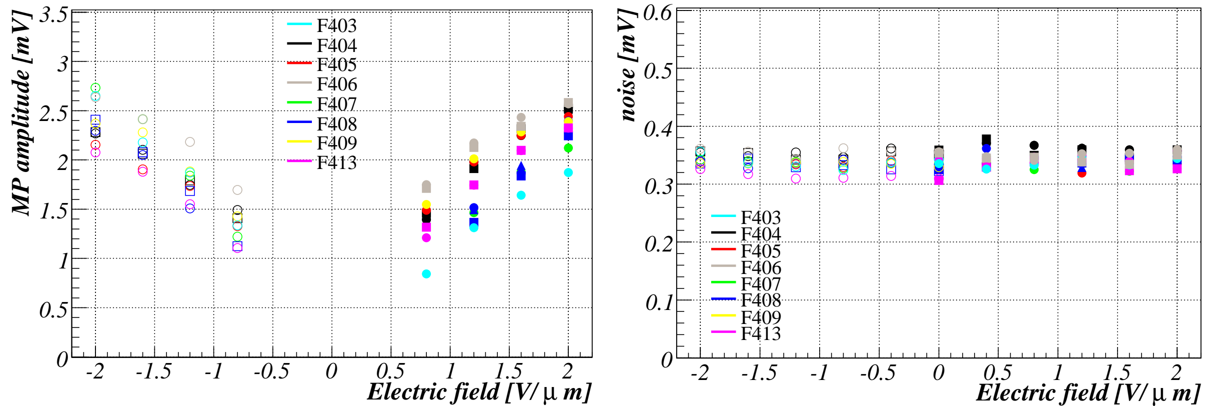

Figure 4.28: *Noise σ_n (right) and MP amplitudes obtained with m1 (closed markers) and m3 (open markers) voltage scans. Different colours distinguish between modules. Some of the scans were repeated and are labelled by different markers.*

Before the test beam at CERN in 2006, eight detector modules were assembled with ceramic diamond assemblies in the configuration envisaged for the final BCM modules, apart from the golden pad, providing bias voltage to the top diamond redundantly[4]. Since by then it was decided that a filter with 200 MHz BWL will be used before further processing of the signal in ATLAS, only voltage scans with 200 MHz BWL applied at the readout (m1 and m3 scans) were performed with these modules, where the last step, at $\pm$1000 V, was extended to 9h, with 30000 recorded events. Noise σ_n and MP amplitude as a function of applied electric field during these scans are presented in figure 4.28 and the noise σ_n, MP amplitudes and currents extracted at $\pm$1000 V are summarised in table 4.6.

Most of the modules show asymmetry for the two bias polarities in terms of extracted MP amplitudes. Furthermore, one can observe that lower leakage currents are measured for the polarities that give better response (higher MP amplitude). If only better polarities are considered, then a typical leakage current of few tens of nA is measured with modules at 2 V/μm electric field, while a MP amplitude of 2.4 mV is typically achieved. With an average noise σ_n of $\sim$0.34 mV this gives a typical SNR of $\sim$7, which translates to a SNR of $\sim$10 for the 45° particle incidence. Module to module variations in MP amplitude are found to be below 15% from the average 2.4 mV.

Some of the scans were repeated and good reproducibility of results can be observed, with variations in MP amplitude up to 5% from the average value at a given voltage, which is less than module to module variations as can be seen in figure 4.28.

Long term behaviour of the MP amplitudes and leakage current from BCM module were investigated for two of the modules, F402 and F406. Here, m1 voltage scan was performed where the step at 1000 V was monitored for several days. Figure 4.29 shows the MP amplitude and current as a function of time measured at 1000 V observed in these long term tests. The MP amplitudes are observed to be quite stable, with variations smaller than $\pm$3% and no

[4]This golden pad was only used in the modules that underwent the qualification tests described in the following section 4.3.2.

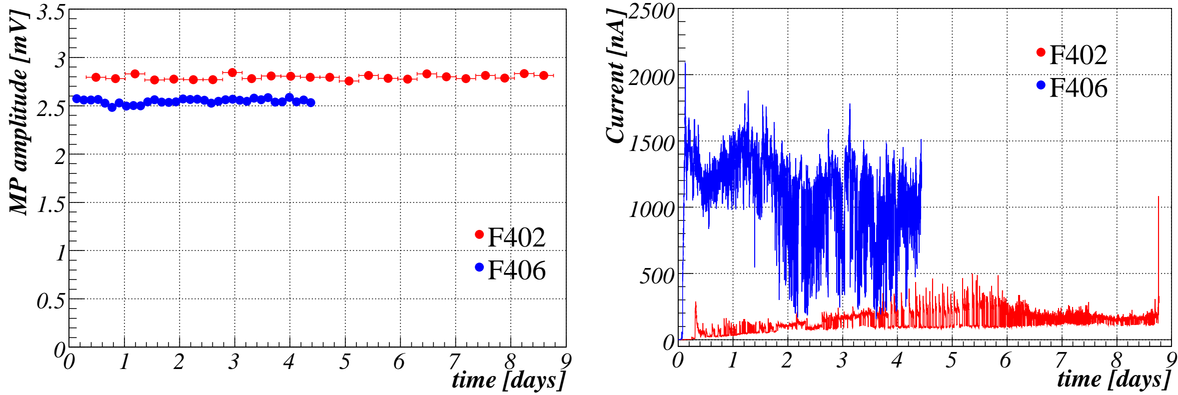

Figure 4.29: Long term behaviour of MP amplitude (left) and leakage current (right) measured at 2 V/μm bias electric field for module F402 (red) and F406 (blue). MP amplitudes were extracted in time slices of 8.5h (∼6500 events) for module F402 and 3h (∼9000 events) for module F406.

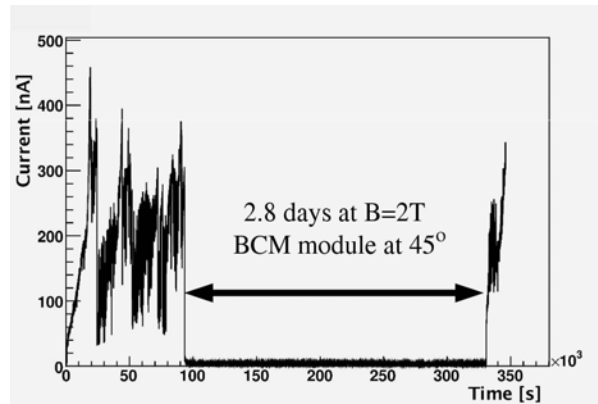

Figure 4.30: Leakage current of BCM detector module F408 at 1000 V. After one day the module was placed in magnetic field of 2 T for 2.8 days.

perceivable drop during the time of testing. On the other hand, the leakage current shows a peculiar behaviour, rising by a factor of 100 or more from its initial value to several hundreds of nA or more on a time scale of days. In addition, it shows an erratic behaviour on a time scale of minutes, jumping up and down by a factor of 10 or more. This phenomenon is not yet understood and it has been observed before in the BaBar experiment at lower electric field of 1 V/μ [E$^+$05]. However, as at Babar, we have also observed this excess currents to vanish, if the diamond is placed in magnetic field of adequate strength and direction. Applying a strong magnetic field of 2 T, as will be in the ATLAS Inner Detector, in a realistic geometry with BCM module inclined by 45°, reduced the current well below 10 nA for a time period of nearly three days (figure 4.30).

Furthermore, noise was observed to be independent of current up to 0.5 μA, as shown in figure 4.31. Here, noise is estimated as the RMS of baseline fluctuations, found in the event waveforms, recorded at the time of leakage current measurement. Since it was also observed

that noise does not depend on bias voltage for fields up to as 3 V/μm, one can conclude that the major contribution to the noise comes from the amplifiers used in the front end electronics.

Module, ceramic assembly	Scan m1, at 1000 V				Scan m3, at -1000 V			
	MPA [mV]	Noise [mV]	SNR	Current [nA]	MPA [mV]	Noise [mV]	SNR	Current [nA]
F403 C11	1.87	0.344	5.4	~750	2.65	0.356	7.4	~350
F404 C9	2.53 2.52 2.51	0.357 0.359 0.354	7.1 7.0 7.1	~300 ~250 ~100	2.27 2.28	0.355 0.357	6.4 6.4	~1100 ~570
F405 C6	2.44	0.347	7.0	~80	2.15	0.339	6.3	~300
F406 C3	2.57 2.58	0.360 0.350	7.1 7.4	~50 ~60	2.64	0.361		~40
F407 C2	2.12	0.341	6.2	~1100	2.73	0.343	8.0	~15
F408 C1	2.40 2.24 2.32	0.347 0.342 0.334	6.9 6.5 6.9	~50 ~30 ~35	2.30 2.41	0.339 0.336	6.8 7.2	~17 ~21
F409 C7	2.39	0.344	6.9	~65	2.37	0.336	7.1	~350
F413 C10	2.32 2.33	0.356 0.327	6.5 7.1	~550 ~30	2.08	0.323	6.4	~450

Table 4.6: *Noise σ_n, MP amplitudes (MPA) and leakage currents extracted from the ±1000 V step of m1 and m3 voltage scans for detector modules equipped with diamond ceramic assemblies. The fit errors, were below 0.01 mV for MP amplitudes and of the order of 0.001 mV for noise σ_n. Currents stated in the table are the values measured near the end of the ±1000 V voltage step. The diamonds and their orientation used in each ceramic assembly can be found in table B.2 of appendix B.*

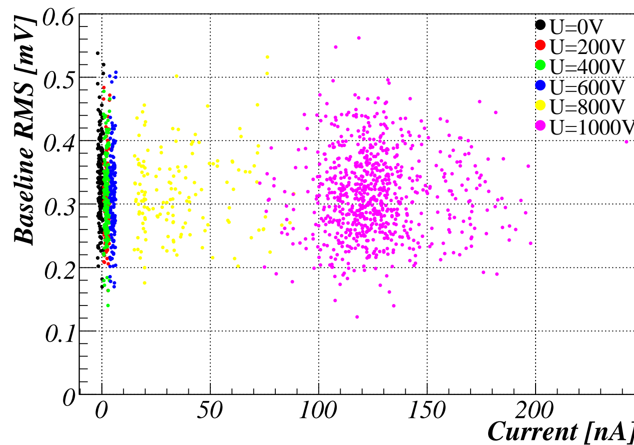

Figure 4.31: *The RMS of baseline fluctuations, extracted for the recorded waveforms, as a function of BCM module current, measured during m1 voltage scan with module F402.*

Quality assurance of final modules

In the late fall of 2007 final modules were assembled and qualification tests were performed in order to select the eight most reliable for installation. Before assembling, all modules were cleaned with a Vigon EFM solution to remove remanents of solder flux and organic pollutants. Afterwards, the modules were subjected to a thermo-mechanical test. Accelerated aging was performed with one of the modules. Its temperature was increased to 140°C for 14 hours. This simulates more than 10 years of operation at 20°, assuming an activation energy of 0.8 eV, characteristic of the epoxy and solder used to assemble the module. Other modules were kept at 80°C for 12 hours to perform an infant mortality test in the readout electronics. Modules could experience similar temperature when the beam-pipe is baked out. A series of thermal cycles was performed afterwards to generate stresses due to the mismatch of thermal expansion coefficients between components in the detector module. Each module experienced ten temperature cycles with zero humidity and temperature ranging from -25^oC to 40°C. Both end points of this range are more extreme than expected under normal ATLAS operation, apart from beam pipe bake out periods. During each step of these thermo-mechanical treatments, all modules were characterised in ^{90}Sr setup to measure their SNR. Comparison of these results with the results measured before the thermo-mechanical treatments shows no significant change in SNR. Thus no module failed during these acceptance tests.

As shown before, the diamond sensors exhibit asymmetry in leakage current and signal amplitude, depending on the polarity. This is understood to be due to the polycrystalline nature of pCVD diamonds. When assembling a BCM detector module, the diamonds were paired up such that their preferred polarities agreed. Half of the modules were build to prefer a positive voltage, while the others prefer a negative voltage configuration. The results of measurements with our ^{90}Sr setup, for all the final modules that underwent the thermo-mechanical treatments, are summarised in table 4.7. Due to the lack of time only the step at $\pm$1000 V was carried out, thus skipping the initial slow ramping up for most of the modules. The first eight modules in table 4.7 were selected for installation in ATLAS.

Noise measurements were repeated after installation of modules on the Beam Pipe Support Structure, where the ATLAS Pixel detector readout system was partially installed, in order to check for noise interference between the two systems. Two of the BCM modules were studied. One (F420) was positioned directly below the part of the Pixel detector readout system that was installed at that time, while the second BCM module (F408) was the furthest away from the Pixel modules. Three noise measurements were performed. For the first, a random trigger was used and whole Pixel detector readout, present at the time, was active. For the other two measurements, the trigger signal was provided by the 40 MHz clock from the Pixel timing module (TIM) simulating the LHC bunch crossing clock for the Pixel detector readout. For one of those two measurements whole available Pixel detector readout was active , while for the other one, only one Pixel detector readout unit was enabled. The noise σ_n of the BCM modules was computed in the same way as with the other measurements described in this thesis. Considering the noise σ_n of the two BCM modules under test, no difference was observed in these tests (random trigger and full Pixel readout, synchronised trigger with full Pixel readout, synchronised trigger with on Pixel detector module active). The observed noise σ_n was slightly lower (by 12%) for

Module, ceramic assembly	at +1000 V				at -1000 V				Pol.
	MPA [mV]	Noise [mV]	SNR	Curr. [nA]	MPA [mV]	Noise [mV]	SNR	Curr. [nA]	
F410 C14	2.74 2.34	0.351 0.332	7.8 7.0	25 20	1.88	0.335	5.6	200	+
F413 C11	2.16	0.307	7.0	250	1.96	0.300	6.5	150	+
F420 C11	2.08	0.342	6.1	350	2.66	0.337	7.9	200	-
F422 C3	2.36	0.325	7.3	45	2.40	0.323	7.4	40	-
F404 C9	2.43	0.369	6.6	70	2.10	0.373	5.6	500	+
F405 C6	2.26	0.327	6.9	35	1.93	0.325	5.9	150	+
F408 C1	2.21	0.329	6.7	55	2.30	0.329	7.0	20	-
F424 C2	2.08	0.327	6.4	700	2.66	0.324	8.2	10	-
F409 C7	1.78	0.307	5.8	100	1.74	0.312	5.6	300	
F401 C7	3.03 2.26	0.449 0.356	6.7 6.3	70 45	2.01	0.355	5.7	550	
F406 C15	2.44 2.44	0.349 0.338	7.0 7.2	35 9	2.21 2.20	0.348 0.341	6.4	150 90	
F409 C16	1.47 1.53	0.319 0.306	4.6 5.0	350 320	1.83 1.45	0.309 0.316	5.9 4.6	1000 1000	

Table 4.7: *MP amplitude, noise σ_n, SNR and leakage current at $\pm$1000 V for the final modules, measured with ^{90}Sr setup. The current stated is the value observed at the end of the measurement. The first eight modules were chosen for installation in ATLAS experiment. The last column gives their preferred polarity.*

both modules compared to the values obtained in the qualification measurements presented in table 4.7. This is thought to be due to the fact that the cables used in these measurements were much longer than the ones used in ^{90}Sr setup. However, the relative difference in noise σ_n between the two modules was the same in the three noise measurements performed.

4.3 Digitisation with NINO

4.3.1 Test beam measurements

In 2007, test beam measurements with spare final detector modules were performed at the CERN SPS high energy pion beam line (H6) with a beam momentum of 120 GeV/c, providing MIP signals. In these tests, the final version of most of the elements of the back and front-end of the BCM system were used, namely signal and power cable connections from detector modules, low and high voltage power supplies for modules, LVDS to optical converters present on the NINO boards and optical receivers. All modules were operated at +1000 V.

A telescope consisting of four crossed finger scintillators was used. Two of them were placed upstream and two downstream of the BCM detector modules under test (figure 4.32). Their cross section covered an area of about $2{\times}2\,\text{mm}^2$. The readout was triggered by the coincidences of all four scintillators. Detector modules were placed on movable x and y stages which were remotely controlled via GPIB interface by a software written in LabView [Lab] and running on a PC.

The readout scheme was identical to the one used during the test beam measurements (section 4.2.3). The analogue signals from detector modules were first amplified by an ORTEC

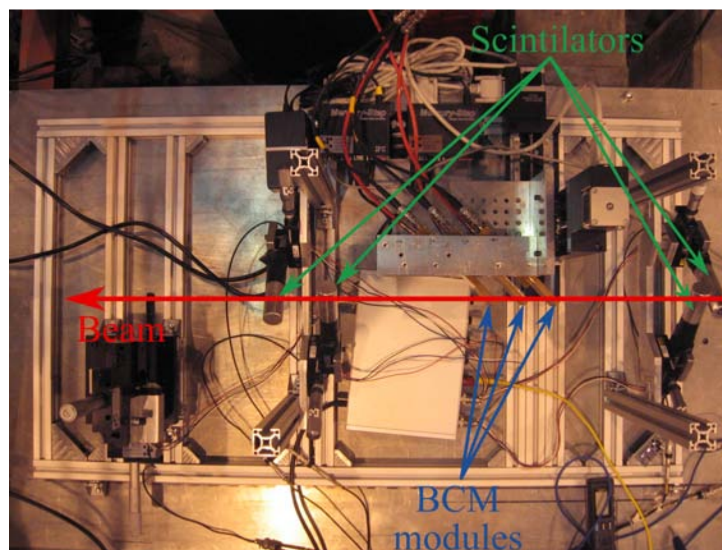

Figure 4.32: *Picture of the setup used for test the beam measurements at the CERN SPS in 2007 with four thin scintillators used for triggering.*

FTA810 fast timing amplifier and the resulting waveforms were recorded with a CAEN sampling ADC. Digital signals were obtained by feeding the signal from the detector module directly into the NINO electronics board. The output signal from NINO board was lead through optical fibres to the optical receiver board where signal waveforms from the NIM monitor output were recorded by the ADC for later analysis.

Three different versions of NINO prototype boards were studied.

- NINO3: This is the NINO board with a circuit as presented in figure D.2 in appendix D. The resistance R_{nn} was fixed to 50 Ω.
- NINO2: Here the resistor in front of the 200 MHz filter (R_{11}) was removed.
- NINO1: NINO2 with removed 200 MHz filter.

The modifications made with NINO2 and NINO1 boards were performed in order to increase the analogue input signal fed into the NINO chip. All three NINO boards had potentiometers for changing the stretch and hysteresis control as well as the discriminator threshold of the NINO chip. The hysteresis control adjusts the difference between the discriminator levels for the rising and falling part of the signal. For more stable operation of the chip, a larger value of this parameter is desirable. Therefore, all three boards had the hysteresis potentiometer set to its maximal position (1.5 V voltage drop over potentiometer), setting the the difference in discriminator levels to maximal value available. Stretch control adjusts the range of NINO output signal widths. By changing the stretch voltage, lower and upper limit of the width range are changed while their difference remains unchanged. Smaller signal widths are preferable for operation in ATLAS. Thus, the width of output signals was set to the minimal value possible on all three prototype boards, corresponding to maximal voltage drop of 1.5 V over the potentiometer.

Each NINO electronics board had two input channels allowing two detector modules to be simultaneously connected to it. On the board both channels were split into high and low input to NINO chip as envisaged for the final BCM system. In the tests described here only the channel with higher signal input signals were considered.

In order to reveal the position of the diamonds, a scan over diamond surface was performed, by moving all the BCM detector modules simultaneously across beam spot in steps of 1 mm while the four trigger scintillators were kept still and aligned with the beam. In the offline analysis, the fraction of events having amplitudes of analogue signal above certain signal threshold was computed for each step. These efficiency plots are shown in figure 4.33 for one of the modules and different signal threshold cuts. The thresholds indicated on each plot are given in units of MP amplitude, which was extracted from the central diamond region. Amplitudes were extracted from a 2.5 ns time window as described in section 4.2.1 and no baseline correction was performed due to the reasons stated in section 4.2.3. The efficiency plots presented here, show more uniform response across the diamond active surface compared to the plots obtained from the 2006 test beam (section 4.2.3). This is due to the fact that here the signal amplitudes were sampled in ten times larger area (2×2 mm^2 active area of scintillators), thus averaging out the non-uniformity of sensor response arising from the grain structure of the diamonds.

The NINO discriminator threshold was varied from run to run to evaluate its effect on the

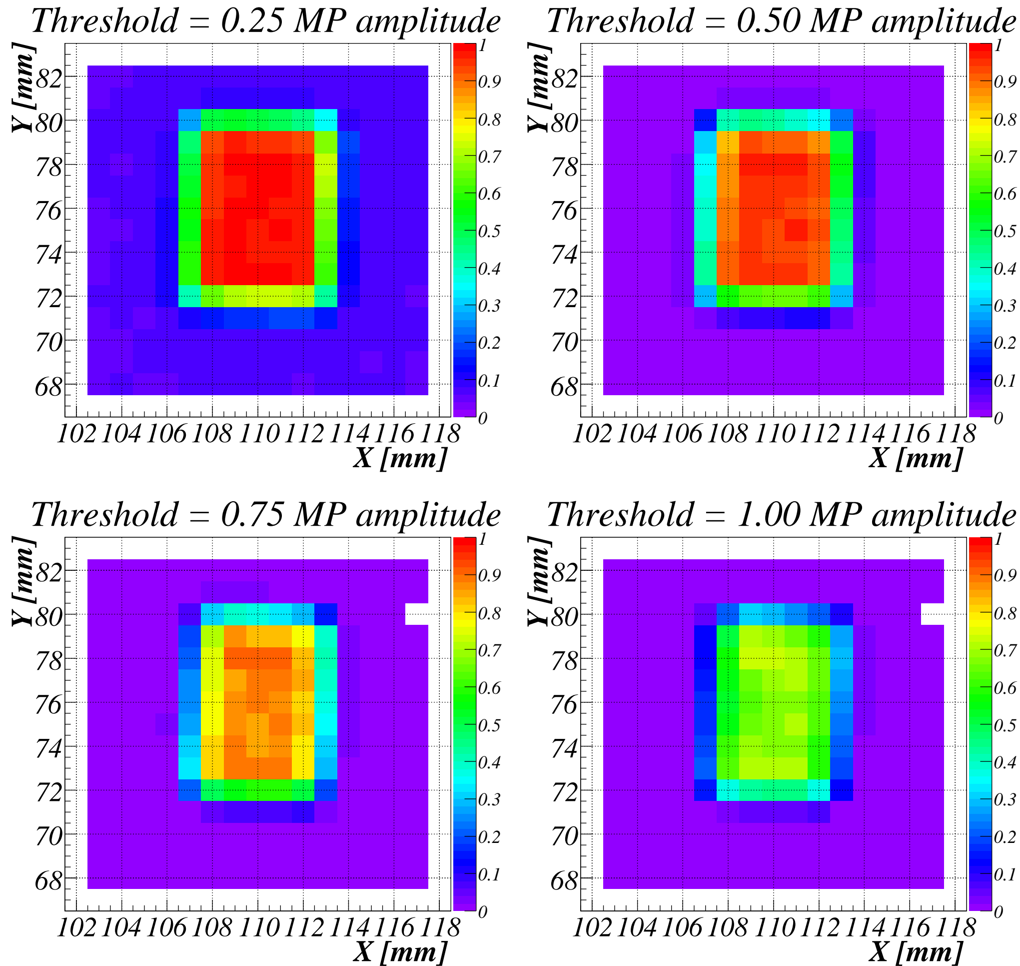

Figure 4.33: *Analogue efficiency as a function of position on the diamond for module F406 calculated as the fraction of analogue signals above a given threshold found in 2×2 mm^2 area (defined by trigger scintillators) at each point. The threshold levels indicated on each plot are given in units of MP amplitude extracted from the central region of the sensor's active surface.*

probability that a pion traversing the diamond sensors produces a signal in the NINO output channel. During these scans, the trigger scintillators were aligned at the centre of the diamonds' active surface (x=110 mm, y=76 mm, see figure 4.33). In the off-line analysis, the signal pulse from NINO was searched in 20 ns time interval, centred around the pulse found in the average NINO waveform. Efficiency at given NINO discriminator thresholds was estimated as the fraction of events with a NINO signal present in this 20 ns time interval. Measured efficiency curves are shown in figure 4.34 for all different configurations of NINO boards and detector modules connected. For most of configurations, threshold scan was repeated at least once. An estimate of thresholds with median efficiency (50% efficiency) can be made from these curves. These results are summarised in table 4.8 where the mean value (averaged over repeated scans) for each configuration is given.

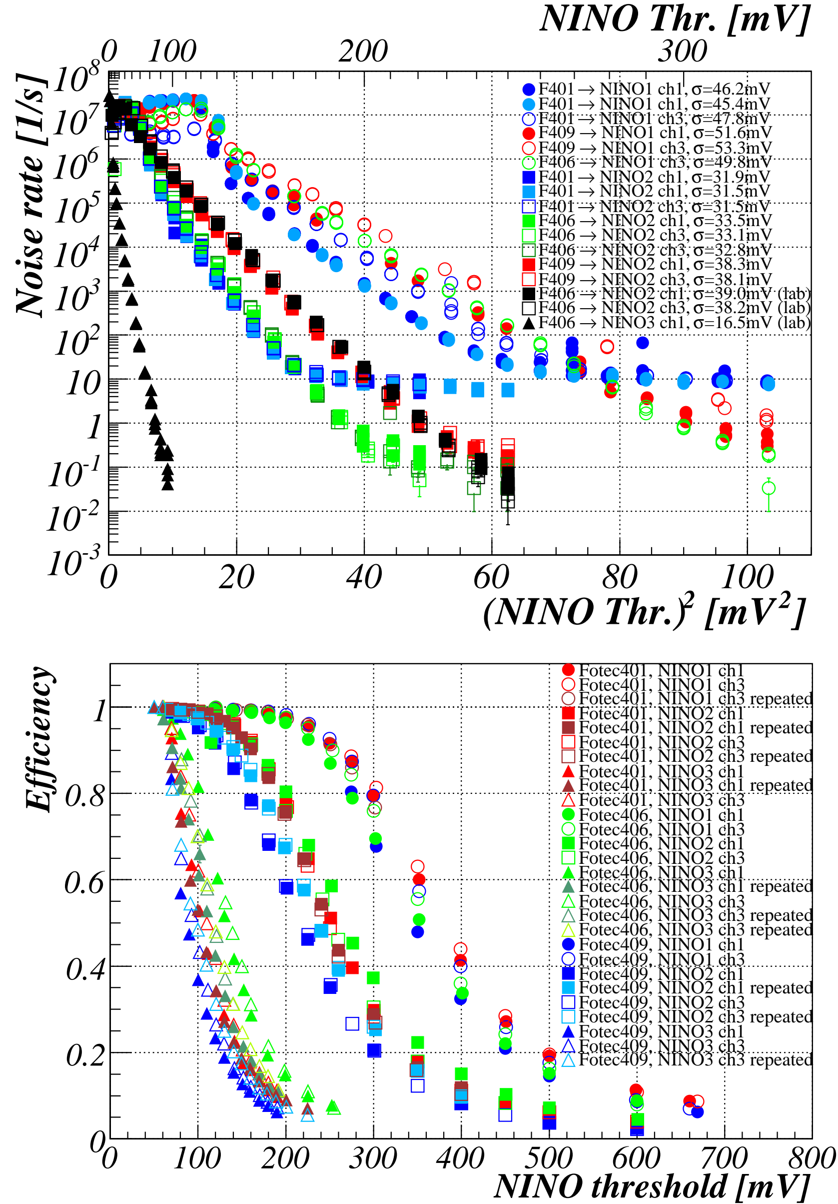

Figure 4.34: *NINO signal efficiency (bottom) and noise rate (up) as function of the NINO discriminator threshold measured with different combinations of spare detector modules and prototype NINO boards in test beam at the CERN SPS in 2007. Colours distinguish between different detector modules and different marker types label different NINO prototype boards. Closed markers refer to configurations when module was connected to the first input channel of the NINO board while open markers refer to the second input channel. The noise rate measurements with the module F406 carried out in a laboratory setup are shown on the left plot as well (black markers).*

Det. Module		F401	F406	F409
Median Threshold [mV]	**NINO1**	380±3	359±5	358±13
	NINO2	249±3	260±8	228±9
	NINO3	106±3	124±9	93±4
Noise [mV]	**NINO1**	46±1	50	52.5±0.8
	NINO2	31.6±0.2	33.1±0.3 38.6±0.4 (lab)	38.2±0.1
	NINO3		16.5 (lab) 14.1 (scaled)	
Median SNR	**NINO1**	8.3	7.2	6.8
	NINO2	7.9	7.9	6.0
	NINO3		8.8 (scaled)	

Table 4.8: *Summary of NINO discriminator threshold at median efficiency estimated from NINO efficiency curves for1 MIP and noise RMS extracted from the fit to measured noise rates in the test beam at CERN SPS in 2007. The values correspond to mean values and their RMS obtained by averaging over the repeated measurements if available. Otherwise a value without an error extracted from a single measurement is listed. Median SNRs, calculated with these values, are listed in the last row. The error on those values is up to 0.5. Noise values estimated with laboratory setup are labelled with "(lab)" and numbers estimated by scaling the noise values obtained in the laboratory to the test beam environment are marker withs "(scaled)".*

During short shutdown when particle beam was absent, the rate of accidental noise hits (noise rate) was measured at the output of the NINO board as a function of the NINO threshold, for each board with different modules connected to them. The result is presented in figure 4.34 as noise rate in logarithmic scale against the square of NINO threshold applied. According to [Ric49], the noise rate N_{NR} in a threshold discriminator readout exhibits the following dependence on threshold U_{Thr}

$$\ln(N_{NR}) \propto \left[-\frac{U_{Thr}^2}{2\sigma^2}\right] \tag{4.3}$$

Here the proportionality factor depends only on upper and lower cut-off frequency of the system. The relation is valid if the noise follows the Gaussian distribution with a width σ. Thus, straight lines in figure 4.34 (right plot) indicate that noise in our system has a Gaussian shape. The noise RMS σ for each configuration of NINO board and detector module were extracted by fitting the function 4.3 to the linear part of measured noise rate versus square of NINO threshold. Using these values, together with the values of threshold at median efficiency, gives a measure for SNR of overall system including both the analogue performance of detector modules and the digital performance of NINO board. These median SNR values, extracted for different configurations, are given in table 4.8 together with corresponding noise RMS σ.

Noise rates in the test beam environment with each spare module were measured only for the NINO1 and NINO2 boards. For the NINO3 with module F406 connected to it, noise rate was measured in the laboratory with shorter signal cable, thus, with lower attenuation compared to the test beam setup, where the final signal cables were used. To estimate the noise value σ in the test beam environment for the NINO3 with module F406, the noise, measured

in a laboratory, was scaled with the appropriate factor. This factor (33.1/38.6) was obtained by comparing the noise measured in the laboratory and test beam with module F406 connected to NINO2 board. The estimated noise value is stated in the table 4.8 together with the median SNR extracted from it.

Comparing the results obtained with module F406, the best performance in terms of SNR is achieved with the NINO3 board. Furthermore, after-pulses were typically observed in the NINO1 and NINO2 waveforms even at higher thresholds due to inadequate termination of signal line at the NINO chip input causing reflection. Thus, it was decided to use the NINO3 version in the final BCM system. In order to increase the input signal into the NINO chip and make the system more manageable, an additional amplifier (Mini Circuit Gali-52, gain 3) was integrated on the final NINO boards.

Timing resolution of analogue signals was evaluated in the same way as described in section 4.2.2. However, in these test beam measurements the events were recorded synchronously with the trigger on all ADC channels. This gave a possibility to use two analogue waveforms (from two different modules) resulting from the same trigger signal but recorded on different ADC channels for computation of the time difference of crossing the threshold signal level in the two waveforms. In this way the contribution of trigger to the timing resolution was eliminated. The width of the Gaussian function fitted to the time difference distribution can be used to estimate the timing resolution. Assuming that the two modules under consideration exhibit the same timing resolution then the extracted Gaussian width divided by $\sqrt{2}$ gives an estimate for timing resolution of the BCM analogue signals. The data runs with trigger scintillators positioned at the central part of the sensors' active area (at x=110 mm, y=76 mm, see figure 4.33) were considered for this analysis.

An example of such a fit to a time difference distribution for analogue signals is presented in figure 4.35 together with the computed timing resolution as a function of threshold signal level (in units of MP amplitude). At low thresholds the timing resolution improves with increasing threshold due to decrease of jitter and time walk. It starts to degrade at higher thresholds on the account of increasing jitter caused by a decrease in average signal slope at the threshold level. One observes the measured timing resolution of the BCM analogue signals to be better than 400 ps for the threshold range scanned in figure 4.35.

These results can be compared to the timing resolution of NINO digital signals. Here, the time difference distributions were calculated in the same way as for analogue signals. However, the signal crossing threshold level was taken at half of the NINO digital pulse height. Same data runs as for determination of NINO efficiency curves were considered for this analysis. Figure 4.36 shows the obtained timing resolution of NINO signals as a function of NINO discriminator threshold for each of the three NINO boards under test, and an example of time difference distribution used to calculate these values. One can observe for digital signal timing resolution to be better than $\sim$800 ps in case of NINO2 and NINO3 boards for the range of scanned NINO discriminator thresholds. With NINO1 better timing resolution was achieved, since this board did not have the 200 MHz filter integrated.

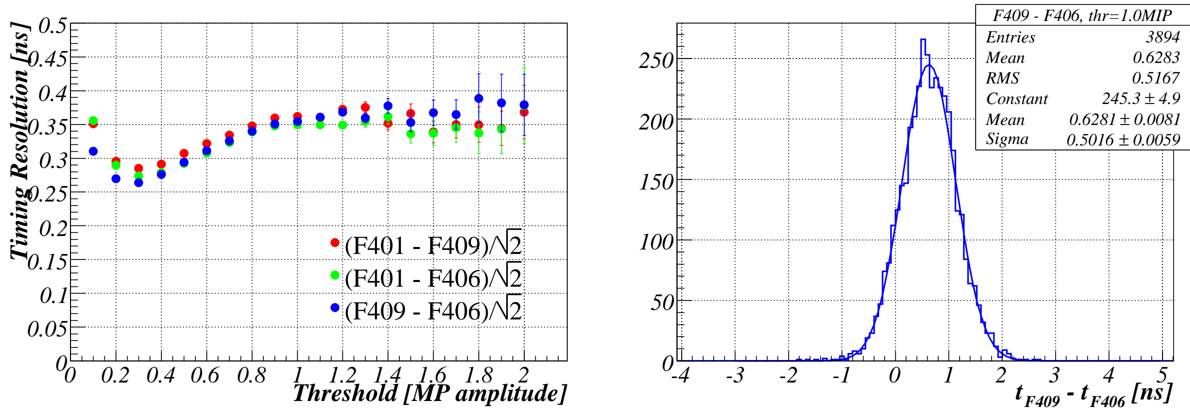

Figure 4.35: *Timing resolution of analogue signals (left) as a function of threshold level of signal crossing in units of MP amplitude. These values were extracted from the time difference distributions of analogue signals on two different ADC channels. Each curve corresponds to a different pair of detector modules (both operated at +1000 V) used in calculation. An example of the time difference distribution with Gaussian fit obtained with modules F409 and F406 at threshold of 1 MP amplitude is shown on the right.*

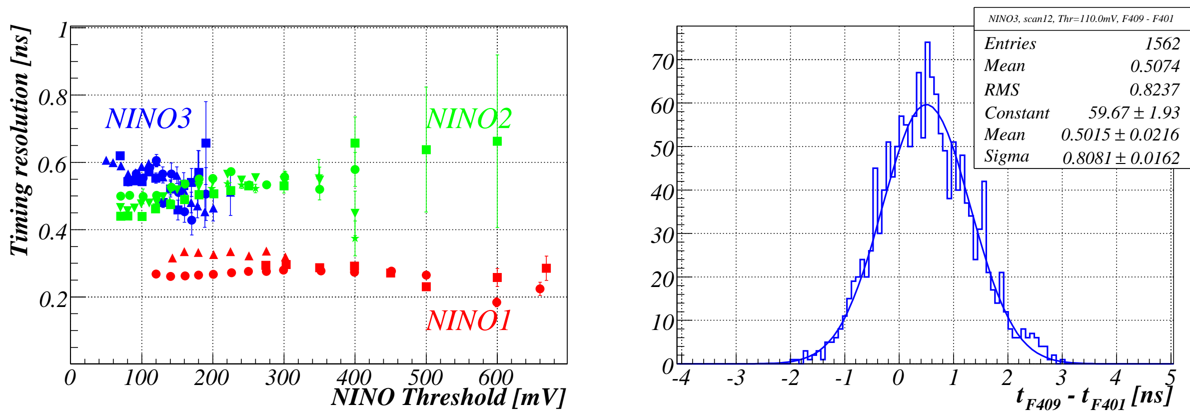

Figure 4.36: *Left: Timing resolution of NINO digital signals as a function of NINO discriminator threshold. The curves were obtained from the time difference distributions for modules F409 and F401 and three NINO boards under test. Different colours refer to different prototype NINO boards and different markers for certain colour distinguish between repeated measurements. Right: An example of time difference distribution measured with NINO3 at 110mV threshold, together with the Gaussian fit.*

4.3.2 Measurements with ^{90}Sr source

All measurements presented in this section were performed with detector module F406 operated at +1000 V. In order to estimate the performance of the final NINO boards in terms of SNR and efficiency, measurements with a spare NINO board were carried out in a laboratory setup. The setup consisted of a ^{90}Sr as a source of β particles mounted above detector module. An aluminium collimator of 2.5 mm thickness was placed between source and module, with a round opening of 2 mm diameter aligned with the source and the central region of diamond active area. Analogue signals from the detector module were first fed through a 1 m coaxial cable to the LeCroy WP950 digital oscilloscope for recording and then through additional 1 m coaxial cable to the input of the NINO board. The digital signal from the NINO board output was taken through optical fibres to the optical receiver board where the NIM monitor output signals were recorded by the oscilloscope. Analogue and NINO digital waveforms were recorded simultaneously with a sampling frequency of 8 GHz. The readout was triggered by the analogue signals, with trigger level set to about 60% of MP amplitude. The channel used for recording of the analogue signals had the input coupling set to 1 MΩ and BWL to 200 MHz. Figure 4.37 shows an example of a two-dimensional histogram containing the NINO signal waveforms recorded during one of the measurement. The histogram with detector module waveforms recorded during the same measurements is also shown.

The efficiency was calculated as the fraction of recorded events with NINO digital signal present in the 20 ns time interval around the position of the pulse found in the average NINO waveform. However the measured efficiency versus NINO threshold curve does not correspond to a 1 MIP response since the readout was triggered by the analogue signals. In order to scale this efficiency to 1 MIP response as expected in ATLAS, the same threshold scan was also performed with the NINO3 board. This board was previously tested in test beam measurements, presented in section 4.3.1, where the final services (apart from the NINO board) were used. The efficiency curves for both NINO boards, as measured with laboratory setup, are shown in figure 4.38. From this figure the median efficiency threshold of 650±10 mV and 140±5 mV can be

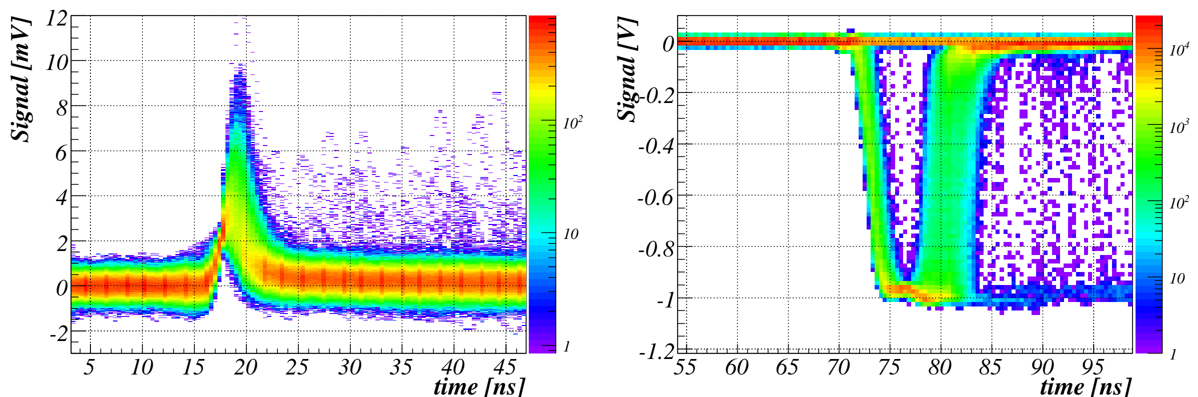

Figure 4.37: Two-dimensional histograms containing all recorded signal waveforms from the detector module F406 (left) and the spare final NINO board (right) with NINO threshold set to 608 mV.

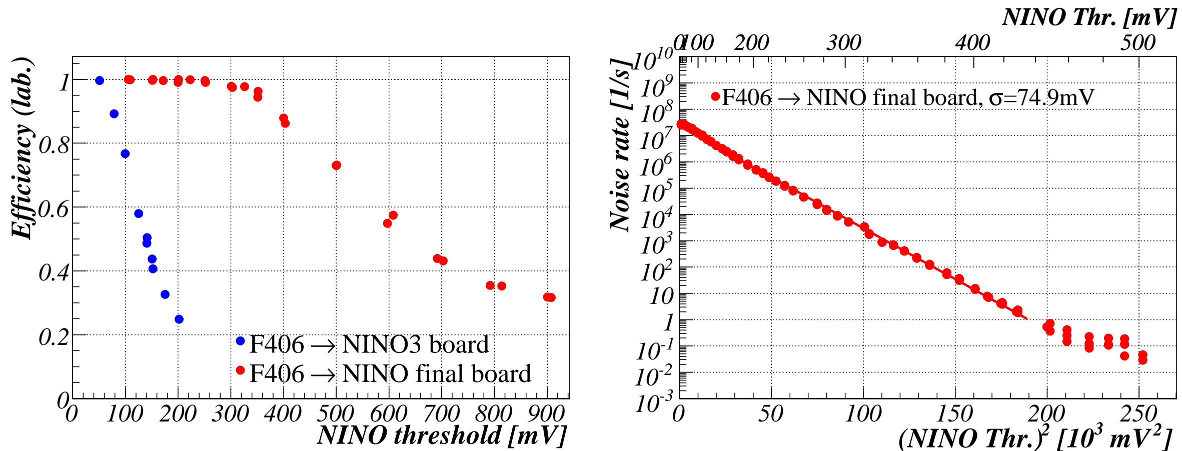

Figure 4.38: *Efficiency (left, red curve) and noise rate (right) measured with module F406 and spare final NINO board with the laboratory setup along with efficiency curve for NINO3 prototype board and module F406 measured with the same setup.*

extracted for the final and NINO3 board respectively. An estimate of 1 MIP efficiency curve for the final NINO board as expected in ATLAS can then obtained by scaling the curve measured in the laboratory by a factor (124/140). This factor was extracted from comparison of median efficiency thresholds obtained with NINO3 in the test beam (table 4.8) and the laboratory environment. This results in 575±30 mV for the threshold at median 1 MIP efficiency for final NINO board.

The noise rate dependence on the NINO discriminator threshold as measured with final NINO board in the laboratory is presented in figure 4.38. By fitting the function 4.3 to the linear part of this curve one obtains σ=74.9 mV for the noise RMS. This result differs from the one expected in ATLAS due to the shorter signal cables used in the laboratory setup yielding lower attenuation. In section 4.3.1, noise rates with NINO2 and module F406 which were measured in the test beam and laboratory environment were presented (see table 4.8). Comparison of these two results gives a scaling factor (33.1/38.6) for transforming noise σ measured in the laboratory to an estimate expected in ATLAS. For the final NINO board this results in 64 mV for the noise RMS σ expected in ATLAS. This value, together with the threshold at median 1 MIP efficiency than give an estimate of 9±0.5 for the median SNR for BCM system in ATLAS.

When fitting the function 4.3 to the measured noise rates for the NINO2 board, the proportionality factor in equation 4.3 was found to be the same for both laboratory and test beam measurements. The result was expected, since this parameter depends only on the bandwidth of the system. Therefore, an estimate for the noise rates of the final NINO board in ATLAS can be calculated from equation 4.3 by including the scaling factor (33.1/38.6) for the σ parameter and inserting the proportionality factor extracted from the fit to the laboratory noise rates.

The two estimates, 1 MIP efficiency and scaled noise rate can be combined in a plot of 1 MIP efficiency as a function of noise rate expected in ATLAS. More indicative is a plot of efficiency versus noise occupancy, where noise occupancy represents the probability to find a noise hit in one LHC bunch crossing interval of 25 ns. The occupancy was calculated by

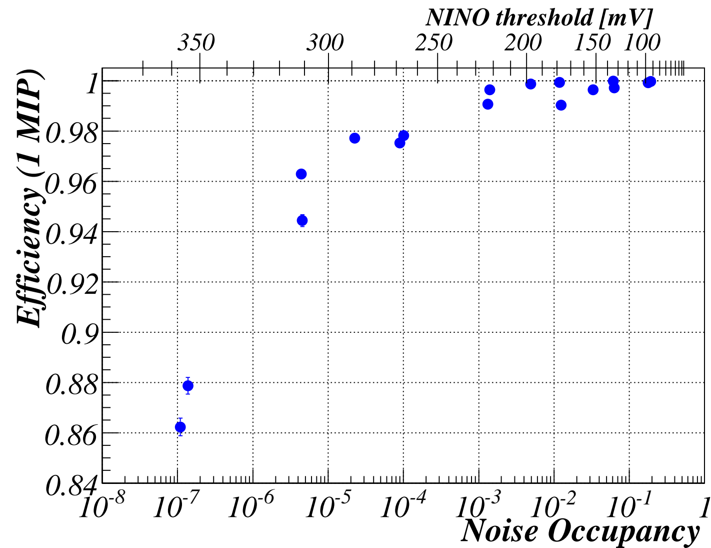

Figure 4.39: *Efficiency for 1 MIP versus noise occupancy as expected for BCM system in ATLAS. Here, noise occupancy represents the probability for finding a noise hit between two consecutive LHC bunch crossings (25 ns).*

multiplying the noise rate with 25 ns, which represents the number of noise hits in one bunch crossing. This approximation for occupancy is valid for the threshold range where noise rate is small compared to the bunch crossing rate of 40 MHz. The efficiency versus noise occupancy curve obtained is shown in the figure 4.39. From this figure, one can estimate a range of NINO thresholds between 230 mV to 300 mV, where the BCM system can be operated with a noise occupancy between 10^{-3} and 10^{-5} and an efficiency between 99% and 96%. However, this plot gives and estimate for a single module. The noise rates of coincident signals from multiple modules is much smaller. The exact level of fake rates will depend on what kind of the logical combination of the eight BCM channels will be used.

Plots of correlations between NINO output signal width and input signal amplitude for different NINO thresholds are presented in figure 4.40 for final NINO board. The width of the NINO signals was calculated at half pulse height, using the same procedure as described in section 4.2.2, and amplitudes of analogue input signals were sampled in 2.125 ns time interval as described in section 4.2.1. The NINO digital signals themselves were used for triggering the readout, thus, triggering on the complete range of input amplitudes, which give a hit on the NINO output. Apart from this, the setup was the same as the one used for measurements discussed previously in this section. The plots show that the width-amplitude correlation is nonlinear. At lower thresholds, part of the NINO hits are due to noise which can be observed as additional peak in the plots at lower input amplitudes and small NINO signal widths. This noise peak disappears at higher thresholds. One can observe a threshold independent lower limit of NINO signal width of ~4 ns. The upper limit drops from 16 ns at the lowest threshold to 11 ns at the highest threshold recorded.

The relation between the NINO discriminator threshold and the threshold on the scale of input amplitudes has been read off from the width-amplitude plots. The input amplitude threshold

at a specific NINO threshold was estimated as the highest value on the x axis of amplitude-width plot below which NINO signals are not observed. The result is shown in figure 4.41. The relation appears to be linear for the NINO thresholds between $\sim$200 and $\sim$700 mV. This range also corresponds to the NINO threshold range where the scaling of efficiency curve, performed previously in this section to estimate the 1 MIP curve expected in ATLAS (figure 4.39), is valid.

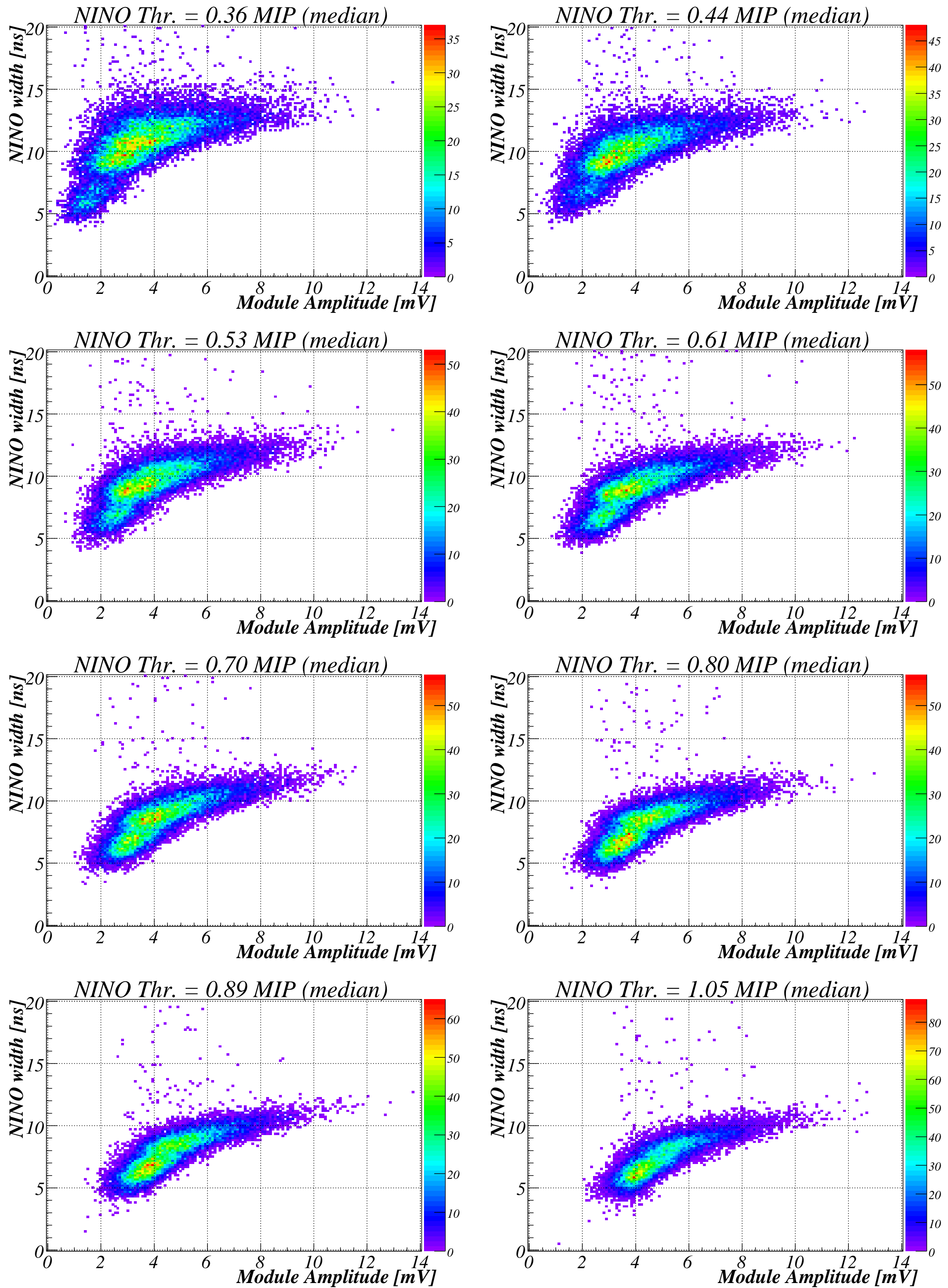

Figure 4.40: *Correlation between the NINO signal pulse width and input analogue signal amplitude of module F406 for different discriminator thresholds on the spare final NINO board. The thresholds are stated in the title of each plot in units of threshold at median 1 MIP efficiency (575 mV), obtained with final NINO board and module F406.*

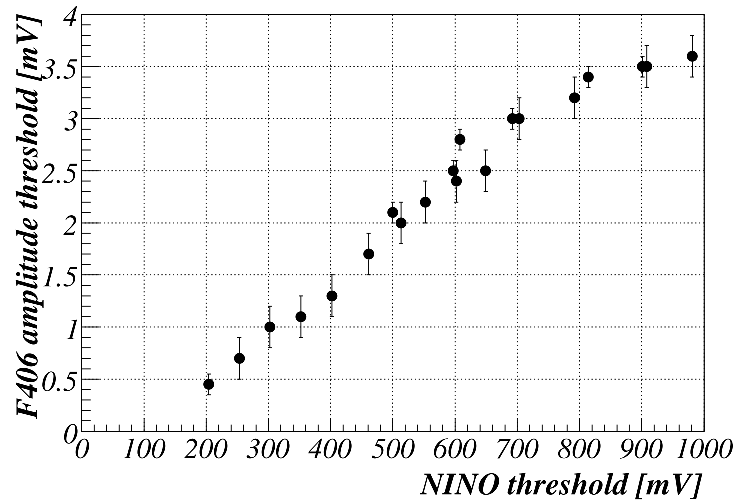

Figure 4.41: *Correlation between NINO discriminator threshold and the threshold on the scale of NINO input signal amplitudes. The values have been estimated from the width-amplitude plots as shown in figure 4.40 obtained with module F406 and spare final NINO board.*

4.3.3 Noise rates of the installed modules

After the installation of NINO boards in ATLAS, the noise rates at the end of full BCM readout chain were measured. The results are presented in figure 4.42. The noise σ values extracted from the Gaussian fits to the measured noise rates for each installed detector module are listed in the table 4.9. Up to 25% variation in estimated noise values can be observed. This variations can be attributed to both detector module to module and NINO chip to chip variations.

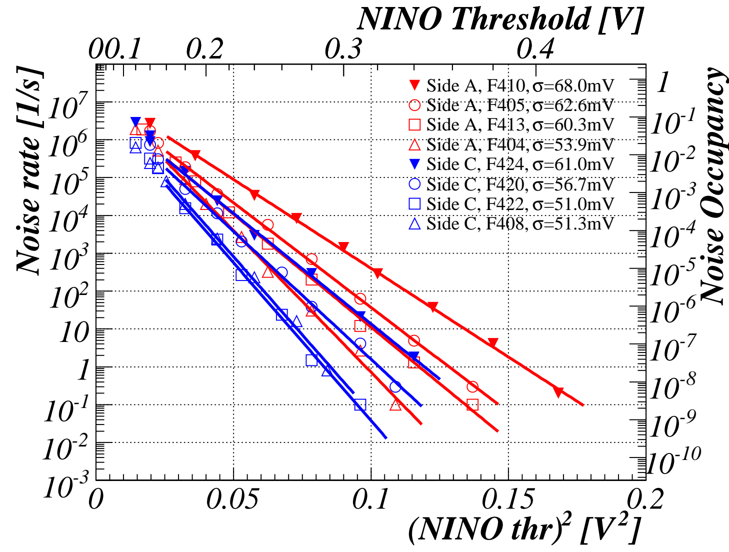

__Figure 4.42:__ Measured noise rates of modules installed in ATLAS at the end of BCM readout chain for all eight channels after installation of NINO boards. Axis on the left side of the plot indicates noise occupancy in one LHC bunch crossing.

Module	Position [Side, (x,y)]	Noise σ [mV]
F410	A, (+x,0)	68.0
F405	A, (0,+y)	62.6
F413	A, (-x,0)	60.3
F404	A, (0,-y)	53.9
F424	C, (+x,0)	61.0
F420	C, (0,+y)	56.7
F422	C, (-x,0)	51.0
F408	C, (0,-y)	51.3

__Table 4.9:__ Noise values extracted from the noise rate measurements presented in figure 4.42. Position of each module in ATLAS is given in the second column.

CHAPTER 5

MEASUREMENTS WITH EPITAXIAL SILICON MATERIAL

The fast response, good spatial resolution and large scale availability make silicon detectors the favourite choice for tracking area of colliding beam experiments as e.g. ATLAS or CMS at the forthcoming LHC. However, the innermost detectors for the planned upgrade of LHC (S–LHC) will have to sustain very large hadron fluences of up to 10^{16} hadrons per cm^2. This poses a considerably larger challenge to their applicability in terms of radiation tolerance, not yet met by the present devices. In order to cope with the much larger multiplicity of events, small sized pixel detectors will be used in the volume close to interaction. This allows a considerably smaller detector thickness while keeping the capacitance at a low level. Thin detectors would then allow a much higher doping concentration at moderate voltages. This large donor reservoir in n-type silicon would then in turn delay the type inversion effect, caused by radiation generated acceptors. Within the framework of the RD50 collaboration, the project with diodes processed on thin n-epitaxial silicon layers was started. It was found that damage generated shallow donors are created in epi samples, which compensate the build up of negative space charge by deep acceptors, pointing to superior radiation tolerance of epi material compared to standard FZ silicon.

One of the requirements for ATLAS BCM sensor material was that it should withstand particle fluences up to 10^{15} cm^{-2}. The promising results in terms of radiation tolerance with thin epi samples were the main motivation to consider these detectors as one of the options for BCM sensor material. However, these results, obtained by the Hamburg group, were extracted from the measurements performed at elevated annealing temperatures of 60°C and 80°C. In order to verify these results, annealing studies at 20°C, a temperature closer to annealing scenario at LHC, were performed for a total period of 3.5 years. The results of this study are presented in the first part of this chapter. The applicability of epi samples in terms of signal properties was checked with the prototype BCM module. The results are reported in the second part of this chapter.

Epitaxial silicon devices studied here were of n-type with nominal resistivity of 50 Ωcm and three different thicknesses 25, 50 and 75 μm. Epi layers were grown on a 500 μm thick, highly doped Cz silicon substrate with resistivity of 0.01 Ωcm. They were manufactured by ITME [ITM], using the vapour-phase epitaxy process, briefly described in section 3.3.2. A more de-

tailed description of the process steps for epitaxial layers produced by ITME can be found in [Dez97]. Pad diodes with active area of $5\times5\,\mathrm{mm}^2$ and guard ring structure were processed by CiS [CiS], using planar processing technology (cf. section 3.3.2).

5.1 Radiation hardness

A set of 22 epi samples of different thicknesses was used to measure the time development of full depletion voltage (or N_{eff}) and leakage current after irradiation. Eight samples were irradiated with 24 GeV/c protons at the CERN PS, while the rest were irradiated with reactor neutrons from the TRIGA II research reactor of Jožef Stefan Institute in Ljubljana. Details on reactor neutron spectrum and its hardness factor are given in [Ž+99]. In both cases the highest particle fluence of 10^{16}cm^{-2} was reached. The samples are listed in table 5.1 together with their thickness and equivalent fluence they were exposed to. For 24 GeV/c protons a hardness factor of 0.62 was used to transform the measured proton fluences to equivalent fluence, corresponding to 1 MeV neutron equivalent fluence.

Neutron Irr.			Proton Irr.		
Sample	**D [μm]**	Φ_{eq} [10^{15} cm^{-2}]	**Sample**	**D [μm]**	Φ_{eq} [10^{15} cm^{-2}]
6837-07-60	75	0.6	6837-07-61	75	1.4
6837-07-57	75	1.0			
6837-07-58	75	2.0			
5856-01-06	50	0.1	6336-03-06	50	6.6
5856-01-30	50	0.6	5856-01-60	50	4.1
5856-01-25	50	1.0	6336-03-07	50	4.1
5856-01-12	50	2.0	5856-01-06	50	6.6
5856-01-40	50	4.0			
5856-01-46	50	8.0			
5856-01-56	50	10.0			
6837-02-10	25	0.02	6337-02-20	25	6.6
6837-02-07	25	0.1	6837-02-23	25	2.2
6837-02-11	25	0.1			
6837-02-08	25	0.2			

Table 5.1: *List of samples used in the annealing study at 20°C. Their thickness and equivalent fluences are given for each sample. The full depletion voltage before irradiation was 25V, 130 V and 275 V for 25 μm, 50 μm and 75 μm samples respectively.*

5.1.1 Experimental setup

Full depletion voltage and leakage current were extracted from capacitance-voltage (C–V) and current-voltage (I–V) characteristic measurements. Capacitance was measured with a Hewlett Packard LCR meter (HP 4284A) while a Keithley 237 source-measure unit was used to supply the external DC bias voltage to the sample. Decoupling capacitors were used to shield the LCR meter from high DC voltages as shown in figure 5.1. All measurements were performed at room temperature with the temperature measured with a Pt100 sensor placed close to the sample. When stored, samples were kept at temperature of 20°C, stable to about $\pm 2^o$C.

Capacitance is determined from the complex impedance and can be calculated from the measured amplitude and phase shift of the current signal response to an AC voltage of a chosen frequency. The AC voltage amplitude was typically kept at 10 mV. The LCR meter offered either a parallel or serial RC model to extract capacitance from the measured complex impedance. Both models differ from the equivalent circuit shown in figure 5.2 which roughly describes a partially depleted diode. The depleted region of a detector can be approximated by a capacitor since the dynamic resistivity of depleted bulk is high ($R_d \gg 1/\pi\omega C_d$), while for frequencies up to about 30 kHz, the undepleated bulk can be considered as a resistor ($R_u \ll 1/\pi\omega C_u$). Thus, for lower frequencies the bulk can be described by a capacitor and resistor in series, making a serial model applicable. With increasing voltage the resistance of undepleted bulk decreases while its capacitance increases ($R_u \propto (1-\sqrt{V/V_{FD}})$, $C_u \propto 1/(1-\sqrt{V/V_{FD}})$). Therefore, at voltages close to V_{FD} the bulk can be described well by a single capacitor and both models should give the same result. However, the parallel model has the advantage that it can take into account changes in the surface current. Since for determination of the V_{FD} one is primarily interested in the shape of C–V curve close the VFD, the parallel model suits better and was used in this work.

The measurements of C-V characteristics were controlled via a standard GPIB bus by a program written in Labview [Lab] running on PC. The (DC) bias voltage was raised in steps, where at each step the sample capacitance was measured with seven different frequencies of the measuring (AC) voltage. The leakage current was also measured at each step. For determination of V_{FD}, the C-V curve obtained at 10 kHz was used. Since it is commonly used by other groups, this choice enables the comparison of results.

The setup allowed the separation of bulk generated current from the guard ring current (see

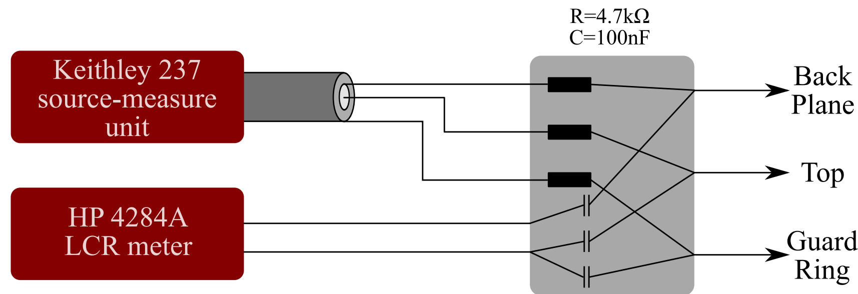

Figure 5.1: Schematic view of the setup used for C–V and I–V measurements. Arrows indicate connections to the back plane, guard ring and top pad.

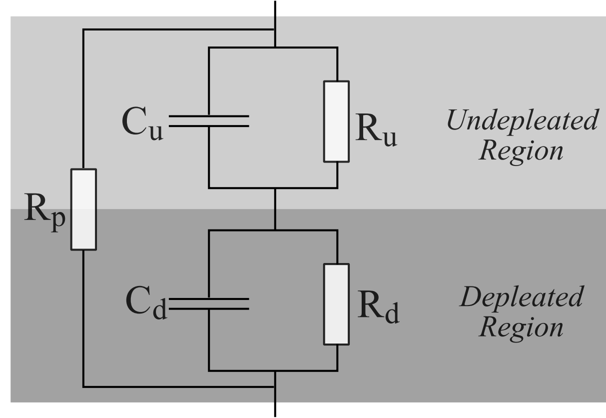

Figure 5.2: A simple electrical model of partially a depleted diode. The depleted and undepleted regions are each represented by a resistor and capacitor in parallel. To account for surface currents, both regions are connected in series with parallel resistor R_p.

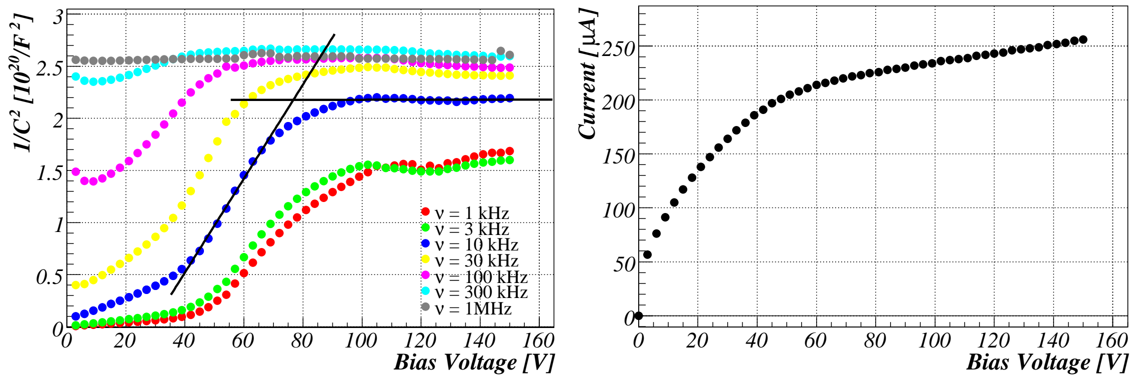

Figure 5.3: The $1/C^2$ versus voltage (left) and I–V characteristic (right) measured with sample 5856-01-46. On the left plot, the straight lines indicate the fits to the slope at low depletion depths and the plateau at full depletion. Their intersection was used as an estimate of the full depletion voltage.

figure 5.1). While both guard ring and the pad were connected to the same potential, only the current flowing through the pad was measured to reduce the contribution of the surface-generated current.

The full depletion voltage was extracted as the position of the kink in the measured $1/C^2$ versus voltage plot. The position of the kink was determined by the intersection of two straight lines, one fitted to the slope before the kink and the other to the plateau at full depletion (see figure 5.3). The effective dopant concentration was calculated from the equation 3.62

$$N_{eff} = \frac{2\epsilon_{Si}\epsilon_0}{e_0 D} V_{FD}, \tag{5.1}$$

where a homogeneous distribution of space charge is assumed over the sample, as discussed in section 3.3.1.

From equations 3.61 and 3.66 it follows that the bulk generation current rises as $\sqrt{V}$ with increasing bias voltage V until the full depletion of sample is reached. However, for the samples used in this work, the measured I–V curves typically did not follow exactly the ideal characteristic, where saturation above the full depletion voltage is expected. An example is shown in figure 5.3. Nevertheless, the leakage current was extracted from the I-V curve at a voltage corresponding to the full depletion voltage.

5.1.2 Annealing of effective dopant concentration

Typical annealing curves of full depletion voltage obtained with epi samples are shown in figure 5.4. The behaviour is opposite to the one observed with highly irradiated n-type standard high resistivity FZ silicon samples, where type inversion can be assumed already directly after irradiation. For FZ samples, part of initial radiation induced damage, which is attributed to acceptors[1], is annealing out within a short time after irradiation. In case of highly irradiated n-type FZ silicon, this initial short term annealing (sometimes called "beneficial annealing") results in full depletion voltage decrease observed at short annealing times. This is followed by a slow increase due to increasing acceptor generation with longer annealing times.

For epi samples, on the other hand, an increase of the full depletion voltage is observed at short annealing times even for samples irradiated with fluences as high as $10^{16}\,\mathrm{cm}^{-2}$. This initial increase is followed by a minimum at about 20 days at 20°C leading to an increase at longer annealing times. This behaviour can be explained by a build up of positive space charge during the irradiation (donor creation). The same behaviour for annealing curves of full depletion voltage is observed in case of proton and neutron irradiation, pointing to the fact the no type inversion immediately after irradiation can be observed in both cases.

Figure 5.5 shows the effective dopant concentration at the end of short term annealing as a

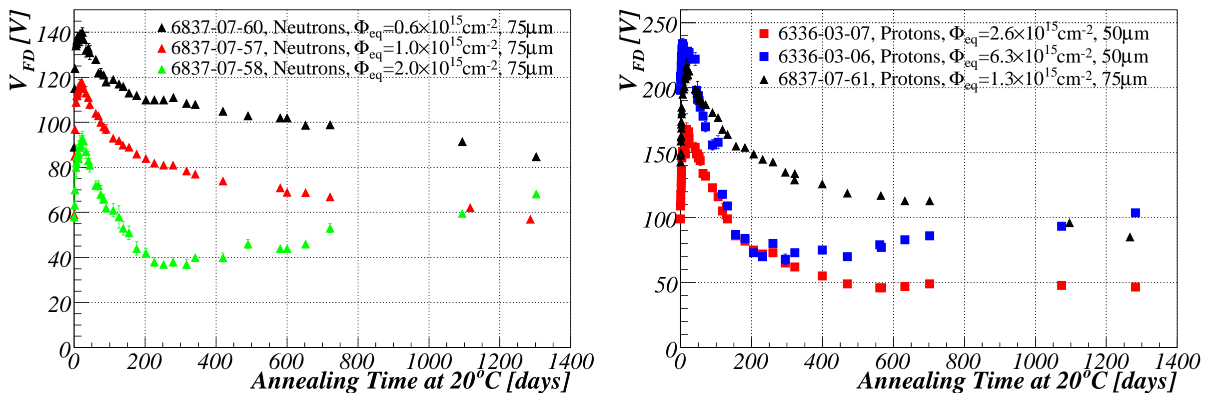

Figure 5.4: *Annealing of full depletion voltage at 20°C measured with neutron (left) and proton (right) irradiated epi samples.*

[1]Studies with FZ silicon showed that more electrically active acceptors than donors are produced during the irradiation (see section).

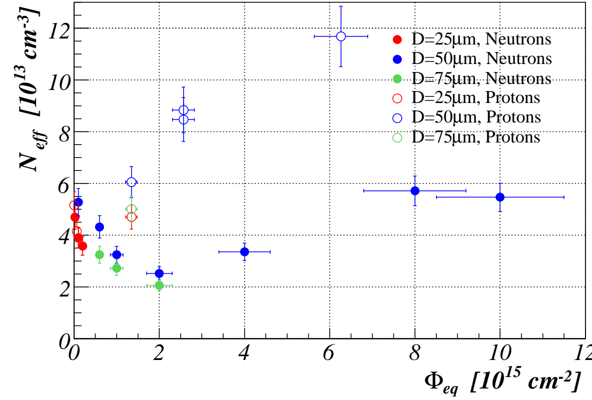

Figure 5.5: *N_{eff} at the end of short term annealing as a function of equivalent fluence for proton (open markers) and neutron (closed markers) irradiated 25μm (red), 50μm (blue) and 75μm (green) samples.*

function of fluence. At this stage of the annealing, neither short nor long term annealing play a significant role. Therefore the values on the plot are approximately only caused by a component corresponding to the stable damage induced during irradiation. If no type inversion directly after irradiation is assumed, then the following picture can be used to explain this plot. The first part of the fluence dependence can be attributed to donor removal. This component is present in n-type FZ silicon as well. It is exponentially saturating with fluence due to the exhaustion of initial doping (donors) in n-type material. In case of epi material, the exhaustion will be delayed compared to n-type FZ since larger values of doping are possible in thin detectors. At larger fluences, the possible creation of acceptors (observed in FZ) is overcompensated by the creation of donors causing an increase in effective dopant concentration N_{eff} (and V_{FD}) with fluence.

The so called Hamburg model is commonly used for description of changes of N_{eff}. The change in N_{eff} compared to its value before irradiation $N_{eff,0}$ is parametrised with three components

$$\begin{aligned}\Delta N_{eff}(\Phi_{eq}, t(T_a)) &= N_{eff,0} - N_{eff}(\Phi_{eq}, t(T_a)) \\ &= N_A(\Phi_{eq}, t(T_a)) + N_C(\Phi_{eq}) + N_Y(\Phi_{eq}, t(T_a))\end{aligned} \tag{5.2}$$

where T_a represents the annealing temperature and N_A describes the short term annealing, N_Y the long term annealing and N_C the stable damage. The short term annealing part, attributed to annealing of negative space charge (acceptors), consists of one exponentially decaying term with a time constant τ_A and amplitude $N_{A,0}$

$$N_A = N_{A,0}\exp(-t/\tau_A). \tag{5.3}$$

In the studies at elevated temperatures, performed by the Hamburg group [L$^+$06b, L$^+$06a], this initial annealing was found to be similar to the one observed in FZ material with the time constants comparable with the ones observed in FZ material.

Stable damage N_C is described with two components. First is an incomplete donor removal

which exponentially depends on fluence with a final value $N_{c,0}$ and donor removal rate c. The other component corresponds to fluence proportional introduction of stable defects with a rate g_C

$$N_C = N_{c,0}(1 - \exp(-c\Phi_{eq})) + g_C\Phi_{eq}. \quad (5.4)$$

In contrast to FZ silicon detectors for which g_C is always positive, in the studies of epi samples at elevated temperatures g_C was found to be negative pointing to additional stable donor creation during irradiation in epi material.

Also different with respect to FZ samples, is the long term annealing. This component was found to exhibit two different contributions in case of epi material. The first one, occurring in the initial phase of long term annealing, was found to be best described by a first order process with a time constant τ_{Y1} and a fluence dependent amplitude $N_{Y1,0}$

$$N_{Y1} = N_{Y1,0}\exp(-t/\tau_{Y1})) = g_{Y1}\Phi_{eq}\exp(-t/\tau_{Y1}). \quad (5.5)$$

The second contribution, observed in the later stage, is more likely to be due to the second order process. The time constants for this part are of the order of 10^4 min at an annealing temperature of 60°C. Thus its effect is not expected to be observed in the annealing studies at 20°C, performed in this work.

In the studies at elevated temperatures, it was found that the introduction rate of effective donors is smaller in case of neutron irradiation. The initial decrease in positive space charge, attributed to donor removal, was found to be much faster for proton than for neutron irradiated samples, where the donor removal constants c were comparable to the ones obtained with FZ silicon. However, it was observed that in case of proton irradiation the introduction rate of positive space charge depends on the epi sample thickness and is related to the concentration of oxygen dimers in the epi silicon. Oxygen dimers are produced during the high temperature process steps, diffusing out of Cz substrate. Due to their much smaller thickness it is plausible that the dimer concentration could be larger in thinner samples, thus explaining the difference in stable damage. For details see [P$^+$05, P$^+$06]. Apart from this difference, all damage parameters were observed to be independent of epi sample thickness.

In order to compare the results at annealing temperature of 20°C performed in the scope of this work with the ones obtained by Hamburg group, the same parameterisation 5.2 was used to describe the annealing of V_{FD}. For each sample, the function 5.2 was fitted to the measured time development to extract parameters N_C, N_A, τ_A, g_{Y1} and τ_{Y1}. Only the results concerning the stable damage and long term annealing are discussed here since those are most important for the annealing scenarios at LHC during the beam off periods.

When calculating the difference ΔN_{eff}, the sign of space charge must be assumed. Since no type inversion is assumed immediately after the irradiation, the space charge at shorter annealing times was taken to be positive and $\Delta N_{eff}(t)$ was calculated as

$$\Delta N_{eff}(t) = |N_{eff,0}| - |N_{eff}(t)| \quad (5.6)$$

where $|N_{eff,0}|$ and $|N_{eff}(t)|$ are values computed from the measured V_{FD} before irradiation and after irradiation at annealing time t respectively.

For highly irradiated epi samples, type inversion at longer annealing times occurs due to

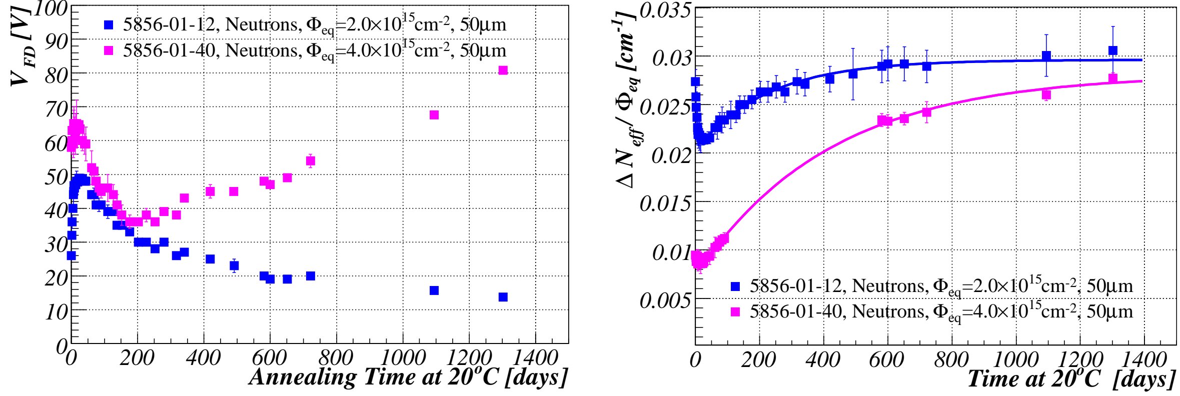

Figure 5.6: *Examples of measured V_{FD} (left) as a function of annealing time at 20°C with corresponding $\Delta N_{eff}/\Phi_{eq}$ annealing (right). The solid lines on the right plot represent the best fit of function 5.2 to calculated $\Delta N_{eff}/\Phi_{eq}$ values.*

build up of negative space charge (acceptors) during the annealing, which compensates the positive space charge (donors) created during irradiation. If the type inversion was observed in the V_{FD} annealing curve of a sample then ΔN_{eff} points after type inversion were calculating by assuming negative space charge at annealing time t

$$\Delta N_{eff}(t) = |N_{eff,0}| + |N_{eff}(t)|. \tag{5.7}$$

However, the measured V_{FD} does not drop to 0 V at annealing times around the type inversion. At this stage of the annealing the space charge is not constant over the depleted region. Thus, the model of V_{FD} extraction from C–V measurements is not applicable in the region of annealing times, where type inversion occurs. For this reason, the measurements around type inversion point were excluded from the fitting of function 5.2 to the measured $\Delta N_{eff}/\Phi_{eq}$ dependence on annealing time.

Figure 5.6 shows two examples of a V_{FD} annealing curve. For one of the samples (pink curve) type inversion can be observed at an annealing time around 200 days at 20°C. When performing the fit of parametrisation 5.2 to the calculated $\Delta N_{eff}/\Phi_{eq}$ dependence on the annealing time, points between 100 and 500 days were excluded (see figure 5.6, right). On the other hand, the blue V_{FD} annealing curve in figure 5.6 indicates that type inversion did not occur for annealing times up to 1300 days.

The results, extracted from the best fit of parametrisation 5.2 to $\Delta N_{eff}/\Phi_{eq}$, are presented in figures 5.7 and 5.8 for the case of neutron and proton irradiated samples respectively. From the plot of stable damage, N_C, as a function of fluence, one can see that the results for samples of two different thicknesses match quite well in case of neutron irradiation as expected. The function 5.4 was fitted to this plot, where data points for both thicknesses were included in the fit. The resulting introduction rate of stable donors, g_C, was found to be $(-6.3\pm1.5)\times10^{-3}$ cm^{-1}, where the error represents the value returned by the fitting procedure. This result agrees with the value -5.0×10^{-3} cm^{-1} obtained by the Hamburg group.

Since no proton irradiations at lower fluences were performed, only the parameter g_C was

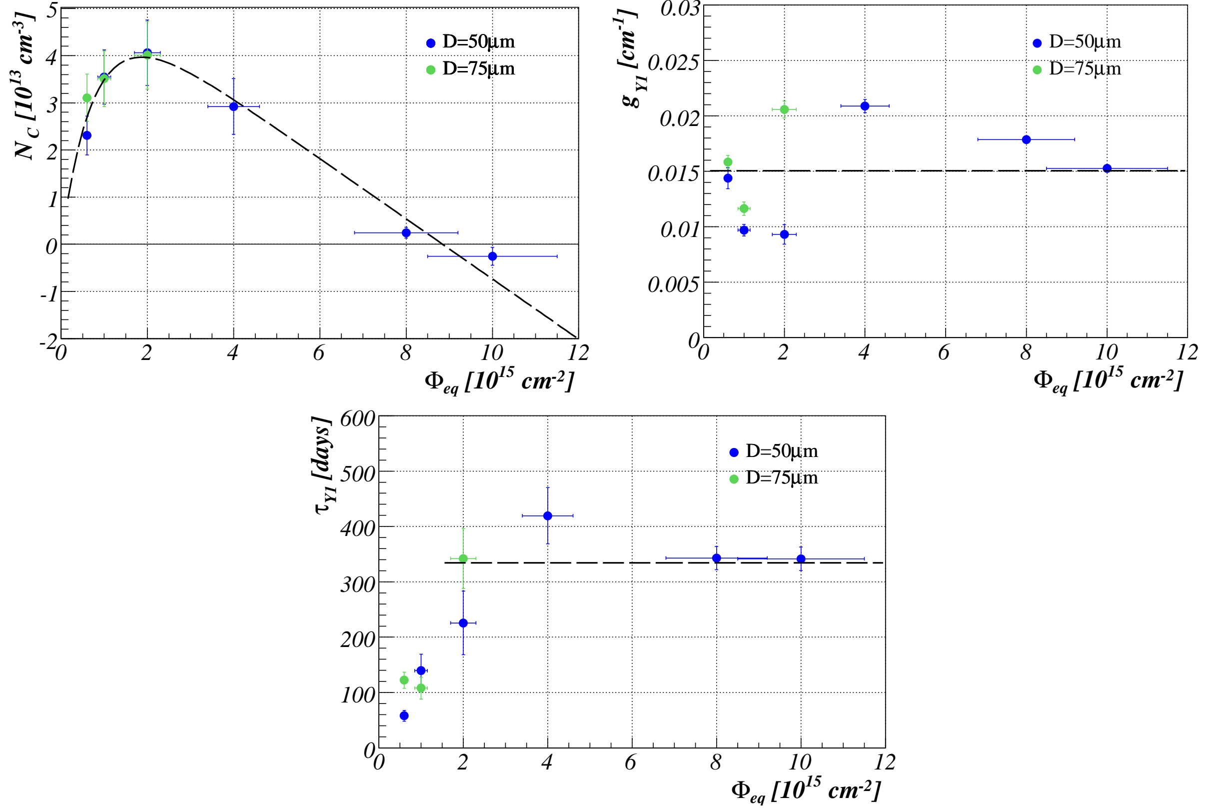

Figure 5.7: *Damage parameters N_C (left), g_{Y1} (right) and τ_{Y1} (bottom) extracted from annealing of full depletion voltage at 20°C for neutron irradiated samples. Blue markers denote samples of 50 μm thickness, while green marks 75 μm samples. Black dashed straight lines denote the mean values averaged over all data points (50 μm and 25 μm) while the dashed curve on the left plot represents the best fit of model function 5.4 to data points.*

extracted from the stable damage dependence on fluence by performing the linear fit to the curve. Here, only the data points for 50 μm samples were considered, since g_C was found to depened on sample thickness by Hamburg group. The value g_C and its error extracted from the fit was found to be $(-1.7{\pm}0.2){\times}10^{-2}$ cm^{-2} which is comparable to the value $-1.1{\times}10^{-2}$ cm^{-1} obtained from studies at the elevated temperatures.

With neutron irradiated samples, the time constant responsible for the first component of long term annealing, τ_{Y1}, seems to be independent of fluence as expected for the first order process. However, this does not hold for lower fluences. Same behaviour was confirmed by the Hamburg group. Possible explanation for fluence dependence of τ_{Y1} at low fluences can be found in [L$^+$06b]. The mean value of τ_{Y1} for fluences above $2{\times}10^{15}$cm^{-2} and its standard error were estimated to be 330±60 days. Somehow larger spread can be observed in introduction rates of defects responsible for the first component of long term annealing g_{Y1}. Its mean value and standard error were found to be $(1.5{\pm}0.4){\times}10^{-2}$ cm^{-1}. In case of proton irradiated samples, mean values and its standard errors for τ_{Y1} and g_{Y1} were found to be 190±60 days and $(2.2{\pm}0.7){\times}$ cm^{-1} respectively.

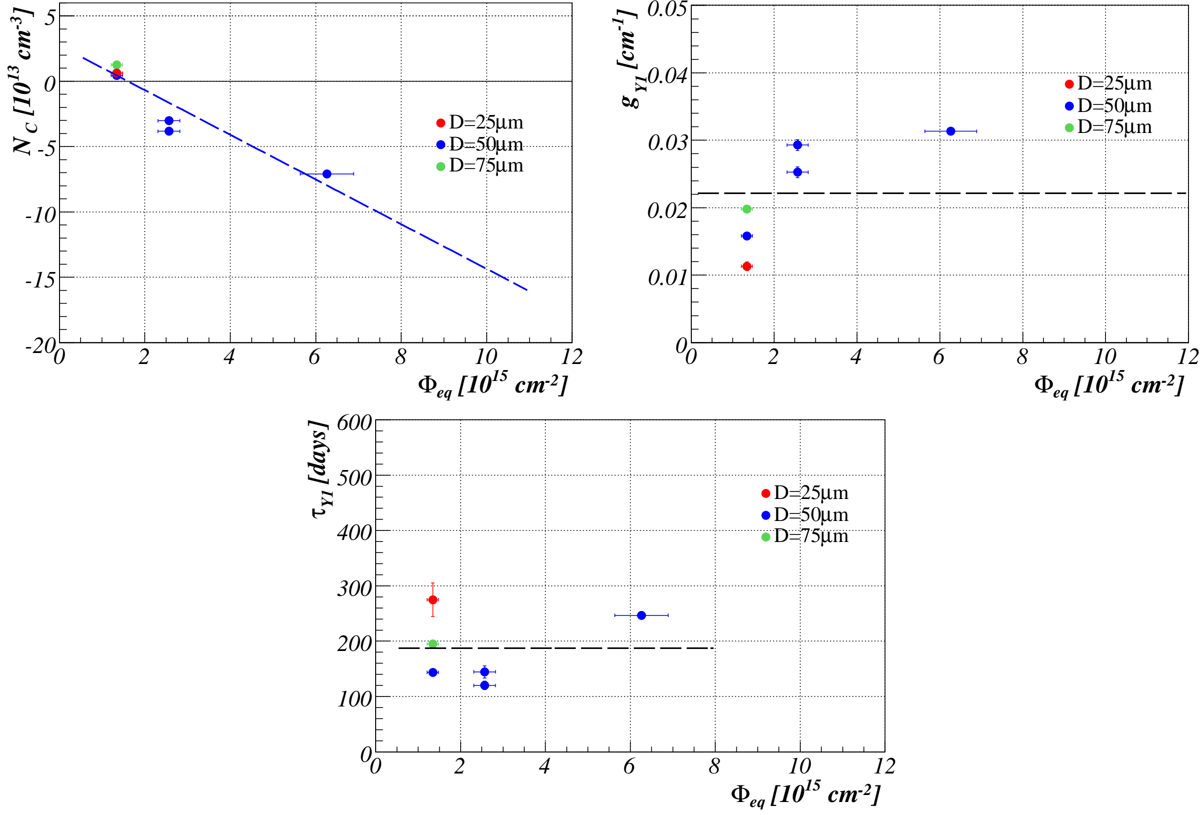

Figure 5.8: *Damage parameters N_C (left), g_{Y1} (right) and τ_{Y1} (bottom) extracted from annealing of full depletion voltage at 20°C for proton irradiated samples. Red markers denote 25 µm, blue markers are for 50 µm samples and green for 75 µm samples. Black dotted lines represent the mean values, averaged over all data points (25, 50 and 25 µm), while blue dotted line represents a straight line fit to the 50 µm data points used to extract introduction rate g_C.*

The Hamburg group reported a value for the time constant τ_{Y1} of around 1.3×10^4 min and 1×10^2 min for annealing temperature of 60°C and 80°C respectively. These numbers indicate that the first order long term annealing process is governed by the same activation energy of E_a=1.3 eV as in standard FZ detectors. Using this activation energy, the values of τ_{Y1} obtained at elevated temperatures translate to about 440 days a 20°C. However, the numbers stated above indicate that the 20°C annealing is slightly faster than expected from annealing at elevated temperatures. Also, compared to the introduction rate of g_{Y1}=2.9×10^{-2} cm^{-1}, obtained by Hamburg group, the results from the present work give somehow lower values.

Damage parameters, connected to stable damage and long term annealing, extracted from the 20°C annealing curves, are summarised in table 5.2.

Damage Parameter	Neutron Irr.	Proton Irr.
$N_{C,0}$ [10^{13}cm^{-1}]	5.6±1.0	
c [10^{-15}cm^{-2}]	1.3±0.2	
g_C [10^{-2}cm^{-1}]	−0.63±0.15	−1.7±0.2 (50 μm samples)
g_{Y1} [10^{-2}cm^{-1}]	1.5±0.4	2.2±0.7
τ_{Y1} [days]	330±60	190±60

Table 5.2: *Damage parameters extracted from annealing curves of full depletion voltage at 20°C.*

5.1.3 Annealing of leakage current

The variation of leakage current with equivalent fluence, Φ_{eq}, is expressed in terms of a damage parameter α by

$$\frac{\Delta I(\Phi_{eq}, T_a, t)}{V} = \alpha(T_a, t)\Phi_{eq}, \tag{5.8}$$

where ΔI represents the current increase compared to the value before irradiation, measured at a certain reference temperature T_r after annealing time t at annealing temperature T_a. However, normally the temperature T_m at which the current measurement is performed differs from the temperature T_r. In this case the leakage current has to be corrected by a factor [Sze02]

$$\frac{I(T_r)}{I_{T_m}} = \left(\frac{T_r}{T_m}\right)^2 \exp\left(-\frac{E_g}{2k_B}\left(\frac{1}{T_r} - \frac{1}{T_m}\right)\right) \tag{5.9}$$

in order to get its corresponding value at T_r. In this work all presented data have been normalised to T_r=20°C, where a value of 1.12 eV was used for the effective energy gap E_g.

The annealing behaviour of leakage current is usually described by [Mol99]

$$\alpha(T_a, t) = \alpha_0 + \alpha_I \exp(-t/\tau_I) - \beta \ln(t/t_0) \tag{5.10}$$

where t_0 is fixed at 1 min. The same parametrisation has been used to describe the leakage current annealing curves at 20°C presented in this work.

Figure 5.9 shows some examples of extracted α during annealing for different irradiated samples, where the solid line represents the best fit of function 5.10 to the measured data.

It was observed that α at a specific annealing time does not depend on the type of silicon material or irradiation particles used. The α value of after 80 min at 60°C was found to be (3.99±0.03)×10^{-17}A/cm [Mol99]. To compare this value with the results obtained at 20°C, presented here, the annealing time axis at 60°C has to be appropriately transformed. This is usually done by introducing a temperature dependent factor [M$^+$99b]

$$\theta(T_a) = \exp\left(\frac{E_I}{k_B}\left(\frac{1}{T_r} - \frac{1}{T_a}\right)\right) \tag{5.11}$$

with an activation energy of E_I=1.09±0.14 eV. Thus, 80 min at 60°C corresponds to about 240h at 20°C. The values α after 240h at 20°C obtained from our data is plotted in figure 5.10. The mean value extracted from this plot as α(240h at 20°C)=(3.9±0.8)×10^{-17} A/cm agrees well with the standard value stated above.

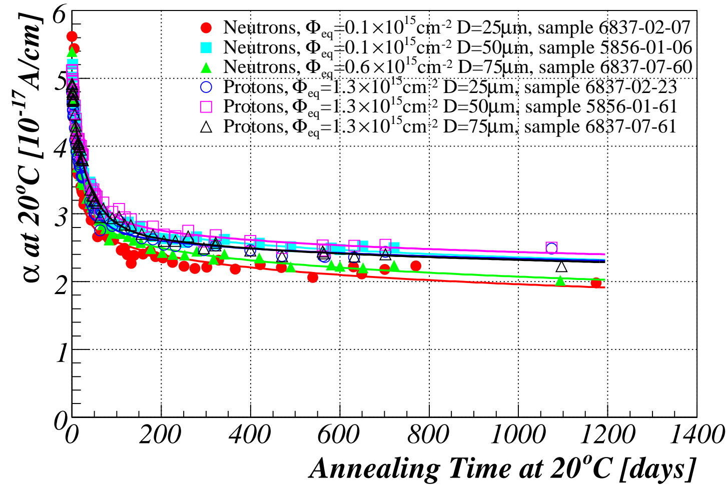

Figure 5.9: *Leakage current annealing curves for some samples at annealing temperature of 20°C, where the leakage current has been calculated at reference temperature of 20°C. Solid lines represent best fit of function 5.10 to the data.*

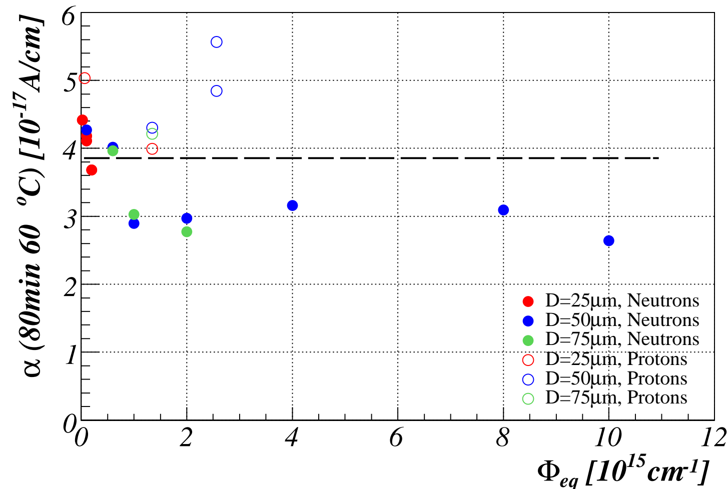

Figure 5.10: *Damage parameter α after 240 h at 20°C, extracted for each sample. Red colour denotes 25 μm, blue 50 μm and green 75 μm samples, where open markers refer to proton and closed to neutron irradiated samples.*

5.2 Measurements with the BCM detector modules

A prototype BCM module was equipped with a non-irradiated 50 μm thick epi silicon sample in order to evaluate its performance with this sensor. The sample's full depletion voltage was $\sim$130 V as extracted from the C–V measurement.

The setup used for the tests described in this section was similar to the one used for the measurements presented in section 4.2.4, consisting of ^{90}Sr as a source of β particles and scintillator as a trigger for minimum ionising particles. Signal waveforms were fed through a 1 m coaxial cable to LeCroy WP950 digital oscilloscope, where they were recorded with a sampling frequency of 8 GHz.

Two voltage scans were performed, one with a 200 MHz BWL and one with the maximum available BWL at the readout oscilloscope (1 GHz). Figure 5.11 shows two-dimensional histograms with all waveforms recorded at a bias voltage 450 V for both BWLs.

Noise was sampled about 30 ns before the signal pulses and signal amplitudes were extracted from a 2.125 ns time interval as described in section 4.2.1. Examples of amplitude and noise distributions, obtained at 450 V for both BWL cases, are shown in figure 5.12. The signal amplitudes observed with the epi sample were quite low which can be seen from figure 5.11 as well. Therefore, it was not possible to resolve the noise and signal peak in amplitude distributions. Nevertheless, assuming that the noise peak represents a minor contribution to the amplitude distribution, the convoluted Landau-Gauss function was fitted to those distributions in order to estimate the most probable value. The values obtained along with the noise RMS

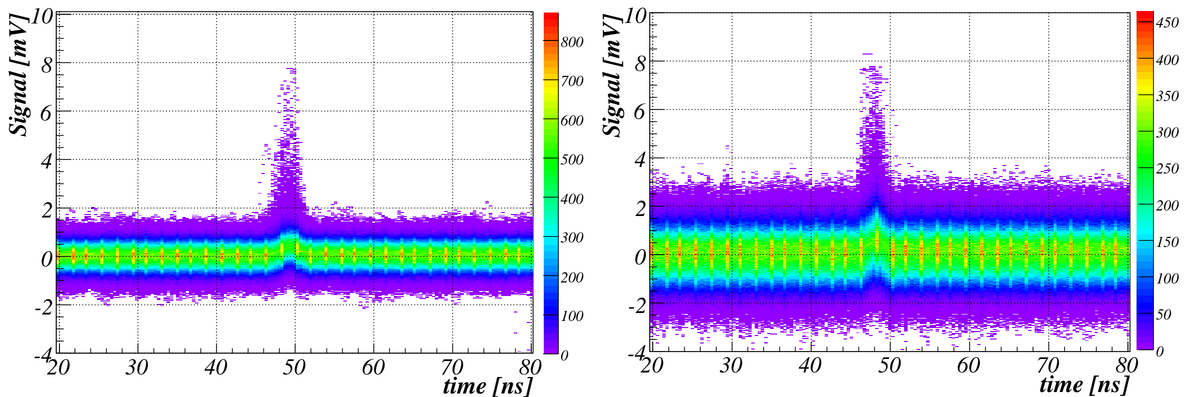

Figure 5.11: Two dimensional histograms of recorded waveforms with 50 μm epi sample at 450 V bias voltage for 200 MHz (left) and no BWL at readout.

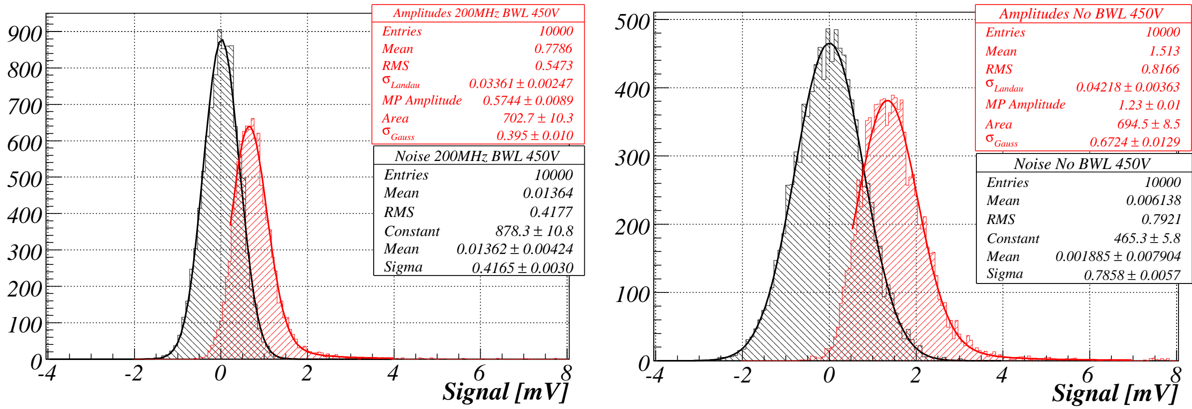

Figure 5.12: *Signal amplitude (red) and noise (black) distributions obtained with a 50 μm epi sample at a bias voltage of 450 V for 200 MHz (left) and 1 GHz BWL at the readout.*

extracted from the amplitude and noise distributions are presented in figure 5.13 as a function of applied bias voltage.

For lower bias voltages, noise decreases with increasing voltage due to increase in width of depletion region which results in lower sensor capacitance. At higher voltages where full depletion is reached, noise saturates at $\sim$0.4 mV when a 200 MHz BWL is set at the readout and at an approximately two times higher value when bandwidth is limited only by the 500 MHz due to front-end electronics. Similarly, the MP amplitude saturates at voltages close to the full depletion voltage where it reaches $\sim$0.6 mV in case of 200 MHz and at a value approximately two times higher if 1 GHz BWL is applied at readout. Combining the results for noise and MP amplitude yields about the same value of SNR for both cases of BWL, with a saturation value around 1.5. However, the values for MP presented in figure 5.13 are overestimated. Proper extraction of amplitude distributions and its MP values was hindered due to the very low signal amplitudes. In case of low signal amplitudes, changing the time interval used for the amplitude extraction can significantly change the MP amplitude.

The saturation of amplitudes at voltages above full depletion voltage is can be explained with assumption that the detector-amplifier system works in a charge sensitive mode. Voltage of 450 V applied to the 50 μm epi sample gives an electric field of 9 V/μm, where the drift velocity of charge carriers is already saturated (see table A.1). With drift velocity of $\sim$10^{7}cm/s assumed one obtains that around t_{dr}=0.5 ns is needed for a charge carrier to drift a distance of the epi sample thickness. On the other hand with 200 MHz and 500 MHz BWL, the shaping time of electronics corresponds to 5 ns and 2 ns respectively, which is more than t_{dr}. Thus, this amplifier-sensor system is operated close to charge sensitive mode, where one expects the signal amplitudes to saturate at voltages above full depletion voltage.

In diamond the drifting of charge carriers is limited due to trapping. In section 3.4.2 it was estimated that our diamond samples have an average drift distance of $\sim$315 μm. At electric field of 2 V/μm diamond is operated close to saturation of charge carrier drift velocity. If one assumes a drift velocity of $\sim$10^{7}cm/s then the charge carriers need around 3 ns to drift over distance of 315 μm. This number is comparable to the shaping time of 5 ns and 2 ns for 200 MHz

or 500 MHz (BWL of our amplifier system) BWL readout. Thus, in case of diamond sensor the sensor-amplifier system is operated in regime between charge sensitive and current sensitive mode.

The assumption that the system with epi diode is operated in charge sensitive mode can also explain much lower amplitudes observed with thin epi device compared to the values obtained with diamond. In the charge sensitive mode, where the measured amplitude correlates with the generated charge, the signal amplitude depends on the thickness of the sample. In a 50 μm epi sample around 4000 electron-hole pairs are in average generated along the minimum ionising particle track. On the other hand in 500 μm diamond 18000 electron-hole pairs are created and for a double decker configuration one expects about 36000 pairs in average after traversing of MIP. Thus, if the system would be operated in charge sensitive mode in both cases, with epi and with pCVD diamond sensor, one would expect about nine times higher average amplitude with diamond.

The signals pulses obtained with epi sample are short and fast, having rise time and FWHM comparable with the diamond sensors. The epi samples also meet the requirement for BCM sensors to be radiation tolerant. But their performance in terms of SNR is inadequate. Therefore, diamonds were chosen for the BCM sensor material.

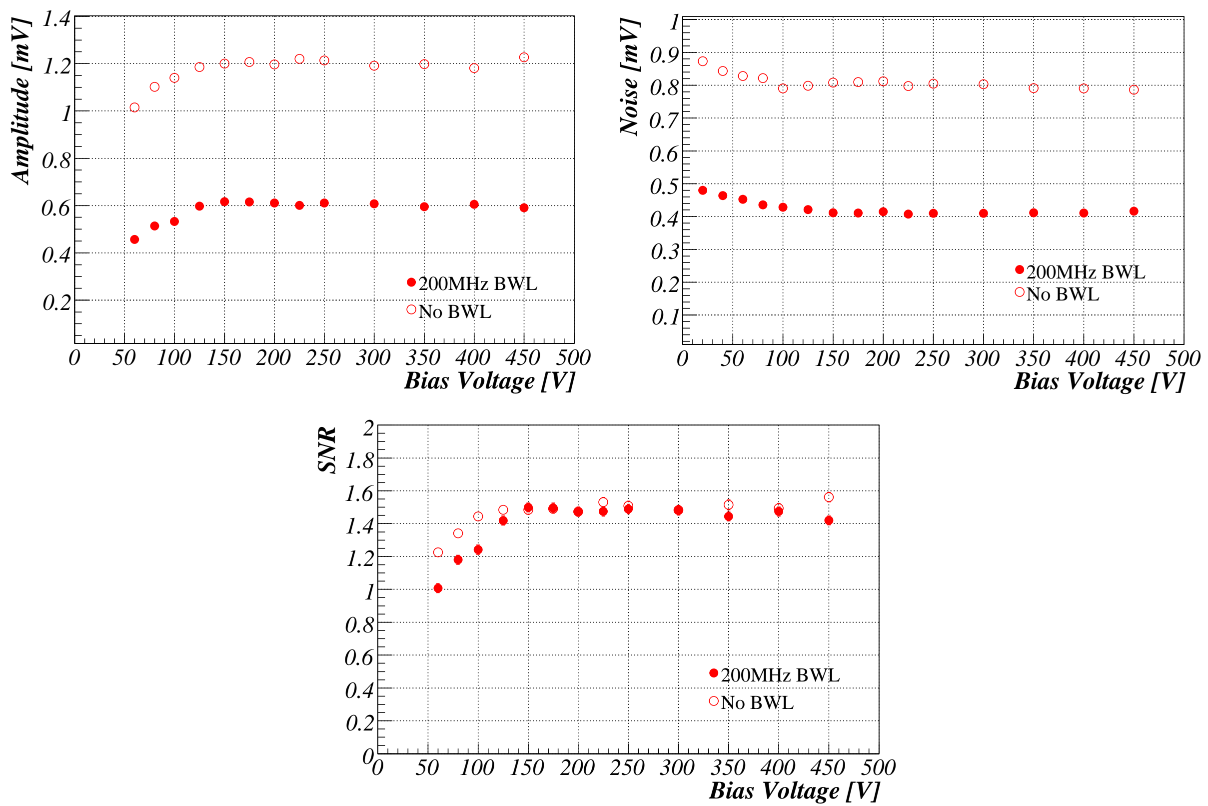

Figure 5.13: *The MP amplitudes (left), noise RMS (middle) and SNR as a function of voltage applied to 50 μm epi sample for 200 MHz (closed markers) and no no BWL (open markers) at readout.*

CHAPTER 6

CONCLUSIONS

The thesis presents the work performed during the development phase of the ATLAS BCM system. The BCM detector modules were envisaged to be located at the innermost parts of the ATLAS detector, with sensors situated close to the interaction point and the beam pipe. Here, particle fluences as high as 10^{15}cm^{-2} are expected in 10 years of LHC operation. Also, very fast analogue signals are required, with rise time up to $\sim$1 ns and signal width below $\sim$3 ns, since the ATLAS BCM system is aimed to monitor the beam conditions close to the interaction point and provide a complementary luminosity measurement on a bunch-bunch basis. For its optimal performance, a MIP sensitivity is desired.

In the search for radiation tolerant sensor material, two options were initially considered: pCVD diamond and n-type epitaxial silicon. The pCVD diamond is known to be radiation hard, being able to withstand particle fluences as high as 2.2×10^{15}cm^{-2} with signal degradation of only 15%, which qualified that material as one of the candidates for BCM sensors.

Annealing studies with thin epitaxial silicon sensors were performed by the Hamburg group in the frame of the RD50 collaboration, which is developing radiation hard semiconductor devices for high luminosity colliders. These studies, carried out at annealing temperatures of 60°C and 80°C, indicated that, in terms of N_{eff}, epi devices exhibit superior radiation tolerance compared to any standard FZ silicon material. Motivated by these results, the epi devices were also considered as a potential candidate for the ATLAS BCM sensors. To verify the results at elevated annealing temperatures, the measurements at annealing temperature of 20°C, which is closer to the annealing scenarios expected at the LHC, were performed for annealing time of about 3.5 years. Epi samples were irradiated, either with reactor neutrons or 24 GeV/c protons up to fluences of 10^{16}cm^{-2}. The results were found to be in agreement with the ones obtained by the Hamburg group.

The N_{eff} stable damage component has two contributions, one is due to incomplete donor removal, while the other is due to the generation of stable defects during irradiation. Donor removal is dominating at low fluences and was observed to occur more rapidly in the proton irradiated samples. The radiation induced stable damage component becomes important with higher fluences. In the study performed in the scope of this work, it was confirmed that in contrast to the case of FZ silicon material, the stable component of radiation induced damage is dominated by donors. The stable damage introduction rate was observed to be g_C=($-$0.62$\pm$0.15)$\times10^{12}$cm^{-2} in case of neutron irradiation and g_C=($-$1.7$\pm$0.2)$\times10^{12}$cm^{-2} for the 50 μm epi samples irradi-

ated with protons. This resulted in a positive space charge immediately after proton or neutron irradiation for the entire fluence range considered. During the initial annealing, the short term component increases the positive space charge due to annealing of irradiation induced acceptors. This results in an initial steep rise in measured V_{FD} at short annealing times after irradiation. The long term annealing component tends to decrease the positive space charge on account of acceptor creation. At higher fluences and longer annealing times, acceptor creation overcompensates the stable donor component, resulting in negative space charge. This acceptor creation during long term annealing would partly compensate the initial increase of V_{FD} due to irradiation induced stable donors. Thus, contrary to the case of FZ silicon, in epi material annealing during beam off periods at the LHC would even be profitable.

The annealing of leakage current was found to follow the behaviour observed in other silicon materials. The value of damage parameter, α, at T_r=20°C after 240h at annealing temperature T_a20^{o}C, was found to be α(240h at 20°C)=(3.9$\pm$0.8)$\times 10^{-17}$ A/cm. Annealing for 240h at 20°C corresponds to 80 min at 60°C if an activation energy of E_I=1.09 eV is used. The measured value α(240h at 20°C) agrees well with the standard value of α=(3.99$\pm$0.03)$\times 10^{-17}$A/cm after 80 min at 60°C.

The BCM front end electronics is based on a two stage amplifier with an overall bandwidth of 500 MHz and housed in a module box together with the sensor. The performance of a BCM prototype module equipped with 50 μm thick epi sample was examined with electrons from a ^{90}Sr source and scintillator as a trigger for MIP signals. Although the signal timing properties were observed to be acceptable for the BCM system, being comparable with diamond signals, the SNR was found to be less than 1.5. On the other hand, measurements showed that, with pCVD diamond, much higher SNR can be achieved. This lead to a decision to use pCVD diamonds for the sensors in the ATLAS BCM system.

Prototype and final modules assembled with diamonds were tested in numerous test beam measurements and measurements with β electrons from the ^{90}Sr source. These tests showed that using two diamond sensors in a double decker configuration increases the SNR. In such a configuration the signals from two diamonds are passively summed before they are amplified by the front-end electronics. Measurements showed that this configuration gives about two times higher MP amplitude while the increase in noise, σ_n, was only around 30%. The noise value σ_n for a double decker assembly was found to be independent of the bias voltage for electric field strengths up to 3 V/μm. Also, noise was observed to be independent of the BCM module leakage current for currents up to 0.5 μA.

Inclining the sensors by 45° with respect to the ionising particles increases the signal by a geometrical factor of $\sqrt{2}$. Given that an average particle track hitting the BCM sensors in ATLAS is expected to be parallel to the beam pipe, the BCM diamond sensors are titled by 45° towards the beam pipe.

In the laboratory setup with ^{90}Sr electrons as a source of MIPs at normal incidence, limiting the bandwidth at readout from 1 GHz to 200 MHz improved the SNR by a factor of $\sim$1.16. Therefore, in ATLAS a 200 MHz fourth order filter is used before the analogue signals are digitised. Test beam measurements with MIP signals showed that limiting the bandwidth from 1 GHz to 200 MHz increases the analogue signal rise time and FWHM by about 70% and 60% respectively. This resulted in a rise time of $\sim$1.5 ns and FWHM of $\sim$2.8 ns, which is acceptable

for the BCM system in ATLAS. With a 300 MHZ BWL applied at readout, the timing resolution of analogue signals was measured to be better than 400 ps in the threshold range between 0.1 and 2 MP amplitude of MIP signal. In a ^{90}Sr setup, typical SNR values of 7.0–7.5 were achieved with final BCM modules for 1 MIP particles at normal incidence and a 200 MHz BWL at readout.

The analogue signal efficiency for MIP particles was scanned over the sensor surface using test beam measurements. The response was observed to be more or less uniform over the sensor active surface for thresholds ranging up to $\sim$0.5 MP amplitude of MIP signal. At higher thresholds the response becomes more non-uniform. The non-uniformity was attributed to the grain structure of the pCVD diamond material.

Electronics boards used for digitisation of analogue signals are based on a NINO chip, which encodes the time-over-threshold information in the width of output LVDS digital pulses. The correlation between input analogue signal amplitude and NINO output signal width is not linear and saturates rather quickly. Thus, in order to increase the dynamic range, the input analogue signal is split with a ratio of around 1:11 into two NINO inputs. The measurements presented in this work were performed with the channel with higher input signal. Different prototype NINO electronics boards were tested with test beam pions at 45° incidence providing MIP signals, where spare final modules and most of the final services were used. A median SNR between 6 and 8.8 was achieved with prototype boards, depending on the board and detector module. The timing resolution of digital signals was found to be better than $\sim$800 ps for NINO discriminator thresholds between $\sim$0.5 and $\sim$1.8 of median MIP signal. These test beam measurements served as input when deciding on the design of final NINO board, where the test board with the best performance in terms of median SNR was chosen. However, in order to extend the NINO threshold range to higher values, thus making the system more manageable, an additional amplification was added to the final NINO boards.

The performance of final NINO boards was examined in a laboratory environment with a final detector module. Efficiency and noise rate dependence on NINO discriminator threshold were measured. Electrons from a ^{90}Sr source were used to evaluate the efficiency curve. In order to estimate the noise rates and 1 MIP efficiencies which can be expected in ATLAS at the end of the BCM readout chain, the noise rate and efficiency curves as measured with the laboratory setup were scaled by appropriate factors. The factors were determined by comparison of laboratory and test beam results, obtained for prototype modules. The estimated median SNR for 1 MIP expected in ATLAS was found to be 9.0$\pm$0.5. Furthermore, for NINO discriminator thresholds between 210 mV and 300 mV, the BCM system is expected to operate with a single hit fake rate between 10^{-3} and 10^{-5} per bunch crossing and 1 MIP efficiency between 99% and 96%. However, the exact level of fake rates per bunch crossing in ATLAS depends on what type of logical combinations of signals from eight BCM modules will be used.

POGLAVJE 7

POVZETEK DOKTORSKEGA DELA

7.1 Uvod

V Evropski organizaciji za jedrske raziskave (CERN) bo predvidoma jeseni 2008 pričel delovati krožni hadronski trkalnik LHC (Large Hdron Collider) [B^+04]. Dva curka protonov bo pospeševal do energije 7 TeV in tako omogočal trke med protoni pri težiščni energiji 14 TeV, ki je približno sedemkrat večja kot pri trenutno največjem hadronskem trkalniku Tevatron v Fermilabu. Curka protonov bosta strukturirana v 2808 gruč, kjer bo vsaka od teh gruč vsebovala 1.1×10^{11} protonov. Časovni interval med dvema sledečima gručama bo 25 ns. Načrtovana trenutna luminoznost LHC-ja znaša $10^{34}\mathrm{cm}^{-2}\mathrm{s}^{-1}$. ATLAS (A Toroidal LHC ApparatuS) [ATL08] je eden izmed eksperimentov ob LHC. Glavna motivacija za njegovo izgradnjo je iskanje odgovora na vprašanje glede veljavnosti Standardnega modela osnovnih delcev ter možno odkritje znakov nove fizike.

Celotna energija, shranjena v enem od protonskih curkov v trkalniku LHC, bo znašala 350 MJ, kar je približno dva reda velikosti več kot pri visoko enrgijskih trkalnikih kot sta Tevatron in HERA. V primeru odpovedi delovanje enega izmed elemntov pospeševalnika lahko posledične izgube curkov poškodujejo tako pospeševalnik kot eksperimente ob njem. Zato so vsi eksperimenti ob LHC razvili svoj zaščitni sistem poleg sistema zagotovoljenga s strani pospeševalnika samega. Pričujoče delo je osredotočeno na sistem za spremljanje kakovosti curka protonov (BCM–Beam Conditions Monitor), ki je bil načrtovan za zaščito detekotrja ATLAS.

Zaradi njune visoke sevalne odpornosti sta bila kot senzorski del v sistemu BCM za ATLAS preizkušena dva različna materiala, polikristalni (pCVD) diamant in tanek epitaksialni (epi) silicij tipa n. Meritve, predstavljene v tem delu, so pokazale, da pCVD diamant nudi boljšo možnost delovanja sistema BCM glede razmerja signal–šum. Zato je bil na koncu kot sensor BCM sistema izbran pCVD diamant.

V nadaljevanju je najprej opisano delovanje sistema BCM za ATLAS, kjer so tudi navedene zahteve za njegovo delovanje. Temu sledita razdelka, kjer so predstavljeni rezultati meritev s pCVD diamantom in epi silicijem. Meritve s pCVD diamantom vključujejo študij analognih in digitalnih signalov skozi različne faze razvoja sistema BCM. Podana je tudi ocena pričakovanega delovanja sistema BCM v ATLAS-u na koncu bralne verige. Predstavljeni so izsledki meritev časovnega razvoja zapornega toka in efektivne koncentracije primesi pri 20°C pri epi diodah različnih debelin, obsevanih s protoni ali nevtroni. Podani so tudi rezultati meritev delovanje BCM detektorskega modula, opremljenga s 50 μm debelo epi diodo.

7.2 Opis sistema BCM pri ATLAS-u

Glavni namen sistema BCM je zaznavanje zgodnjih znakov nestabilnosti protonskih curkov ter zaščita detektorja ATLAS proti škodljivim izgubam protonskih curkov preko proženja signala za zaustavitev protonskih curkov. Sistem BCM bo omogočal spremljanje trenutnega toka delcev v bližini interakcijske točke in s tem možnost razlikovanja med normalnimi dogodki, ki so posledica trkov protonov, ter anomanimi dogodki, ki pripadajo ozadju. Poleg tega bo omogočal tudi merjenje tenutne luminoznosti, kar bo predstavljalo komplementarno informacijo k sistemu LUCID [Sou06], glavnemu sistemu za spremljanje luminoznosti pri eksperimentu ATLAS.

Zunaj detektorja ATLAS, na obeh straneh interakcijske točke pri z=$\pm$18 m, leži 18 m dolg bakren kolimator TAS. V primeru nezgode[1] lahko začne protonski curek strgati po kolimatorju TAS ali po curkovni cevi. To povzroči plaz delcev v smeri curka, ki lahko poškodujejo detektor ATLAS. Poleg teh nezgodnih izgub curka so prisotne tudi naravne izgube. Te vključujejo interakcije protonov v halu curka s kolimatorjem TAS, v bližini vhoda v območje detektorja ATLAS. Druga možnost so interakcije protonov iz curka z atomi plina (H_2, CO_2, CH_4,...) ostalega v curkovni cevi v področju znotraj detektorja ATLAS. Oboje povzroči plaz delcev v smeri curka protonov.

Če postavimo dve BCM detektorski postaji pri z=z_{bcm} simetrično okrog interakcijske točke, potem plaz delcev, ki izhaja iz $|z|$>$|z_{bcm}|$, zadane najbližjo detektorsko postajo ob času δt=$2z/c$ prej kot postajo na drugi strani interakcijske točke (slika 7.1). Po drugi strani trki protonov, ki se zgodijo v interakcijski točki ob vsakem prehodu gruče protonov v curku, dajo koincidenčni signal v obeh detektorskih postajah vsakih 25 ns. Za optimalno ločevanje med normalnimi dogodki, ki so posledica trkov protonov, ter anomalnimi dogodki, ki so rezultat nezgodnih ali naravnih izgub curka, morata postaji BCM ležati pri z_{bcm}=$\pm$1.9 m okrog interakcijske točke. To ustreza časovni razliki δt=12.5 ns. Tako bo plaz delcev, ki so posledica anomanih dogodkov, povzročil signal na najbližji postaji 6.25 ns pred samim trkom protonov v interackijski točki ("zadetki izven časa"), medtem ko sekundarni delci iz interakcije doseżejo obe postaji 6.25 ns po sami interakciji ("zadetki v času"). Tako lahko anomalne dogodke identificramo po zadetkih "izven časa", zadetke "'znotraj časa" pa uporabimo za spremljanje trenutne luminoznosti.

V ATLAS-u je osem BCM detektorskih modulov instaliranih na podporno strukturo (slika 7.2). Ta struktura podpira tudi Blazinični detektor, ki je eden izmed poddetektrskih sistemov v Notranjem detektorju pri eksperimentu ATLAS. Na vsaki strani interakcijske točke,

[1] Do nezgode lahko pride zaradi nepravilne nastavitve katerega od magnetov v fazi vbrizgavanja protonskih curkov v LHC ali odpovedi delovanja enega od magnetov.

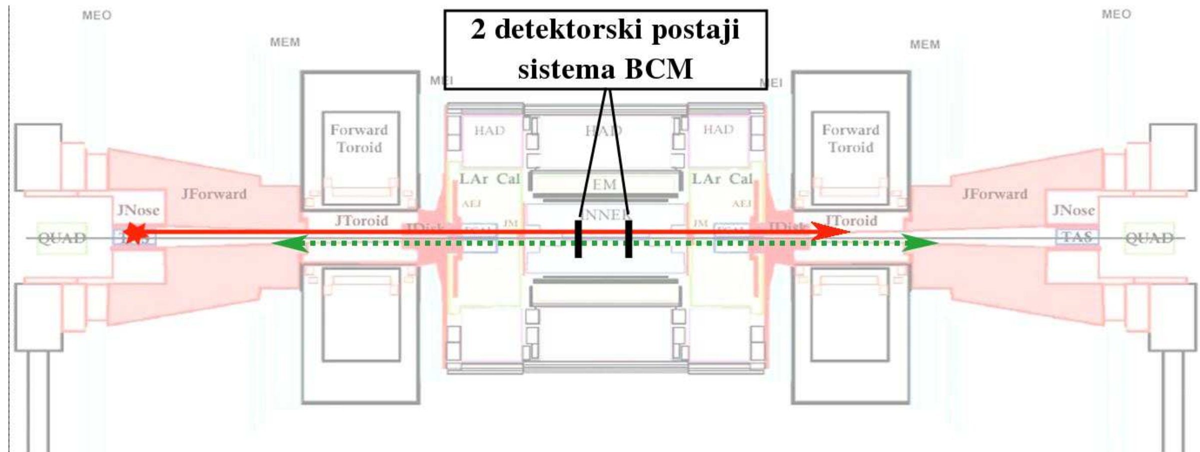

Slika 7.1: Detektor ATLAS z dvema detektorskima postajama BCM pri $\pm z_{bcm}$. Plaz delcev (redč) doseže levo postajo z_{bcm}/c preden pride do trkov v interakcijski točki. Sekundarni delci iz interakcij (zeleno) to postajo dosežejo z_{bcm}/c po interakciji ter dajo koincidenčne signale na obeh postajah BCM.

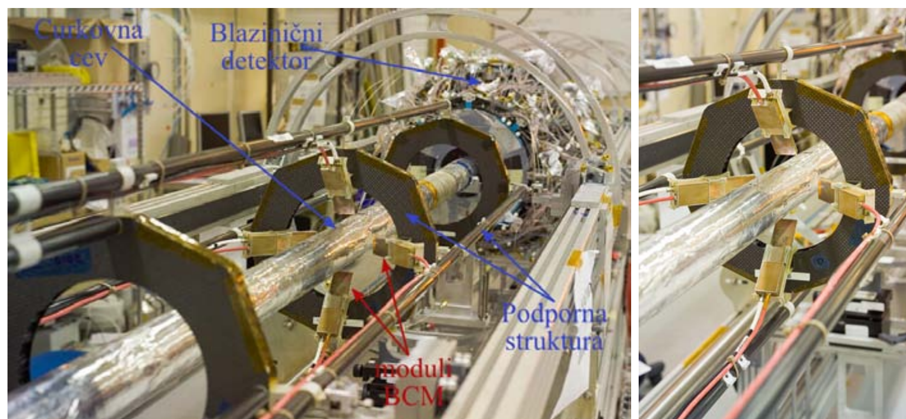

Slika 7.2: Detektorskih moduli sistema BCM instalirani na podporni strukturi.

pri z=184 cm, so štirje detektorski moduli sistema BCM, ki so postavljeni simetrično pri ϕ=0°, 90°, 180° in 270°. Nameščeni so tako, da senzor v modulu leži pri r~55 mm (psevdorapidnost η~4.2) od protonskega curka, kjer kot med normalo na senzor in curkovno cevjo oklepa 45°. (slika 7.3)

Sistem BCM v ATLAS-u bo prvi sistem za spremljanje kakovosti žarka znotraj eksperimenta, ki bo temeljil na meritvah ob vsakem prehodu gruče protonov (na skali ns). Podobni sistemi pri ostalih eksperimentih ob LHC ter pri eksperimentih BaBar in CDF temeljijo na merjenju akumulirange pretoka delcev, ki je integriran preko časovne skale μs.

Za optimalno razlikovanje med normalnimi in anomalnimi dogodki mora biti sistem BCM občutljiv na minimalno ionizirajoče delce (MIP delci). Prav tako je občutljivost na minimalno ionizirajoče delce (občutljivost 1 MIP) potrebna za meritve luminoznosti. Okolje z visoko stopnjo obsevanja ter visoka pogostost interakcij v ATLAS-u postavljata težke zahteve za senzorje

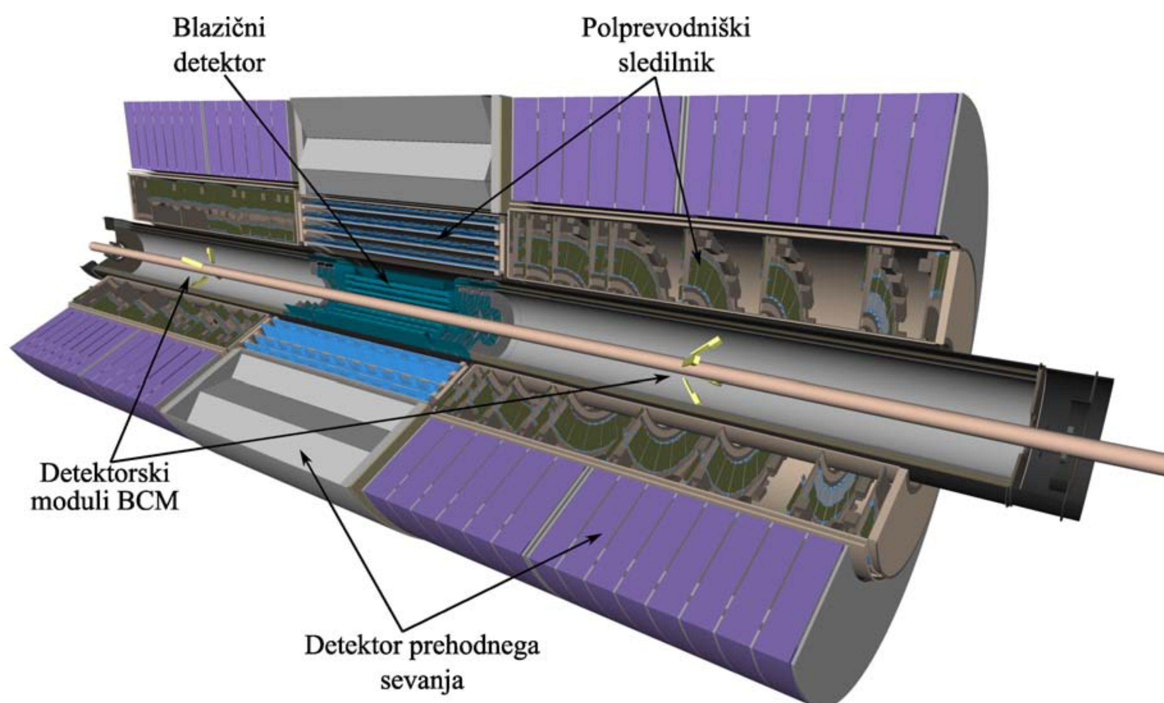

Slika 7.3: *Položaj detektorskih modulov sistema BCM v detektorji ATLAS. Označeni so tudi najbolj notranji deli detektorja ATLAS.*

in elektroniko v BCM detektorskih modulih. V 10 letih delovanja pospeševalnika LHC bo sevalno polje na lokaciji senzorjev predvidoma znašalo okrog 10^{15} delcev (večinoma pionov) na cm^2. Prdevidene ocene ionizacijske doze so $\sim$0.5MGy. Zaradi visoke pogostosti prehodov protonskih gruč, ki znaša 40 MHz, je potrebno hitro procesiranje signalov. Zahtevani so signalni pulzi z dvižnim časom $\sim$1 ns, širine $\sim$3 ns ter postavitev signala na osnovni signalni nivo v manj kot $\sim$10 ns.

Instalirani BCM detektorski moduli so pokriti s sloji, ki so potrebni za delovanje Blazičnega detektorja. Kakršnokoli posredovanje je malo verjetno, saj bi zahtevalo razstavitev teh slojev. Zato morajo biti BCM detektorski moduli enostavni, robustni ter brez tveganih sestavnih delov.

7.2.1 Detektorski moduli

Končni BCM detektorski moduli, instalirani v detektorju ATLAS, vsebujejo polikristalne (pCVD) diamante, ki služijo kot sensorski material sistema. Ti sensorji so rezultat sodelovanje kolaboracije RD42 [RD4] ter proizvajalca Element Six Ltd [E6]. Polikristali so bili gojeni s procesom kemijskega naparjevanja (Chemical Vapour Deposition) [PK95]. Senzorji so debeli okrog 500 μm, s površino 1×1 cm^2. Obe strani senzorjev sta metalizirani s Ti–Pt–Al kontakti površine 8×8 cm^2, ki so bili narajeni na Univerzi v Ohiu, ZDA.

Časovne lastnosti tokovnega signala, ki ga inducira inoizirajoiči delec v pCVD diamantnem senzorju, so določeni z veliko hitrostjo nosilcev naboja v električnem polju ter kratkimi časi za ujemanje nosilcev naboja na pasteh tudi pred obsevanjem. Da bi dosegli visoke in ozke signalne pulse bodo senzorji delovali blizu saturacijske hitrosti nosilcev naboja (>10^7cm/s), pri zunanji napetosti ±1000 V, ki bo omogočala električno polje jakosti 2 V/μm. Sevalna odpornost pCVD diamantov je bila preverjena pri fluenci 2.2×10^{15} protonov na cm^2, kjer je bilo opaženo le $\sim$15% poslabšanje nabojnega signala [A$^+$03]. Zaradi velike energijske špranje (E_g=5.47 eV) diamanta, so za diamantne senzorje značilni tudi nizki temni tokovi. S tipičnim pCVD diamantnim senzorjem, uporabljenim v sistemu BCM, je bil izmerjen temni tok pod 100 pA pri napetosti ±1000 V. Izmerjena razdalja zbiranja naboja [2] pri tej napetosti pa je tipično znašala $\sim$220 μm (glej razdelek 7.3).

Da bi povečali amplitudo signalov sta uporabljena dva diamantna senzorja, kjer sta signala iz obeh diamantov pred ojačevalno stopnjo pasivno sešteta. Notranji elektrodi diamantov v tej sestavi sta ozemljeni in povezani na linijo, ki vodi do ojačevalca, medtem ko sta zunanji elektrodi povezani na zunanjo napetost. Tako se v obeh diamantih ustvari električno polje jakosti 2 V/μm, ko to sensorsko sestavo priključimo na napetost ±1000 V. Pri prehodu nabitega delca skozi to sestavo dobimo na signalni liniji vsoto induciranih signalnih tokov iz obeh diamantov.

Diamanta sta prilepljena na dva keramična (Al_2O_3) vsadka, na katerih so sledi Al–Pt metalizacije (slika 7.4). Tako vsadka združita signalni elektrodi obeh diamantov. Spodnji diamant je prilepljen na tanko keramično ploščico, kjer so sledi metalizacije za nadaljno vodenje signalne

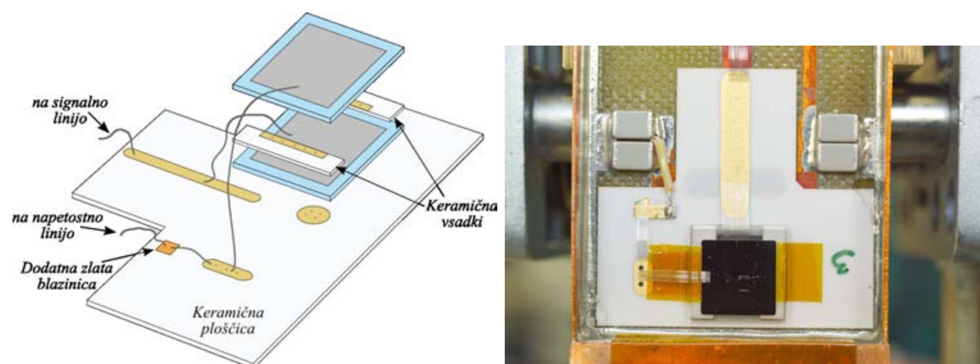

Slika 7.4: *Levo: konfiguracija sestava z dvema diamantnima senzorjema. Desno: Slika senzorjev v detektorskem modulu.*

[2]Angl. charge collection distance [Zha94].

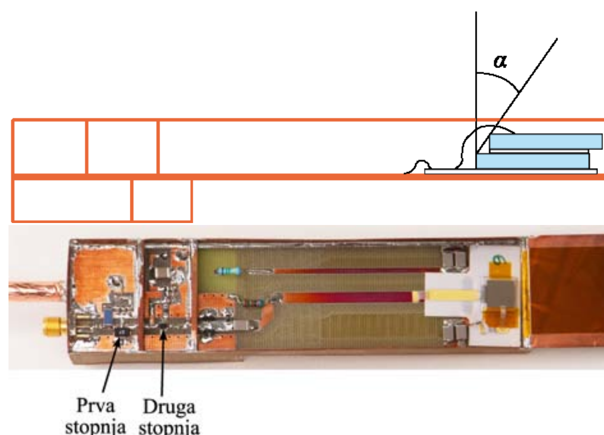

Slika 7.5: *Zgoraj: Shema detektorskega modula z dvema diamantoma, gledano od strani. Spodaj: Fotografija modula.*

in napetostne linije. Celoten sensorski sestav s keramično ploščico je prilepljen na napetostno linijo v detektorskem modulu. Zgornji diamant je zamaknjen bližje robu modula, tako da je kot α=45° (slika 7.5). Tako je površina, kjer oba diamanta prispevata k signalu, večja saj so moduli instalirani v detekotrju ATLAS nagnjeni proti žarkovni cevi za 45°. Detektorski moduli so narejeni iz materiala G10.

Visoka napetost je vodena do spodnje ravnine spodnjega diamanta preko malih metaliziranih luknjic v keramični ploščici ter preko tankih žičk do zgornje elektrode zgronjega diamanta. Dodatno je do zgornje elektrode zgornjega diamanta visoka napetost vodena še preko zlate blazinice in tankih žičk.

Združen signal je preko tankih žičk voden od zgornje elektrode do elektronskega vezja, kjer 5 cm dolga linija 50 Ω vodi do ojačevalne stopnje (slika 7.5). Tako je sevalno polje na področju ojačevalne stopnje približno 30% nižje kot na področju senzorjev. Elektroniko znotraj modulov, namenjno procesirnaju analognih signal, je razvil Fotec [FOT]. Sestavljena je iz dveh stopenj tokovnega ojačanja. Prva stopnja vsebuje 500 MHz Agilent MGA–62563 nizkošumni ojačevalec, druga pa ojačevalec Mini Circuit serije Gali–52. Ojačan signal je nadalje peljan do 50 Ω koaksialnega kabla.

7.2.2 Celotna bralna shema

Analogni signal iz vsakega od osmih detektorskih modulov so vodeni preko 14 m dolgih kablov na območje, kjer je možna uporaba nekoliko manj sevalno odporne elektronike[3] Ta elektronika, ki bo služila za digitizacijo analognih signalov, temelji na uporabi čipa NINO [A$^+$04]. Čip NINO služi kot ojačevalec in diskriminator z zmožnostjo meritve časa nad pragom (angl. time–over–threshold, TOT). Vhoden analogni signalni pulz pretvori v LVDS digitalni pulz ob fiksnem času po prihodu vhodnega signala. Naboj na vhodu je zakodiran preko časa nad pra-

[3]Ocenjena ionizacijska doza na tem mestu je okrog 10 Gy v 10 letih.

gom v širino izhodnega digitalnega pulza. Tako je slednja korelirana z amplitudo vhodnegal pulza.

Vsak od osmih detektorskih modulov je povezan na enega od elektronskih vezji, ki vsebuje čip NINO (slika D.1). To vezje vhodni signal najprej filtrira preko nizko pasovnega filtra četrtega reda s frekvenčno pasovno širino 200 MHz. To dodatno filtriranje je bilo vključeno, ker so meritve pokazala, da izboljša signal–šum BCM detekorski modulov. Meritve so tudi pokazale, da se TOT odziv NINO čipa v odvisnosti od NINO diskriminacijskega praga saturira precej hitro. Za povečanje dinamičnega območja občutljivosti NINO čipa je po filtriranju signal razdeljen na dva vhod v NINO čip v približnem razmerju 1:11. Sledeča dva digitalna signala sta zatem pretvorjena v optični signal. Vsi optični signali (16, dva za vsak detektorski modul) so vodeni preko 70 m dolgih optičnih kablov do sobe izven ATLAS detektorja. Tu so nadalje pretvorjeni v PECL električne signale in povezani na dva Xilinx Vitrex-4 razvojna modula, ki vsebujeta FPGA (Field Programmable Gate Array) čip. FPGA čip bo procesiral signale v realnem času, določil širino signalnih pulzov ter njihov čas prihoda za vsakega od osmih modulov. Čip bo imel vprogramirano logiko za odločitev ali so pogoji curka dobri ali ne in poslal prožilni signal za zaustavitev curka v primeru zanane večje izgube curka.

7.3 Osnove delovanja silicijevih in diamantnih detektorjev

Silicijevi detekotrji so v osnovi diode (p–n stiki) oziroma polja diode z izbrano geometrijo na silicijevi rezini in delujejo podobno kot ionizacijska celica. V diodi se okrog p–n stika ustvari območje osiromašenja, kjer je gostota nosilcev naboja zelo nizka. V tem območju je prisoten prostorski naboj, ki ga tvorijo ionizirane primesi. Ta prostorski naboj ustvari električno polje v območju osiromašenja. Pare elektron–vrzel, ki nastanejo pri prehodu ionizirajočega delca skozi slicij, zaznamo kot tokvni sunek. K izmerjenemu signalu prispevajo le pari, ki nastanejo v osiromašenem območju, saj je le tam prisotno električno polje, ki pare loči. Za čim večje razmerje signal–šum je pri delovanju detektorja nanj priključena dovolj visoka zaporna napetost, tako da je osiromašena celotna prostornina detektorja. Običajno je gostota primesi ne p[4] strani stika v diodi, precej manjša kot na strani n[5]. V tem primeru se debelina osiromašene plasti izraža kot

$$w_{scr}(V) = \sqrt{\frac{2\epsilon_{Si}\epsilon_0}{e_0|N_{eff}|}V}, \tag{7.1}$$

kjer je ϵ_0 dielektričnost, ϵ_{Si} dielektrična konstanta silicija, V zaporna napetost na diodi in N_{eff} efektivna koncentracija ioniziranih primesi[6] na strani z manjšo koncentracijo primesi (n stran). Tako je napetost potrebna z popolno osiromašenje diode (napetost popolnega osiromašenja) določena z enačbo

$$V_{FD} = \frac{e_0|N_{eff}|D^2}{2\epsilon_{Si}\epsilon_0}, \tag{7.2}$$

kjer je D debelina detektorja.

Napetost V_{FD} lahko določimo z merjenjem kapacitete, C, v odvisnosti od zaporne napetosti, V. V primeru, da je N_{eff} konstantna po debelini vzorca, je ta odvisnost dana z

$$C(V) = \frac{\epsilon_{Si}\epsilon_0 S}{w} = \sqrt{\frac{|N_{eff}|e_0\epsilon_{Si}\epsilon_0}{2V}}S, \tag{7.3}$$

kjer je S aktivna površina vzorca. Od tod sledi, da kapaciteta vzorca pada z naraščajočo zaporno napetostjo, dokler ni osiromašen celoten vzorec. Za napetosti nad V_{FD} pa se kapaciteta ne sperminja več. Tako lahko napetost V_{FD} (in s tem N_{eff}) določimo iz pložaja kolena v izmerjeni odvisnosti kapacitete od zaporne napetosti.

[4] V p tipu so primesi akceptorjev. Ionizirani akceptorji okrog stika ustvarijo negativen prostorski naboj.

[5] V n tipu imamo primesi donorjev. Okrog stika ti ionizirani donorji ustvarijo pozitiven prostorski naboj.

[6] Efektivna koncentracija primesi je določena kot razlika med koncentracijo ioniziranih donorjev, N_D, in koncentracijo ioniziranih akceptorjev, N_A, $N_{eff} = N_D - N_A$

Zaradi visoke upornosti diamanta, v diamantnih detekorjih ni potrebno ustvariti območja osiromašenja. Dovolj sta dve elektrodi na obeh straneh rezine diamanta, ki jih priključimo na naptost. Visoka upornost diamanta potem prepreči prisotnost visokih temnih tokov in s tem omogoči nizek šum tudi brez osiromašenja.

Ionizirajoči delec po poti skozi detektor generira pare epektron-vrzel. Te pare loči električni polje prisotno v detektorju ob njegovem delovanju. Potovanje prostih nosilcev naboja v električnem polju inducira tokovni sunek na elektrodah detekotrja [Ram39]. Med potovanje se lahko prosti nosilci ujamejo na pasteh. Če so emisijski časi za izsevanje ujetih nosilcev naboja dovolj dolgi, ujet naboje ne prispeva k tvorbi signala.

Pasti lahko nastanejo kot posledica obsevanja. Zaradi polikristalne narave pCVD diamantu, so v tem materialu pasti prisotne tudi pred obsevanjem. Tako je v diamantnem detektorju potovanje generiranih prostih nosilce naboja omejeno tako z debelino detektorja kot z dolžino preden se naboji ujamejo na pasteh. Kvaliteta pCVD diamanta je običajno navedena z izmerjeno količino imenovano *razdalja zbiranja naboja* [Zha94], ki je definirana kot

$$\delta^{ccd} = D\frac{Q_{ind}}{Q_{gen}}, \tag{7.4}$$

kjer je Q_{ind} izmerjen naboj in Q_{gen} generiran naboj pri prehodu ionizirajočega delca.

7.4 Meritve s pCVD diamanti

BCM detektorski moduli so bili v različnih fazah razvoja preiskušeni tako z β elektroni iz izvora ^{90}Sr v laboratoriju kot v različnih testnih curkih delcev. V tem razdelku so predstavljeni le rezultati meritev, ki so pomembneje vplivali na razvoj sistema BCM. V zadnjem delu so predstavljeni tudi rezultati meritev, ki so vključevale digitizacijo analognih signalov s končno in prototipnimi različicami elektronskega vezja z NINO čipom. Kot omenjeno v razdelku 7.2.2 je vhodni analogni signal razdeljen na dva dela v razmerju 1:11 pred vhodom v NINO čip. Vse meritve z moduli, ki vsebujejo NINO čip ter ustrezno elektroniko, so bile opravljene z vhodom z večijim vhodnim signalom.

Izpostavitev pCVD diamantnega senzorja ionizirajočemu sevanju lahko poveča njegovo učinkovitost zbiranja naboja [F$^+$92, B$^+$98]. Ta efekt je znan kot "polnenje"[7]. Polikristalni diamant je sestavljen iz več monokristalnih diamantnih zrn različnih velikosti in orientacij. Ti monokristali rastejo v stebričasti obliki, kjer se širina posameznih stebrov povečuje skozi rast kristala. Na robovih monokristalnih zrn je kristalna mreža zelo deformirana. Robovi tako predstavljajo območja, kjer je koncentracija električno aktivnih defektov zelo visoka [M$^+$99a, Oh99]. Ti defekti tvorijo enrgijske nivoje znotraj energijske špranje in lahko ujamejo nosilce naboja. Fenomen polnenja pripisujejo polnenju defektov z globokimi energijskimi nivoji, za katere so značilni dolgi emisijski časi. Nosilci naboja, sproščeni ob prehodu ionizirajočega delca, se ujamejo na teh pasteh in jih pasivirajo. Napolnjeno stanje lako vzdrži nekaj mesecev, če je diamant hranjen v temi pri sobni temperaturi.

BCM diamantni senzorji bodo vseskozi delovanje ATLAS eksperimenta v napolnjenem stanju zaradi stalne prisotnosti ionizirajočih delcev. Zato so bili za stabiliziranje efekta polnenja vsi diamantni senzorji, uporabljeni pri meritvah, opisanih v tem razdelku, pred meritvami izpostavljeni ^{90}Sr z aktivnostjo 37 MBq za en dan.

Če ni navedeno drugače, so bili pri vse meritvah uporabljeni diamantni senzorji, ki imajo približno enake lastnosti kot senzorji v modulih instaliranih v ATLAS-u. Te so podane v razdelku 7.2.1. V večini primerov je detekorski modul vseboval dva diamanta v konfiguraciji predvideni za sistem BCM v ATLAS-u (glej razdelek 7.2.1).

[7] Angl. "pumping" včasih "priming" [Mei99].

7.4.1 Detektorski moduli

Meritve v testnem curku

Prototipna različa BCM detektorskih modulov je bila preizkušena v testnem curku nizko energijskih protonov v splošni bolnišnici v Massachusetsu (MGH–Massechusats General Hospital), Boston, ZDA ter v testnem curku visoko energijskih protonov na protonskem sinhrotronu SPS v CERN-u. Pri MGH so protoni z energijo 125 MeV in 200 MeV omogočali signale ekvivalentne 3.8 in 2.7 MIP. Spodaj navedene izmerjene amplitude pulzov pri teh meritev so skalirane na 1 MIP. Pri SPS v CERN-u so protoni z gibalno kolčino 110 GeV/c ustrezali 1 MIP-u. Tako pri MGH kor pri SPS meritvah je bil časovni potek signala iz BCM detekotrskih modulov zabeležen z digitalnim osciloskopom, do katerega so bili signali vodeni preko 16 m dolgega koaksialnega kabla. Pri MGH meritvah je frekvenčna pasovna širina uporabljenega osciloskopa znašala 4 GHz, pri SPS pa je bila le ta nastavljena na 1 GHz ali 200 MHz. Zajem podatkov je bil večinoma prožen s koincidenčnim signalom dveh scintilatorjev z efektivno površino 4×4 mm^2. V primeru MGH meritev sta bila oba scintilatorja postavljena za dvema BCM detektorskima moduloma gledano v smeri curka protonov, pri SPS pa sta bila dva detektorska modula postavljena med oba scintilatorja.

Pri analizi podatkov je bil za vsak dogodek narejen popravek osnovnega nivoja v časovnem poteku signala. Za vsak dogodek je bila izračunan povprečna vrednost signala S_{bl} na časovnem intervalu 10 ns pred signalnim pulzom. Celotni časovni potek signala za ta dogodek je bil nato premaknjen za vrednost $-S_{bl}$.

Za vsak set podatkov je bil izračunan povprečen časovni potek signala. Amplituda pulza v posameznih dogodkih je bila nato odčitana kot največja vrednost signala v $\sim$2 ns časovnem intervalu okrog mesta, kjer je v povprečnem časovnem poteku signala nastopal vrha pulza. Na enem od setov podatkov sta bila preizkušeni tudi dva druga postopka iskanja amplitude pri posameznem dogodku. Pri prvem je bil polinom tretje stopnje prilagajan časovnemu poteku okrog pulza, pri drugem pa je bila uporabljena funkcija $\left(\frac{t-t_0}{\tau}\right)^n \mathrm{e}^{-(t-t_0)/\tau}$[8]. Najbolj verjetna amplituda (MP amplituda) je bila določena iz prilagajanja konvolucije Landauove in Gaussove funkcije k dobljeni porazdelitvi amplitud. Vrednosti MP amplitude, dobljenih iz treh različnih postopkov določanja amplitude pri posameznih dogodkih, so se razlikovale na nivoju 5%. Zato je bil pri nadaljni analizi uporabljen prvi omenjen postopek, saj je omogočal hitrejšo obdelavo podatkov. Ta postopek je bil uporablje pri vseh nadaljnih analizah podatkov.

Za določitev šuma je bil signal vzorčen ob fiksnem času pred pulzom v časovnem poteku signala posameznih dogodkov. Za oceno šuma je bila uporabljena širina σ_n Gaussove funkcije, priliagajane na dobljeno porazdelitev. Enaka postopka za določanje šuma σ_n in MP amplitude sta bila uprabljena pri vseh nadaljnih analizah meritev predstavljenih v tem delu. Navedena razmerja signal–šum se tako nanašajo na razmerje med MP amplitudo in šumom σ_n, dobljenih iz porazdelitev amplitud in šuma.

Meritve s prototipi detekorskih modulov so pokazali sledeč:

[8] Oblika izhodnega napetostnega signala po vbrizganju trenutnega tokovnega pulza $Q_{in}\delta(t)$ je dana z $\left(\frac{nt}{\tau}\right)^n \mathrm{e}^{-\frac{nt}{\tau}}$ za CR-RC^n elektronsko vezje [Spi05]. Tu je τ (dvižni čas) časovna konstanta diferenciatorja (CR) in je enaka časovni konstanti posameznih n integratorjev (RC).

- Nagib modulov za 45° proti smeri curka delcev poveča MP amplitudo za pričkovan geometriski faktor $\sqrt{2}$.
- Izmerjena vrednost šuma σ_n je bila neodvisna od jakosti električnega polja do 2 V/μm
- Pri električnem polju 2 V/μm in frekvenčni pasovni širini 4 GHz na bralnem osciloskopu se je z uporabo dveh 360 μm debelih diamantnih senzorjev MP amplituda povečala za približno faktor dva v primerjavi z enim senzorjem debeline 470 μm. Šum σ_n pa se je povečal le za 30%, kar se je odrazilo v več kot 50% večjem razmerju signal–šum.
- Pri električnem polju 2 V/μm omejitev frekvenčne pasovne širine na bralnem osciloskpu iz 1 GHz na 200 MHz izboljša razmerje signal–šum, saj zmanjša MP amplitudo za $\sim$30% vendar zmanjša šum σ_n za skoraj 60%.
- Izmerjena povprečni dvižni čas in povprečna širina pulza na polovici njegove višine (FWHM) nista kazala odvisnosti od električnega polja do jakosti 2 V/μm.
- Pri 1 GHz frekvenčni pasovni širini na bralnem osciloskpu je izmerjen povprečeni dvižni čas pulza znašal okrog 0.85 ns. Z omejitvijo na 200 MHz se je ta povečal na 1.5 ns.
- Izmerjena povprečena FWHM širina pulza je pri 1 GHz frekvenčni pasovni širini na bralnem osciloskpu znašala približno 1.75 ns. Ob omejitevi na 200 MHz se je ta povečala na 2.8 ns.

Meritve z izvorom ^{90}Sr

Sestavni deli postavite eksperimenta, uporabljene pri the meritvah, so ^{90}Sr kot izvor β elektronov, dva 2.5 mm debela Al kolimatorja ter scinitilator. Eden od kolimatorjev je bil postavljen med detektorski modul ter scinitilaotr, drugi kolimator pa med modul in izvor ^{90}Sr. Kolimatorja sta imela okrogli odprtnini s premerom 2 mm, ki sta bili skupaj s ^{90}Sr poravnani na centralni del diamantnih senzorjev. Scintilator je služil za proženje na 1 MIP signale, ki so jih po prehodu skozi diamant inducirali elektroni na elektrodah senzorjev.

Signali iz BCM modulov so bili vodeni preko 0.5 m dolgega koaksialnega kabla do digitalnega ozciloskopa LC546A LeCroy, ki je služil za beleženje časovnega poteka signalov iz BCM modulov s frekvenco vzorčenja 4 GHz. Meritve opisane v tem razdelku so bile opravljene s končno različico BCM detetktorskih modulov pri napetostih do $\pm$1000 V (polje 2 V/μm) ter s frekvenčna pasovno pasovno širino 1 GHz ali 200 MHz na bralnem osciloskopu. Skozi posamezno meritev je bil merjen tud temni tok detektorskega modula z uporabo merilne enote Keithely 237, ki je služila tudi kot napetostni izvor.

Spodaj so navedeni pomembnejši izsledki teh meritev.

- Neodvisnost Šuma σ_n od električnega polja v senzorjih je bila potrjena do jakosti 3 V/μm. Pri 200 MHz frekvenčni širini na bralnem osciloskopu je bila tipična izmerjena vrednost šuma σ_n 0.34 mV.

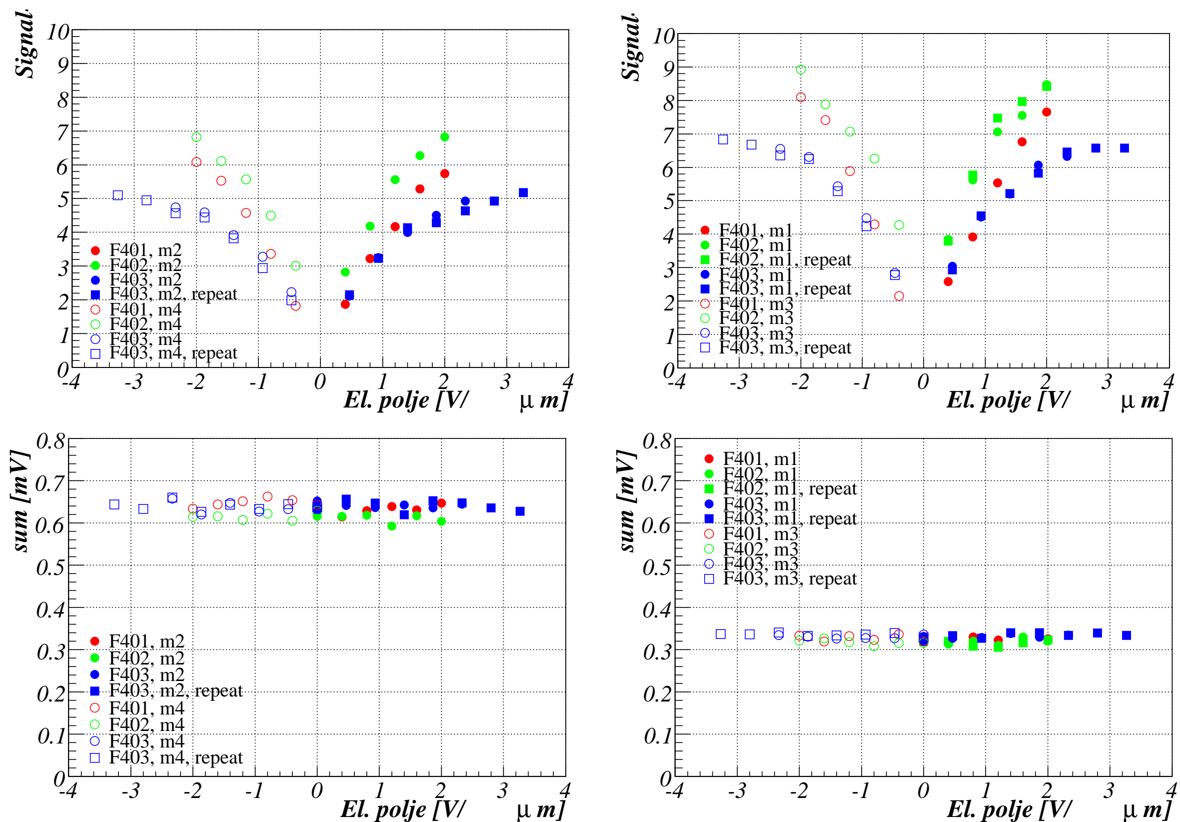

Slika 7.6: Šum σ_n in razmerje signal–šum treh detektorskih modulov BCM, pri frekvenčni pasovni širini 1 GHz (levo) in 200 MHz (desno) na bralnem osciloskopu. Meritve so bile narajene s ^{90}Sr kot izvorom 1 MIP delcev. Modra barva označuje modul, ki je imel diamanta stanjšana iz 500 μm na 300μm. Ostala dva modula sta vsebovala 500μm diamante.

- Pri omejitvi frekvenčne pasovne širine na bralnem osciloskopu iz 1 GHz na 200 MHz je bilo opaženo izboljšanje razmerja signal–šum za faktor ∼1.3, saj se je šum tipično zmanjšal za več kot 50%, MP amplituda pa za manj kot 35%. Ti rezultati se skladajo z meritvami predstavljenimi v prejšnjem razdelku.

- Eden izmed modulov je bil opremljen z diamantoma, ki sta bila stanjšana na 300 μm iz originalnih 500 μm. Ta module je bil preizkušen do električnega polja 3 V/μm. Tanjšanje diamantov ni povzročilo nobene speremebe v izmerjenem šumu σ_n. Vendar je bila izmerjena MP amplituda nižja pri električnih poljih do jakosti 2 Vμ/m. Pri višijh električnih poljih pa se izmerjena MP amplituda pri tanjših diamantih počasi približuje saturacijski vrednosti zaradi stauracije hitrosti nosilcev naboja v električnem polju (slika 7.6).

- Pri frekvenčni širini 200 MHz na osciloskopu, in napetosti ±1000 V znaša tipična izmerjena MP amplituda okrog 2.4 mV za polarnosti napetosti, ki dajo boljši odzive glede MP amplitude. Od tod sledi, da pri pravokotnem vpadu lahko pričakujemo razmerje signal–šum ∼7, oziroma ∼10 pri vpadu delca pod kotom 45°. Variacije med moduli v izmerjeni MP amplitude so bile pod 15% od povprečne vrednosti 2.4 mV. Primerjava ponovljenih

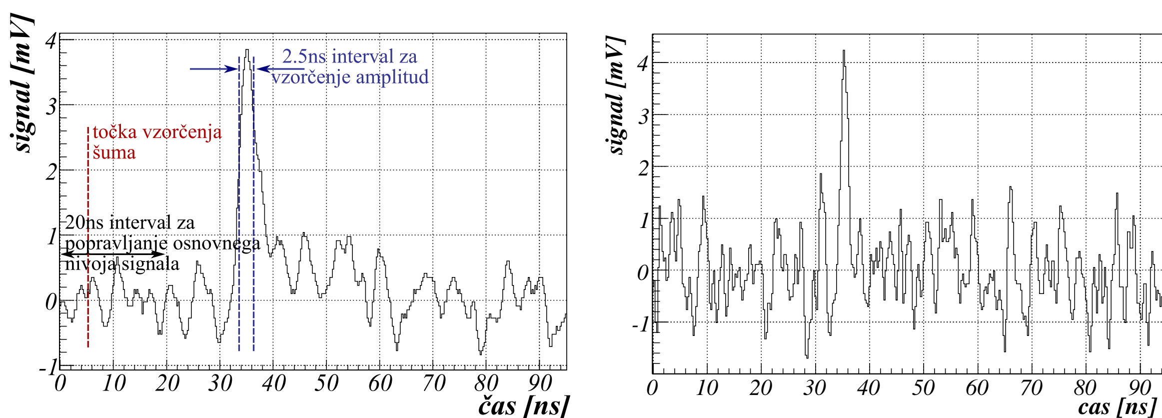

Slika 7.7: *Tipičen časovni poteke signala zabeležen pri 200 MHz (levo) in 1 GHz (desno) frekvenčni pasovni širini na bralnem osciloskopu pri meritvah v laboratoriju s* ^{90}*Sr kot izvorom 1 MIP signalov.*

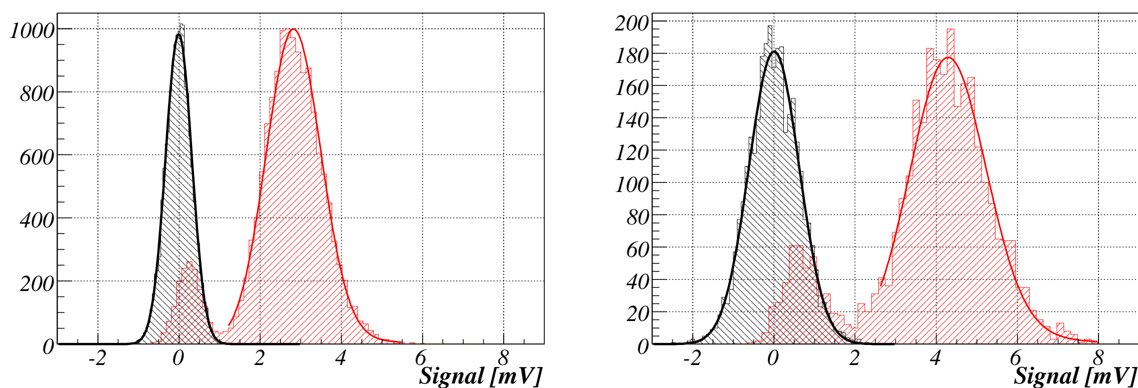

Slika 7.8: *Porazdelitev šuma (črna) in amplitude (rdeča) za detektorski modul F402 izmerjen pri napetosti 1000 V (polje 2 V/μm) ter frekvenčni pasovni širini (levo) 200 MHz in (desno) 1 GHz na bralnem osciloskopu. Meritve so bile narajene s* ^{90}*Sr kot izvorom 1 MIP delcev.*

meritvev je pokazala do 5% varijacije v ocenjenih MP amplitudah. Primer časovnega poteka signala enega dogodka je prikazan na sliki 7.7 za obe frekvenčni pasovni širini. Tipični porazdeltvi amplitud in šuma pri 2 V/μm sta prikazani na sliki 7.8.

- Pri električnih poljih jakosti 2 V/μm je tipično opaženo eratično obnašanje izmerjenga temnega toka detektorskih modulov. Ta lahko naraste za faktor 100 ali več od začetne vrednosti do nekaj 100 nA na časovni skali dni. Eratično obnajšanje je prisotno tudi na časovni skali minut, kjer tok lahko pade in naraste za faktor 10 ali več. Izvor tega obnašanja ni znan. Bil je opažen tudi pri experimentu Babar [E$^+$05]. Te tokovi se precej zmanšajo, če je diamant postavljen v magnetno polje ustrezne jakosti in smeri. V Notranjem detektorju pri ATLAS eksperimentu bo magnetno polje znašalo 2 T. Ko je bil BCM modul v magnetnem polju z jakostjo 2 T in pod kotom 45° glede na smer polja, tako kot je bilo predvideno v ATLAS-u, je bila v časovnem obdobju treh dni vrednost izmerjenega

tok pod 10 nA.

- Vrednost izmerjenga šuma ni kazala odvisnosti od temnega toka za tokove do 0.5 μA.

7.4.2 Digitizacija s čipom NINO

Meritve v testnem curku

Tri različice prototipnih modulov z NINO čipom so bile preizkušene v testnem curku protonov v SPS-u v CERN-u. Gibalna količina protonov je bila 120 GeV/c, kar ustreza 1 MIP-u. Pri teh meritvah so bili uporabljeni trije rezervni končni detektorski moduli, ki so bili skozi vse meritve priključeni na napetosti +1000 V.

Časovni potek digitalnih signalov iz treh NINO modulov je bil bran z ADC enoto s pogostosjo vzorčenja 2 GHz ter frekvenčno pasovno širino 300 MHz. Zajem podatkov je bil prožen s koincidenčnim signalom štirih prekrižanih scintilatorjev velikosti $2{\times}2\,\mathrm{mm}^2$, kjer sta bila dva postavljena pred in dva za detektorskimi modulu v curku protonov. Pri analizi je bila prisotnost NINO signalov v časovnem poteku signalov iskana v 20 ns intervalu okoli mesta pulza v povprečnem časovnem poteku signala.

Izmerjene so bile odvisnosti učinkovitosti detekcije 1 MIP delcev v odvisnosi od praga diskriminacije v NINO čipu (slika 7.9). Učinkovitost pri danem NINO pragu je bila izračunana kot delež dogodkov, pri katerih je bil NINO signal prisoten v prej omenjenem 20 ns intervalu. Iz izmerjenih krivulj učinkovitosti so bile določene vrednosti NINO praga pri 50% učinkovitosti (mediana NINO prag).

Med vmesnimi ustavitami curka protonov so bili izmerjene tudi pogostosti naključnih zadetkov, N_{NR}, v odvisnosti od NINO praga U_{Thr}, kar je prikazano na sliki 7.9. Če je šum porazdeljen po Gaussovi funkcij s širino σ_n je ta odvisnost je podana z

$$\ln(N_{NR}) = K\left[-\frac{U_{Thr}^2}{2\sigma^2}\right] \tag{7.5}$$

kjer je sorazmernostni faktor odvisen le od spodnje in zgornje frekvenčne meje sistema. S prilagajanjem funkcije 7.5 rezultatom na sliki 7.9 so bile določene vrednosti šuma σ_n v enotah NINO praga. Razmerje NINO praga pri 50% učinkovitosti in šuma σ_n v enotah NINO praga nam da median razmerje signal–šum, ki predstavlja merilo za razmerje signal-šum BCM sistema na koncu bralne verige.

Različica NINO modula, ki je dala največje median razmerje signal–šum je bila izbrana za digitizacjo analognih signalov sistema BCM v ATLAS-u. Tej različici je bila v končni fazi dodana še dodatna ojačevalna stopnja (Mini Circuit, Gali–52) pred filtrom, da bi povečali vhodni signal v NINO čip in s tem razširili dinamično območje občutljivosti.

Pri nekaj meritvah je bil z ADC enoto zabeležen časovni potek analognih signalov iz treh detektorskih modulov hkrati. Iz teh meritev je bila ocenjena časovna ločljivost analognih signalov v odvisnosti od signalnega praga. Za vsak dogodek je bila izračunana razlika med časom, ko signal iz enega od detektorskih modulov prečka signalni prag ter časom, ko je prag prečkal signal iz drugega detektorskega modula. S prilagajanjem Gaussove funkcije k porazdelitvi teh

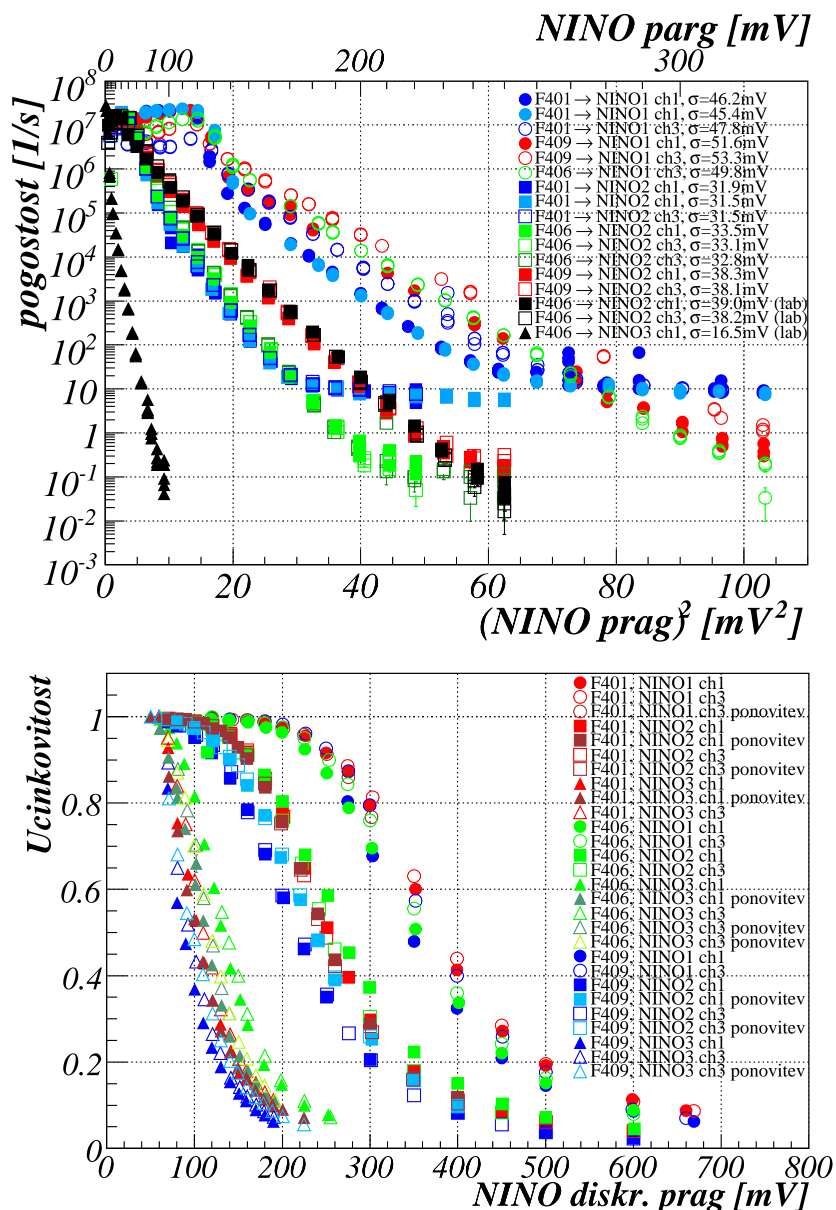

Slika 7.9: *Učinkovitost detekcije 1 MIP delcev (spodaj) in pogostost naključnih zadetkov (zgoraj) v odvisnosti od NINO diskriminacijskega praga, izmerjena s prototipnim NINO moduli. Barva razlikujejo med tremi končnimi detektorskimi moduli, simboli pa med tremi različnimi protoptipnimi NINO moduli. Prazni in polni simboli ločujejo dva različna vhodna kanala NINO modula (oba z večjim deležem vhodnega signala). Črne meritve pogostosti naključnih zadetkov so bile narejene v laboratoriju, ostale pa z merilnim sistemom, uporabljenim v testnem curku. Vse krivulje učinkovitosti na spodnjem grafu so bile izmerjene s testnim curkom.*

časovnih razlik, dobimo oceno za širino porazdelitve σ_{td}. Ob predpostavki, da je časovna ločljivost obeh detektorskih modulov enaka, nam dobljena širina porazdelitve σ_{td} deljena s $\sqrt{2}$ daje oceno za ločljivost analognih signalov. Ocenjena ločljivost je bila boljša kot 400 ps za vrednosti signalnih pragov med 10% MP amplitude in dvakratno vrednostjo MP amplitude.

Na podoben način je bila ocenjena tudi časovna ločljivost digitalnih NINO signalov. Tu je bil prag prehoda signala postavljen na polovico višine digitalnega NINO pulza. Pri vseh treh prototipnih različicah NINO modulov, so bile ocenjene vrednosti časovne ločljivosti NINO signalov boljše kot 800 ps za NINO diskriminacijske pregove med polovico in 1.8 median NINO diskriminacijskega praga.

Meritve s ^{90}Sr

Vse meritve predstavljene v tem razdelku so bile izveden z enim izmed rezervnih končnih detekotorskih modulov (F406), ki je skozi meritve deloval pri napetosti +1000 V. Da bi ocenili delovanje končnih NINO modulov v ATLAS-u, je bil eden izmed rezervnih končnih NINO modulov preizkušen v laboratoriju.

Postavitev eksperimenta z izvorom ^{90}Sr je bila podobna kot pri meritvah opisanih v razdelku 7.4.1. Analogni signali iz detektorskega modula so bili peljani preko 1 m dolgega koaksialnega kabla do bralnega osciloskopa in od tu dalje preko 1 m koaksialnega kabla do NINO modula. LVDS izhodni signal iz NINO modula so bili nato peljani preko optičnega kabla do optičnega sprejemnika. Ta je optične signale pretvoril v NIM signale, ki so bili prebrani z osciloskopom. Branje istočasnega časovnega poteka analognih in digitalnih signalov je bilo proženo z analognim signalom, kjer je bil prožilni nivo nastavljen na približno 60% vrednosti MP amplitude analognih pulzov. Pri osciloskopu je bila na kanalu za branje analognih signalov frekvenčna pasovna širina nastavljena na 200 MHz.

Izmerjena je bila učinkovitost detekcije v odvisnosti od NINO diskriminacijskega praga, kjer je vrednost median NINO prag znašala 650$\pm$10 mV. Ker je bilo branje signalov proženo na analogne signale same, ta krivulja opisuje učinkovitost za detekcijo delcev, ki ustrezajo več kot 1 MIP. Da bi ocenili učinkovitost za 1 MIP pri končnih NINO modulih v ATLAS-u, je bila na enak način izmerjan še krivulja učinkovitosti z enim izmed prototipnih NINO modulov. Primerjava median NINO praga, odčitanega iz te krivulje, z njegovo vrednostjo iz meritev v testnem curku je dala transformacijski faktor (124/140). S tem faktorjem lahko pretvorimo celotno krivuljo učinkovitosti, izmerjeno v laboratoriju, v krivuljo učinkovitosti za 1 MIP, ki jo pričakujemo v ATLAS-u, saj so bile pri meritvah v testnem curku 1 MIP protonov uporabljene enake signalne povezave kot v ATLAS-u. Od tod sledi, da v ATLAS-u lahko pričakovujemo median NINO prag 575$\pm$30 mV.

Z rezervnim končnim NINO modulom je bila izmerjena tudi odvisnosti pogostosti naključnih zadetkov od NINO praga. Od tod je bil s prilagajanjem funkcije 7.5 ocenjen šum σ_n, ki je znašal 74.9 mV. V laboratorijski postavitvi eksperimenta so bili uporabljeni krajši signalni kabli kot so bili predvideni v ATLAS-u, kar rezultira v manjši atenuaciji signala pri laboratorijskih meritvah. Da bi ocenili pogostost naključnih zadetkov pričkovano v ATLAS-u, je bila v laboratoriju izmerjena pogostost naključnih zadetkov tudi z enim od prototipnih NINO modulov, za katerega je bila pogostost naključnih zadetkov izmerejen tudi z eksperimentalno postavitvijo,

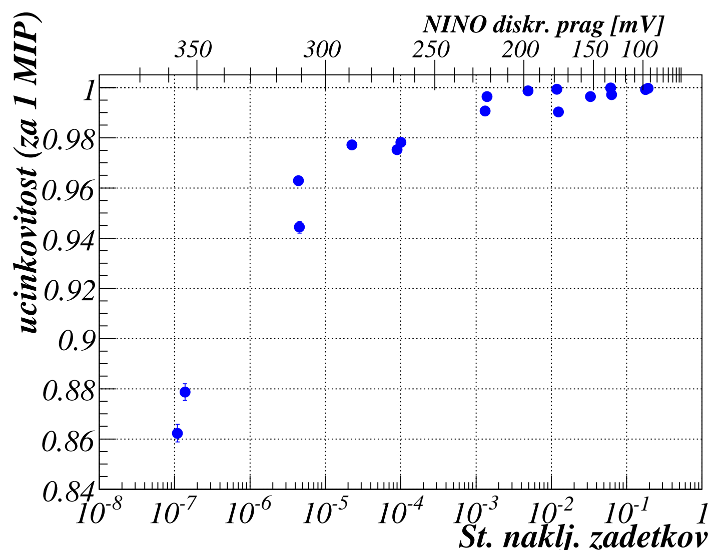

Slika 7.10: *Ocenjena učinkovitost za detekcijo 1 MIP delca v odvisnosti od števila naključnih zadetkov (v enem detektorskem modulu) v časovnem intervalu med prehodoma dveh zaporednih gruč (25 ns), ki jo pričakujemo v ATLAS-u.*

uporabljeno pri meritvah v testnem curku. Iz primerjava šuma σ_n, dobljenega iz krivulje izmerjene v laboratoriju, z vrednostjo iz postavitve v testnem curku dobimo faktor (33.1/38.6). Ta faktor služi za pretvorbo šuma σ_n izmerjenga v laboratoriju v ustrezno vrednost, ki jo pričakujemo v ATLAS-u. Tako dobimo, da šum σ_n, ki bi ga pričakovali za rezervni končni NINO modul v ATLAS-u, znaša 64 mV, kar skupaj z ocenjenim median NINO pragom da oceno 9$\pm$0.5 za median razmerje signal–šum.

Vrednost sorazmernostnega faktorja K v enačbi 7.5 je bila pri meritvah s prototipnim NINO modulom približno enaka v obeh primerih, tako z laboratorijsko postavitvijo kot s postavitvjo uporabljeno pri meritvah v testnem curku. Rezultat je pričakovan, saj je ta faktor odvisen le od zgornje in spodnje frekvenčne meje sistema. Torej lahko krivuljo pogostosti naključnih zadetkov, ki jo pričakujemo za končni NINO modul v ATLAS-u, izračunamo preko enačbe 7.5, kjer šum σ_n pomnožimo s faktorjem (33.1/38.6) za sorazmernostni faktor K pa vstavimo vrednost, ki smo jo dobili iz laboratorijskih meritev.

Skalirani odvisnosti pogostost naključnih zadetkov in učinkovitosti detekcije 1 MIP delcev od NINO praga lahko združimo v en graf. Namesto pogostost naključnih zadetkov lahko vzamemo število naključnih zadetkov, ki jih pričakujemo v času 25 ns, ki ustreza časovnemu intervalu med dvema gručama protonov pri protonskem curku v ATLAS-u. Ta graf je prikazan na sliki 7.10. Od tod lahko ocenimo, da lahko na intervalu NINO pragov med 230 mV in 300 mV sistem BCM deluje z učinkovitostjo med 99% in 96% ter s številom naključnih zadetkov med 10^{-3} in 10^{-5} v času med prehodoma dveh sledečih gruč protonov.

Krivulja 7.10 je podana za en detektorski modul. Pogostost naključnih zadetkov pri koincidenci signalov iz večih detekorskih modulov je precej manjši. Natančeno število naključnih zadetkov v ATLAS-u bo odvisno od vrste logičnih kombinacij osmih BCM detektorskih module, ki bo dejansko uporabljena.

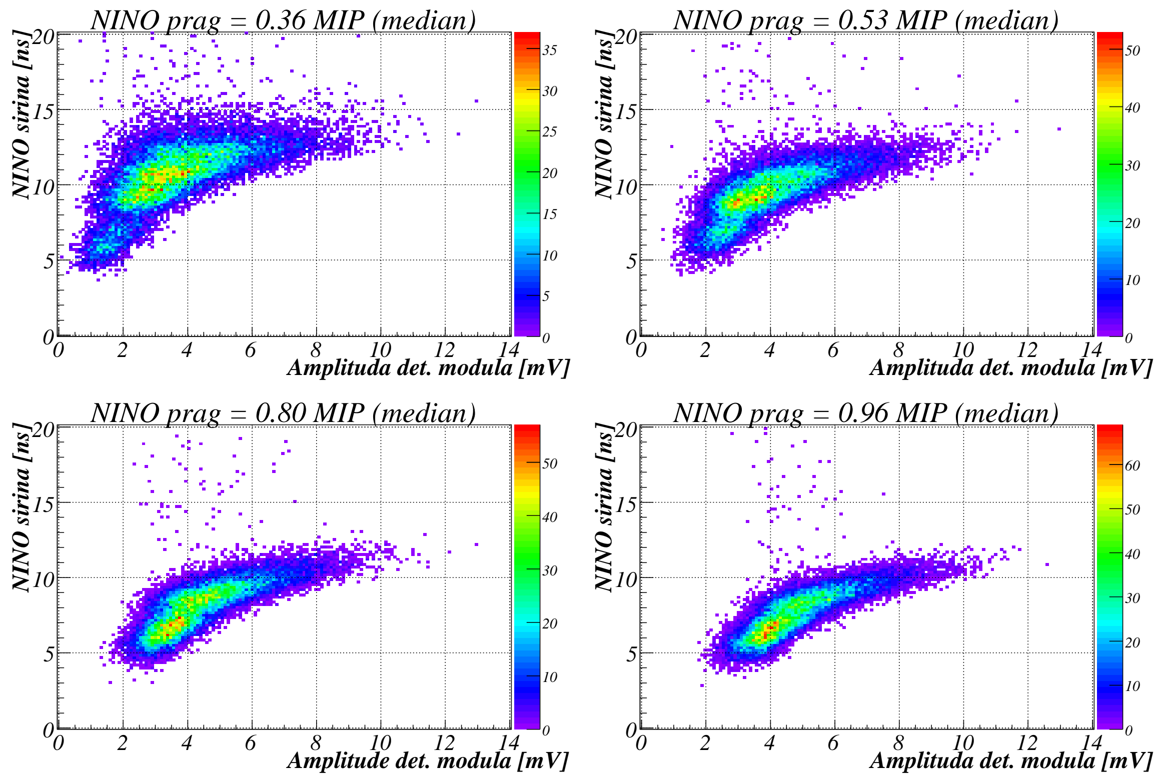

Slika 7.11: *Korelacija med širino izhodnih NINO signalov ter amplitudo vhodnih analognih signalov enega izmed končnih modulov (F406) pri različnih NINO diskriminacijskih pragovih rezervnega končnega NINO modula. NINO pragovi so navedeni na grafih in so podani v enotah median NINO praga krivulje za učinkovitost detekcije 1 MIP delca (575 mV).*

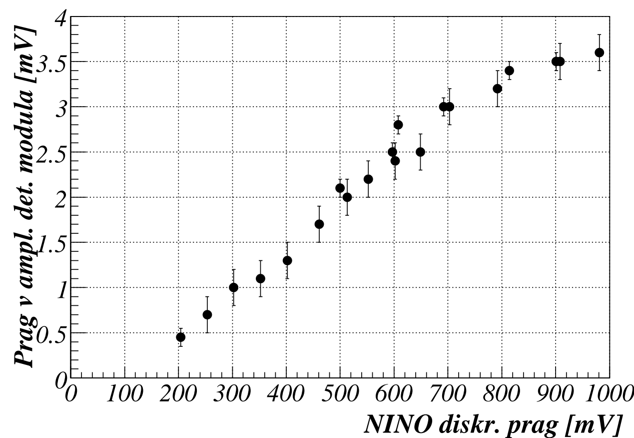

Slika 7.12: *Korelacija med NINO diskriminacijskim pragom in pragom na skali amplitud vhodnega analognega signala. Slednje vrednosti so bile odčitane iz grafov kot so prikazani na sliki 7.4.2.*

Slika 7.4.2 kaže izmerjeno korelacijo med širino NINO digitalnih signalov ter amplitudo vhodnih analognih signalov. Tu je bila širina NINO signala izračunana na polovici njegove višine, amplitude analognih signalov pa so bile vzorčene na 2.125 ns intervalu po postopku opisanem v razdelku 7.4.1. Pri teh meritvah so bili za prožilni signal uporabljeni kar NINO digitalni signali. Razen tega je bila postavitev meritve enaka kot opisano v začetku tega razdelka. Grafi 7.4.2 kažejo da korelacija širina–amplituda ni linearna in se kar hitro saturira.

Iz grafov 7.4.2 je bila odčitana povezava med NINO diskriminacijskim pragom ter vrednostjo, ki mu pripada na skali vhodnih amplitud. Pri danem NINO pragu je bila ustrezna vrednost praga na skali amplitud ocenjena kot najvišja vrednost amplitude na osi x v grafih 7.4.2, pod katero ne dobimo nobenega NINO signala. Rezultat je prikazana na sliki 7.11 Na območju NINO pragov med $\sim$200 mV in $\sim$700 mV je povezava približno linearna. Na tem intervalu NINO pragov je zgoraj opisano skaliranje krivulj učinkovitosti za oceno 1 MIP krivulje, ki jo pričakujemo v ATLAS-u, veljavno.

7.5 Meritve z epitaksialnim silicijem

Kolaboracija RD50, ki razvija sevalno odporne polprevodniške detektorje za bodoče visokoenrgijske trkalnike, je pričela projekt s tankimi epitaksialnimi (epi) diodami tipa n. Rezultati projekta so kazali na precej večjo sevalno odpornost tega materiala v primerjavi s standardnim silicijevim materialom tipa n z visoko upornostjo. Ena izmed zahtev za senzorski material sistem BCM v ATLAS-u je bila, da mora vzdržati fluence reda velikosti 10^{15} delcev na cm^2. Obetjoči rezultati glede sevalne odpornosti epi diod, ki jih je dobila Hamburška skupina v okviru kolaboracije RD50, so bili glavna motivacija, da so bile epi diode obravnavane kot kandidat za senzorski material sistema BCM. Meritve okrevanja epi diod po obsevanje, ki jih je izvedla Hamburška skupina, so bile narejeni pri temperaturah okrevanja 60°C in 80°C [L^+06b, L^+06a]. Da bi preverili rezultate teh meritev, smo v okviru razvoja sistema BCM za ATLAS, izvedli meritve okrevanja epi diod po obsevanju skozi 3.5 let pri temperaturi 20°C, temperaturi, ki je bližje scenariju okrevanja v ATLAS-u. Rezultati teh meritev so predstavljni v prvem delu tega razdelka. Možnost uporabe epi diod v sistemu BCM je bila preverjena tudi z detekorskimi moduli. Rezultati teh meritev so predstavljeni v zadnjem delu tega razdelka.

Epi diode, uporabljene v tem delu, so bile tipa n z nominalno upornostjo 50 Ωcm ter treh različnih debelin, 25 μm, 50 μm ter 75 μm. Epi material je bil gojen na 500 μm debeli podlagi Czochralskega silicija z upornostjo 0.01 Ωcm. Proizvajalec ITME [ITM], je ta material naredil z uporabo procesa epitaxialnega naparjevanje [Dez97]. Metaliziranje blazinīčaste epi diode z aktivno pošino 5×5 mm^2 ter prisotno strukturo zaščitnih obročev je naredil CiS [CiS] z uporabo tehnologije planarnega procesiranja [Sze02, Lut99, Spi05, Kem80, Kem84].

7.5.1 Sevalna odpornost epitaksialnih diod

Energijske izgube ob prehodu delca skozi silicijev kristal lahko razdelimo na inoiziacijske in neionizacijske (NIEL iz angl. non-ionising energy loss). Zaradi hitre rekombinacije nosilcev naboja ionizacijske poškodbe ne povzročijo dolgotrajnejših sprememb kristalne merže. Po drugi strani pa neionizacijske izgube vodijo do trajnejših poškod, ki so posledica premikov Si atomov iz kristalne mreže, pri čemer nastanejo praznine (V) ter medmrežni Si atomi (I). Večji del teh V in I se rekombinira, del njih pa potuje po kristalni mreži ter reagira z ostalimi primesmi v silicijevi mreži ter tvori nove kompleksnejše poškodbe v kristalni mreži. Te poškodbe ustvarijo dodatne energijske nivoje v energijski špranji, ki v splošnem poslabšajo delovanje detektorja. Vpliv poškodb na delovanje detektorja se odraža kot

- Sprememba effektivne koncentracije primesi N_{eff}, ki vodi v povečanje napetost popolnega osiromašenja V_{FD}.
- Povečanje zapornega tok, kar povzroči povečanje šuma ter prispeva k segrevanju senzorja, ter večji porabi moči.
- Poslabšanje učinkovitosti zbiranaj naboja, saj se del prostih nosilcev naboja, sproščenih ob prehodu ionizirajočega delca, ujame na poškodbah.

Za dan kristal in vrsto delca poškodbena funkcija, $D(E)$, opiše neinoizacijske energijske izgube v odvisnosti od energije vpadnega delca E. Navadno se poškodbe primerjajo s poškodbami, ki bi jih povzročili nevtroni z energijo 1 MeV. Tako definiramo *ekvivalentno fluenco* Φ_{eq}, ki predstavlja fluenco nevtronov z energijo 1 MeV, ki bi povzročila enake nionizacijske enrgijske izgube kot dejanska fluenca Φ_A delcev vrste A z energijsko porazdelitvijo $d\Phi_A/dE$. Dejanska in ekvivalentna fluenca sta potem povezani s tako imenovanim *poškodbenim koeficientom* κ_A, $\Phi_{eq} = \kappa_A \Phi_A$.

V tem delu je bilo uporabljeno 22 epi diod različnih debelin (25 μm, 50 μm in 75 μm) za meritve časovnega razvoja napetosti poplonega osiromašenja V_{FD} (in N_{eff}) ter zapornega toka po obsevanju. Osem vzorecv je bilo obsevanih s 24 GeV/c protoni v protonskem sinhrotronu PS v CERN-u. Ostali vzorci so bili obsevani z reaktorskimi neutroni v reaktorju TRIG1 II na Institutu Jožef Stefan v Ljubljani. Podrobnosti o spektru reaktorskih netronov ter njegovem poškodbenem koeficientu so podane v [Ž$^+$99]. Pri 24 GeV protonih je bil uporabljen poškodbeni koeficient κ=0.62. Tako s protoni kot z nevtroni je bila najvišja dosežena fluenca delcev Φ=10^{16}cm^{-2}.

Napetost popolnega osiromašenja V_{FD} (in od tod N_{eff} preko enačbe 7.2) smo določili iz meritve kapacitete C v odvisnosti od zaporne napetosti, V (enačba 7.3). Iz krivulje $1/C^2(V)$ smo določili presečišče premic, prilagajanih na naraščajoči del pred kolenom in saturirani del za njim. To prescišče smo vzeli za oceno napetosti popolnega osiromašenja.

Vrednost zapornega toka smo določili iz izmerjene krivulje odvisnosti zaporngne toka od zaporne napetosti. Pri idealni karakteristiki bi se tok pri napetostih nad V_{FD} saturiral. Pri naših vzorcih jasna saturacija tipično ni bila opažena, zato smo vrednost zapornega toka odčitali pri napetosti V_{FD}.

Časovni potek efektivne koncentracije primesi

Časovni potek okrevanja napetosti popolnega osiromašenja, V_{FD}, po obsevanju, ima tri prispevke: kratkoročno okrevanje, ki je pomembno na krajši časovni skali, dolgoročno okrevanje, ki dominira obnašanju na daljših časovnih skalah in stabilno komponento. Slednja se s časom okrevanja ne spreminja. Tipičen časovni potek okrevanja V_{FD}, izmerjen z epi vzorci po obsevanju, je prikazan na sliki 7.13. Obnašanje je nasprotno obnašanju, ki ga opazimo pri močno obsevanih standardnih silicijevih diodah tipa n z visoko upornostjo, kjer opazimo inverzijo tipa že takoj po obsevanju [9]. Pri standardnem siliciju se v začetku okrevanja del škode, nastale z

[9]Meritve s standardnim silicijem tip n kažejo da se med obsevanje kreira več električno aktivnih akceptorjev kot donorjev [L$^+$01]. Ti akceptorji prispevajo negativen prostorski naboj. Tako se pri visokih fluencah material

obsevanje, zamnjša. V primeru močno obsevanih silicijevih diodah tipa n to začetno kratkoročno okrevanje rezultira v zmanjšanju V_{FD} pri kratkih časih okrevanja. Temu sledi počasno naraščanje V_{FD}, ki je posledica generacije akceptorjev skozi daljši čas okrevanja.

V nasprotju s tem, pri epi diodah opazimo naraščanje V_{FD}v fazi kratkoročnega okrevanja tudi pri močno obsevanih vzorcih. Temu začetnemu porastu sledi padanje V_{FD} pri daljših časih okrevanja, ki je posledica komponente dolgoročnega okrevanja. Tako obnašanje lahko razložimo z generacijo pozitivnega prostorskega naboja (kreacija donorjev) med obsevanje. Enako časovno obnašanje V_{FD} opazimo tako po obsevanju s protoni ko z nevtroni, kar kaže na dejstvo v obeh primerih takoj po obsevanju tip materiala ni invertiran.

Slika 7.14 kaže odvisnost N_{eff} od ekvivalentne fluence, kjer je bila koncentracija N_{eff} izmerejena po koncu kratkoročnega okrevanaj. V tej fazi okrevanja tako kratkoročno kot dolgoročno okrevanje ne igrata pomembne vloge. Zato so vrednosti N_{eff} v grafu večinoma posledica le stabilne komponente škode nastale z obsevanje. Če privzamemo, da takoj po obsevanju epi material ni invertiran niti pri visokih fluencah, lahko za graf 7.14 uporabimo sledečo razlago. Prvi del odvisnosti od fluence lahko pripišemo odstranjevanju donorjev z obsevanjem, ki je prisoten tudi pri obsevanju standradnega silicija tipa n. Ta komponenta se eksponentno saturira s fluenco zaradi izčrpanja začetnih primesi donorjev, prisotnih v n materialu pred obsevanjem. V primeru tankega epi materiala je to izčrpanje zakasnjeno zaradi večje začetne koncentracije donorjev kot pri standardnem n siliciju. Pri večjih fluencah je možna kreacija akceptorje[10] presežena s kreacijo donorjev, ki povzročijo porast N_{eff} (in s tem V_{FD}) s fluenco.

Za opis spermemb v N_{eff} po obsevanju se uporablja tako imenovana *Hamburška parametrizacija*. Tu je spremeba vrednost efektivne koncentracije primesi ob času t po obsevanju,

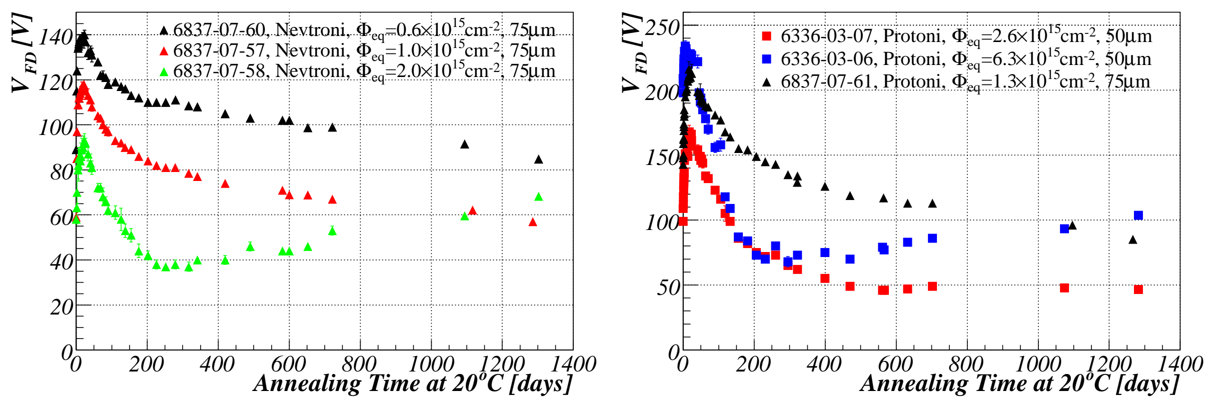

Slika 7.13: *Izmerjene vrednosti V_{FD} skozi okrevanje pri 20°C za epi diode obsevane z neutroni (levo) in protoni (desno). Fluenca in debelina za vsako od diode so podane v legendi.*

tipa n, ki ima pred obsevanjem v območju osiromašenja pozitiven prostorski naboj, začne efektivno obnašati kot p tip. Od tod ime “inverzija tipa”.

[10] Ta je opažena pri standardnem siliciju.

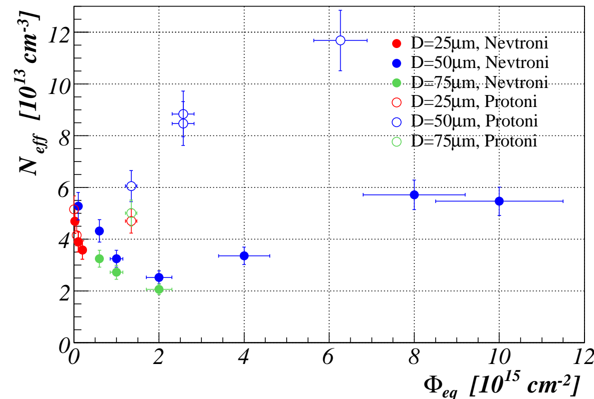

Slika 7.14: *N_{eff} ob koncu kratkoročnega okrevanja pri 20° kot funkcija ekvivalentne fluence za epi diode obsevane s protoni (prazni simboli) in nevtrone (polni simboli).*

$N_{eff}(t)$, v primerjavi z koncentracijo pred obsevanjem, $N_{eff,0}$, podana z

$$\Delta N_{eff}(\Phi_{eq}, t(T_a)) = N_{eff,0} - N_{eff}(\Phi_{eq}, t(T_a)) = N_A(\Phi_{eq}, t(T_a)) + N_C(\Phi_{eq}) + N_Y(\Phi_{eq}, t(T_a)), \quad (7.6)$$

kjer N_A opisuje kratkoročno okrevanje, N_Y dolgoročno okrevanje in N_C stabilno komponento. T_A predstavlja temperaturo pri kateri se okrevanje dogaja. V našem primeru je bilo to 20°C. Kratkoročno okrevanje, ki ga pripisujemo okrevanju negativnega prostorskega naboja (manjšanju števila akceptorjev) je parametrizirana z eksponentno padajočim členom, ki pada s časovno konstanto τ_A in ima amplitudo $N_{A,0}$

$$N_A = N_{A,0}\exp(-t/\tau_A). \quad (7.7)$$

Stabilna komponenta škode je opisana z dvema prispevkoma. Prvi predstavlja odstranjevanje donorjev s pogostostjo c in je eksponentno odvisna od fluence z začetno vrednostjo $N_{c,0}$. Drugi prispevek ustreza generaciji stabilnih defektov, ki je sorazmerna fluenci s pogostostjo g_C:

$$N_C = N_{c,0}(1 - \exp(-c\Phi_{eq}) + g_C\Phi_{eq}. \quad (7.8)$$

Za razliko od standardnega silicija, kjer je g_C vedno pozitiven, je bil pri epi materialu g_C negativen, kar kaže na kreacijo dodatnih donorjev med obsevanjem pri epi materialu.

Hamburška skupina je pri meritvah pri povišanih temperaturah okrvanje opazila, da ima dolgoročna komponent okrevanje pri epi materialu dva prispeka. Prvi je pomemben v začetni fazi dologoročnega okrevanja in ga lahko opišemo kot

$$N_{Y1} = N_{Y1,0}\exp(-t/\tau_{Y1}) = g_{Y1}\Phi_{eq}\exp(-t/\tau_{Y1}). \quad (7.9)$$

Drugi prispevek je pomemben v pozni fazi dolgoročnega okrevanja. Vpliv tega prispevka v naših meritvah nismo opazili, saj bilo obdobje 3.5 let v katerem smo spremljali okrevanje pri 20° prekratko[11].

[11] Hamburška skupina navaja red velikosti 10^4min za karakteristični čas tega prispevka pri temperaturi okrevanja 60°C. Ta čas je pri okrevanju pri 20°C precej daljši.

Parameter	Nevtroni	Protoni
$N_{C,0}$ [10^{13}cm^{-1}]	5.6±1.0	
c [10^{-15}cm^{-2}]	1.3±0.2	
g_C [10^{-2}cm^{-1}]	−0.63±0.15	−1.7±0.2 (50 μm vzorci)
g_{Y1} [10^{-2}cm^{-1}]	1.5±0.4	2.2±0.7
τ_{Y1} [days]	330±60	190±60

Tabela 7.1: *Parametri dobljeni s prilagajanjem funkcije 7.6 meritvam okrevanja pri 20°C.*

Hamburška skupina je opazila, da je odstranjevanje donorjev (parameter c) pri protonskem obsevanju precej hitrejši kot pri nevtronskem. V obeh primerih je bil c primerljiv z vrednostjo izmerjeno s standardnim silicijem. Opazili so tudi, da je g_C pri protonskem obsevanju odvisen od debeline epi vzorca. Potencialno razlaga efekta je podana v [P$^+$05, P$^+$06]. Za vse ostale parametre odvisnost od debeline vzorca ni bila opažena.

Rezultati dobljeni iz prilagajanja parametrizacije 7.6 našim meritvam so zbrani v tabeli 7.1. Ti rezultati se ujemajo z rezultati, ki jih navaja Hamburška skupina iz meritev pri povišanih temperaturah okrevanja. Iz naših meritev je bilo možno oceniti parameter c le za nevtrone, saj v primeru protonov ni bilo dovlj podatkov pri nizkih fluencah. Ocenjena pogostost generacije stabilnih efektivnih donorjev g_C je pri epi vzorcih obsevanih s protoni manjša kot v primeru nevtronskega obsevanja. Ta parameter smo pri protonih ocenili smo za 50μm.

Časovni potek efektivne koncentracije primesi

Spreminjanje zapornega toka po obsevanje običajno izrazimo s parametrom α

$$\frac{\Delta I(\Phi_{eq}, T_a, t)}{V} = \alpha(T_a, t)\Phi_{eq}, \tag{7.10}$$

Tu $\Delta I(t)$ predstavlja povečanje zapornega toka glede na vrednost pred obsevanjem, merjena pri referenčni temperaturi T_r, ob času t po obsevanju, kjer je okrevanje potekalo pri temperturi T_a. Temperatura T_r je temperatura pri kateri navajamo tok. V našem primeru je temperatura okrevanja T_a=20°C, tok in parameter α pa sta navedena pri T_r=20°C.

Obnašanje okrevanja parametra α običajno opišemo z

$$\alpha(T_a, t) = \alpha_0 + \alpha_I \mathrm{exp}(-t/\tau_I) - \beta \mathrm{ln}(t/t_0) \tag{7.11}$$

kjer je t_0=10 min. Nekaj primerov izmerjenega okrevanja je prikazanih na sliki 7.15, skupaj z rezultatom prilagajanja.

Meritve so pokazale, da α ni odvisna od vrste silicijevega materiala in ne od tega ali so obsevalni delci nevtroni ali nabiti hadroni [Mol99]. Vrednost parametra α izmerjena pri T_r=20°C po 80 min pri T_a=60°C je $\alpha^s(T_a = 60^o\mathrm{C}, t = 80\mathrm{min})$=(3.99±0.03)×$10^{-17}$A/cm.

Naše meritve so bile narejen pri T_a=20°C. Da bi jih primerjali s standardno vrednostjo $\alpha^s(T_a = 60^o\mathrm{C}, t = 80\mathrm{min})$, je bilo potrebno časovno os pri 60°C pretvoriti v os za 20°C. To se

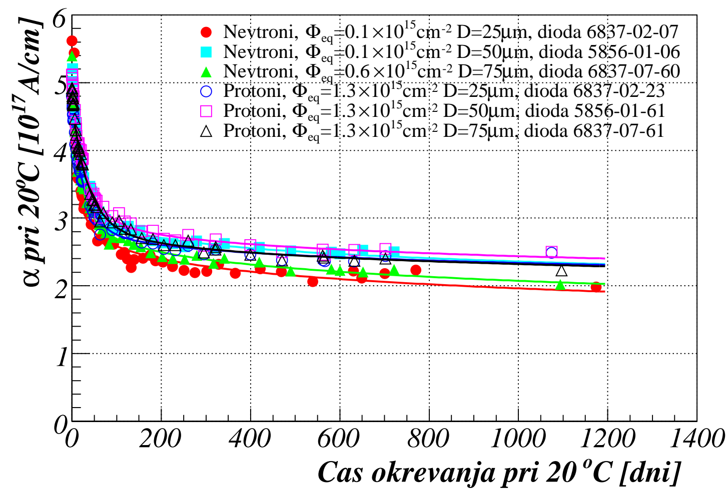

Slika 7.15: *Časovni potek okrevanja (pri T_a=20°C) zapornega toka za nekaj primerov obsevanih diod. Zaporni tok je naveden pri referenčni temperaturi T_r=20°C. Črte predstavljajo rezultat prilgajanja funkcije 7.11.*

običajno naredi tako, da vpeljemo temperaturno odvisen časovni faktor

$$\theta(T_a) = \exp\left(\frac{E_I}{k_B}\left(\frac{1}{T_r} - \frac{1}{T_a}\right)\right), \tag{7.12}$$

z aktivacijsko energijo E_I=1.09±0.14 eV. S to transformacijo dobimo, da 80 min pri T_a=60°C ustreza okrog 240 h pri T_a=20°C. Povprečna vrednost parametra α, ki smo jo izmerili z našimi vzorci 240 h po obsevanju, je bila α(240h at 20°C)=(3.9±0.8)×10^{-17} A/cm, kar se ujema s standardno vrednostjo $\alpha^s(T_a = 60^o\mathrm{C}, t = 80\mathrm{min})$.

7.5.2 Meritve z BCM detektorskim modulom

Da bi preverili delovanje prototipne različice BCM detektorskega modula z epi senzorskim materialom, smo ga opremili s 50 μm debelo neobsevano epi diodo. Izmerjena vrednost V_{FD} te diode je bila 130 V. Postavite merilnega sistema je bila enaka kot pri meritvah s pCVD diamanti in izvorom ^{90}Sr (glej razdelek 7.4.1). Meritve so bile narejene pri različnih zapornih napetosti do 450 V ter dvema frekvenčnima pasovnima širinam na bralnem osciloskopu, 200 MHz in 1 GHz. Slika 7.16 kaže histogram časovnega poteka signala iz modula, kjer so vključeni vsi zabeleženi dogodki, pri zaporni napetosti 450 V za oba primera frekvenčne pasovne širine.

Amplitude so bile vzorčene na interavlu 2.125 ns. Primera porazdelitev amplitud in šuma za obe frekvenčni pasovni širini je prikazan na sliki 7.17. Amplitude pulzov so bile precej nizke, kar je razvidno tudi iz slike 7.16. Zato, ni bilo možno razločiti amplitudni in šumni vrh v porazdelitvah amplitud, saj je bil v vseh primerih opažen samo en vrh. Kljub temu smo iz teh porazdelitev ocenili MP amplitudo s prilagajanjem konvolucije Gaussove in Landauove funkcije. Ocenjene vrednosti so prikazana na sliki 7.18 skupaj z ocenjenim šumom σ_n ter razmerjem signal–šum.

Pri nizkih zapornih napetostih šum narašča z napetostjo zaradi večanja debeline območja osiromašenja v epi diodi. Pri napetostih nad V_{FD} se šum saturira pri $\sim$0.4 mV v primeru 200 MHz frekvenčne pasovne širine na osciloskopu oziroma pri dvakrat večji vrednosti pri frekvenčni pasovni širini 1 GHz. Podobno se MP amplituda saturira pri $\sim$0.6 mV za 200 MHz in pri dvakrat večji vrednosti za frekvenčno pasovno širino 1 GHz. Tako za oba primer frekvenčne pasovne širine dobimo okrog 1.5 za razmerje signal–šum na območju saturacije. Vendar, so vrednosti MP amplitude precenjene, saj je bilo določanje amplitude oteženo zaradi njihovih zelo nizkih vrednosti.

Signal z epi senzorji so bile glede časovnih lastnosti sperejmljivi za sistem BCM[12]. Epi material tudi dosega zahtevo po sevalni odpornosti senzorja v BCM sistemu. Vendar je delovanje BCM detektorskega modula z epi diodo nwustrezno glede razmerja signal-šum. Zato je bil za

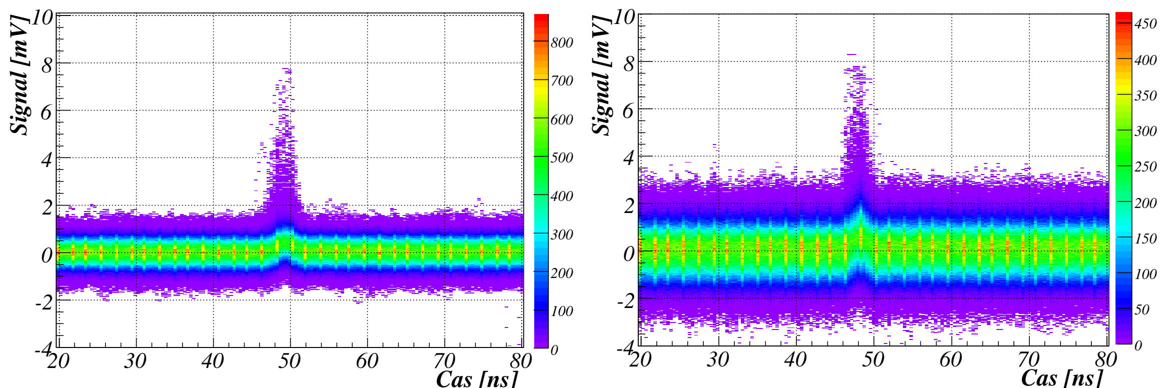

Slika 7.16: *Dvodimenzionalni histogram časovnih potekov vseh dogodkov zajetih s 50 μm epi diodo pri zaporni napetosti 450 V ter frekvenčni pasovni širini 200 MHz (levo) in 1 GHz na bralnem osciloskopu.*

[12]Širina in dvižni čas sta primerljiva z vrednostimi v diamantu.

senzor v sistemu BCM izbran pCVD diamant.

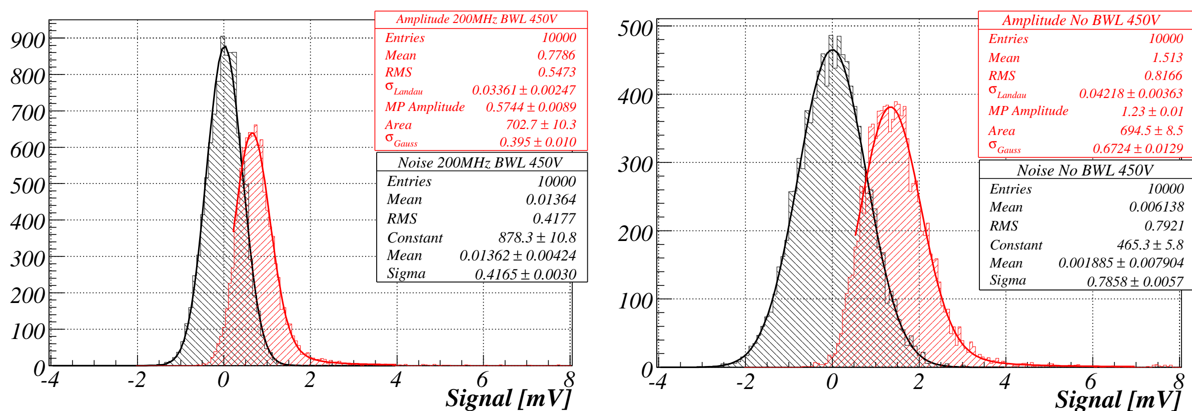

Slika 7.17: *Porazdelitev amplitud (rdeča) in šuma (črna) izmerjena s 50 µm epi diodo pri zaporni napetosti 450 V ter 200 MHz (levo) oziroma 1 GHz frekvenčni pasovni širini na bralnem osciloskopu.*

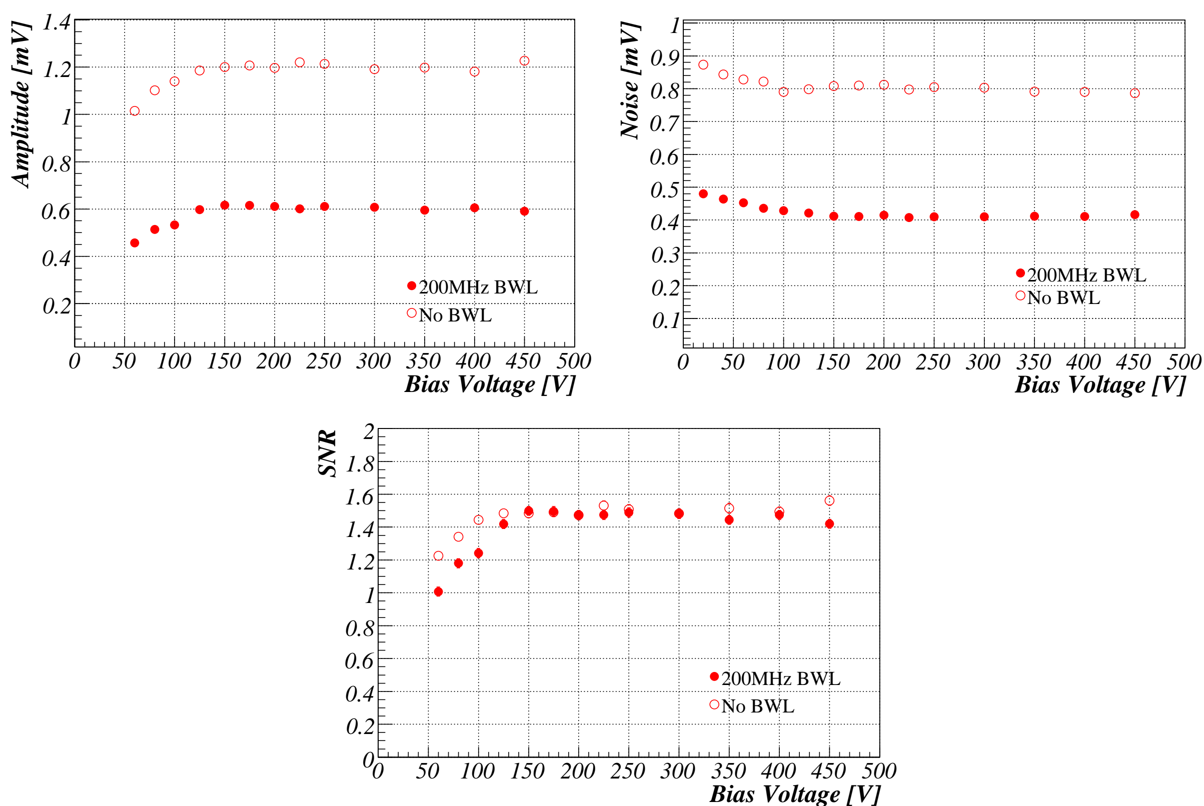

Slika 7.18: *Odvisnost izmerjenih MP amplitud (levo), šuma σ_n (desno) ter razmerja signal–šum (spodaj) od zaporne napetosti na 50 µm epi diodi pri 200 MHz (polni simboli) ali 1 GHz (prazni simboli) na bralnem osciloskopu.*

7.6 Zaključek

V disertaciji je predstavljeno delo opravljeno skozi razvojno fazo sistema BCM za detektor ATLAS. Za detektorske module sistema je bilo predvideno, da bodo locirani v najbolj notranjih delih detekorja ATLAS, s senzorji na območju blizu interakcijske točke ter curkovne cevi. Tu so pričakovane fluence delcev reda velikosti 10^{15}cm^{-2} v 10 letih delovanja pospeševalnika LHC. Ker je cilj sistema BCM spremljanje pogojev curka blizu interakcijske točke in merjenje luminoznosti na skali ns, morajo biti analogni signali sistema BCM hitri z dvižnim časom $\sim$1 ns ter širino $\sim$3 ns. Poleg tega je za optimalno delovanje sistem BCM zaželjena občutljiv na 1 MIP delce.

V iskanju sevalno odpornega senzorskega materiala sta bili v začetku obravnavani dve možnosti: tanek epitaksialni (epi) silicij tipa n in polikristalni (pCVD) diamant. Za pCVD diamant velja mnenje, da je sevalno odporen. Meritve kažejo, da se pri fluenci 2.2×10^{15}cm^{-2} nabojni signal zmanjša le za 15%, kar je ta material uvrstilo med kandidate za senzor sistema BCM.

Hamburška skupina je v okviru kolaboracije RD50, ki razvija sevalno odporne polprevodniške detektorje za prihodnjo generacijo visokoenrgijskih pospeševalnikov, s tankimi epi senzorji tipa n opravila meritve časovnega okrevanja po obsevanju pri temperaturah 60°C in 80°C. Te meritve so nakazovale, da je epi material precej bolj sevalno odporen glede N_{eff} (oziroma V_{FD}) v primerjavi s standardnim silicijem. Na podlagi teh rezultatov so bili epi senzorji sprejeti kot eden izmed potencialnih kandidatov za senzor v sistemu BCM. Da bi te rezultate preverili tudi pri temperturah, ki so bližje scenarijem okrevanja pri LHC, smo za obsevane epi vzorce izmerili časovni potek okrevanja efektivne koncentracije primesi in zpornega toka pri temperaturi okrevanja 20°C. Meritve so potekale približno 3.5 let. Epi diode so bile obsevane z reaktorskimi nevtroni ali 24 GeV/c protoni do fluenc 10^{16}cm^{-2}. Resultati, ki smo jih dobili so se skladali z rezultati, ki jih navaja Hamburška skupina in kažejo, da je za razliko od standardnega silicija okrevanje med obdobji, ko curek v pospeševalniku LHC ni prisoten, lahko celo koristno.

Elektronika za procesiranje analognih signalov v sistemu BCM temelji na dvostopenjskem ojačevanju s frekvenčno pasovno širino 500 MHz. Ta elektronika je skupaj s senzorji vsebovana v detekotrskem modulu sistema BCM. Delovanje prototipne različice detektorskega modula s 50 μm diodo je bilo preizkušeno v laboratorijskem merilnem sistemu z izvorom ^{90}Sr ter scintlatorjem kot prožilcem za 1 MIP signale. Izmerjeno razmerje signal-šum je bilo manjše kot 1.5. To je vodilo do odločitve, da uporabimo pCVD diamant kot senzor v sistemu BCM, saj so rezultati z njim pokazali precej boljše razmerje signal–šum.

Tako prototipna kot končna različica detektorskih modulov z diamantnimi senzorji sta bili preizkušeni v številnih meritvah v testnem curku delcev ter meritvah z elektroni iz ^{90}Sr. Ti testi so pokazali, da uporaba dveh diamantov, kjer je signal pasivno seštet pred ojačanjem, poveča

razmerje signal–šum v primerjavi z enim diamantom. V primerjavi z enim diamantom je konfiguracija z dvema diamantoma dala približno dvakrat večjo MP amplitudo, medtem, ko je šum narasel le za $\sim$30%. Zato je ta konfiguracija uporabljena v sistemu BCM.

Izmerjen šum detektorskega modula z dvema diamantoma je bil neodvisen od jakosti električnega polja v diamantih do vrednosti 3 V/μm. Prav tako šum ni kazal odvisnosti od temnega toka detektorskega modula za vrednosti tokov do 0.5 μA.

Pri nagibu senzorje za kot 45° glede na vpadni ionizirajoči delec se je izmerjena MP amplitude povečala za pričakovan geometrijski faktor $\sqrt{2}$. Zato so v ATLAS-u diamantni senzorji nagnjeni za 45° proti curkovni cevi.

Laboratorijske meritve z elektroni iz ^{90}Sr kot izvorom 1 MIP delcev pri normalnem vpadu so pokazale, da omejitev frekvenčne pasovne širine na bralnem osciloskopu iz 1 GHz na 200 MHz poveča razmerje signal–šum za faktor $\sim$1.16. Zato je bil za delovanje sistema BCM v ATLAS-u predviden 200 MHz fliter četrtega reda za filtriranje analognih signalov pred digitizacijo. Meritve v testnem curku 1 MIP delcev so pokazale, da omenjena omejitev frekvenčne pasovne širine poveča dvižni čas pulza za $\sim$70% ter poveča njegovo širino za $\sim$60%. Izmerjen povprečen dvižni čas je pri 200 MHz frekvenčni pasovni širini znašal $\sim$1.5 ns, povprečna širina pulza na polovici njegove višine pa $\sim$2.8 ns, kar je za delovanje sistema BCM sprejemljivo. Pri frekvenčni pasovni širini 300 MHz je bila izmerjena časovna ločljivost analognih signalov boljša kot 400 ps na območju pragov med 10% in dvakratno MP amplitudo. Pri 200 MHz frekvenčni pasovni širini in električnem polju 2 V/μm v obeh diamantih je tipično razmerje signal–šum, izmerjeno v laboratoriju s ^{90}Sr, znašalo 7-7.5.

Moduli z elektronskim vezjem za digitizacijo temeljijo na čipu NINO. Slednji zakodira informacijo o amplitudi vhodnega analogne pulza v širino izhodnega digitalnega pulza. Korelacija med vhodno amplitudo in izhodno širino je nelinearna in se saturira precej hitro. Zato je pri končnih NINO modulih za povečanje dinamičnega območja, vhodni analogni signal razdeljen v približnem razmerju 1:11 na dva vhoda v čip NINO. Z enim izmed rezervnih končnih NINO modulov smo ocenili njegovo delovanje, ki ga pričakujemo v ATLAS-u. Na koncu bralne verige sistema BCM pričakovano median razmerjen signal–šum za 1 MIP delec znaša 9$\pm$0.5. Na območju NINO diskriminacijskih pragov med 210 mV in 300 mV pričakujemo učinkovitost detekcije 1 MIP signala med 99% in 96% ter od 10^{-3} do 10^{-5} naključnih zadetkov na enem detektorskem modulu v času med prehodoma dveh zaporednih gruč protonov.

Acknowledgements

Since everyone reads at least the acknowledgements I better write this in English! ☺

This thesis represents not only my part of the work involved with the BCM but also reflects the contribution and help from many other people. So I would like to thank all those that made this work possible. Thank you all! That's it!! Bye! Just joking! ☺ I would like to thank my supervisors Vladimir Cindro and Marko Mikuž for hiring me in the first place, since they knew very little of me until it was too late for them to fire me. Also I am very thankful for their help with the numerous discussions about the strange world of diamond and silicon devices and for steering me in the right direction without being too controlling. To Vladimir I am especially grateful for his effort of carefully reading the present thesis and helping me make it more sensible.

My special thanks goes to... hmmm... what's his name... oh, ja, Andrej Gorišek ☺ who guided me through the hardware life during the past five years and taught me how to make the best out of experimental work. Without Andrej the numerous test beams and lab measurements would have been impossible. I am thankful to him for pushing me to follow his demanding ideas of what and how things should be done since these ideas always turned out to be correct. I think that you, Andrej, will make a very good big boss of some group one day! ☺

Thanks go to the rest of the Si–ATLAS group in Ljubljana, Gregor Kramberger, Erik Margan, Marko Zavrtanik, Matej Batič, Igor Mandič, Borut Kerševan and Boštjan Maček who have offered their help and advice.

I would also like to thank to other BCM people, William Trischuk, Harris Kagan, Heinz Pernegger, for answering my sometimes silly questions about diamonds and for many discussions, either during the famous BCM meetings or "traditional BCM collaboration dinners".

I would also like to acknowledge the Bonn telescope group, Lars Reuen, Markus Mathes and Jaap Velthuis, for the operation of their detector, their valuable assistance in the 2006 test beam and for providing the track files.

It has been fun to work with Michael Niegl to whom I owe many thanks for helping me during the SPS test beams last year and making those days spent in the Prévessin hall much more bearable. Many thanks go to Thomas Kittelmann for providing the very much needed distraction from the test beam by organising many Tuesday AMR sessions, not necessarily on Tuesdays, without those, my occasional stays at CERN would not be as fun as they were. I am also very grateful to Thomas for reading my thesis blabla and de-randomising my usage of "the" and "a" in it. ☺ By the way, for those who didn't know already, VP1 is COOL stuff! Just look at picture 2.6. Nice colours, Thomas! ☺

I also thank Benjamin Tišler for convincing me to study physics in the first place. Finally, I wish to thank my family and friends, Petra Tomše, Marko Uplaznik, Matej, Thomas, Miha and Ewa Stanecka for their support and understanding for the lack of my social skills in the past few months.

BIBLIOGRAPHY

[A+03] RD42 Collaboration W. Adam et al. The development of diamond tracking detectors for the LHC. *Nucl. Instr. Methods A*, 541:79–86, 2003.

[A+04] F. Anghinolfi et al. NINO: an ultra-fast and low–power front–end amplifier and discriminator ASIC for the multi-gap resistive plate chambers. *Nucl. Instr. Methods A*, 533:183–187, 2004.

[AM76] N.W. Ashcroft and N.D. Mermin. *Solid State Physics*. Saundrers College Publishing, International edition, 1976.

[AST85] Annual book of astm standards, May 1985. ASTM Commite E-10 on Nuclear Tcehnology and Application, Vol. 12.02, chapter ASTM E722–85, p.324-329,.

[ATL08] The ATLAS collaboration. The ATLAS Experiment at the CERN Large Hadron Collider. *J. Inst.*, 3:1–422, 2008.

[B+] J. Bohm et al. Power supply and power distribution system for ATLAS silicon strip detectors. Stockholm, September 2001, (CERN-2001-005).

[B+98] T. Behnke et al. Development of diamond films for particle detector applications. *Diam. Rel. Mat.*, 7:1553–1557, 1998.

[B+03] RD42 Collaboration, M. Bruzzi et al. Status of the R&D activity on diamond particle detectors. *Nucl. Instr. Methods A*, 511:124–131, 2003.

[B+04] O. Brüning et al., editors. *LHC Design Report*. CERN-2004–003, 2004.

[B+07] W. de Boer et al. Radiation hardness of diamond and silicon sensors compared. *Phys. Stat. Sol. A*, 204:3004–3010, 2007.

[Bac90] P.K. Bachmann. *Diamond deposition*, volume 2. 1990.

[Bic88] H. Bichsel. Straggling in thin silicon detectors. *Rev. of Modern Phys.*, 60:663–669, 1988.

[BM85] G.L. Bona and F. Meier. Observation of the spin-orbit splitting at the valence band edge of silicon by spin-polarized photoemission. *Sol. Stat. Commun.*, 55:851–855, 1985.

[Boc04] D. Bocian. Accidental beam losses during injection in the interaction region IR1. LHC Project Note 335, January 2004.

[Brü01] O. Brüning. Mechanisms for beam losses and their time constants. *Proc. of the LHC Workshop, Chamonix*, pages 264–268, 2001.

[C+64] C.D. Clark et al. Intrinsic edge absorption in diamond. *Proceedings of the Royal Society of London, Series A*, 277(1370):312–329, 1964.

[C+79a] C. Canali et al. Diamond nuclear radiation detector. *Nucl. Instr. Methods A*, 160:73–77, 1979.

[C+79b] C. Canali et al. Electrical properties and performances of natural diamond nuclear radiation detectors. *Nucl. Instr. Methods A*, 160:73–77, 1979.

[CAE] `http://www.caen.it`. CAEN, Via Vetraia, 11, 55049 - Viareggio (LU) - ITALY.

[CDS] `http://cdsweb.cern.ch/`.

[CiS] CiS, Institute für Mikrosensorik GmbH, Konrad–Zuse Strasse 14, D99099 Erfurt, Germany.

[CRG] M.J. Catrula, T.D. de la Rubia, and G.H. Glimer. Point defect production, geometry and stability in silicon: A molecular dynamics simulation study. Fall meeting of the Materials Research Society (MRS), Boston, MA (United States), 29 Nov - 3 Dec 1993.

[Dez97] B. Dezillie. *Radiation hardness studies of epitaxial silicon particle detectors for applications at the CERN Large Hadron Collider*. PhD thesis, University Joseph Fourier–Grenoble 1, 1997.

[E+] R. Eusebi et al. A diamond based beam condition monitor for the CDF experiment. Proceedings of the 2006 IEEE Nuclear Science Symposium, to appear in IEEE Trans. Nucl. Sci..

[E+05] A.J. Edwards et al. Radiation monitoring with CVD diamonds in BaBar. *Nucl. Instr. Methods A*, 552:176–182, 2005.

[E6] Element Six Ltd., King's Ride Park, Ascot, Berkshire, SL5 8BP, Unite Kingdom.

[F+92] P.J. Fallon et al. Trapping levels in pulse-counting synthetic diamond detectors. *Diam. Rel. Mat.*, 1:1185–1189, 1992.

[F+99] RD42 Collaboration, M. Friedl et al. Cvd diamond detectros for ionizing radiation. *Nucl. Instr. Methods A*, 435:194–201, 1999.

[FOT] FOTEC, Viktor Kaplan Str. 2, A-2700 Wr. Neustadt, Austria.

[G+93] P. Griffin et al., Nov. 1993. SAND92-0094, SANDIA Natl. Lab.

[H+00] RD42 Collaboration, F. Hartjes et al. Pulse height distribution and radiation tolerance of CVD diamond detectors. *Nucl. Instr. Methods A*, 447:245–250, 2000.

[HA93] M. Huhtinen and P. Aarino. Estimation of pion induced desplacement damage in silicon, 1993.

[HA99] M. Huhtinen and P. Aarino. Pion induced displacement damage in silicon devices. *Nucl. Instr. Methods A*, 335:580–582, 1999.

[Hal52] R.N. Hall. Electron–hole recombination in germanium. *Phys. Rev.*, 87:387, 1952.

[ISE] Iseg Spezialelektronik GmgH, D-01454 Radeberg/OT Rossendorf Germany.

[ITM] Institute of Electronic Materials Technology (ITME), ul. Wolczynska 133, 01-919 Warsaw, Poland.

[K+74] S.F. Kozlov et al. Diamond nuclear radiation detector. *Nucl. Instr. Methods A*, 117:277–283, 1974.

[K+75] S.F. Kozlov et al. Preparation and characteristcs of natural diamond nuclear radiation detectors. *IEEE Trans. Nucl. Sci.*, 22:160–173, 1975.

[K+77] S.F. Kozlov et al. Diamond dosimeter for x-ray and γ-radiation. *IEEE Trans. Nucl. Sci.*, 24:235–237, 1977.

[K+92] A.Y. Konobeyev et al. Neutron displacement cross-sections for structural materials below 800 Mev. *J. Nucl. Mat.*, 186:117–130, 1992.

[K+01] J. Koike et al. Displacement threshold energy for iia diamond. *Apll. Phys. Lett.*, 60:1450–1452, 2001.

[K+07] RD42 collaboration, H. Kagan et al. Development of diamond tracking detectors for high luminosity experiments at the LHC, 2007. RD42 Status report, CERN/LHCC 2008-002, LHCC–RD-012.

[K+08] RD42 collaboration, H. Kagan et al. Development of diamond tracking detectors for high luminosity experiments at the LHC, 2008. RD42 Status report, CERN/LHCC 2008-005, LHCC–RD-016.

[Kag] Private communication with Harris Kagan.

[Kei] `http://www.keithley.com`. Keithley Instruments Inc, 28775 Aurora Road, Cleveland Ohio 44319, USA.

[Kem80] J. Kemmer. Fabrication of low noise silicon radiation detectors by the planar process. *Nucl. Instr. Methods A*, 169:499–502, 1980.

[Kem84] J. Kemmer. Improvement for detector fabrication by the planar process. *Nucl. Instr. Methods A*, 226:89–93, 1984.

[Kra03] G. Kramberger. *Signal Development in irradiated silicon detectors*. PhD thesis, University of Ljubljana, 2003.

[L+63] J. Lindhard et al. Integral equations governing radiation effects. *Kgl. Danske Videnskab. Selskab. Mat.–fys. Medd.*, 33:2–42, 1963.

[L+80] V.A.J. van Lint et al. *Mechanisms of radiation effects in electronic materials, Volume I*. John Wiley and Sons, 1980.

[L+87] M.S. Lazo et al. Silicon and silicon dioxide neutron damage function. *Tech. report SAND87-0098 Vol.1,*, pages 85–103, 1987.

[L+01] RD48 Collaboration, G. Lindström et al. Radiation hard silicon detectors–developments by the RD48 (ROSE) collaboation. *Nucl. Instr. Methods A*, 466:308–326, 2001.

[L+06a] G. Lindström et al. Epitaxial silicon detectors for particle tracking–Radiation tolerance at extreme hadron fluences. *Nucl. Instr. Methods A*, 568:66–71, 2006.

[L+06b] G. Linström et al. Radiation tolerance of epitaxial silicon detectors at very high proton fluences. *Nucl. Instr. Methods A*, 556:451–458, 2006.

[Lab] Labview, graphical software tool for developing measurement applications. `http://www.ni.com`. National Instruments Corporation, 11500 N Mopac Expwy, Austin TX 78759-3504, USA.

[Lut96] G. Lutz. Effects of deep level defects in semiconductor detectors. *Nucl. Instr. Methods A*, 377:234–243, 1996.

[Lut99] G. Lutz. *Semiconductor radiation detectors: Device Physics*. Springer, 1999.

[M+96] C. Manfredotti et al. A study of polycrystalline cvd diamond by nuclear techniques. *Phys. Stat. Sol. A*, 154:327–350, 1996.

[M+99a] C. Manfredotti et al. IBIC investigation of radiation induced effects in cvd and natural diamond. *Nucl. Instr. Methods A*, 426:156–163, 1999.

[M+99b] M. Moll et al. Leakage current of hadron irradiated silicon detectors–meatrial dependence. *Nucl. Instr. Methods A*, 426:87–93, 1999. and refernces therin.

[Mei99] D. Meier. *CVD Diamond Sensors for Particle Detection and Tracking*. PhD thesis, Universität Heilderberg, 1999.

[Mol99] M. Moll. *Radiation induced damage in Silicon particle Detectors–microscopic defects and macroscopic properties*. PhD thesis, University of Hamburg, 1999. DESY-THESIS-1999-040.

[N+80] F. Nava et al. Electron effective masses and lattice scattering in natural diamond. *Sol. Stat. Commun.*, 33:475–477, 1980.

[O+98] A. Oh et al. Development of diamond films for particle detector applications. *Diam. Rel. Mat.*, 7:1553–1557, 1998.

[Oh99] A. Oh. *Particle Detection with CVD Diamond*. PhD thesis, University of Hamburg, 1999.

[P+94] M.A. Plano et al. Thickness dependence of the electrical characteristics of chemical vapor deposited diamond films. *Apll. Phys. Lett.*, 64:193–195, 1994.

[P+05] I. Pintilie et al. Radiation induced donor generation in epitaxial and Cz diodes. *Nucl. Instr. Methods A*, 552:56–60, 2005.

[P+06] I. Pintilie et al. Stable radiation induced donor generation in silicon diodes. *Nucl. Instr. Methods A*, 556:197–208, 2006.

[PK95] L.S. Pan and D.R. Kania, editors. *Diamond: Electronic Properties and Applications*. Kluver Academic Publishers, 1995.

[R+93] M. Rohlfing et al. Quasiparticle band-structure calculations for C, Si, Ge, GaAs and SiC using Gaussion-orbital basis set. *Phys. Rev. B*, 48(24):17791–17805, 1993.

[Ram39] S. Ramo. Currents induced by electron motion. *Proc. I. R. E.*, 27:584–585, 1939.

[Rau62] C. J. Rauch. *Proc. of 6th Int. Conf. on the Physics of Semiconductors, Exeter, UK*, pages 276–280, 1962.

[RD4] `http://rd42.web.cern.ch/RD42`. CERN RD42 collaboration: "CVD Diamond Radiation Detector Development".

[Ric49] S. O. Rice. Mathematical analysis of random noise. *Bell System Technical Journal*, 23, 24:228–332, 46–156, 1949.

[Rob76] M.T. Robinson. The theory of radiation induced defect production. In N.L. Peterson and S.D. Harkenss, editors, *Radiation Damage in Metals*, pages 1–27. American Society for Metals Publication, 1976.

[S+89] Y. Shi et al. A numerical study of cluster center formation in neutron–irradiate silicon. *J. Appl. Phys.*, 67:1116–1118, 1989.

[S+99] G.P. Summers et al. Damage correlations in semiconductors exposed to gamma, electron and proton radiation. *IEEE Transactions on Nuclear Science*, 40:p.1372–1379, 1999.

[Sou06] J. Soukup. LUCID: Technical design report. CERN EDMS ATL-UL-ES-0001, 2006.

[Spi05] H. Spieler. *Semiconductor Detector Systems*. Oxford University Press, 2005.

[SR52] W. Shockley and W.T. Read. Statistics of the recombination of holes and electrons. *Phys. Rev.*, 87:835–842, 1952.

[Sze81] S.M. Sze. *Physics of Semiconductor Devices*. John Wiley and Sons, Inc., 2nd edition, 1981.

[Sze02] S.M. Sze. *Semiconductor Devices: Physics and Technology*. John Wiley and Sons, Inc., 2nd edition, 2002.

[T^+02] J. Treis et al. A modular pc based silicon microstrip beam telescope with high speed data acquisition. *Nucl. Instr. Methods A*, 490:112–123, 2002.

[Tar] D. Tardif. Beam accident signatures in the ATLAS BCM. Beam–induced backgrounds and radiation losses, CERN, June 12th 2008.

[Thu75] C.D. Thurmond. The standard thermodynamic functions for the formation of electrons and holes in Ge, Si, GaAs, and GaP. *J. Electrochem. Soc.*, 122:1133–1141, 1975.

[Tre02] J. Treis. *Development and operation of novel PC based high speed beam telescope for particle tracking using souble sided silicon microstrip detectors*. PhD thesis, Universität Bonn, 2002.

[Y^+06] W. M. Yao et al. Review of particle physics. *J. Phys. G*, 33:1, 2006.

[Z^+60] S. Zwerdling et al. Internal impurity levels in semiconductors: experiments in p-type silicon. *Phys. Rev. Lett.*, 4(4):173–176, 1960.

[Z^+93] S. Zhao et al. volume 302, page 257. Material Research Society Symposium Proceedings, 1993.

[$\check{Z}^+99$] D. Žontar et al. Time development and flux dependence of neutron-irradiation induced defects in silicon pad detectors. *Nucl. Instr. Methods A*, 426:51–55, 1999.

[Zha94] S. Zhao. *Characterization of the Electrical Properties of Polycrystalline Diamond Films*. PhD thesis, Ohio State University, 1994.

APPENDIX A

PROPERTIES OF SILICON AND DIAMOND

Property	Silicon	Diamond
Atomic number	28.09	12.01
Mass density ρ_m [g/cm^3]	2.329 [Sze02]	3.515 [Lut99]
Proton number	14	6
Breakdown electric field ε^{br} [V/cm]	$\sim 3\times10^5$	$1–20\times10^6$
Dielectric constant ϵ	11.9	5.7
Energy gap E_g [eV]	1.12	5.47
Intrinsic resistivity ρ [Ωcm]	3.3×10^5 [Sze02]	$>10^{15}$
Mobility $\mu_{e,h}$ [cm^2/Vs]		
electron	1420	2150$\pm$200
hole	470	1700$\pm$280
Saturation velocity $v_{e,h}^{sat}$ [cm/s]		
electron	10^7	1.5×10^7
hole	9×10^6	1.05×10^7
Displacement energy E_R [eV]	11–25 [CRG]	37–48 [K$^+$01]
Average number of electron–hole pairs in 100 μm created by 1 MIP	8000	3600
Energy to create electron–hole pair [eV]	3.6 eV [Bic88]	13 eV [K$^+$75, C$^+$79b]
MIP ionisation loss [MeV/cm]	2.9 [Zha94]	4.7 [Zha94]

Table A.1: *Structural and electronic properties of silicon and natural diamond at 293 K. The values are taken from [PK95] unless stated otherwise.*

APPENDIX B

I–V MEASUREMENTS OF BARE DIAMONDS AND ASSEMBLIES

Diamond Sample	Current [A]			
	+1000 V on narrow side	**-1000 V on wide side**	**-1000 V on narrow side**	**+1000 V on wide side**
A230-2	1.8×10^{-11}	-4.3×10^{-11}	-3.2×10^{-9} -2.4×10^{-9}	4×10^{-10}
A230-9	3.2×10^{-11}	-2.1×10^{-11} -2.3×10^{-11}	-3.4×10^{-11}	4.4×10^{-11}
A382-7	9.6×10^{-10}	-8.2×10^{-10}	-5.3×10^{-11}	1×10^{-10}
A382-8	3.8×10^{-12}	-5.0×10^{-12}	-6.4×10^{-12}	9.6×10^{-12}
A382-9	2.5×10^{-12}	-4.4×10^{-12} -1.1×10^{-11}	-5.3×10^{-12}	1.2×10^{-11} 1.0×10^{-11}
A382-10	3.2×10^{-11}	-5.2×10^{-11}	-1.6×10^{-9}	1.4×10^{-9} 2.3×10^{-9}
A382-11	3.0×10^{-11}	-1.7×10^{-11}	-1.8×10^{-11}	1.8×10^{-11}
A382-12	5.4×10^{-10}	-2.9×10^{-10}	-7.5×10^{-12}	1.3×10^{-11}
A382-15	7.6×10^{-12} 6.7×10^{-11}	-2.7×10^{-11} -2.7×10^{-11}	-1.8×10^{-8} -1.4×10^{-9}	2.0×10^{-9} 1.7×10^{-9}
A422-3	9.2×10^{-11}	-8.2×10^{-11}	-3×10^{-11}	4.6×10^{-11}
A422-4	3.6×10^{-9}	-4.9×10^{-9}	-3.5×10^{-11}	3.8×10^{-11}
A422-6	2.2×10^{-12}	-4.2×10^{-12}	-1.3×10^{-12}	3.6×10^{-12}
A422-9	2.1×10^{-11}	-2.2×10^{-11}	-1.5×10^{-11}	1.7×10^{-11}
A422-11	8.3×10^{-9}	-1.2×10^{-10}	-3.7×10^{-12}	3.5×10^{-12}
CDS-160	2.1×10^{-8}	-3.2×10^{-10}	-5.6×10^{-10}	1.2×10^{-9}
CDS-161	2.2×10^{-11}	-5.4×10^{-11}	-2.2×10^{-9}	2.1×10^{-9}
A230-8	6.9×10^{-11}	-4.4×10^{-11}	-2.0×10^{-11}	1.1×10^{-11}
A230-10	8.7×10^{-11}	-8.0×10^{-11}	-2.4×10^{-10}	4.4×10^{-10}
A422-5	5.7×10^{-10}	-3.8×10^{-10}	-6.4×10^{-12}	8.9×10^{-12}
A422-7	1.9×10^{-9}	-3.8×10^{-10} -2.4×10^{-9}	-8.5×10^{-10}	1.7×10^{-10}
46TO-1	1.9×10^{-10}	-2.0×10^{-10}	-6.8×10^{-9}	1.4×10^{-9}
46TO-4	4.4×10^{-10}	-1.5×10^{-10}	-1.9×10^{-11}	9×10^{-9}

Table B.1: *Currents of pCVD diamond samples at $\pm$1000 V, extracted from I–V measurements. The first sixteen samples in table were mounted in detector module installed in ATLAS, while others were used to assemble spare modules.*

Ass.	Upper Diamond	Lower Diamond	Current [A] at		Current stability at	
			+1000 V	-1000 V	-1000 V	+1000 V
C1	A382-11w	A382-8n	7.6×10^{-11}	-1.6×10^{-11}		
C2	A382-15w	A382-12w	8×10^{-10}	-4.2×10^{-8}	after 8h $\sim$3.5nA	
C3	A230-2n	CDS-161w	3.5×10^{-11} 6×10^{-11}	-3.3×10^{-9}	after 9h <30nA	
C6	A422-4w	A422-3n	3.5×10^{-11}	-2.3×10^{-11}	after 0.5h <40pA	after 0.5h <1nA
C9	A230-9n	A422-6n	5×10^{-11}	-5×10^{-11}	after 2.4h $\sim$6nA	after 2.4h <4nA
C10	A382-9n	A422-11w	6.3×10^{-11}	-3.5×10^{-11}	after 2.4h <7nA	after 2.4h <0.15nA
C11	A382-7n	CDS-160n	3.7×10^{-8}	-9.1×10^{-11}	after 2.4h $\sim$0.1μA	after 2.4h $\sim$12nA
C5	A382-7w	CDS-160n	2.6×10^{-8}	-1×10^{-9}	after 2.4h <250nA	after 2.5h $\sim$20nA
C7	A422-7n	A422-5w	1.3×10^{-9} 2.5×10^{-9}	-1.9×10^{-8}	after 24h $\sim$17nA	after 24h $\sim$55nA
C14	A382-10w	A422-9w	5×10^{-9}	-2.2×10^{-11}	after 3.8h $\sim$9nA	after 3.8h $\sim$2nA
C15	A230-10w	A230-8w	1×10^{-10}	-1.4×10^{-10}	after 3.8h <1.4nA	after 3.8h <0.1μA
C16	46TO-4w	46TO-1n	4.1×10^{-11}	-2.8×10^{-9}	after 3.8h $\sim$80nA	after 3.8h $\sim$20nA

Table B.2: *Currents of diamond ceramic assemblies at $\pm$1000 V, extracted from I–V measurements (columns 4 and 5) and currents of diamond ceramic assemblies measured after voltage of $\pm$1000 V was applied for a certain time (column 6 and 7). Columns 2 and 3 report the diamonds and their orientation in the assembly. Here "w" denotes the case of diamond being oriented in a way that its wide side is facing away from the ceramic baseboard, similarly "n" refers to diamond's narrow side facing away from the baseboard. The BCM detector modules installed in ATLAS were equipped with first eight assemblies stated in the table.*

APPENDIX C

BCM DETECTOR MODULES

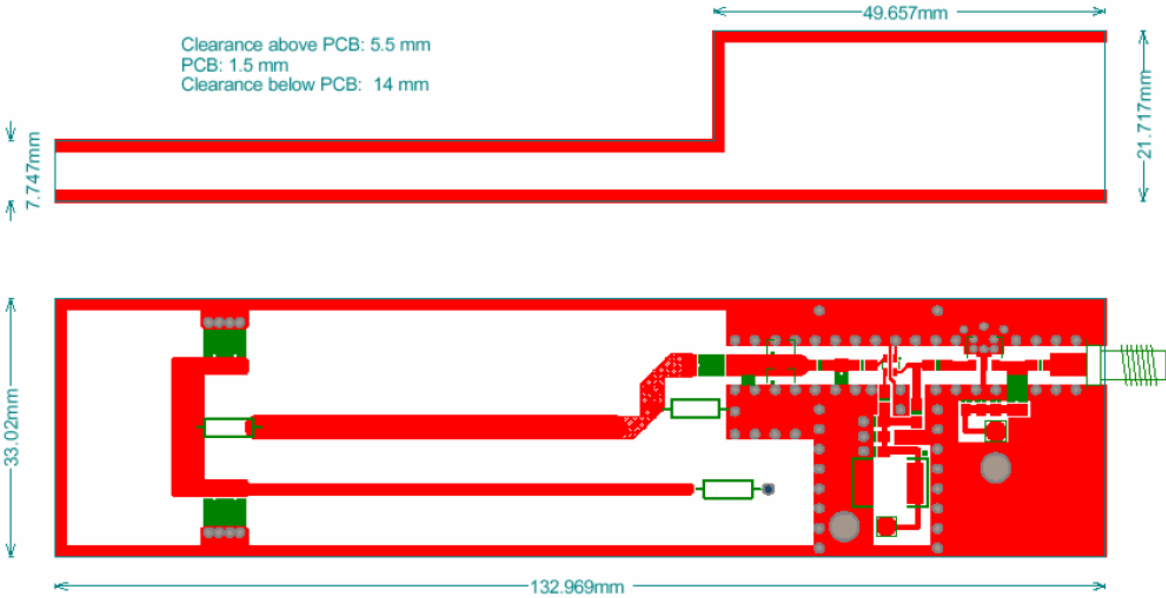

***Figure C.1:** Outer dimensions of final BCM modules F40X.*

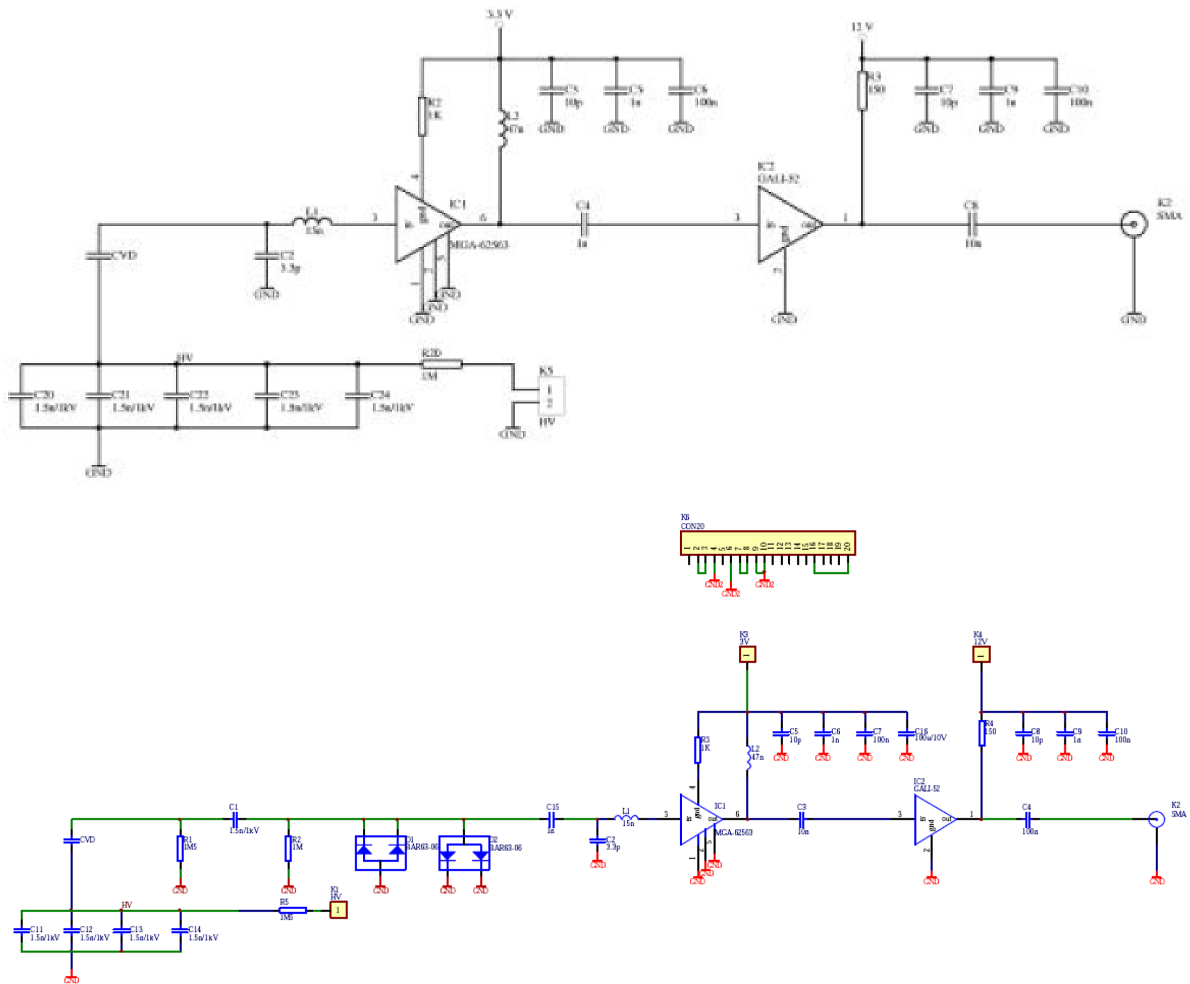

Figure C.2: *Schematic of the front end electronics in prototype (top) and final (bottom) BCM detector modules.*

APPENDIX D

NINO ELECTRONICS BOARD

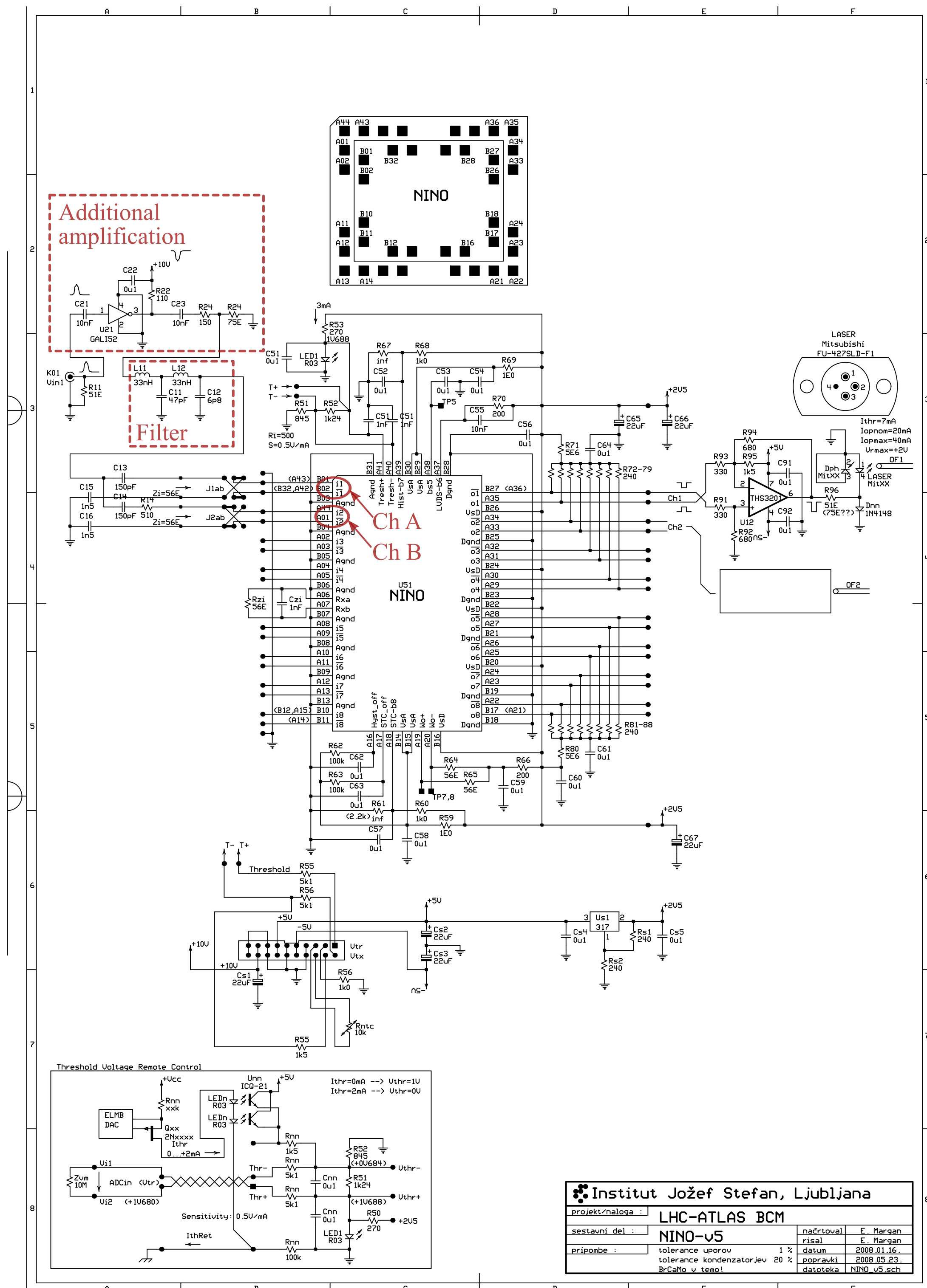

Figure D.1: *Final electronics board with NINO chip, used for digitisatino of ATLAS BCM analogue signals. The input signal is split with a ratio of about 1:11 into two inputs to NINO chip. The "Ch A" on the schematics markes the input with higher and "Ch B" the input with lower signal.*

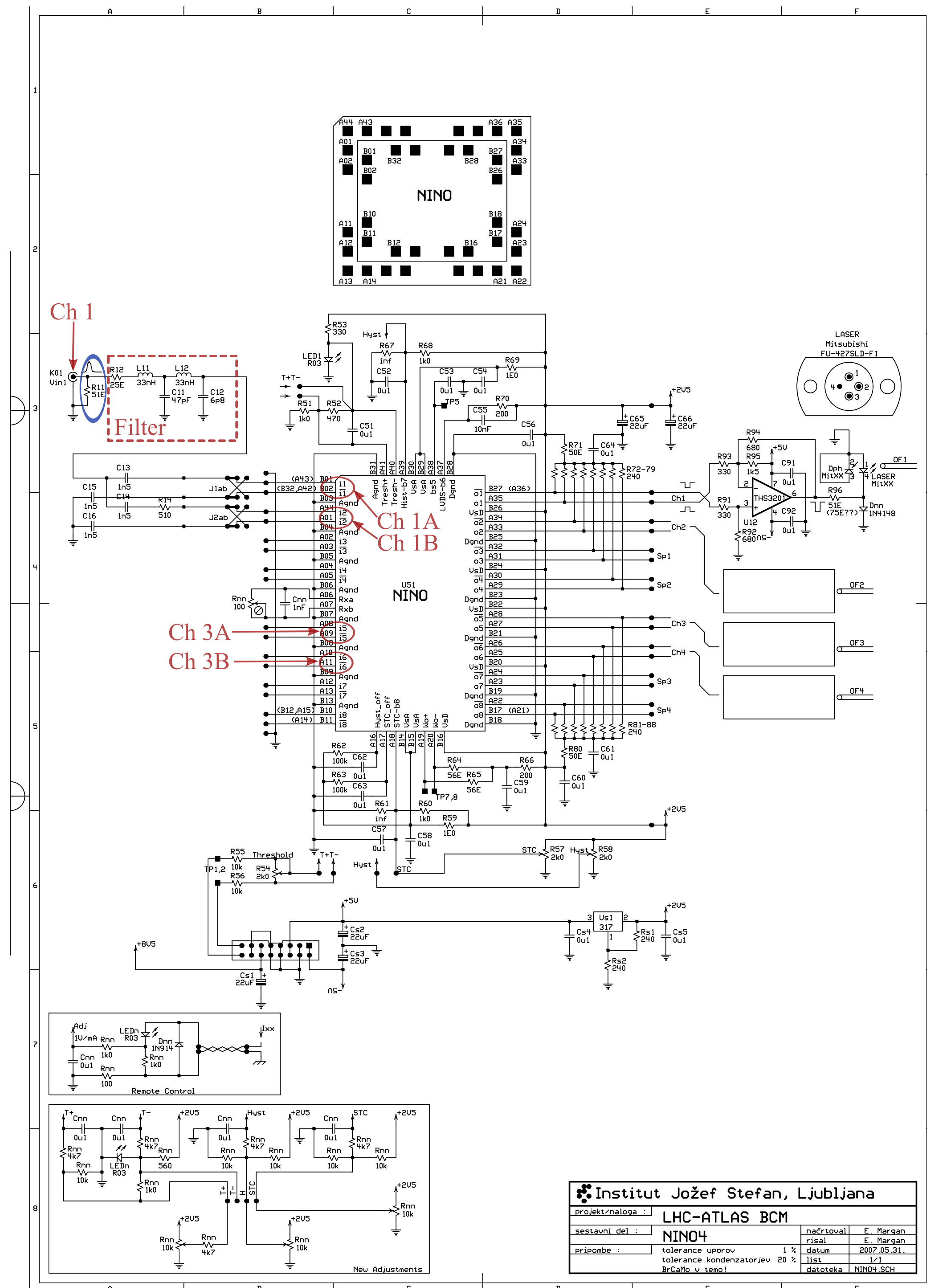

Figure D.2: *The NINO1 prototype electronics board. The NINO2 and NINO1 prototype boards had the resistor* R_{11} *(blue circle) removed. All prototype boards used had two input channels (Ch1, Ch3). Figure includes the schematic for one input channel which is split into two NINO chip inputs (Ch1A and Ch1B). The schematic for the other channel was identical.*

Spodaj podpisana Irena Dolenc izjavljam, da je disertacija rezultat samostojnega raziskovalnega dela.

Irena Dolenc

Ljubljana, 2008